

Catalytic substrate oxidation
by transition-metal NHC complexes in water

Yoshihiro Shimoyama

February 2019

Catalytic substrate oxidation
by transition-metal NHC complexes in water

Yoshihiro Shimoyama
Doctorial Program in Chemistry

Submitted to the Graduate School of
Pure and Applied Sciences
in Partial Fulfillment of the Requirements
for the Degree of Doctor of Philosophy in
Science

at
the University of Tsukuba

Contents

Chapter 1. General introduction

- 1-1 Substrate oxidation by metal-oxo/oxyl complexes in nature
- 1-2 Model complexes for metalloenzymes performing substrate oxidations
- 1-3 Importance of metal-oxyl species in benzene oxidation
 - 1-3-1 Copper-oxyl species for catalytic benzene hydroxylation
 - 1-3-2 "Oxo wall" between group 8 and 9 elements in the periodic table
 - 1-3-3 Iron-oxyl species for arene hydroxylation
 - 1-3-4 Strategies to generate "highly reactive" M-O• species with group 8 elements
- 1-4 Properties of *N*-heterocyclic carbene (NHC)
 - 1-4-1 Fundamentals of NHC
 - 1-4-2 Catalytic reactions by Ru-NHC complexes
 - 1-4-3 Catalytic reactions by Pd-NHC complexes
- 1-5 Purpose of this research
- Reference and notes

Chapter 2. Redox properties of ruthenium(II) complexes having two NHC moieties

- 2-1 Introduction
- 2-2 Synthesis and characterization of $[\text{Ru}^{\text{II}}(\text{C}^{\wedge}\text{Py}^{\wedge}\text{C})(\text{bpy})(\text{L})](\text{PF}_6)_n$ (L = MeCN, n = 2 (**1**); L = Cl, n = 1 (**2**))
- 2-3 Structural analysis in solid and solution states of $[\text{Ru}^{\text{II}}(\text{C}^{\wedge}\text{Py}^{\wedge}\text{C})(\text{bpy})(\text{L})](\text{PF}_6)_n$
- 2-4 Photochemical properties of $[\text{Ru}^{\text{II}}(\text{C}^{\wedge}\text{Py}^{\wedge}\text{C})(\text{bpy})(\text{L})](\text{PF}_6)_n$
- 2-5 Redox properties of $[\text{Ru}^{\text{II}}(\text{C}^{\wedge}\text{Py}^{\wedge}\text{C})(\text{bpy})(\text{L})](\text{PF}_6)_n$
- 2-6 Conclusions
- 2-7 Experimental section
- Reference and notes

Chapter 3. A ruthenium(III)-oxyl complex bearing strong radical character

- 3-1 Introduction
- 3-2 Synthesis and characterization of $[\text{Ru}^{\text{III}}(\text{BPIIm})(\text{bpy})(\text{L})]^{n+}$ (L = Cl, n = 1 (**5**); L = OH₂, n = 2 (**6**))
- 3-3 Synthesis and characterization of $[\text{Ru}^{\text{III}}(\text{BPIIm})(\text{bpy})(\text{OH}_2)](\text{ClO}_4)_3$ (**7**·(ClO_4)₃)
- 3-4 Formation and characterization of $[\text{Ru}^{\text{III}}(\text{O}^{\bullet})(\text{BPIIm})(\text{bpy})]^{2+}$ (**8**)
- 3-5 Catalytic reactivity for substrate oxidation by **8** as reactive species
- 3-6 Conclusions
- 3-7 Experimental section
- Reference and notes

Chapter 4. Catalytic oxidative cracking of benzene rings in water

- 4-1 Introduction
- 4-2 Catalytic oxidative cracking of benzene rings (OBC) in acidic water
- 4-3 Scope and limitation of the catalytic OBC reactions
- 4-4 Mechanistic insights into the catalytic OBC reactions
- 4-5 Kinetic analysis on the catalytic OBC reactions

4-6 A proposed mechanism of the catalytic OBC reaction

4-7 Conclusions

4-8 Experimental section

Reference and notes

Chapter 5. Catalytic oxidative cracking of halogenated benzene derivatives by a palladium(II)-NHC complex in water

5-1 Introduction

5-2 Synthesis and characterization of a palladium(II)-NHC complex (**9**)

5-3 Catalytic OBC reactions of halogenated benzene derivatives

5-4 Scope and limitation in the OBC reaction of benzene- and halogenated-benzene derivatives

5-5 Mechanistic insights on the OBC reaction of dihalogenated benzenesulfonates

5-6 Formation and characterization of palladium-oxygen species

5-7 A proposed mechanism of the catalytic OBC reaction by **9** with Oxone[®]

5-8 Conclusions

5-9 Experimental section

Reference and notes

Concluding remarks

List of publications, supplementary publications and patents

Acknowledgements

Chapter 1

General introduction

1-1 Substrate oxidation by metal-oxo/oxyl complexes in nature

High-valent metal-oxo species are very important as reactive species in substrate oxidation by natural enzymes. For example, heme-containing oxygenation enzymes, cytochrome P450s (CytP450s), generate high-valent iron(IV)-oxo porphyrin π -radical cation species, so-called “Compound I”, by reductive activation of molecular oxygen by the heme-iron center.¹ Compound I in the CytP450 catalysis has a thiolate ligand derived from a cysteine residue at the *trans* position of the oxo ligand. The reaction cycle starts from formation of a high-spin iron(III) complex from the “Resting state” involving a low-spin iron(III) complex by capture of a substrate into the hydrophobic pocket near the active site, followed by removal of the axially-ligated water molecule (Figure 1-1). Then, $1e^-$ -reduction of the high-spin iron(III) center proceeds to form an iron(II) species, owing to the positive shift of the reduction potential for the iron(III) center due to the release of the aqua ligand. The iron(II) complex formed reductively activates dioxygen to form an iron(III)-superoxo complex. The iron(III)-superoxo species converts into an iron(III)-hydroperoxo species by $1e^-/1H^+$ proton-coupled electron-transfer (PCET) reduction. Finally, the reactive species, Compound I, is formed through O-O bond heterolysis of the hydroperoxo ligand to release a water molecule. Compound I oxidizes a variety of organic substrates, captured in the pocket, and turns into the starting low-spin iron(III)-aqua complex to complete the catalytic cycle (Figure 1-1).

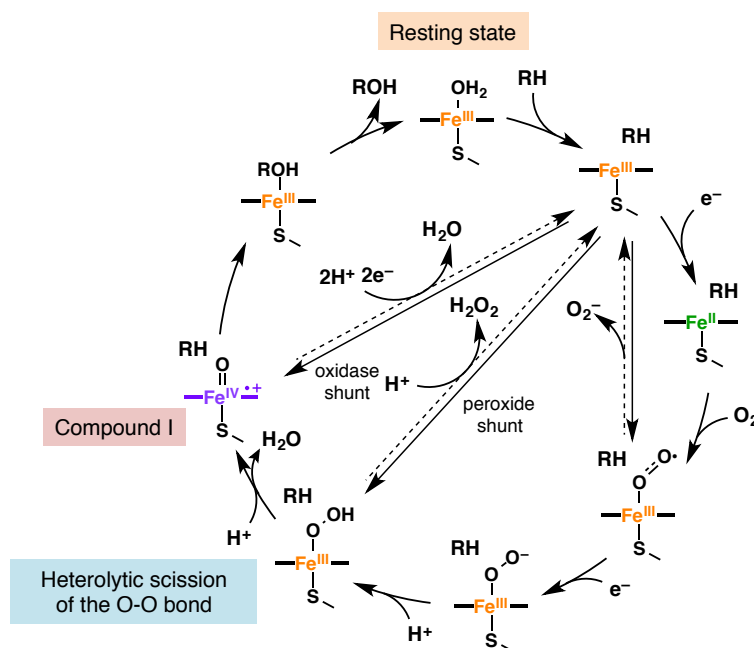


Figure 1-1. The catalytic cycle of substrate oxidation by cytochrome P450.¹

On the other hand, non-heme-type high-valent iron(IV)-oxo species are also found in oxidation enzymes.² For example, α -ketoglutarate-dependent taurine dioxygenase (TauD), which catalyze selective hydroxylation of taurine at the α -position, has been widely investigated.³ The reaction mechanism of TauD is described in Figure 1-2; the resting iron(II) species reacts with dioxygen to afford an iron(III)-superoxo species, and the distal oxygen atom of the superoxo ligand, not coordinating to the iron(III) center, reacts

with the bidentate α -ketoglutarate ligand to form a bicyclic complex. Then, an iron(IV)-oxo complex is formed through O-O bond homolysis, followed by decarboxylation of the α -ketoglutarate ligand. This reactive iron(IV)-oxo species obtained can abstract a hydrogen atom from taurine as a substrate and oxygenate it through an oxygen-rebound mechanism. The catalytic cycle is completed after

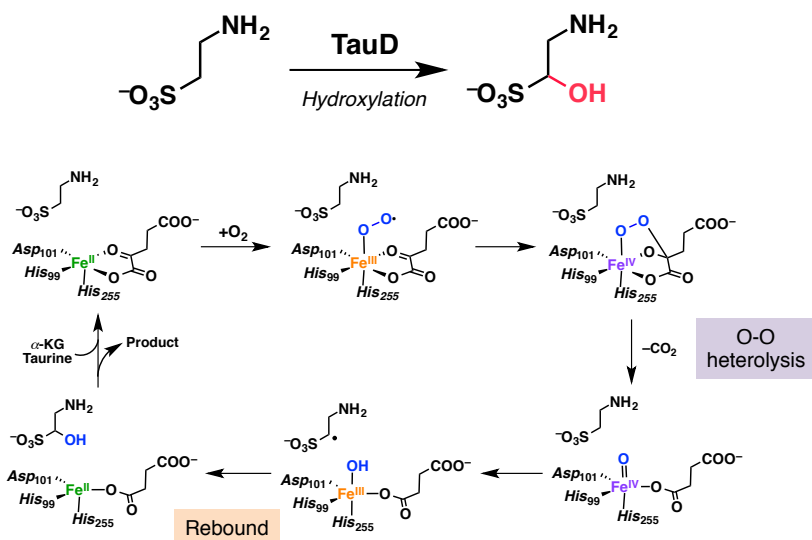


Figure 1-2. A proposed catalytic cycle of taurine hydroxylation by TauD.³

dissociation of the hydroxylated taurine and succinic acid, affording α -ketoglutarate and taurine molecules into the catalytic center.

As a non-heme iron enzyme, soluble methanemooxygenase (sMMO) is also widely known by the fact that it includes a bis(μ -oxo)-diiron(IV) species, which is called as “Compound Q”, as the active oxidant and can oxidize extremely stable methane to afford methanol with molecular oxygen as an oxidant under mild conditions (Figure 3).⁴ In MMOH_{Ox} as the resting state, the diiron center binds to four carboxylates of amino-acid residues, two imidazoles, and one water molecule, and the two iron centers are bridged by two hydroxo and one carboxylate ligands (Figure 1-3(b, left)). The MMOH_{Ox} is reduced to form MMOH_{Red} , which reacts with molecular oxygen to afford a diiron(III) species bridged by a peroxide ligand, so-called

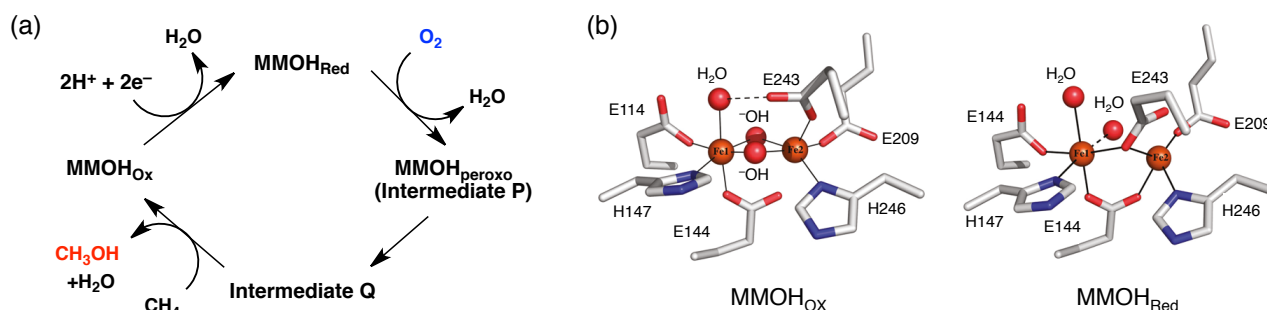


Figure 1-3. (a) Catalytic cycle of methane hydroxylation by sMMO.⁴ (b) Crystal structures of the diiron centers in MMOH_{Ox} (Protein data bank (PDB) ID: 1MTY, left) and MMOH_{Red} (PDB ID: 1FYZ, right).^{4d, 4e}

“Compound P”. In sMMO, compound P reacts with a proton to promote the O-O bond homolysis and afford “Compound Q”. In a density functional theory (DFT) study, the electronic structure of compound Q has been

proposed as not a diiron(IV) bis- μ -oxo species but an electronically equivalent iron(III)-iron(IV) mixed-valent species, bridged by one oxyl (O \bullet) and one oxo ligands (Figure 1-4).⁵

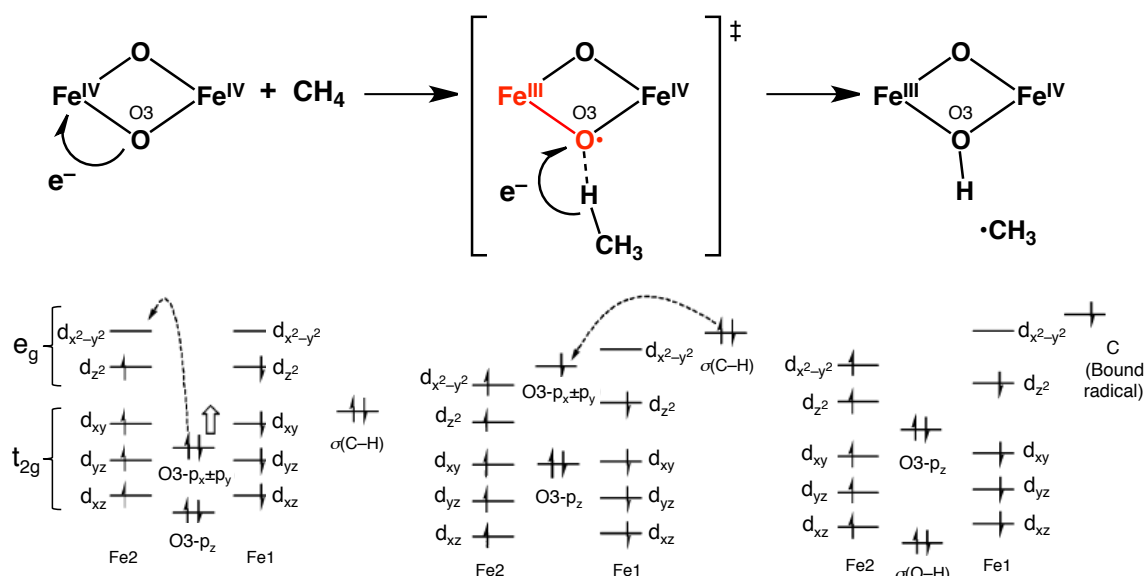


Figure 1-4. Schematic molecular orbitals of compound Q and the transition state of the hydrogen abstraction from methane, and formation of a radical intermediate, obtained by DFT calculations.⁵ The orbital energies are not drawn to scale and are only intended to show the qualitative pattern.

Monomeric copper-oxyl species have been also proposed as reactive intermediates in substrate oxidation reactions, catalyzed by copper-containing enzymes such as dopamine β -monooxygenase (D β M),⁶ peptidylglycine α -hydroxylating monooxygenase (PHM),⁷ lytic polysaccharide monooxygenases (LPMOs),⁸ on the basis of theoretical studies. For example, LPMOs utilize molecular oxygen and an electron donor to catalyze oxidative cleavage of insoluble polysaccharides.⁸ The active site of LPMO (Figure 1-5(a)) contains a mononuclear copper center ligated by two histidine residues. The reactive species for C-H oxidation is considered to be a Cu^{II}-O \bullet species, not Cu^{II}-O₂⁻ one, based on theoretical studies.⁸

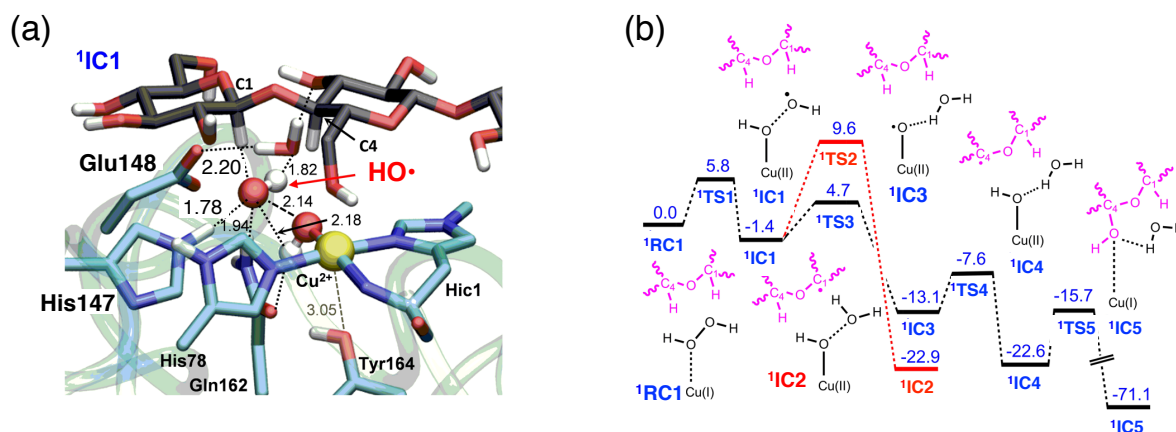


Figure 1-5. (a) Hydrogen-bonding network around the HO \bullet radical in an intermediate (¹IC1 in (a)) formed in LPMO active site. (b) Relative energies calculated by QM/MM methods (UB3LYP/B2, kcal/mol) for the reaction profile of the Cu^I-H₂O₂ intermediate formed in LPMO in the presence of polysaccharide.¹⁰

It is known that the LPMO catalysis can be activated also with use of hydrogen peroxide as an oxidant in the presence of sub-stoichiometric amount of an external reductant.⁹ The Cu^I-H₂O₂ adduct in LPMO has a singlet ground state, and it undergoes homolytic O-O bond cleavage to form a Cu^{II}-OH species and HO• radical with an activation barrier of 5.8 kcal/mol (Figure 1-5(b)).¹⁰ The HO• radical is fixed by strong hydrogen bonding with His147 (1.78 Å) and a water molecule (1.82 Å) (Figure 1-5(a)) and weak hydrogen bonding with Gln162 is also proposed (1.94 Å). Two possible pathways are considered for the substrate oxidation in LPMO: hydrogen-atom transfer (HAT) from the anomeric carbon of an adjacent sugar molecule by the trapped HO• radical (¹TS2 in Figure 1-5(a)), and HAT from Cu^{II}-OH to HO• to afford Cu^{II}-O• species as the reactive species for hydrogen atom abstraction from the anomeric carbon (¹TS3 in Figure 1-5(a)).¹⁰ The former pathway has a relatively large activation barrier compared to the latter pathway by 4.9 kcal/mol. It is suggested that the relatively lower activation barrier is derived from the fixation of the HO• radical by hydrogen bonding as mentioned above to direct the oxygen-centered radical in HO• to a C-H bond of the C4 position of a substrate (Figure 1-5(a)). Furthermore, this hydrogen-bonding network is assumed to prevent the HO• radical from moving outside from the hydrophobic site around the reaction center. The Cu^{II}-O• formed has a high spin density of 0.83 on the O atom and a long Cu-O bond of 1.89 Å, compared to those of other Cu-O bonds, which are estimated to be *ca.* 1.72 Å based on DFT calculations.¹¹ Reflecting the strong radical character of the Cu^{II}-O• species, HAT from the C4 position of the sugar requires to overcome a small activation barrier of only 5.5 kcal/mol. This result suggests that the Cu^{II}-O• is a highly reactive species for C-H activation.

As mentioned above, M-O• species, that has a terminal oxygen-centered radical bound to a metal center with a single bond, has been considered as a putative reactive species in substrate oxidation by natural enzymes.

1-2 Model complexes for metalloenzymes performing substrate oxidations

There have been a number of reports for substrate oxidation by model complexes inspired by biological substrate oxidation.^{2, 12} For example, iron-porphyrin complexes have been reported as model complexes of heme-containing oxidation enzymes.¹³ Groves and co-workers have investigated olefin and cycloalkane oxidation reactions by an iron(IV)-oxo porphyrin- π -radical cation species, formed by reactions of the corresponding iron(III)-porphyrin complexes with iodosylbenzene or *m*-chloroperbenzoic acid as oxidants, in organic solvent (Figure 1-6).¹⁴ The model complexes exhibited versatile and unique reactivity toward oxidation of organic substrates to afford the corresponding oxygenated products.

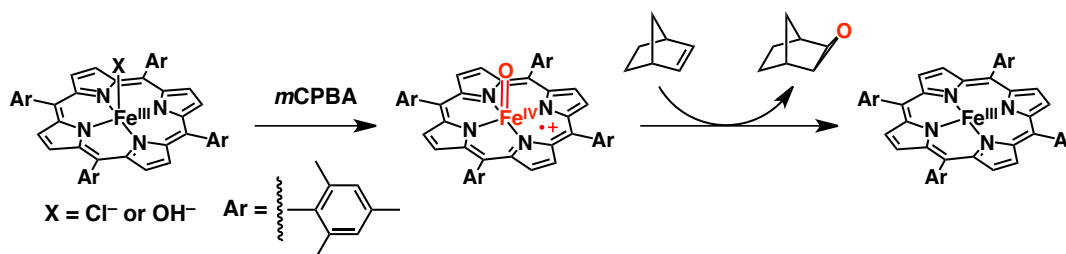


Figure 1-6. Substrate oxidation by a synthetic model of compound I, formed in CH₂Cl₂/MeOH = 4:1 (v/v) at -78 °C.^{14c}

Groves and Nam surveyed oxidation of styrene and ethylbenzene derivatives by iron(IV)-oxo porphyrin- π -radical cation species, having perfluorophenyl groups at the *meso* position of the porphyrin

ligand, in CH_2Cl_2 at -80°C .^{14, 15} In the kinetic analysis on oxidation of styrene derivatives, Hammett plots were provided for the second-order rate constants to discuss the electronic effects of substituents on styrene derivatives. The plots have showed a slope (ρ) of -0.9 for the reactions by the $\text{Fe}^{\text{IV}}=\text{O}$ complex having Cl^- as an axial ligand at the *trans* position of the oxo ligand, whereas a slope of -1.8 for those having trifluoromethanesulfonate (OTf^-) as an axial ligand (Figure 1-7(b)).¹⁵ This indicates that the electronic effects of substituents on styrene derivatives for styrene epoxidation were smaller in the case of the Cl^- ligand as an axial ligand, compared to the case using OTf^- as the axial ligand due to the *trans* influence of the axial ligands (Figure 1-7(b)).¹⁵ In a literature reported by Gross and Nimri, the axial-ligand effect was explained by destabilization of the $\text{Fe}^{\text{IV}}=\text{O}$ bond due to a strongly σ -donating axial ligand.¹⁶ As exemplified by this example, axial ligands at the *trans* position of oxo ligands strongly influence the reactivity of iron(IV)-oxo porphyrin- π -radical cation species toward olefin epoxidation.

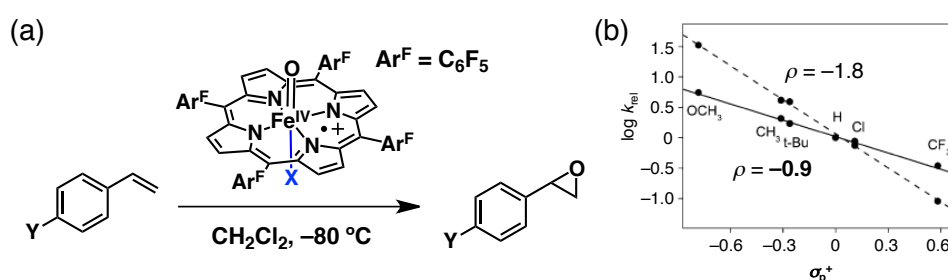


Figure 1-7. (a) Epoxidation of styrene derivatives by $[\text{Fe}^{\text{IV}}(\text{O})(\text{X})(\text{TPP-F}_{20}^{*\text{+}})]^{2+}$ ($\text{X} = \text{OTf}$ or Cl) (b) Hammett plots for relative second-order rate constants ($k_{\text{X}}/k_{\text{H}}$) for epoxidation of styrene derivatives ($\text{Y} = \text{OCH}_3, \text{CH}_3, t\text{-Bu}, \text{H}, \text{Cl}, \text{CF}_3$) by $[\text{Fe}^{\text{IV}}(\text{O})(\text{X})(\text{TPP-F}_{20}^{*\text{+}})]^{2+}$ (dashed line: $\text{X} = \text{OTf}$, solid line: $\text{X} = \text{Cl}$).¹⁵

Nam and co-workers have also reported catalytic hydroxylation of ethylbenzene with an *in-situ* generated iron(IV)-oxo porphyrin π -radical cation complex under various reaction conditions.¹⁵ In the study, hydroxylation of ethylbenzene by $[\text{Fe}^{\text{IV}}(\text{O})(\text{X})(\text{TPP-F}_{20}^{*\text{+}})]^{2+}$ ($\text{X} = \text{MeCN}$ or Cl) afforded different product distributions; phenylethanol was obtained upon using $[\text{Fe}^{\text{IV}}(\text{O})(\text{Cl})(\text{TPP-F}_{20}^{*\text{+}})]^{2+}$, whereas ethylbenzoquinone was obtained upon using $[\text{Fe}^{\text{IV}}(\text{O})(\text{X})(\text{TPP-F}_{20}^{*\text{+}})]^{2+}$ ($\text{X} = \text{MeCN}$ or OTf). This result indicates that the regio-selectivity in ethylbenzene hydroxylation by $[\text{Fe}^{\text{IV}}(\text{O})(\text{X})(\text{TPP-F}_{20}^{*\text{+}})]^{2+}$ depends on its axial ligands, “X” (Figure 1-8); however, rational explanation for this regio-selectivity was not provided.¹⁵

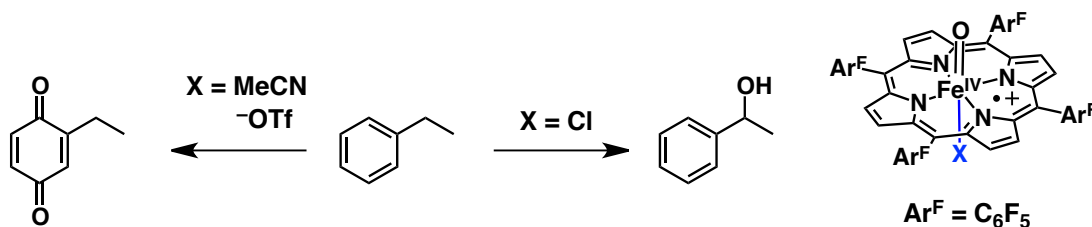


Figure 1-8. Regio-selectivity by axial ligands in ethylbenzene oxidation by $[\text{Fe}^{\text{IV}}(\text{O})(\text{X})(\text{TPP-F}_{20}^{*\text{+}})]^{2+}$.¹⁵

Model compounds for iron(IV)-oxo reactive intermediates in non-heme iron enzymes have been also reported;² for example, Que and co-workers reported a non-heme iron(IV)-oxo complex bearing a pentadentate pyridylamine ligand, $[\text{Fe}^{\text{IV}}(\text{O})(\text{N4Py})]^{2+}$ (Figure 1-9, left), which can oxidize aliphatic alkanes such as cyclohexane or 2,3-dimethylbutane at room temperature (Figure 1-9).¹⁷ $[\text{Fe}^{\text{IV}}(\text{O})(\text{N4Py})]^{2+}$ showed

remarkable reactivity in hydroxylation of C-H bonds of cyclohexane having a BDE value of 99.3 kcal/mol. In addition, plots of logarithm of the second-order rate constants (k_2) for C-H oxidation of various substrates by $[\text{Fe}^{\text{IV}}(\text{O})(\text{N4Py})]^{2+}$ against bond-dissociation energy (BDE) values of the substrates showed linear correlation (Figure 1-9, right). This indicates the oxidation of substrates proceeds through hydrogen-atom abstraction in a common pathway.¹⁷

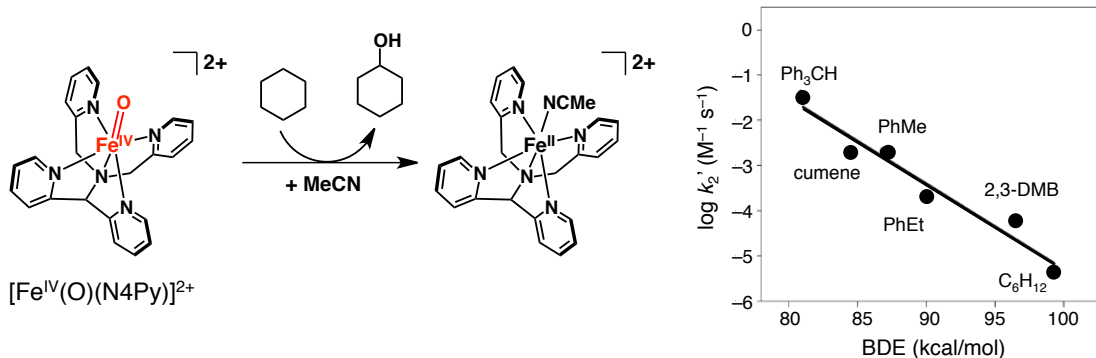


Figure 1-9. Substrate oxidation by $[\text{Fe}^{\text{IV}}(\text{O})(\text{N4Py})]^{2+}$ as a model complex for iron(IV)-oxo species in non-heme iron enzymes (left) and logarithm plots of 2nd-order rate constants in substrate oxidation by $[\text{Fe}^{\text{IV}}(\text{O})(\text{N4Py})]^{2+}$ (black filled circles) against their BDE values (right).¹⁷

Furthermore, Que, Nam, and their co-workers reported the effects of σ -donating ability of axial ligands at the *trans* position of the oxo ligand in an iron(IV)-oxo complex, having tetramethylcyclam (= 1,4,8,11-tetramethyl-1,4,8,11-tetraazacyclotetradecane), on the reaction rates for dihydroanthracene oxidation in MeCN (Figure 1-10).¹⁸ In this study, MeCN, CF_3COO^- , N_3^- , and a thiolate derivative (RS^-) were employed as the axial ligands; the reactivity of the iron(IV)-oxo complexes increased in this order. The RS^- is known to exert strong σ -donation, and compound I in the CytP450s also has this-type thiolate ligand as the axial ligand. The tendency revealed by Nam and co-workers indicates that the σ -donation of axial ligands at the *trans* position to the oxo ligand increases the reactivity not only of iron(IV)-oxo porphyrin π -radical cation complexes but also of non-heme iron(IV)-oxo species.

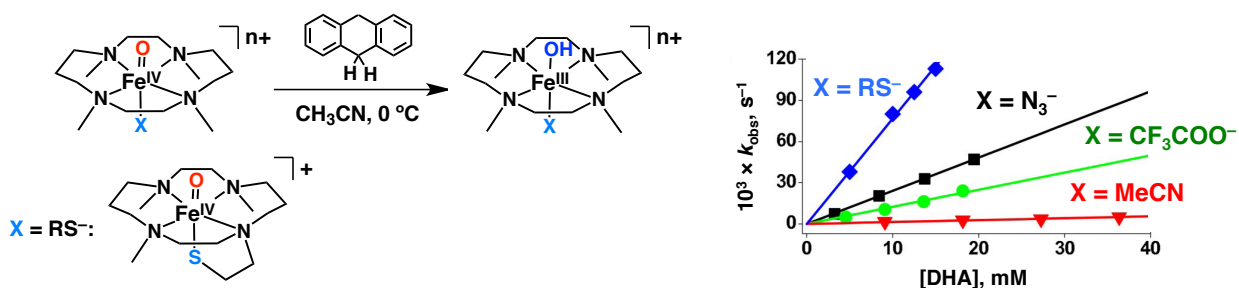


Figure 1-10. Axial-ligand tuning of the reactivity of $[\text{Fe}^{\text{IV}}(\text{O})(\text{TMC})(\text{X})]^{n+}$ ($n = 1$ for $\text{X} = \text{N}_3^-$, CF_3COO^- , $n = 2$ for $\text{X} = \text{NCMe}$) in dihydroanthracene (DHA) oxidation.¹⁸

As exemplified by the high-valent metal-oxo species described above, the reactivity of metal-oxo complexes in substrate oxidation can be enhanced by the introduction of electron-donating axial ligands, which can perturb the electronic structures of metal-oxo species to enhance the reactivity. On the basis of this strategy to increase the reactivity of metal-oxo complexes, synthetic metal-oxo species can perform

oxidation of highly inert substrates such as benzene and methane.

1-3 Importance of metal-oxyl species in benzene oxidation

Benzene is one of the most stable compounds against oxidative decomposition, since the bond dissociation energy of C-H bonds in benzene is 111 kcal/mol,¹⁹ which is even larger than that of methane (105 kcal/mol). In addition, benzene has a significantly high oxidation potential (+2.46 V vs SCE),²⁰ which prevents benzene from undergoing 1e⁻-oxidation. However, there have been a lot of reports about metal-oxygen species that can oxidize benzene at ambient temperature (See below).

1-3-1 Copper-oxyl species for catalytic benzene hydroxylation

Kodera and coworkers have recently reported selective hydroxylation of benzene catalyzed by a dicopper(II) complex, having an ethylene-bridged polypyridyl ligand, [Cu₂(μ-OH)(6-hpa)](ClO₄)₃ (6-hpa = 1,2-bis(2-(bis(2-pyridylmethyl)aminomethyl)-6-pyridyl)ethane) (**Cu₂(6-hpa)**), with H₂O₂ as a sacrificial oxidant (Figure 1-11).²¹ The main product from the reaction was identified as phenol based on gas chromatography and ¹H NMR spectroscopic analysis. A time profile of the phenol production catalyzed by **Cu₂(6-hpa)** revealed the highest turnover frequency (TOF) of 1010 h⁻¹ and the highest turnover number (TON) of 12,000 after 40 h, compared to other homogeneous catalysts with H₂O₂ as an oxidant.²² Upon using a 1:1 mixture of C₆H₆ and C₆D₆ as a substrate, kinetic isotope effect (KIE) was determined as 1.04, which indicates that C-H bond cleavage of benzene is not involved in the rate-limiting step. In addition, the active species of benzene hydroxylation obtained from **Cu₂(6-hpa)** is probably not a hydroxyl radical (•OH), since KIE values reported for Fenton-type reactions are in the range of 1.7 – 1.8.²³

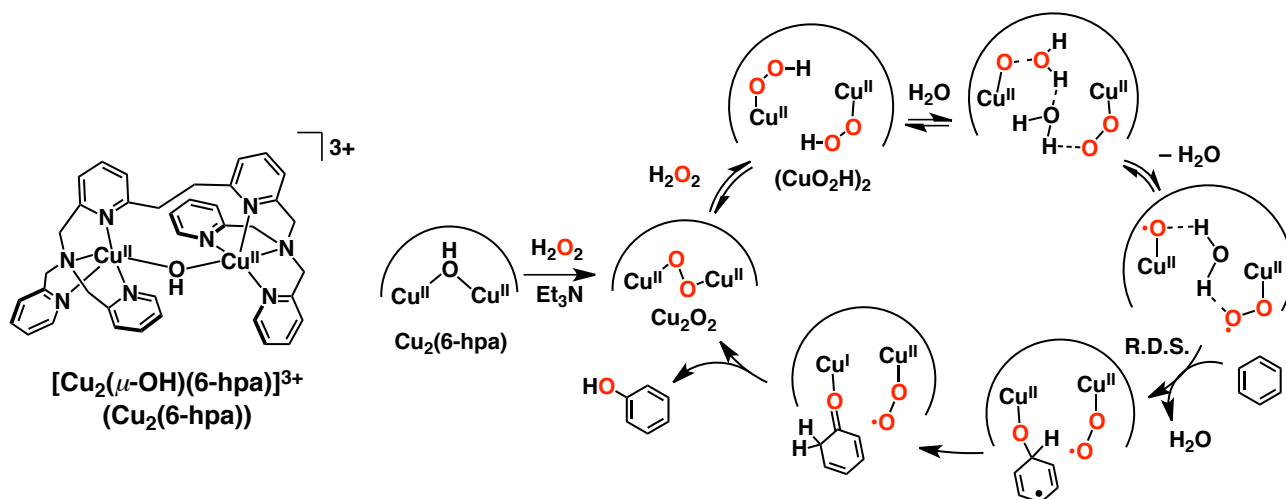


Figure 1-11. A proposed mechanism of H₂O₂ activation by [Cu₂(μ-OH)(6-hpa)]³⁺ (**Cu₂(6-hpa)**) and its benzene hydroxylation.²¹

In the case of nitrobenzene, toluene or phenol used as substrates, initial TOFs are in the order as follows: phenol ~ toluene >> nitrobenzene. This indicates that higher electron density of the aromatic ring in the substrate gives a higher initial TOF value. Therefore, the reactive species formed from the catalyst should bear an electrophilic character in the benzene hydroxylation. The regio-selectivity of the oxidation sites for the substrates was revealed to be the *ortho* and *para* positions for toluene, the *ortho* positions for nitrobenzene, and the *para* position for phenol, which also implies that the active species generated from the

catalyst have an electrophilic radical character, *i.e.* a copper-bound oxyl radical.

Upon addition of 1 equiv of H₂O₂ to Cu₂(6-hpa) in MeCN containing Et₃N (5.0 equiv) at -40 °C, an end-on *trans*-peroxodicopper(II) complex (Cu₂O₂) was obtained (Figure 1-11, middle). On the other hand, upon addition of an excess amount of H₂O₂ to Cu₂(6-hpa), the Cu₂O₂ complex rapidly reacted to afford bis(hydroperoxo-copper(II)) complex ((CuO₂H)₂, Figure 1-11). The two intermediates, Cu₂O₂ and (CuO₂H)₂, have been characterized by resonance Raman spectroscopy, where Cu₂O₂ and (CuO₂H)₂ showed Raman bands at 821 and 846 cm⁻¹, respectively. These bands were isotopically shifted by 43 and 53 cm⁻¹, respectively, with addition of H₂¹⁸O₂. These Raman bands are assigned to the O-O stretching bands of the peroxy or hydroperoxy ligands, on the basis of the Raman shifts for those reported so far.²⁴ Since the reaction rate of this conversion process of Cu₂O₂ showed saturation behavior against the H₂O₂ concentration, a pre-equilibrium process should be operative involving the Cu₂O₂ complex and H₂O₂.²¹ Kodera and coworkers have argued reaction pathways based on DFT calculations; however, any direct evidences have not been provided to support the formation of Cu^{II}-O• or Cu^{II}-OO• species. In the reaction mechanism, it is proposed that the (CuO₂H)₂ complex releases a H₂O molecule reversibly and the hydrogen bonding of the H₂O molecule with an oxyl ligand bound to the Cu^{II} center stabilizes the Cu^{II}-oxyl and peroxy species (Figure 1-11).

Catalytic benzene hydroxylation reactions to afford phenol have been also reported by Pérez and co-workers, using Cu^I(Tp^X)(NCMe) complexes (Tp^X = hydrotrispyrazolylborate derivatives) as catalysts and H₂O₂ as an oxidant in MeCN.²⁵ The Cu^I catalysts react with H₂O₂ to generate monomeric Cu^{II}-O• species, probably through the O-O bond heterolysis of H₂O₂ (Figure 1-12). The catalytic systems have provided phenol with 92% selectivity and benzoquinone in 8% yield. The KIE value of the benzene hydroxylation was determined to be 1.12 ± 0.01 with use of an equimolar mixture of C₆H₆ and C₆D₆ as a substrate. The KIE value is also out of the range (1.7 – 1.8) of those reported for Fenton-type hydroxylation of benzene.²³ In this case, the formation of bis-aryl derivatives derived from homo-coupling of aryl radicals as one of typical products was not observed. Furthermore, the benzene conversion into phenol is not significantly affected even in the presence of radical-trapping reagents such as CCl₄ or CBrCl₃, and chloro- or bromobenzene were obtained in very low yields (*ca.* 0.5%). These results indicate that the main pathway in the benzene hydroxylation reaction should not involve generation of phenyl radicals.²⁶ In addition, electronic substituent effects on the benzene ring have been surveyed for the benzene hydroxylation and negative slopes were observed in the Hammett plots: ρ = -0.75 for Cu(Tp^{*Br})(NCMe) and -1.1 for Cu(Tp^{Br3})(NCMe). The negative slopes indicate electrophilic character of the Cu-O• complexes as the reactive species.²⁷

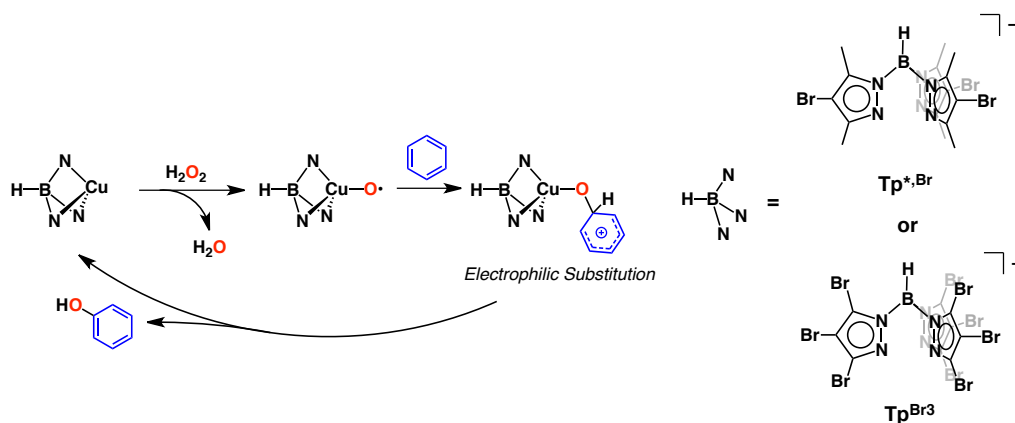


Figure 1-12. Schematic representation of benzene oxidation to phenol, catalyzed by Cu^I(Tp^X)(NCMe).²⁵

As described above, metal-oxyl species are highly important for oxidation of extremely inert aromatic compounds through an electrophilic attack mechanism under mild conditions. Therefore, formation of metal-oxyl species is one of promising strategies to develop efficient catalytic oxidation of organic substrates, which should be hard to be functionalized by traditional metal-oxo complexes under mild conditions.

1-3-2 “Oxo wall” between group 8 and 9 elements in the periodic table

In high-valent metal-oxo species, a double or triple bond is formed between the metal center and oxygen atom, where the π electrons of the oxide anion form a π bond with a vacant $d\pi$ orbital of the metal ion.²⁸ As previously described by Gray and Winkler, there is a wall between group 8 and 9 transition metal in periodic table named as “oxo wall”, which divides whether multiple bond can be formed or not between a metal center and the oxo ligand (Figure 1-13).^{29,30} In light of the concept, the earlier elements than group 8 in the +IV state can form double or triple bonds with the oxo ligand. On the other hand, the later elements than

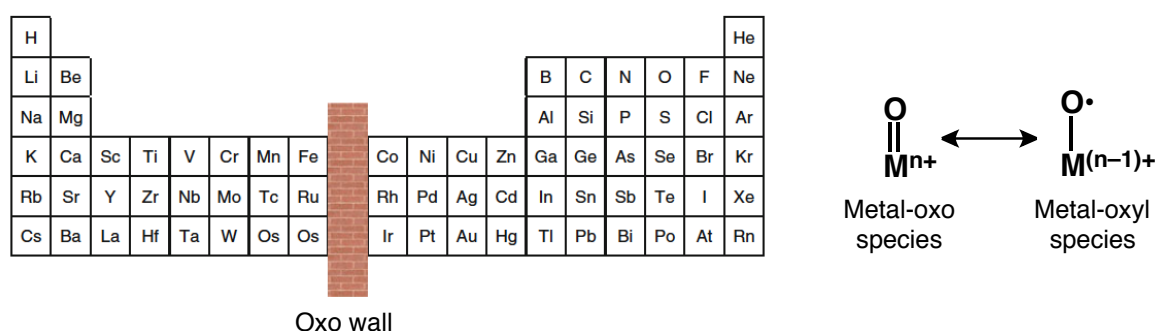


Figure 1-13. “Oxo wall” between group 8 and 9 elements in the periodic table (left) and resonance structures of metal-oxo and metal-oxyl species (right).²⁹

the group 9 in the +IV state cannot form multiple bonds with an oxo ligand to afford metal-oxyl (M-O•) complexes, due to the occupation of the π^* orbitals of the metal center.³¹ It is considered as one of resonance structures of a metal-oxo complex.

As described above, copper lies on the right side of the “oxo wall”, and thus copper cannot form multiple bonds with a terminal oxido ligand. In contrast to Cu-oxyl complexes, metal(IV)-oxo species consisting of a metal ion in the left side of the “oxo wall” (e.g. iron, ruthenium, osmium, ...) are predicted not to oxidize benzene molecules, since in general they can not form metal-oxyl species.

1-3-3 Iron-oxyl species for arene hydroxylation

Cytochrome P450s are known to oxidize a benzene molecule catalytically at ambient temperature.³² Due to the chemical inertness of benzene, cytochrome P450s can not oxidize a benzene molecule through

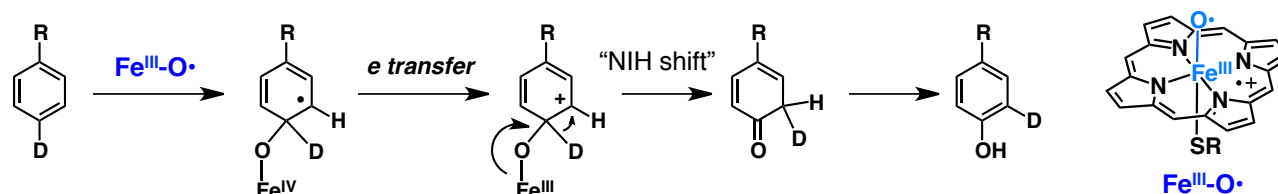


Figure 1-14. An alternative mechanism in benzene hydroxylation by iron(IV)-oxyl species through the NIH shift.³⁴

hydrogen-atom abstraction as observed in their alkane oxidation nor through a $1e^-$ oxidation processes. These assumptions are also suggested by the small isotope effects (0.95 – 1.27), determined for oxidation of deuterium-labeled chlorobenzene derivatives by cytochrome P450s.³³ As an alternative mechanism of benzene hydroxylation, non-concerted addition of an iron(IV)-oxyl species to the aromatic ring is proposed for the reaction catalyzed by an ammonia monooxygenase of *Nitrosomonas europaea*, one of heme-containing enzymes, on the basis of “NIH shift” (NIH = National Institutes of Health) (Figure 1-14).³⁴ The NIH shift is one of a migration reaction observed at the *para*-position of a substituent in a benzene ring (see Figure 1-14); a deuterium shifted from the *para* position of the substituent “R” to the *meta* position in intermediates formed by electrophilic addition of the iron(IV)-oxo complex.

An iron(III)-oxyl species have been also proposed as an intermediate for oxidation of aromatics catalyzed by (4-hydroxyphenyl)pyruvate dioxygenase (HPPD).³⁵ HPPD is an (α -keto acid)-dependent mononuclear non-heme iron enzyme, which oxidizes (4-hydroxyphenyl)pyruvate as a substrate. HPPD oxidizes the substrate through an electrophilic attack mechanism of iron(IV)-oxo intermediates, which results in a hydroxylated product of aromatics, homogentisate (HG) (Figure 1-15(a)). In the reaction mechanism proposed on the basis of the theoretical studies, elongation of the Fe-O bond of the iron(IV)-oxo intermediate occurs in the transition state to form the corresponding iron(III)-oxyl species. The first step in the hydroxylation of aromatics by the iron(IV)-oxo species is proposed as the attack of the iron(IV)-oxo intermediate on the aromatic ring to form a σ -complex (Figure 1-15(a)) and this process proceeds with a Gibbs free energy change (ΔG) of +5 kcal/mol and the activation energy (E_a) of +16 kcal/mol. The Fe-O bond is elongated in the reaction process from 1.65 Å in **R-1** to 1.74 Å in **TS-1** (Figure 1-15(a)). At the transition state, not only elongation of the Fe-O bond but also loss of the *d*-orbital character in the α -LUMO orbital were observed; as a result of the latter, all the α -spin electron of the LUMO is localized in the iron center (Figure 1-15(b)). This indicates that the iron(IV) center is reduced to the high-spin Fe^{III} state,

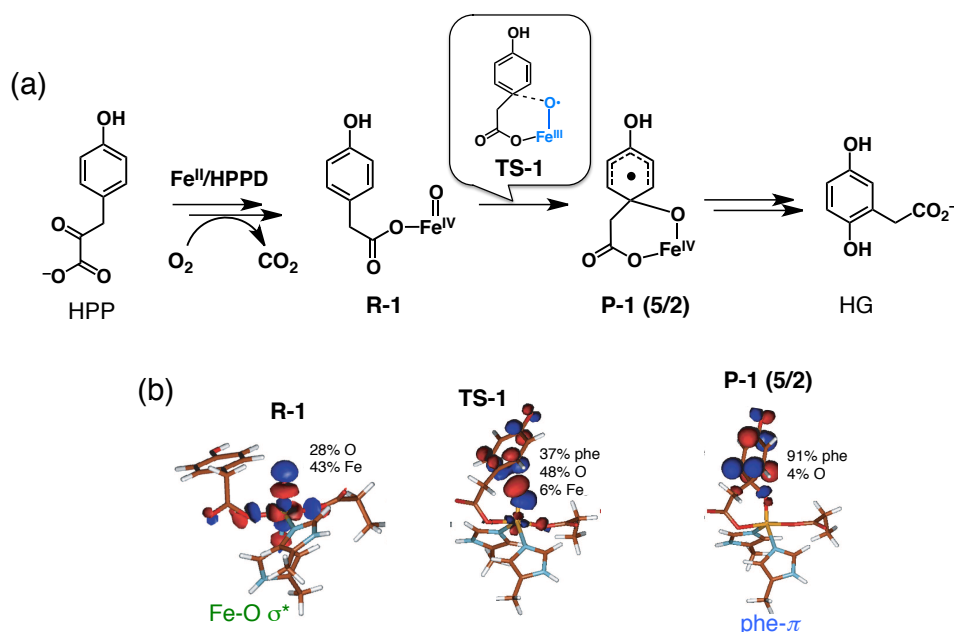


Figure 1-15. (a) Schematic representation of decarboxylative formation of non-heme iron(IV)-oxo species, followed by electrophilic attack by an iron(IV)-oxo intermediate to the benzene ring, resulting in HG production. (b) The α -LUMO orbitals of **R-1**, **TS-1** and **P-1(2/5)** in electrophilic attack of the iron(IV)-oxo intermediate to an aromatic ring as shown in Figure 1-15(a).³⁵

and simultaneously, the α -LUMO has distribution at the terminal oxygen (p-orbital in O) with 48% occupancy. A hole generated at the oxygen p-orbital allows us to elucidate the ligand as the oxyl ligand, formed by oxidation of the oxo ligand. As mentioned above, the Fe-O bond elongation resulted in the formation of iron(III)-oxyl species in the transition state of electrophilic attack of the iron(IV)-oxo species. Thus, iron-oxyl species have been considered as a reactive species of benzene hydroxylation, which inspired the author to form metal-oxyl species with earlier transition-metal elements than group 8.

1-3-4 Strategies to generate “highly reactive” M-O• species with group 8 elements

There have been strategies known for generation of M-O• species with earlier transition metal elements than group 8. For example, Soper and co-workers reported utilization of a redox-active moiety in an auxiliary ligand to generate M-O• species.³⁶ In their work, strategies to obtain metal-oxyl species have been considered to obtain single-electron occupancy in a metal-oxo π^* -symmetry anti-bonding orbital^{29,31} or to remove an electron from a metal-oxo π -bonding orbital.³⁶ The latter is applied by Soper and co-workers to a novel five-coordinate rhenium(VI)-oxo complex, bearing 2,4-di-*tert*-butyl-6-(phenylamido)phenolate ($[\text{ap}^{\text{Ph}}]^{2-}$) and 2,4-di-*tert*-butyl-6-(phenylamido)semiquinolate ($[\text{isq}^{\text{Ph}}]^-$) as the $1e^-$ -oxidized species of $[\text{ap}^{\text{Ph}}]^{2-}$ (Figure 1-16).³⁶ The unique properties of $\text{Re}^{\text{VI}}(\text{O})(\text{ap}^{\text{Ph}})(\text{isq}^{\text{Ph}})\text{Cl}$ ($\text{Re}^{\text{VI}}(\text{O})$) is derived from symmetry-allowed mixing of a Re-O π bond with an orbital of the semiquinone-type ligand, $[\text{isq}^{\text{Ph}}]^-$. The mixing of a Re-O π bond gives an oxyl radical character of the oxo ligand. Intramolecular charge transfer at closed-shell oxo ligands is a new strategy for formation of metal-oxyl species, showing unique reactivity with a lower activation barrier.

The qualitative π -orbital interactions in $\text{Re}^{\text{VI}}(\text{O})$ are shown in Figure 1-17. As shown in Figure 1-17(a), the metal-based unpaired electron (d^1) does not satisfy single-electron occupancy of a metal-oxo π^* antibonding orbital due to orthogonality of the d_{xy} orbital to the Re-O_{oxo} π -bonding orbital. However, the $[\text{isq}^{\text{Ph}}]^-$ ligand at the *trans* position to the oxo ligand has its unpaired electron in a π -symmetry orbital, which overlaps with the d_{xz} orbital of the Re center and contributes to overlap with the Re-O π bonds (Figure 1-17(b)). Such symmetry-allowed mixing of the $[\text{isq}^{\text{Ph}}]^-$ ligand with a Re-O π bond provides an overlapping of the $[\text{isq}^{\text{Ph}}]^-$ singly-occupied molecular orbital with the Re-O_{oxo} π -bonding orbital. These mixing of a π -orbital of $[\text{isq}^{\text{Ph}}]^-$ and Re-O_{oxo} π -bonding orbitals causes decrease of the bond order for the Re-O_{oxo} bond

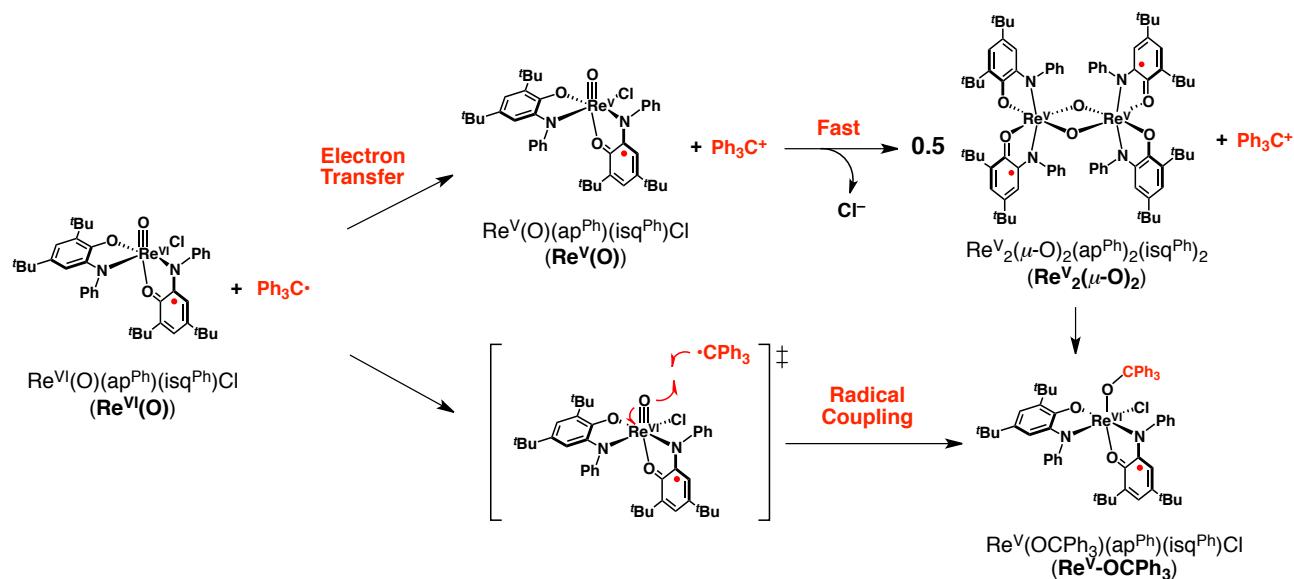


Figure 1-16. The reaction of a Re^{VI} -oxo species ($\text{Re}^{\text{VI}}(\text{O})$) with trityl radical.³⁶

from 3.0 to 2.5. However, the oxidation potentials of $[\text{ap}^{\text{Ph}}]^{2-}$ and O^{2-} imply that intramolecular ET from O^{2-} to $[\text{isq}^{\text{Ph}}]^{-}$ has a large energy barrier, and thus, it is not appropriate to describe the electronic structure of $\text{Re}^{\text{VI}}(\text{O})$ at the ground-state as $\text{Re}^{\text{VI}}(\text{O})(\text{ap}^{\text{Ph}})_2\text{Cl}$, which absolutely has an oxyl radical ligand.³⁶ Contribution of the oxyl radical character to the electronic structure of $\text{Re}^{\text{VI}}(\text{O})$ was reflected on the very slow reaction with the trityl radical, $\text{Ph}_3\text{C}\cdot$, to afford Ph_3COH and a deoxygenated metal complex at 25 °C. Two possible reaction mechanisms were proposed for formation of the alkoxide complex ($\text{Re}^{\text{V}}\text{-OCPh}_3$ in Figure 1-16): *i.e.*, initial outer-sphere ET as the first step to give $\text{Re}^{\text{V}}(\text{O})$, and direct $\text{Ph}_3\text{C}\cdot$ addition to $\text{Re}^{\text{VI}}(\text{O})$ to give $\text{Re}^{\text{V}}\text{-OCPh}_3$. However, the former mechanism was concluded as unlikely, because the $1e^-$ -reduced product of $\text{Re}^{\text{VI}}(\text{O})$, $[\text{Re}^{\text{V}}(\text{O})(\text{ap}^{\text{Ph}})(\text{isq}^{\text{Ph}})\text{Cl}]^-$ ($\text{Re}^{\text{V}}(\text{O})$), performs rapid formation of a bis(μ -oxo) dimer, $\text{Re}^{\text{V}}_2(\mu\text{-O})_2(\text{ap}^{\text{Ph}})_2(\text{isq}^{\text{Ph}})_2$ ($\text{Re}^{\text{V}}_2(\mu\text{-O})_2$), which cannot react with Ph_3C^+ to give Ph_3COH . Thus, the latter mechanism seems more reasonable. It is noteworthy that all of the closed-shell rhenium-oxo complexes, reported so far

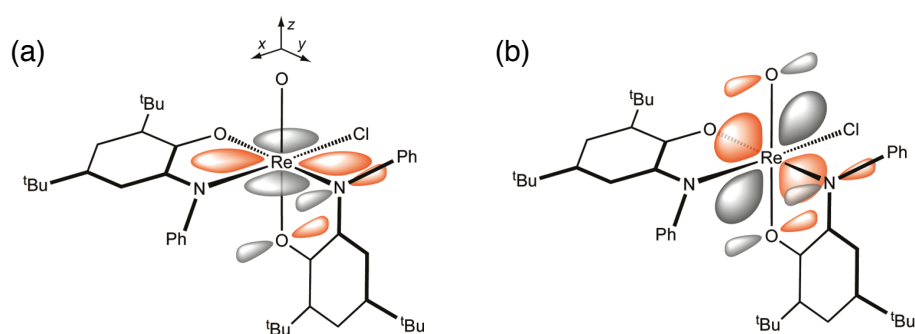


Figure 1-17. Schematic descriptions of qualitative π -orbital interactions in $\text{Re}^{\text{VI}}(\text{O})$.³⁶

including complexes capable of oxo transfer reactions to other substrates, have been inert to $\text{Ph}_3\text{C}\cdot$.^{37, 38} Consequently, $\text{Re}^{\text{VI}}(\text{O})$ unprecedentedly reacted with $\text{Ph}_3\text{C}\cdot$, in spite of the fact that $\text{Re}^{\text{VI}}(\text{O})$ was neither a strong oxidant nor a ground-state oxyl radical. In addition, the reduction potential is lower by *ca.* 550 mV than that of ferrocenium, and thus $\text{Re}^{\text{VI}}(\text{O})$ cannot oxidize even PPh_3 through ET.

Tanaka and co-workers also reported formation and crystallization of $\text{Ru}^{\text{II}}\text{-O}\cdot$ complexes, having redox-active quinone ligands, by deprotonation from aqua ligands of the corresponding Ru^{III} complexes.³⁹ The details of their works are described in the introductory part of Chapter 3 in this thesis.

A number of reports have been delivered on catalytic and stoichiometric substrate oxidation by high-valent Ru-oxo complexes formed through proton-coupled electron transfer (PCET)⁴⁰ oxidation of lower valent Ru-aqua complexes,⁴¹ and several reports have been published for Ru-oxo formation through oxygen-atom transfer (OAT) with peroxides,⁴² pyridine-*N*-oxides,⁴³ and iodosylarenes as oxidants.⁴⁴ In addition, as electronically equivalent species to $\text{Ru}^{\text{n}+}$ -oxo complexes, $\text{Ru}^{(\text{n}-1)+}$ -oxyl ($\text{n} \geq 3$) complexes have been also considered as highly important reactive species in oxidation reactions.⁴⁵ For example, Kojima and co-workers reported a series of Ru^{III} complexes, having tris(2-pyridylmethyl)amine derivatives, and their catalytic reactivity toward cyclohexane oxidation with *m*CPBA as a terminal oxidant (Figure 1-18).⁴⁶ The report has described the catalytic reaction mechanism of alkane oxidation by $\text{Ru}^{\text{III}}\text{-TPA}^{\text{COOEt}}$, having electron-withdrawing ethoxycarbonyl (COOEt) groups at the 4-positions of two pyridine rings of the TPA ligand (Figure 1-18), as a catalyst with use of *m*CPBA as an oxidant. The complex shows redox potentials at -0.05 V ($\text{Ru}^{\text{II}}/\text{Ru}^{\text{III}}$) and $+1.53$ V ($\text{Ru}^{\text{III}}/\text{Ru}^{\text{IV}}$) vs Fc/Fc^+ , which indicates that the electron density at the ruthenium center decreased compared to that of ruthenium(III) complex having the unsubstituted TPA ligand by introduction of strongly electron-withdrawing substituents on the pyridine rings. A KIE value for

cyclohexanol (CyOH) formation catalyzed by $\text{Ru}^{\text{III}}\text{-TPA}^{\text{COOEt}}$ was determined to be 4.3 based on the product ratio in catalytic oxidation of 1:1 mixture of cyclohexane and cyclohexane- d_{12} . This KIE value is comparable to those of hydrogen-atom abstraction by free radicals (5.6 – 6.3),⁴⁷ which indicates a strong radical character of the reactive species.⁴⁸ In the time-course of product formation in the catalytic cyclohexane oxidation by $\text{Ru}^{\text{III}}\text{-TPA}^{\text{COOEt}}$, no induction period was observed. In the isotope-labeling

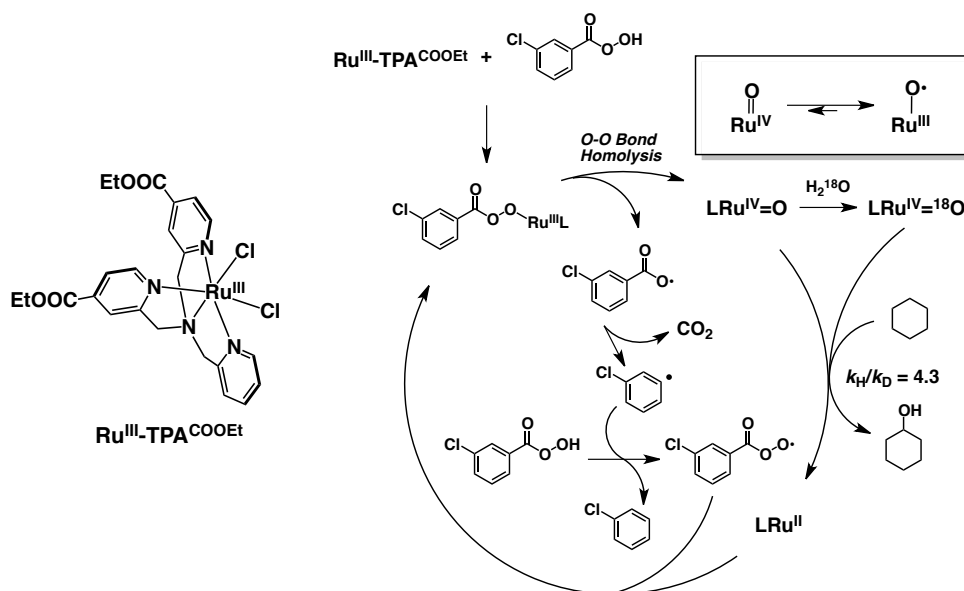


Figure 1-18. Structures of the catalyst, $\text{Ru}^{\text{III}}\text{-TPA}^{\text{COOEt}}$ (left), and a proposed reaction mechanism of catalytic hydroxylation of cyclohexane by $\text{Ru}^{\text{III}}\text{-TPA}^{\text{COOEt}}$ as a catalyst and *m*CPBA as a sacrificial oxidant (right).⁴⁶

experiment in the presence of H_2^{18}O , 100% ^{18}O incorporation to CyOH was observed. These results indicate that the reaction of $\text{Ru}^{\text{III}}\text{-TPA}^{\text{COOEt}}$ with *m*CPBA in acetonitrile affords a Ru-oxo species as a reactive species toward cyclohexane oxidation and this reactive species was characterized by resonance Raman spectroscopy. A Raman band derived from the Ru-O stretching vibration was observed at 752 cm^{-1} in the presence of H_2^{16}O , which completely shifted to 708 cm^{-1} in the presence of H_2^{18}O . This value of 752 cm^{-1} was relatively low compared to those reported for $\text{Ru}^{\text{IV}}=\text{O}$ or $\text{Ru}^{\text{V}}=\text{O}$ complexes, indicating a weaker Ru-O bond in the reactive species. Such high reactivity with the KIE value of 4.3, the feasible quantitative isotopic exchange of $\text{Ru}^{\text{IV}}=\text{O}$ species, and the lower energy of the Ru-O stretching vibration suggest $\text{Ru}^{\text{III}}\text{-O}\cdot$ character of the $\text{Ru}^{\text{IV}}=\text{O}$ intermediate, which is probably derived from intramolecular electron transfer from the O^{2-} ligand to the ruthenium(IV) center due to the high redox potential of the Ru(III)/Ru(IV) redox couple for $\text{Ru}^{\text{III}}\text{-TPA}^{\text{COOEt}}$.

Methodologies for formation of reactive metal-oxyl species with earlier metal elements than group 8 have been also suggested by using 3d-transition metal elements. McGrady and co-workers have reported a theoretical study on electronic structures of a manganese-porphyrin complex, $[\text{Mn}^{\text{V}}(\text{Porp})(\text{O})(\text{OH})]$ (Porp = porphyrinato), in the singlet, triplet, and quintet spin states. They have also described potential energy surfaces of dimethylsulfide oxidation by $[\text{Mn}^{\text{V}}(\text{Porp})(\text{O})(\text{OH})]$ in various spin states (Figure 1-19).⁴⁹ The most stable structure of $[\text{Mn}^{\text{V}}(\text{Porp})(\text{O})(\text{OH})]$ at the ground state was in the triplet ground state, having spin densities on the Mn center by +3.04, on O by -0.89, and on the Porp ligand by -0.27, and the Mn-O bond length was estimated to be 1.78 \AA . On the basis of the spin-density map of $[\text{Mn}^{\text{V}}(\text{Porp})(\text{O})(\text{OH})]$ (Figure

1-19(a) bottom), the electronic structure of $[\text{Mn}^{\text{V}}(\text{Porp})(\text{O})(\text{OH})]$ can be described as $[\text{Mn}^{\text{IV}}(\text{Porp})(\text{O}\cdot)(\text{OH})]$. In addition, the triplet state showed the very small activation barrier of the dimethylsulfide oxidation in the potential energy surfaces, compared to those in the quintet or singlet states (Figure 1-19(b)). These results indicate that the $\text{Mn}(\text{IV})\text{-O}\cdot$ complex, having a long M-O_{oxo} bond, is the most reactive state

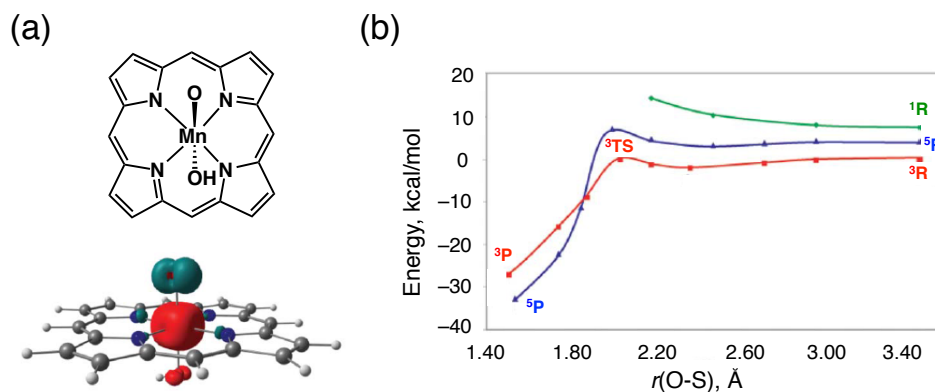


Figure 1-19. (a) Structure of $[\text{Mn}^{\text{V}}(\text{Porp})(\text{O})(\text{OH})]$ and its spin density map in the triplet spin state (^3R). (b) DFT-calculated potential energy surfaces of dimethylsulfide oxidation by $[\text{Mn}^{\text{V}}(\text{Porp})(\text{O})(\text{OH})]$ in the singlet (^1R), triplet (^3R) and quintet (^5R) states.⁴⁹

among other spin states in the dimethylsulfide oxidation.

On the basis of the theoretical analysis as mentioned above, a highly reactive $\text{Mn}(\text{IV})\text{-O}\cdot$ complex can be generated with strongly σ -donating O^{2-} or OH^- ligands as axial ligands at the *trans* position of the oxo ligands to elongate the M-O_{oxo} bond.^{49, 50} Therefore, Groves and co-workers synthesized and characterized *trans*-dioxo manganese-porphyrin complex, $[\text{Mn}^{\text{V}}(\text{O})_2(\text{TPFPP})]^-$ (TPFPP = 5,10,15,20-tetrakis(pentafluorophenyl)porphyrinato), and investigated the reactivity toward oxidation of olefins.⁵¹ Contrary to the expectation, $[\text{Mn}(\text{O})_2(\text{TPFPP})]^-$ was not reactive toward oxidation of olefins, whereas $[\text{Mn}^{\text{V}}(\text{O})(\text{TPFPP})(\text{OH}_2)]$, generated by addition of trifluoroacetic acid, performed an instantaneous oxidation reaction with cyclooctene even at -70°C (Figure 1-20).⁵¹ They rationalized the low reactivity of $[\text{Mn}^{\text{V}}(\text{O})_2(\text{TPFPP})]^-$ toward oxidation of organic substrates relative to $[\text{Mn}^{\text{V}}(\text{O})(\text{TPFPP})(\text{OH}_2)]$ based on negative net charge and lower reduction potential of $[\text{Mn}^{\text{V}}(\text{O})_2(\text{TPFPP})]^-$ species compared to $[\text{Mn}^{\text{V}}(\text{O})(\text{TPFPP})(\text{OH}_2)]$.⁵¹ Therefore, to generate reactive metal-oxyl species toward oxidation of relatively inert substrates, introduction of electronically neutral and strongly σ -donating ligands at the *trans* position of the oxo ligand is necessary to achieve no or less negative shifts of the reduction potential for the metal-oxyl complexes. As one of the candidates for the ligands satisfying the criteria, the author of this thesis has focused on *N*-heterocyclic carbene (NHC) ligands.

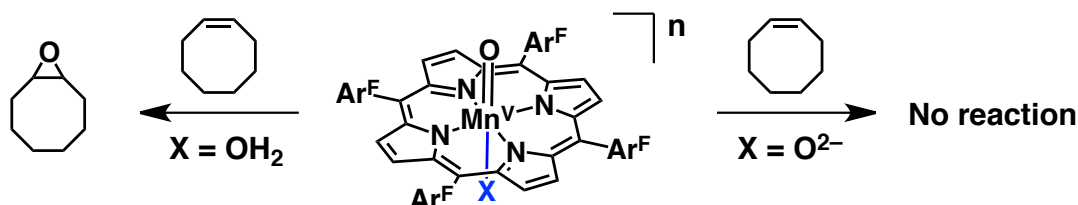


Figure 1-20. Relationships between axial ligands and reactivity in olefin epoxidation by Mn-O complexes ($n = +1$ for $\text{X} = \text{OH}_2$, $n = 0$ for $\text{X} = \text{O}^{2-}$).⁵¹

1-4 Properties of *N*-heterocyclic carbene (NHC)

1-4-1 Fundamentals of NHC

In principle, a carbene has only six electrons on its C atom and a carbene is an octet-rule-unsatisfied species, consisting of an electronically unsaturated sp^2 -carbon.⁵² Carbenes are categorized into two groups, defined by the spin states of the carbene carbon atoms. One is so-called “triplet carbene”, in which the carbene carbon and its two neighboring atoms are fixed to linear arrangement by two sterically bulky substituents on the neighboring atoms, and the carbene carbon has the two unpaired electrons in two p -orbitals (Figure 1-21).⁵³ The other is so-called “singlet carbene”, which shows a bent arrangement, having a lone pair of two electrons in the sp^2 -carbene-carbon (Figure 1-21).⁵³

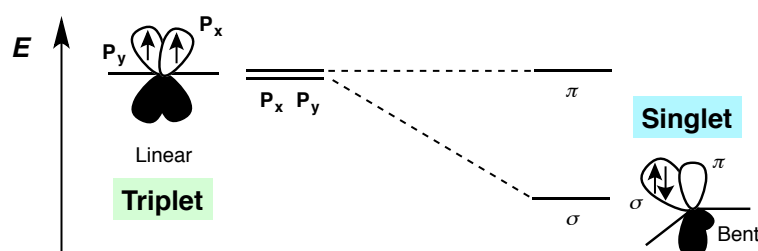


Figure 1-21. An Energy diagram of atomic orbitals on a carbene carbon.⁵³

The latter singlet carbenes can be further classified by neighboring atoms. The carbenes, having two hetero atoms such as N, O or F adjacent to the carbene carbons, are referred as “Fischer-type” carbenes and the hetero atoms exhibit electrophilicity and π -donating ability to the carbene carbons and thus the carbene carbons also show electrophilicity.⁵⁴ On the other hand, carbenes, having no neighboring hetero atoms adjacent to the carbene carbon, are called as “Schlock-type” carbenes, which show nucleophilicity.⁵⁵ A Fischer-type carbenes have all 6 electrons in the sp^2 orbital of the carbene carbon and form strong interaction with a low-valent metal center in its metal complexes.⁵⁴ In contrast, a Schlock-type carbene has 5 electrons in the sp^2 orbital and 1 electron in the p orbital of the carbene carbon and exert strong interaction with high-valent metal center in its metal complexes.⁵⁵ However, Schlock-type metal-carbene complexes are highly unstable due to its electron-poor character, and thus investigation of the catalytic reactivity is generally difficult.^{55a}

In 1991, Arduengo and co-workers successfully synthesized a stable metal-free carbene and determined the X-ray crystal structure for the first time.⁵⁶ The carbene reported by Arduengo is a singlet carbene, named as “*N*-heterocyclic carbene (NHC)”, and the NHC can be generated by deprotonation from the 2-position of an imidazolium cation, having highly bulky adamantyl groups on the nitrogen atoms, with sodium hydride as a strong base (Figure 1-22).⁵⁶ Since then, properties and reactivity of metal complexes having stable carbene ligands have been widely investigated.⁵³ There are two reasons proposed for

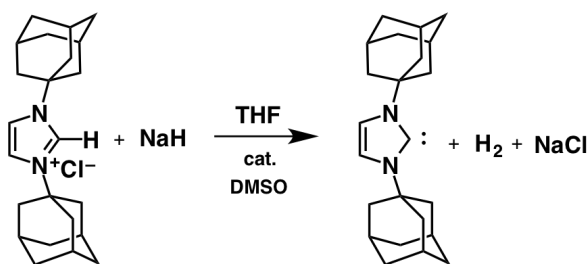


Figure 1-22. A formation of free-base *N*-heterocyclic carbene (NHC).⁵⁶

stabilization of the singlet state in the electronic structure of the NHC by Bertrand:⁵³ First, the cyclic structure including the carbene carbon makes the N-C-N bond angle of the imidazole ring narrower resulting bent rearrangement, which causes a larger energy gap between the σ - and π -orbital of the carbene carbon (Figure 1-21); second, the σ -electron-withdrawing nature of the neighboring nitrogenslowers the energy level of σ -orbitals formed between the carbene carbon and the neighboring atoms, whereas π -electron-donating nature of the neighboring nitrogen atoms destabilizes the π -orbitals between the carbene carbon and the neighboring atoms. These factors play a role to stabilize the singlet state. The neighboring nitrogen atoms exhibit σ -electron-withdrawing and π -electron-donating abilities to the carbene carbon, which makes the σ -orbital between C and N atoms stable (inductive effects) and the π -orbital unstable (mesomeric effects).⁵³ The σ -electron-withdrawing substituents inductively stabilize the σ nonbonding orbital by increasing its s character and leave the $p\pi$ orbital intact. The σ - $p\pi$ gap is increased and the singlet state is favored (Figure 1-23(a)). On the other hand, the energy of the vacant $p\pi$ orbital is increased by interaction with the substituent's lone pairs. Since the σ -orbital remains intact, the σ - $p\pi$ gap should be increased (Figure 1-23(b)). Accordingly, energy gap between the σ - and π -orbitals is enlarged (Figure 1-23).

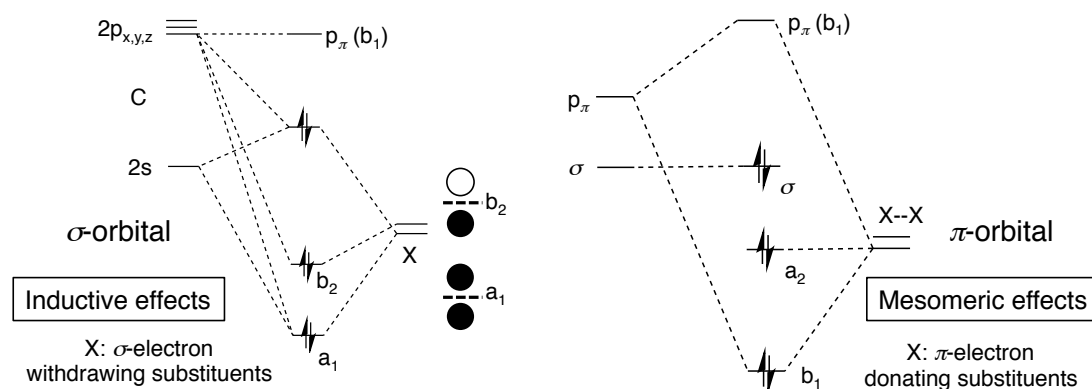


Figure 1-23. NHC behaves as a singlet carbene due to increase of the σ - $p\pi$ gap by inductive effects (a) and mesomeric effects (b) of the neighboring nitrogen atoms.⁵³

Generally, NHC as ligands in metal complexes are known to show strong σ -donation to the metal center, which not only makes the metal center electron-rich, but also makes the ligand at the *trans* position of the NHC ligand highly labile.⁵⁷ These tendencies are confirmed by the research on palladium- and platinum-NHC complexes.^{57, 58} In addition, the octet-rule-unsatisfied and electronically unsaturated carbene carbon can accept π -back donation from the metal center with the vacant p-orbital. However, since the vacant p-orbital on the carbene carbon in NHC is stabilized by π -electron-donation from lone pairs of the neighboring nitrogen atoms, π -back donation from the metal center is weakened compared to that of conventional carbene ligands.⁵⁹ A theoretical analysis revealed that π -back donation occupied at least 10% of the whole metal-NHC interaction.⁶⁰ In addition, there are other experimental evidences of the existence of the π -back donation from the metal center to the NHC ligand.^{61, 62} For example, Bielawski and co-workers investigated the chemical shifts of ¹H NMR signals for the protons on an olefin ligand at the *trans* position of the NHC ligand in a rhodium(I) complex, whose NHC ligand has substituents on 4,5-positions of the imidazole ring (Figure 1-24).⁶¹ As a result, the introduction of a stronger electron-withdrawing substituent on the NHC ligand caused down-field shifts of the ¹H NMR signals of the olefin ligands. This result indicates that the substituents on the NHC ligand can regulate the σ -donating ability of the carbene carbon to manipulate the electron density at a metal center. Substituent effects of the NHC ligands have also been

investigated on the vibration frequencies of the C-O bonds in $\text{Rh}^{\text{I}}\text{-CO}$ complexes, which have the CO ligand at the *trans* position of NHC ligands. Likewise, introduction of stronger electron-withdrawing substituents on the NHC ligands makes the stretching vibration energy of a C-O bond in the CO ligand higher. This result indicates decrease of π -back donation from the Rh^{I} center to the CO ligand and resultant strengthening of the C-O bond by introducing stronger electron-withdrawing substituents on NHC ligands. These results indicate that NHC ligands show π -accepting ability from metal centers, and in particular, accept π -back donation more strongly from the Rh^{I} center upon introduction of electron-withdrawing substituents on the NHC ligands.⁶¹

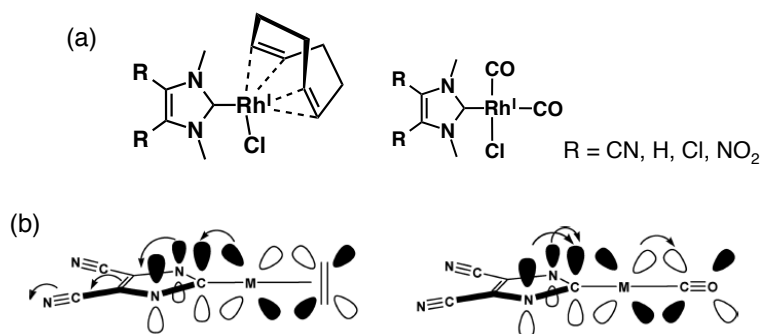


Figure 1-24. Structures of $\text{Rh}^{\text{I}}\text{-NHC}$ complexes (a) and schematic descriptions of dominant resonance contributions for the complexes having CN groups (b).⁶¹

Additionally, Nolan and co-workers conducted several NMR spectroscopic analyses for platinum(II) complexes, having different π -conjugating NHC ligands.⁶² The ^{13}C NMR signal of the carbene carbon shifted to the upper field in benzene- d_6 in the use of π -conjugated NHC ligands, whereas the ^{195}Pt NMR signal in a Pt complex, having a π -conjugated NHC ligand, shifted to the lower field compared to that in a Pt complex having saturated NHC ligands in CD_2Cl_2 .⁶² This indicates that electron density on the platinum center decreased, whereas that on the carbene carbon increased in the π -conjugated NHC ligand. On the basis of these results and theoretical analysis, it is suggested that NHC ligands show π -accepting ability.⁵⁹⁻⁶²

Furthermore, electrochemical properties of iron(II) complexes, having bis-NHC or NHC-pyridine ligands, have been studied (Figure 1-25);⁶³ interestingly, redox potentials of the $\text{Fe}^{\text{II}}/\text{Fe}^{\text{III}}$ redox couples showed difference by *ca.* 60 mV between the two iron(II) complexes. This small difference in the redox potentials indicates that the NHC ligands in the iron(II) complexes not only exhibit stronger σ -donation to the iron(II) center but also accept larger π -electrons from iron(II) center, comparable to the pyridine ligand.⁶³

As mentioned above, NHCs have attracted much attention from the researchers as ligands of metal complexes, since NHCs show both strong σ -donating and π -accepting abilities upon coordination, and also exert strong *trans* influence to the ligands at the *trans* position. Based on these properties, a lot of reports have been provided on catalytic activity of metal-NHC complexes (See below).

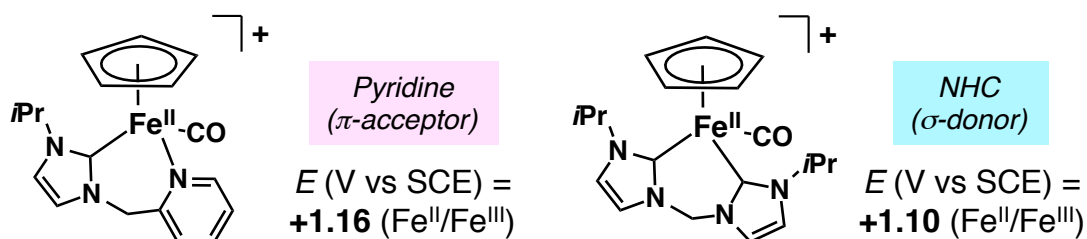


Figure 1-25. $\text{Fe}^{\text{II}}\text{-NHC}$ complexes and their redox potentials in CH_2Cl_2 .⁶³

1-4-2 Catalytic reactions by Ru-NHC complexes

Among a lot of catalysts having NHC ligands, 4d transition metal complexes have been utilized by virtue of their durability in catalysis derived from its large crystal-field splitting of 4d transition metal complexes, compared to that of 3d transition-metal complexes.⁶⁴ Grubbs and co-workers discovered a highly reactive ruthenium catalyst, having an NHC ligand and an alkylidene ligand, to perform olefin metathesis (Figure 1-26).⁶⁵ This ruthenium complex, named as 2nd-generation Grubbs catalyst, has attracted remarkable attention because of its significant improvement of the catalytic activity toward olefin metathesis and high stability against oxidation, moisture and heat, compared to the 1st-generation Grubbs catalyst having a phosphine ligand instead of the NHC ligand.⁶⁶

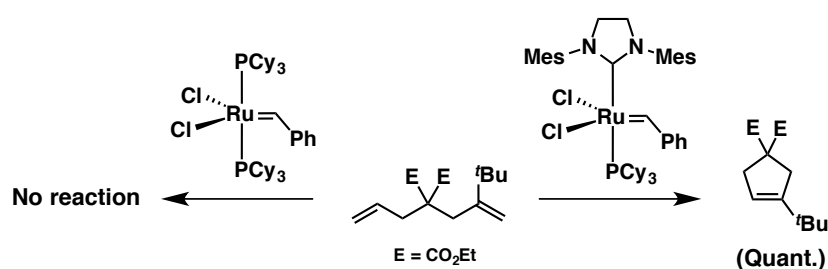


Figure 1-26. Comparison of the reactivity between the two catalysts (5 mol%) for a ring-closing olefin metathesis at 45 °C.⁶⁵

Llobet and co-workers reported regio-selective epoxidation of olefin derivatives in CH_2Cl_2 using a Ru(II)-aqua complex, having a rigid tridentate NHC ligand, as a catalyst (Figure 1-27).⁶⁷ The Ru(III) complex obtained by oxidation of the Ru(II) complex showed disproportionation into the corresponding Ru(II) and Ru(IV) species, because of strong σ -donating and π -accepting ability of the NHC ligand, the former of which stabilizes the Ru(IV) species and the latter stabilizes the Ru(II) species. Generally, when unstable radical intermediates are formed by $1e^-$ -oxidation of organic substrates, radical coupling proceeds as an undesired side reaction.⁶⁸ In contrast, this ruthenium-NHC complex shows $2e^-$ -redox process ($\text{Ru}^{\text{II}}/\text{Ru}^{\text{IV}}$) in one step through the disproportionation, which suppresses the side reaction derived from radical intermediates to lower the regio-selectivity.⁶⁷ As the results, regio-selective epoxidation of olefins were successfully achieved with this Ru-NHC catalyst, whereas *cis,trans*-isomerization occurred through rotation of the C-C single bond, if radical intermediates would be formed.

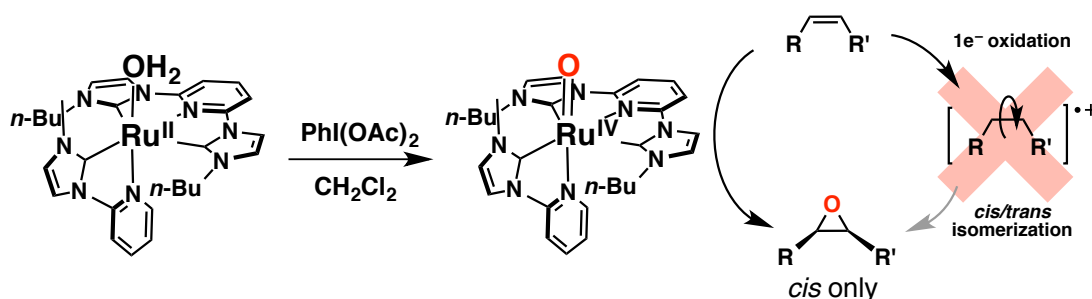


Figure 1-27. A regio-selective olefin epoxidation catalyzed by a Ru-NHC complex.⁶⁶

In addition, catalytic dehydrogenative oxidation of alcohols has been reported to afford carboxylic acids by a Ru^{II}-NHC catalysts in basic water under air (Figure 1-28).⁶⁹ In spite of the fact that NHC ligands have comparable σ -donating ability to electron-rich trialkyl phosphine ligands, the Ru^{II}-NHC complexes can

be used as catalysts even under air in water, whereas the electron-rich trialkyl phosphine ligands itself and their Ru^{II} complexes cannot be used under air due to their air-sensitivity.^{70, 71}

As mentioned above, ruthenium complexes having NHC ligands have showed unique and effective catalytic reactivity not only in organic solvent but also in water.

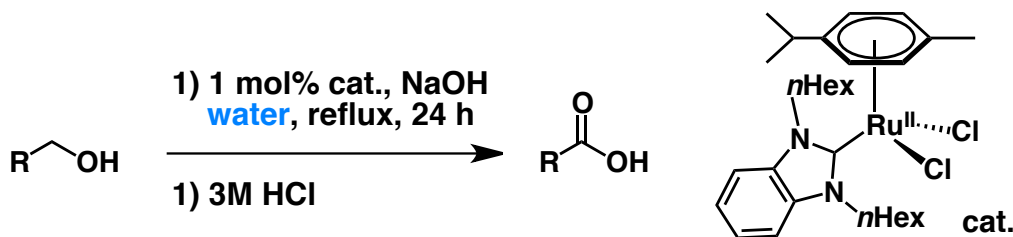


Figure 1-28. Catalytic dehydrogenative oxidation of alcohols to carboxylic acids by a Ru^{II}-NHC catalyst.⁶⁹

1-4-3 Catalytic reactions by Pd-NHC complexes

Palladium catalysts have been widely investigated for C-C and C-heteroatom coupling so far.⁷² In particular, a lot of palladium-NHC complexes have been reported to perform catalytic transformations of aryl halides, more efficiently than palladium complexes having traditional phosphine ligands.⁷³ Recently, palladium-NHC catalysts have been employed for various cross-coupling reactions including Heck reaction,⁷⁴ Suzuki-Miyaura cross-coupling,⁷⁵ Sonogashira coupling,⁷⁶ Tsuji-Trost reaction,⁷⁷ and Hiyama reaction,⁷⁸ and the reactions have been performed even in water.⁷⁹ Advantages of NHC ligands in catalysis of palladium complexes are originated from the following properties: NHC complexes exhibit high durability under oxidative and acidic conditions, and NHC ligands have a strong σ -donating ability to the metal center

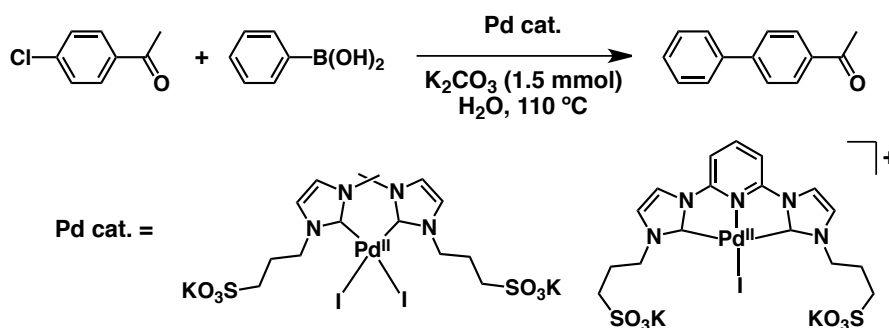


Figure 1-29. Aqueous Suzuki-Miyaura reaction of aryl chloride and phenylboronic acid using Pd-NHC catalysts.⁸⁰

and π -accepting ability from the metal center. These properties make it possible to stabilize both low-valent Pd(0) and high-valent Pd(IV) centers. For example, Peris and co-workers have reported palladium catalysts, having sulfonate-functionalized-NHC ligands, utilized for Suzuki-Miyaura cross-coupling reactions in water (Figure 1-29).⁸⁰ Even upon using relatively inert aryl chlorides as substrates, the palladium-NHC catalysts catalyze the catalytic cross-coupling reaction in water with yield up to 85% and the maximum turnover number (TON) reached to 37,000.⁸⁰

Strassner *et al.* have reported that palladium(II) complexes having bis(NHC) chelating ligands perform catalytic oxidation of methane or propane into the corresponding alcohol derivatives (esters) under strong acidic conditions.⁸¹ Similar oxidation reactions of methane were pioneered by Periana with a platinum complex as a catalyst;⁸² however, it is noteworthy that analogous platinum complexes immediately

decompose into platinum black in trifluoroacetic acid (CF₃COOH), whereas Pd-bis(NHC) complexes afford yellow transparent solutions in CF₃COOH and exhibit no decomposition even after 20 h. Therefore, Pd-bis(NHC) complexes having two bromide ligands can perform catalytic conversion of methane into methanol derivatives in TFA (Figure 1-30); however, Sheldon's⁸³ and Periana's systems⁸² did not show any catalytic activity toward methane oxidation under the same conditions.

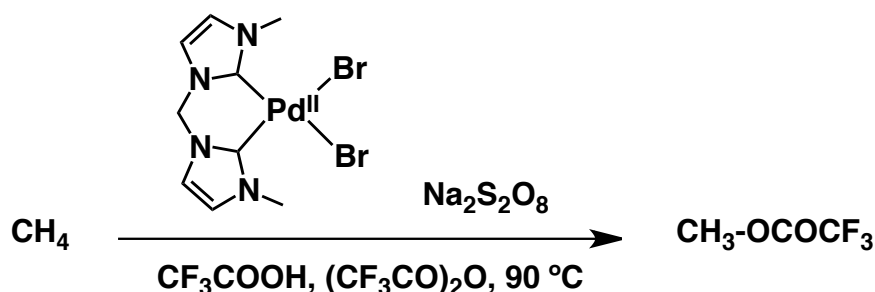


Figure 1-30. Catalytic conversion of methane to methanol derivative in trifluoroacetic acid.⁸¹

As mentioned above, palladium-NHC complexes have performed various catalytic reactions such as cross-coupling reactions and C-H activation of methane by virtue of the oxidative and acidic durability.

1-5 Purpose of this research

In this thesis, the author of this thesis has investigated the redox and structural properties of ruthenium complexes having pincer-type tridentate NHC ligands. On the basis of the redox and structural properties, a novel methodology to stabilize Ru^{III}-O• species by using NHC-chelate ligands has been provided, and the formation and characterization of the species have been successfully made using various spectroscopic methods. The catalytic reactivity of the Ru^{III}-O• complex in oxidation of organic substrates in water has been also revealed. Based on the strong radical character, the Ru^{III}-O• species has been applied to catalytic oxidative cracking of benzene rings to afford formic and carboxylic acids as useful products in water under mild conditions. It should be noted that formic acid formed can be used as a H₂ source in a one-pot treatment by simple pH adjustment. In addition, a Pd-NHC complex, having the NHC chelate ligand, also has been applied to catalysis for oxidative cracking of halogenated benzene derivatives under mild conditions to afford carboxylic acids such as formic acid by using a cheaper oxidant in water. In the reactions, the NHC ligand plays an indispensable role in stabilization of Pd intermediates formed from the Pd complex during the reaction to provide mechanistic insights.

Reference and notes.

- (1) (a) L. G. Denisov, T. M. Makris, S. G. Sligar, I. Schlichting, *Chem. Rev.* **2005**, *105*, 2253–2278. (b) I. Schlichting, J. Berendzen, K. Chu, A. M. Stock, S. A. Maves, D. E. Benson, R. M. Sweet, D. Ringe, G. A. Petsko, S. G. Sligar, *Science* **2000**, *287*, 1615–1622.
- (2) M. Costas, M. P. Mehn, M. P. Jensen, L. Que, *Chem. Rev.* **2004**, *104*, 939–986.
- (3) (a) J. M. Bollinger, Jr., J. C. Price, L. M. Hoffart, E. W. Barr, C. Krebs, *Eur. J. Inorg. Chem.* **2005**, 4245–4254. (b) P. J. Riggs-Gelasco, J. C. Price, R. B. Guyer, J. H. Brehm, E. W. Barr, J. M. Bollinger, Jr., C. Krebs, *J. Am. Chem. Soc.* **2004**, *126*, 8108–8109.
- (4) (a) W. Wang, A. D. Liang, S. J. Lippard, *Acc. Chem. Res.* **2015**, *48*, 2632–2639. (b) M.-H. Baik, M. Newcomb, R. A. Friesner, S. J. Lippard, *Chem. Rev.* **2003**, *103*, 2385–2420. (c) B. J. Brazeau, R. N.

- Austin, C. Tarr, J. T. Groves, J. D. Lipscomb, *J. Am. Chem. Soc.* **2001**, *123*, 11831–11837. (d) A. C. Rosenzweig, C. A. Frederic, S. J. Lippard, P. Nordlund, *Nature* **1993**, *366*, 537–543. (e) D. A. Whittington, S. J. Lippard, *J. Am. Chem. Soc.* **2001**, *123*, 827–838. (f) C. E. Tinberg, S. J. Lippard, *Acc. Chem. Res.* **2011**, *44*, 280–288.
- (5) M.-H. Baik, B. F. Gherman, R. A. Friesner, S. J. Lippard, *J. Am. Chem. Soc.* **2002**, *124*, 14608–14615.
- (6) J. P. Klinman, *J. Biol. Chem.* **2006**, *281*, 3013–3016.
- (7) E. E. Chufán, S. T. Prigge, X. Siebert, B. A. Eipper, R. E. Mains, L. M. Amzel, *J. Am. Chem. Soc.* **2010**, *132*, 15565–15572.
- (8) S. Kim, J. Ståhlberg, M. Sandgren, R. S. Paton, G. T. Beckman, *Proc. Natl. Acad. Sci. USA* **2014**, *111*, 149–154.
- (9) B. Bissaro, Å. K. Røhr, G. Müller, P. Chylenski, M. Skaugen, Z. Forsberg, S. J. Horn, G. Vaaje-Kolstad, V. G. H. Eijsink, *Nat. Chem. Biol.* **2017**, *13*, 1123–1128.
- (10) B. Wang, E. M. Johnson, P. Li, S. Shaik, G. J. Davies, P. H. Walton, C. Rovira, *ACS Catal.* **2018**, *8*, 1346–1351.
- (11) S. Huber, M. Z. Ertem, F. Aquilante, L. Gagliardi, W. B. Tolman, C. J. Cramer, *Chem. Eur. J.* **2009**, *15*, 4886–4895.
- (12) (a) W. Nam, S. K. Choi, M. H. Lim, J.-U. Rohde, I. Kim, J. Kim, C. Kim, L. Que, Jr., *Angew. Chem., Int. Ed.* **2003**, *42*, 109–111. (b) K. Yamaguchi, Y. Watanabe, I. Morishima, *J. Am. Chem. Soc.* **1993**, *115*, 4058–4065. (c) H. Fujii, *J. Am. Chem. Soc.* **1993**, *115*, 4641–4648. (d) O. Cussó, X. Ribasm, M. Costas, *Chem. Commun.* **2015**, *51*, 14285–14298. (e) S. T. Kleespies, W. N. Oloo, A. Mukherjee, L. Que, Jr., *Inorg. Chem.* **2015**, *54*, 5053–5064. (f) S. V. Kryatov, E. V. Rybak-Akimova, S. Schindler, *Chem. Rev.* **2005**, *105*, 2175–2226.
- (13) (a) J. T. Groves, T. E. Nemo, R. S. Myers, *J. Am. Chem. Soc.* **1979**, *101*, 1032–1033. (b) P. R. O. de Montellano, *Chem. Rev.* **2010**, *110*, 932–948. (c) J. N. Rodríguez-López, D. J. Lowe, J. Hernández-Ruiz, A. N. P. Hinter, F. García-Cánovas, R. N. F. Thorneley, *J. Am. Chem. Soc.* **2001**, *123*, 11838–11847.
- (14) (a) J. T. Groves, Y. Watanabe, *J. Am. Chem. Soc.* **1986**, *108*, 507–508. (b) J. T. Groves, T. E. Nemo, *J. Am. Chem. Soc.* **1983**, *105*, 5786–5791. (c) J. T. Groves, R. C. Haushalter, M. Nakamura, T. E. Nemo, B. J. Evans, *J. Am. Chem. Soc.* **1981**, *103*, 2884–2886.
- (15) W. J. Song, Y. O. Ryu, R. Song, W. Nam, *J. Biol. Inorg. Chem.* **2005**, *10*, 294–304.
- (16) Z. Gross, S. Nimri, *Inorg. Chem.* **1994**, *33*, 1731–1732.
- (17) J. Kaizer, E. J. Klinker, N. Y. Oh, J.-U. Rohde, W. J. Song, A. Stubna, J. Kim, E. Münck, W. Nam, L. Que, Jr., *J. Am. Chem. Soc.* **2004**, *126*, 472–473.
- (18) C. V. Sastri, J. Lee, K. Oh, Y. J. Lee, J. Lee, T. A. Jackson, K. Ray, H. Hirao, W. Shin, J. A. Halfen, J. Kim, L. Que, Jr., S. Shaik, W. Nam, *Proc. Natl. Acad. Sci. USA* **2007**, *104*, 19181–19186.
- (19) Y.-R. Luo, *Handbook of Bond Dissociation Energies in Organic Compounds*, 1st ed., CRC Press LLC: Boca Raton, FL, 2003, p 39.
- (20) P. B. Merkel, P. Luo, J. P. Dinnocenzo, S. Farid, *J. Org. Chem.* **2009**, *74*, 5163–5173.
- (21) T. Tsuji, A. A. Zaoputra, Y. Hitomi, K. Mieda, T. Ogura, Y. Shiota, K. Yoshizawa, H. Sato, M. Kodera, *Angew. Chem., Int. Ed.* **2017**, *56*, 7887–7890.
- (22) (a) Y. Morimoto, S. Bunno, N. Fujieda, H. Sugimoto, S. Itoh, *J. Am. Chem. Soc.* **2015**, *137*, 5867–5870. (b) M. Yamada, K. D. Karlin, S. Fukuzumi, *Chem. Sci.* **2016**, *7*, 2856–2863.
- (23) R. Augusti, A. O. Dias, L. L. Rocha, R. M. Lago, *J. Phys. Chem. A* **1998**, *102*, 10723–10727.

- (24) R. R. Jacobson, Z. Tyeklar, A. Farooq, K. D. Karlin, S. Liu, J. A. Zubieta, *J. Am. Chem. Soc.* **1988**, *110*, 3690–3692.
- (25) L. Vilella, A. Conde, D. Balcells, M. M. Diaz-Requejo, A. Lledós, P. J. A. Pérez, *Chem. Sci.* **2017**, *8*, 8373–8383.
- (26) K.-B. Cho, X. Wu, Y.-M. Lee, Y.-H. Kwon, S. Shaik, W. Nam, *J. Am. Chem. Soc.* **2012**, *133*, 20222–20225.
- (27) S. P. de Visser, K. Oh, A.-R. Han, W. Nam, *Inorg. Chem.* **2007**, *46*, 4632–4641.
- (28) W. A. Nugent, J. M. Mayer, *Metal-Ligand Multiple Bonds*, Wiley, New York, **1988**.
- (29) (a) J. R. Winkler, H. B. Gray, *Struct. Bonding* (Berlin) **2012**, *142*, 17–28. (b) J. R. Winkler, H. B. Gray, *Acc. Chem. Res.* **2018**, *51*, 1850–1857.
- (30) K. P. O’Halloran, C. Zhao, N. S. Ando, A. J. Schultz, T. F. Koetzle, P. M. B. Piccoli, B. Hedman, K. O. Hodgson, E. Bodyr, M. L. Kirk, S. Knottenbelt, E. C. Depperman, B. Stein, T. M. Anderson, R. Cao, Y. V. Geletii, K. I. Hardcastle, D. G. Musaev, W. A. Neiwert, X. Fang, K. Morokuma, S. Wu, P. Kögerler, C. L. Hill, *Inorg. Chem.* **2012**, *51*, 7025–7031.
- (31) J. M. Mayer, *Acc. Chem. Res.* **1998**, *31*, 441–450.
- (32) F. P. Guengerich, *Chem. Res. Toxicol.* **2001**, *14*, 611–650.
- (33) K. R. Korzekwa, D. C. Swinney, W. F. Trager, *Biochemistry* **1989**, *28*, 9019–9027.
- (34) (a) T. Vannelli, A. B. Hooper, *Biochemistry* **1995**, *34*, 11743–11749. (b) B. Meunier, S. P. de Visser, S. Shaik, *Chem. Rev.* **2004**, *104*, 3947–3980.
- (35) M. L. Neidig, A. Decker, O. W. Choroba, F. Huang, M. Kavana, G. R. Moran, J. B. Spencer, E. I. Solomon, *Proc. Natl. Acad. Sci. USA.* **2006**, *103*, 12966–12973.
- (36) C. A. Lippert, K. I. Hardcastle, J. D. Soper, *Inorg. Chem.* **2011**, *50*, 9864–9878.
- (37) R. H. Holm, *Chem. Rev.* **1987**, *87*, 1401–1449.
- (38) R. R. Conry, J. M. Mayer, *Inorg. Chem.* **1990**, *29*, 4862–4867.
- (39) (a) K. Kobayashi, H. Ohtsu, T. Wada, T. Kato, K. Tanaka, *J. Am. Chem. Soc.* **2003**, *125*, 6729–6739. (b) K. Kobayashi, H. Ohtsu, T. Wada, K. Tanaka, *Chem. Lett.* **2002**, 868–869.
- (40) (a) M. H. V. Huynh, T. J. Meyer, *Chem. Rev.* **2007**, *107*, 5004–5064. (b) D. R. Weinberg, C. J. Gagliard, J. F. Hull, C. F. Murphy, C. A. Kent, B. C. Westlake, A. Paul, D. H. Ess, D. G. McCafferty, T. J. Meyer, *Chem. Rev.* **2012**, *112*, 4016–4093. (c) K. Gardner, J. M. Mayer, *Science* **1995**, *269*, 1849–1851.
- (41) (a) S. Ohzu, T. Ishizuka, Y. Hirai, H. Jiang, M. Sakaguchi, T. Ogura, S. Fukuzumi, T. Kojima, *Chem. Sci.* **2012**, *3*, 3421–3431. (b) Y. Hirai, T. Kojima, Y. Mizutani, Y. Shiota, K. Yoshizawa, S. Fukuzumi, *Angew. Chem., Int. Ed.* **2008**, *47*, 5772–5776. (c) T. Kojima, Y. Hirai, T. Ishizuka, Y. Shiota, K. Yoshizawa, K. Ikenuma, T. Ogura, S. Fukuzumi, *Angew. Chem., Int. Ed.* **2010**, *49*, 8449–8453. (d) R. A. Binstead, T. J. Meyer, *J. Am. Chem. Soc.* **1987**, *109*, 3287–3297. (e) B. A. Moyer, T. J. Meyer, *J. Am. Chem. Soc.* **1978**, *100*, 3601–3603. (f) J. J. Conception, J. W. Jurss, J. L. Templeton, T. J. Meyer, *J. Am. Chem. Soc.* **2008**, *130*, 16462–16463. (g) F. Liu, J. J. Conception, J. W. Jurss, T. Cardolaccia, J. L. Templeton, T. J. Meyer, *Inorg. Chem.* **2008**, *47*, 1727–1752.
- (42) J. T. Groves, R. Quinn, *Inorg. Chem.* **1984**, *23*, 3844–3846.
- (43) R. Ito, N. Umezawa, T. Higuchi, *J. Am. Chem. Soc.* **2005**, *127*, 834–835.
- (44) C.-M. Che, W.-T. Tang, W.-T. Wong, T.-F. Lai, *J. Am. Chem. Soc.* **1989**, *111*, 9048–9056.
- (45) Y. Shiota, J. M. Herrera, G. Juhász, T. Abe, S. Ohzu, T. Ishizuka, T. Kojima, K. Yoshizawa, *Inorg. Chem.* **2011**, *50*, 6200–6209.
- (46) T. Kojima, K. Hayashi, S. Iizuka, F. Tani, Y. Naruta, M. Kawano, Y. Ohashi, Y. Hirai, K. Ohkubo, Y.

- Matsuda, S. Fukuzumi, *Chem.–Eur. J.* **2007**, *13*, 8212–8222.
- (47) T. Kojima, H. Matsuo, Y. Matsuda, *Chem. Lett.* **1998**, 1085–1086.
- (48) A. A. Fokin, P. R. Schreiner, *Chem. Rev.* **2002**, *102*, 1551–1594.
- (49) W. M. C. Sameera, J. E. McGrady, *Dalton Trans.* **2008**, 6141–6149.
- (50) D. Balcells, C. Raynaud, R. H. Crabtree, O. Eisenstein, *Inorg. Chem.* **2008**, *47*, 10090–10099.
- (51) N. Jin, M. Ibrahim, T. G. Spiro, J. T. Groves, *J. Am. Chem. Soc.* **2007**, *129*, 12416–12417.
- (52) C. D. Montgomery, *J. Chem. Educ.* **2015**, *92*, 1653–1660.
- (53) D. Bourissou, O. Guerret, F. O. Gabbaï, G. Bertrand, *Chem. Rev.* **2000**, *100*, 39–92.
- (54) (a) E. O. Fischer, A. Maasböl, *Angew. Chem., Int. Ed. Engl.* **1964**, *3*, 580–581. (b) K. H. Dötz, J. Stendel, Jr., *Chem. Rev.* **2009**, *109*, 3227–3274.
- (55) (a) R. R. Schrock, *J. Am. Chem. Soc.* **1974**, *6*, 6796–6797. (b) J. Ushio, H. Nakatsuji, T. Yonezawa, *J. Am. Chem. Soc.* **1984**, *106*, 5892–5901.
- (56) A. J. Arduengo, R. L. Harlow, M. Kline, *J. Am. Chem. Soc.* **1991**, *113*, 361–363.
- (57) A. Kumar, M. Katari, P. Ghosh, *Polyhedron* **2013**, *52*, 524–529.
- (58) E. Chardon, G. Dahm, G. Guichard, S. Bellemin-Lapponnaz, *Organometallics* **2012**, *31*, 7618–7621.
- (59) H. Jacobsen, A. Correa, A. Poater, C. Costabile, L. Cavallo, *Coord. Chem. Rev.* **2009**, *253*, 687–703.
- (60) H. Jacobsen, A. Correa, C. Costabile, L. Cavallo, *J. Organomet. Chem.* **2006**, *691*, 4350–4358.
- (61) (a) D. M. Khramov, V. M. Lynch, C. W. Bielawski, *Organometallics* **2007**, *26*, 6042–6049. (b) M. D. Sanderson, J. W. Kamplain, C. W. Bielawski, *J. Am. Chem. Soc.* **2006**, *128*, 16514–16515.
- (62) S. Fantasia, J. L. Petersen, H. Jacobsen, L. Cavallo, S. P. Nolan, *Organometallics* **2007**, *26*, 5880–5889.
- (63) L. Mercs, G. Labat, A. Neels, A. Ehlers, M. Albrecht, *Organometallics* **2006**, *25*, 5648–5656.
- (64) D. F. Shriver, P. W. Atkins, G. H. Langford, *Inorganic Chemistry* 5th ed., Oxford University Press, Oxford, **1990**.
- (65) (a) M. Scholl, S. Ding, C. W. Lee, R. H. Grubbs, *Org. Lett.* **1999**, *1*, 953–956. (b) G. C. Vougioukalakis, R. H. Grubbs, *Chem. Rev.* **2010**, *110*, 1746–1787.
- (66) P. Schwab, M. B. France, J. W. Ziller, R. H. Grubbs, *Angew. Chem., Int. Ed.* **1995**, *34*, 2039–2041.
- (67) (a) E. Masllorens, M. Rodríguez, I. Romero, A. Roglans, T. Parella, J. Benet-Buchholz, M. Poyatos, A. Llobet, *J. Am. Chem. Soc.* **2006**, *128*, 5306–5307. (b) L. Vaquer, P. Miró, X. Sala, F. Bozoglian, E. Masllorens, J. Benet-Buchholz, X. Fontrodona, T. Parella, I. Romero, A. Roglans, M. Rodríguez, C. Bo, A. Llobet, *ChemPlusChem* **2013**, *78*, 235–243.
- (68) (a) T. G. Traylor, A. R. Miksztal, *J. Am. Chem. Soc.* **1987**, *109*, 2770–2774. (b) T. G. Traylor, F. Xu, *J. Am. Chem. Soc.* **1988**, *110*, 1953–1958.
- (69) J. Malineni, H. Keul, M. Möller, *Dalton Trans.* **2015**, *44*, 17409–17414.
- (70) J.-H. Choi, L. E. Heim, M. Ahrens, M. H. G. Precht, *Dalton Trans.* **2014**, *43*, 17248–17254.
- (71) Z.-Y. Tang, Q.-S. Hu, *J. Am. Chem. Soc.* **2004**, *126*, 3058–3059.
- (72) (a) P. Ruiz-Castillo, S. L. Buchwald, *Chem. Rev.* **2016**, *116*, 12564–12649. (b) N. Kambe, T. Iwasaki, J. Terao, *Chem. Soc. Rev.* **2011**, *40*, 4937–4947. (c) A. Suzuki, *J. Organomet. Chem.* **1999**, *576*, 147–168. (d) A. Biffs, P. Centomo, A. D. Zotto, M. Zecca, *Chem. Rev.* **2018**, *118*, 2249–2295.
- (73) (a) E. A. B. Kantchev, C. J. O'Brien, M. G. Organ, *Angew. Chem., Int. Ed.* **2007**, *46*, 2768–2813. (b) G. C. Fortman, S. P. Nolan, *Chem. Soc. Rev.* **2011**, *40*, 5151–5169.
- (74) M. Taige, A. Zeller, S. Ahrens, S. Goutal, E. Hardtweck, *J. Organomet. Chem.* **2006**, *692*, 1519–1529.
- (75) C. Gstöttmayr, B. Volker, H. Eberhatdt, *Angew. Chem., Int. Ed.* **2002**, *41*, 1363–1365.
- (76) R. Batey, M. Shen, A. Lough, *Org. Lett.* **2002**, *4*, 1411–1414.

- (77) Y. Sato, T. Yoshino, M. Mori, *J. Organomet. Chem.* **2005**, *690*, 5753–5758.
- (78) J. Yang, L. Wang, *Dalton Trans.* **2012**, *41*, 12031–12037.
- (79) (a) H. D. Velazquez, F. Verpoort, *Chem. Soc. Rev.* **2012**, *41*, 7032–7060. (b) E. Levin, E. Ivry, C. E. Diesendruck, N. G. Lemcoff, *Chem. Rev.* **2015**, *115*, 4607–4692.
- (80) F. Godoy, C. Segarra, M. Poyatos, E. Peris, *Organometallics* **2011**, *30*, 684–688.
- (81) (a) M. Muehlhofer, T. Strassner, W. A. Hermann, *Angew. Chem., Int. Ed.* **2002**, *41*, 1745–1747. (b) D. Munz, T. Strassner, *Angew. Chem., Int. Ed.* **2014**, *53*, 2485–2488.
- (82) R. A. Periana, D. J. Taube, S. Gamble, H. Taube, T. Satoh, H. Fujii, *Science* **1998**, *280*, 560–564.
- (83) G.-J. T. Brink, I. W. C. E. Arends, R. A. Sheldon, *Science*, **2000**, *287*, 1636–1639.

Chapter 2

Redox properties of ruthenium(II) complexes having two *N*-heterocyclic carbene moieties

2-1 Introduction

Transition-metal complexes bearing *N*-heterocyclic carbene (NHC) ligands have been widely studied for several decades.¹ In particular, 4d transition metals are capable of forming highly stable coordination bonds with NHC ligands and they have been applied to construction of catalytic systems.² Among them, Ru^{II} and Ru^{III} complexes having NHC ligands have been used to catalysis such as substrate oxidation (Figure 2-1(a))³ and water oxidation (Figure 2-1(b)).⁴ They also have gathered much attention to the

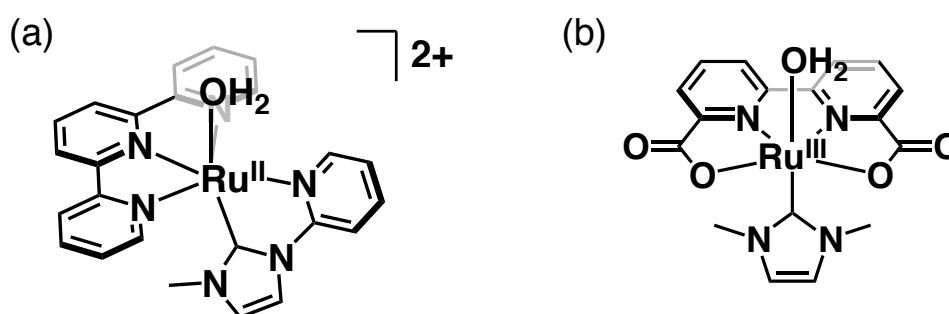


Figure 2-1. Ru-NHC catalysts for substrate oxidation (a)^{3a} and water oxidation (b).^{4a}

photochemical properties;⁵ for example, the strong coordination of an NHC ligand to a central Ru^{II} atom allowed us to elongate the lifetime of the excited state related to the emission, compared to its polypyridyl

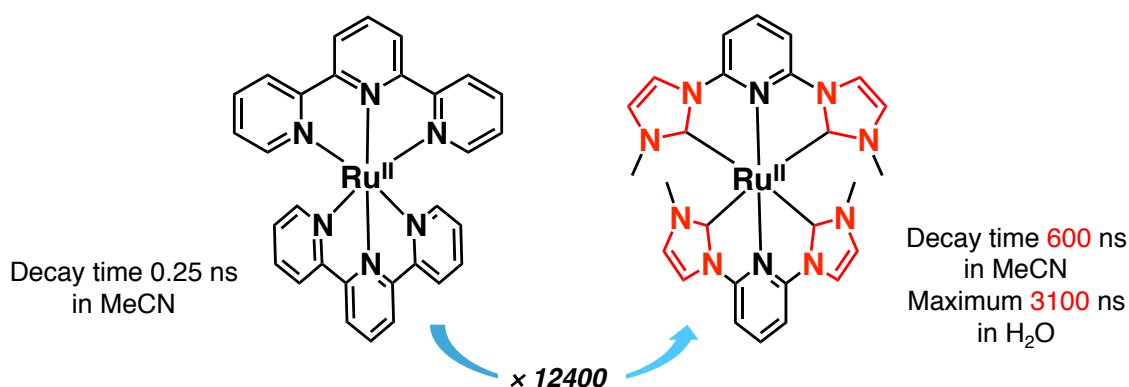


Figure 2-2. A Ru-NHC complex exhibiting a long life-time of the excited state related to the emission.⁵

analogs (Figure 2-2).⁵ Although plenty of reports on Ru-NHC complexes have been delivered, the effects of NHC ligands on the electronic structures of Ru-NHC complexes have been scarcely reported.⁶ In this chapter, the author has successfully synthesized and characterized two novel Ru^{II} complexes, which have 2,2'-bipyridyl (bpy) and a pincer-type tridentate ligand with two NHC moieties as the ancillary ligands. The pincer-type ligand coordinates to the central Ru^{II} atom in the meridional manner. In the Ru^{II} complexes, intramolecular CH/ π interaction is formed between the ^{*i*}Pr groups of the NHC moieties and the bpy ligand to fix the two NHC moieties in different circumstances each other.

2-2 Synthesis and characterization of $[\text{Ru}^{\text{II}}(\text{C}^{\wedge}\text{Py}^{\wedge}\text{C})(\text{bpy})(\text{L})](\text{PF}_6)_n$

Syntheses of $[\text{Ru}^{\text{II}}(\text{C}^{\wedge}\text{Py}^{\wedge}\text{C})(\text{bpy})(\text{MeCN})]^{2+}$ (**1**) and $[\text{Ru}^{\text{II}}\text{Cl}(\text{C}^{\wedge}\text{Py}^{\wedge}\text{C})(\text{bpy})]^+$ (**2**) [$\text{C}^{\wedge}\text{Py}^{\wedge}\text{C}$ = 2,6-bis(3-isopropylimidazol-2-ylidene)pyridine] are shown in Figure 2-3. Complexes **1** and **2** were obtained by refluxing the solution of *in-situ* generated $[\text{Ag}^{\text{I}}(\text{C}^{\wedge}\text{Py}^{\wedge}\text{C})]$ complex and $[\text{Ru}^{\text{II}}\text{Cl}_2(\text{bpy})(\text{dmsO})_2]$ in MeCN for **1** and CH_2Cl_2 for **2** in the dark.



Figure 2-3. Synthesis of $[\text{Ru}^{\text{II}}(\text{C}^{\wedge}\text{Py}^{\wedge}\text{C})(\text{bpy})(\text{L})]^{n+}$ (**1**: L = MeCN, n = 2. **2**: L = Cl, n = 1).

Characterization of **1** and **2** was performed with ^1H NMR spectroscopy (Figure 2-4(a), (b)), ESI-TOF-MS spectrometry (Figure 2-4(c), (d)), elemental analysis, and X-ray crystallography. In the ^1H NMR spectra in acetonitrile- d_3 , characteristic four doublets were observed in the range of 0.5 – 1.4 ppm for both **1** and **2**. This indicates that all methyl groups are in different magnetic environments due to inhibition of rotation around the terminal isopropyl groups (see below). In the ESI-TOF-MS spectra, MS peaks derived from $[\mathbf{1} - \text{MeCN} + \text{F}]^+$ for **1** and $[\mathbf{2}]^+$ for **2** were observed at $m/z = 600.18$ (sim.: 600.20) and 616.15 (sim.: 616.15), respectively.

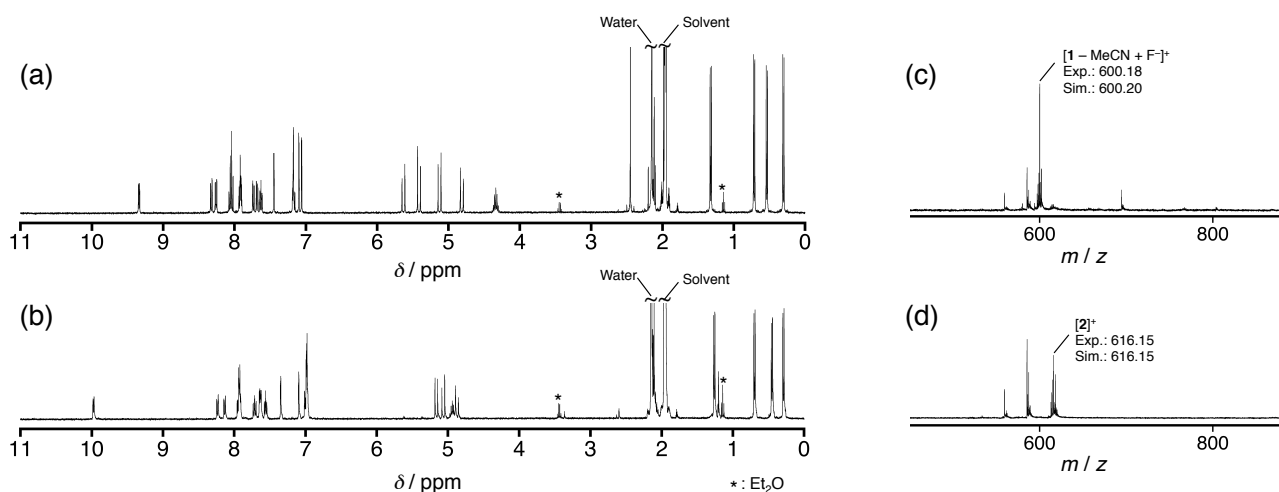


Figure 2-4. ^1H NMR spectra of **1** (a) and **2** (b) in acetonitrile- d_3 . ESI-TOF-MS spectra of **1** (c) and **2** (d).

2-3 Structural analysis in solid and solution states of $[\text{Ru}^{\text{II}}(\text{C}^{\wedge}\text{Py}^{\wedge}\text{C})(\text{bpy})(\text{L})](\text{PF}_6)_n$

The crystal structures of **1**·(PF₆)₂ and **2**·PF₆ (Figure 2-5) clearly reveal that the coordination manner of the $\text{C}^{\wedge}\text{Py}^{\wedge}\text{C}$ ligands is meridional (Figure 2-5). Selected bond lengths and bond angles around the ruthenium centers of **1** and **2** are summarized in Table 2-1. The bond lengths of Ru-N8(CH₃CN) in **1**·(PF₆)₂ and Ru-Cl in **2** are 2.041(2) and 2.4348(6) Å, respectively. These values are within the range of the corresponding bond lengths observed in other Ru^{II} complexes having an acetonitrile molecule (2.03–2.44 Å)⁷ or a chloride ion

(2.39–2.52 Å)⁸ as a ligand. In addition, the bond lengths between the central Ru^{II} atom and NHC carbons (Ru–C11 and Ru–C1)

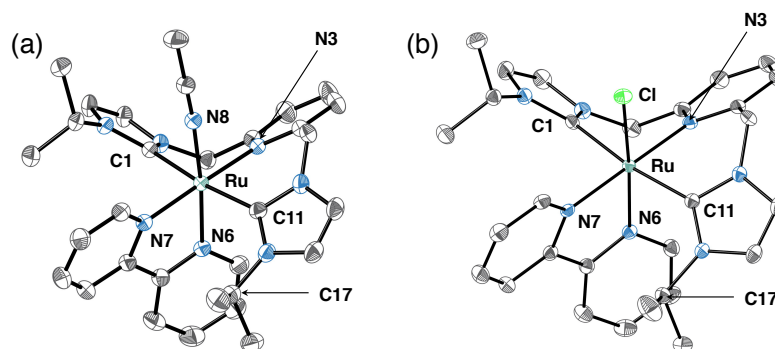


Figure 2-5. Oak-ridge thermal ellipsoid plots (ORTEP) drawings of **1** (a) and **2** (b).

in **1**·(PF₆)₂ are 2.093(2) and 2.097(2) Å, respectively, and those in **2**·PF₆ are 2.0824(19) and 2.1149(19) Å, respectively. These values are longer than those of Ru–C bonds (1.98–2.00 Å) observed in other Ru^{II}–NHC complexes.^{3d,9} This indicates the strong *trans* influences exerted by strong σ donating NHC ligands that are positioned mutually at the *trans* positions.¹⁰

Table 2-1. Selected bond lengths (Å) and angles (°) of the crystal structures for **1**·(PF₆)₂ and **2**·PF₆

	1 ·(PF ₆) ₂	2 ·PF ₆
Bond length, Å		
Ru-X	2.041(2) (X = N8)	2.4348(5) (X = Cl)
Ru-C1	2.097(2)	2.1149(19)
Ru-C11	2.093(2)	2.0824(19)
Ru-N3	2.149(2)	2.1604(16)
Ru-N6	2.0511(19)	2.0202(16)
Ru-N7	2.053(2)	2.0490(16)
Bond angle, °		
C1-Ru-C11	173.42(9)	172.35(7)
C11-Ru-N3	87.78(8)	86.81(7)
C1-Ru-N3	86.00(8)	86.08(7)
C11-Ru-X	91.67(8) (X = N8)	88.90(5) (X = Cl)
C1-Ru-X	86.20(8) (X = N8)	88.63(5) (X = Cl)
C11-Ru-N7	96.29(9)	97.27(7)
C1-Ru-N7	90.13(8)	90.10(7)
C11-Ru-N6	90.00(8)	87.58(7)
C1-Ru-N6	92.74(8)	95.92(7)
N6-Ru-N7	78.50(8)	78.73(6)

The ^1H NMR spectra of **1** and **2** in acetonitrile- d_3 (Figure 2-2(a) and (b)) exhibited complicated spectral patterns derived from the structures of **1** and **2** despite of their meridional coordination arrangements mentioned above. This indicates that complexes **1** and **2** show C_1 symmetry due to non-flexibility of the NHC ligand twisted at the CH_2 linkers. The ^1H NMR signals, assigned to the protons at the 6-position of the pyridine moieties in the bpy ligand close to the axial ligands, were observed at 9.3 ppm for **1** and 10.0 ppm for **2**. The large down-field shift of the ^1H NMR signal in **2** compared to that of **1** indicates that there is hydrogen-bonding interaction between the proton at the 6-position of the bpy ligand and the chloro ligand in

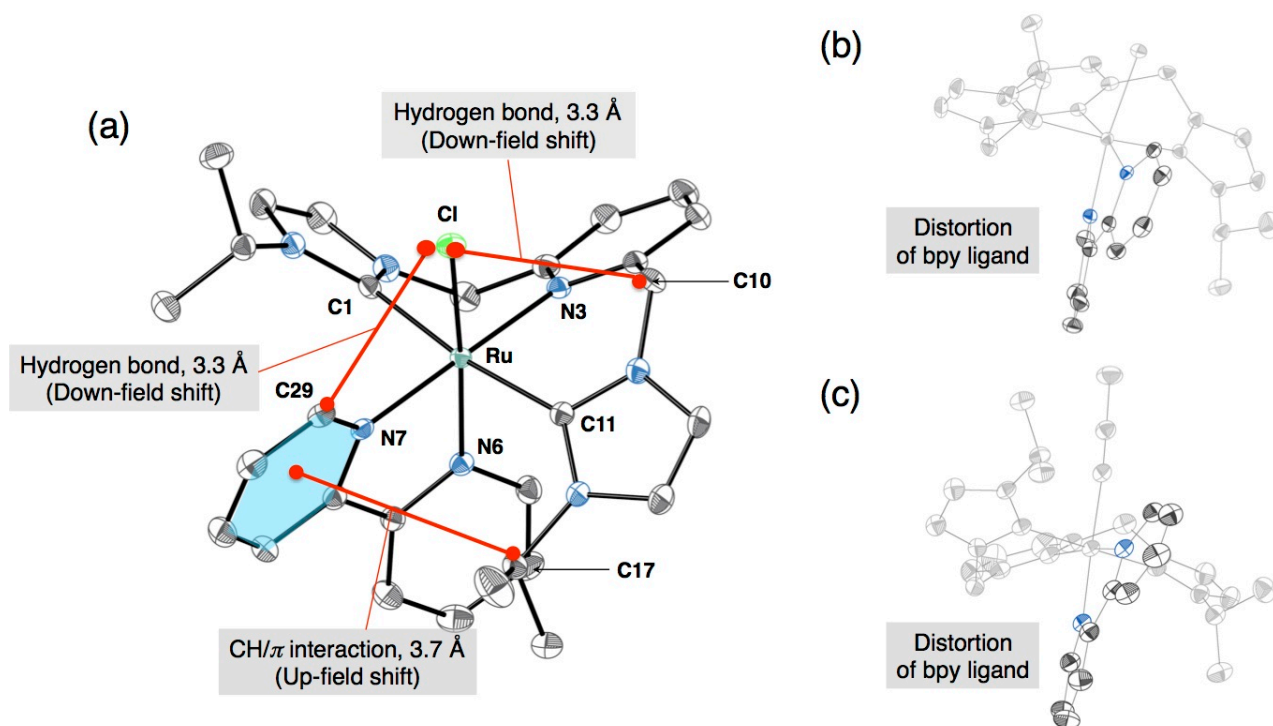


Figure 2-6. (a) ORTEP drawing of **2** and three selected distances with the tendency of changes of ^1H -NMR chemical shifts shown in parentheses. ORTEP drawings of **2** (b) and **1** (c) to highlight the bpy ligands.

2 (Figure 2-6).^{3d} ^1H NMR signals of the methylene moieties showing two AB quartets were observed in the range from 4.8 to 5.6 ppm for **1**. These chemical shifts were comparable to those of Ru^{II} complexes having

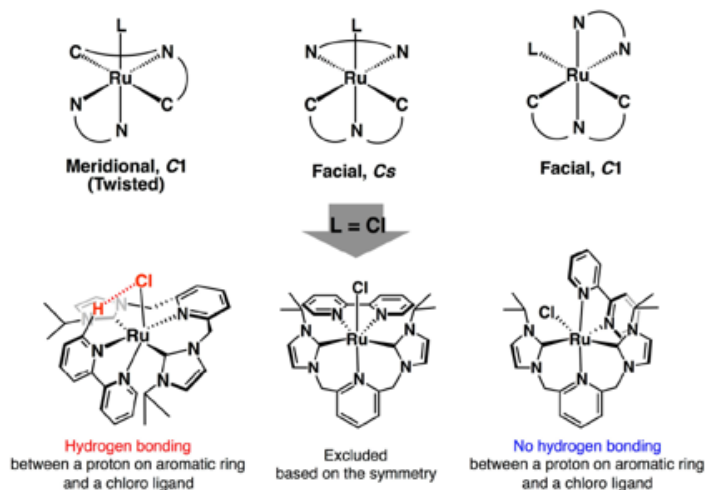


Figure 2-7. Three possible structural isomers of **2**.

two similar bis-NHC ligands.¹¹ The ¹H NMR spectrum of **2** showed an AB quartet and two AX doublets in the range from 4.9 to 7.0 ppm for the methylene moieties. The large downfield shift of one of the AX doublets for **2** due to the methylene protons should be derived from intramolecular hydrogen bonding between the chloro ligand and one methylene proton as shown in Figure 2-6.

Three possible structural isomers can be considered for **1** and **2**: one meridional and two facial isomers (Figure 2-7). Since **1** and **2** should be in the C₁ symmetry as indicated by the ¹H NMR spectra, one of the facial isomers in the C_s symmetry can be excluded. In addition, the hydrogen bonding between the chloro ligand and the proton at the 6-position of the bpy ligand in **2**, as mentioned above, should not be observed in the other facial isomer. The features observed in the ¹H NMR spectra indicate that the C[^]Py[^]C coordinates to the central Ru^{II} atom in the meridional manner in both **1** and **2**, as confirmed by the X-ray crystallography. In the crystal structures, the bpy ligand in both **1** and **2** was strongly distorted due to the steric repulsion of one of the isopropyl moieties bound to the NHC ligand (Figure 2-6(b), (c)). The distance between C17 and the centroid of the pyridine ring containing N7 atom was *ca.* 3.7 Å, which was in the range of 2.9–3.8 Å that CH/π interaction can be formed.¹² This interaction suggests shielding of the proton by the ring current to afford large upfield shifts (~ 2 ppm) of the ¹H NMR signals, assigned to protons bound to the methine carbons based on two-dimensional NMR measurements (Figures 2-8). ¹H-¹H COSY measurements allowed us to observe obvious cross peaks for the methylene protons in the left (including C1 atom in Figure 2-6) and right arms (including C11 atom in Figure 2-6) of complexes **1** and **2**, which helped to assign the desymmetrized ¹H NMR signals. However, complete assignments of the ¹H NMR signals were impossible only by ¹H-¹H COSY measurements, since ¹H NMR signals of the imidazole moieties cannot be distinguished. Therefore, nuclear Overhauser effect (NOE) of **1** in acetonitrile-*d*₃ was investigated to assign the desymmetrized ¹H NMR signals (Figure 2-9). In the NOE measurements, an NOE was observed between ¹H NMR signals for one of the terminal methyl groups in the NHC imidazole rings, appearing at δ 0.71 ppm, and for the proton at the 5-position of the imidazole ring, appearing at δ 7.06 ppm (Figure 2-9(a)). Another NOE correlation was observed between ¹H NMR signals for the proton at the 4-position of the imidazole ring, appearing at δ 7.44 ppm, and for the bridging methylene proton, appearing at δ 5.41 ppm (Figure 2-9(b)). ¹H NMR signals for the bridging methylene

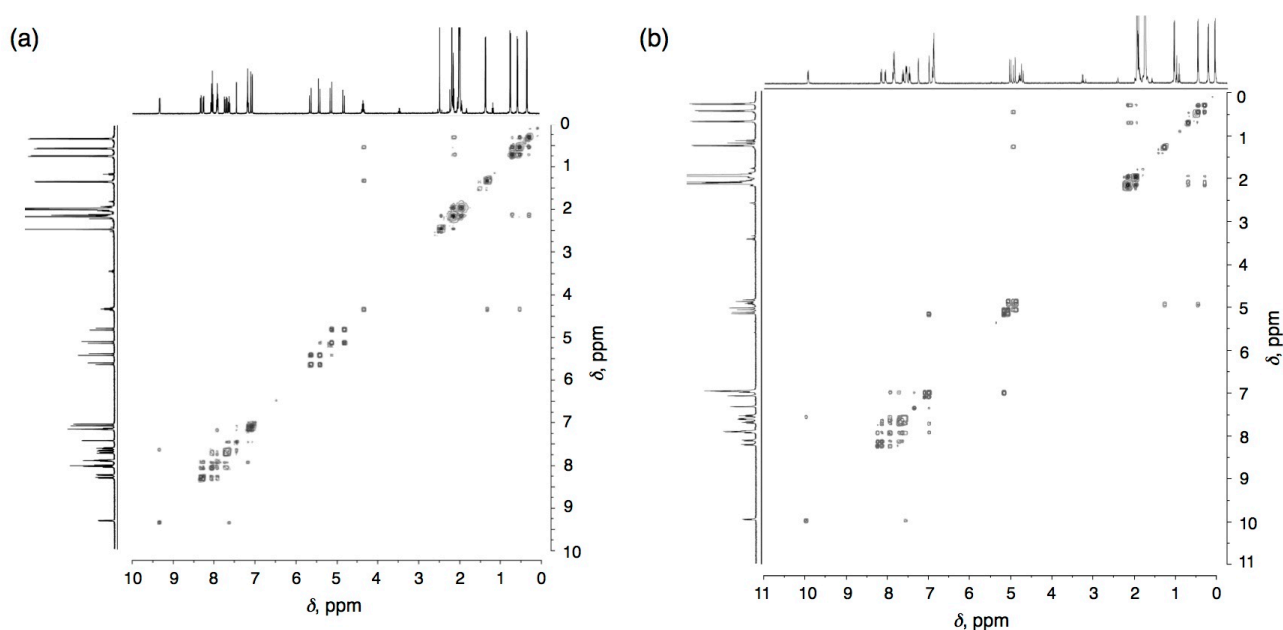


Figure 2-8. ¹H-¹H COSY of **1** (a) and **2** (b) in acetonitrile-*d*₃.

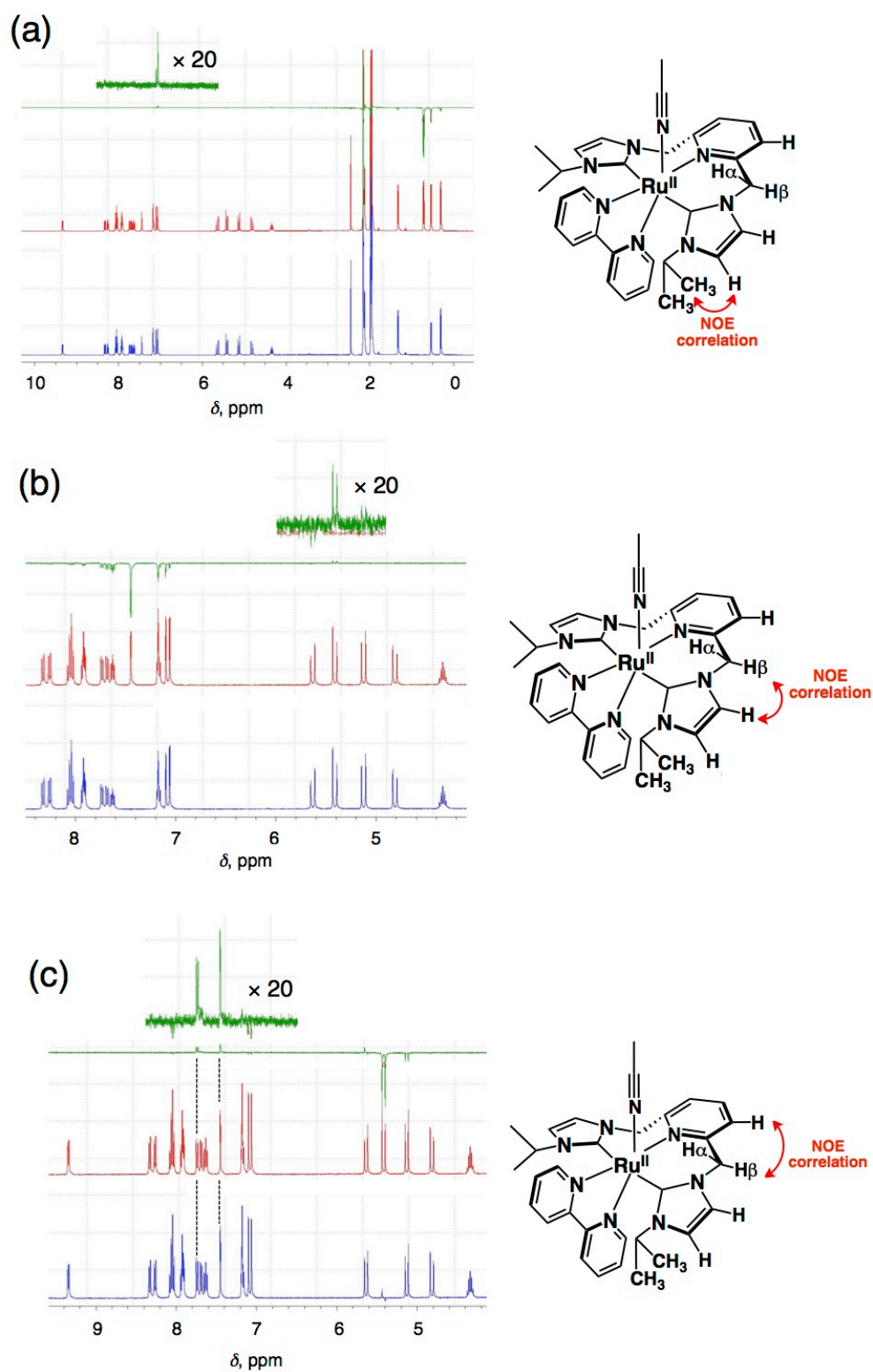


Figure 2-9. Differential NOE measurements on complex **1** in acetonitrile- d_3 at 298 K with irradiation at 0.7 ppm (a), 7.4 ppm (b), and 5.4 ppm (c). Red spectra indicate the spectrum without irradiation. Blue spectra indicate the spectrum with irradiation. Green spectra indicate the differential spectra (blue – red).

proton, appearing at δ 5.41 ppm and for the proton at the 3-position of the pyridyl ring, appearing at δ 7.68 ppm also showed NOE correlation (Figure 2-9(c)). The schematic representations of these NOE measurements were shown in the right side of Figure 2-9. In addition, variable-temperature ^1H NMR measurements in the range from 298 to 348 K were conducted for **1**; as a result, the ^1H NMR signals did not show any significant change of chemical shifts and the symmetry-broken ^1H NMR signals of **1** maintained in the temperature range (Figure 2-10). This indicates that the CH/π interaction assists the stabilization of the distorted conformation of the $\text{C}^{\wedge}\text{Py}^{\wedge}\text{C}$ ligand in **1** and the two NHC moieties do not flip to show the seesaw-like motion that makes the two NHC moieties equivalent in the NMR time scale.¹³

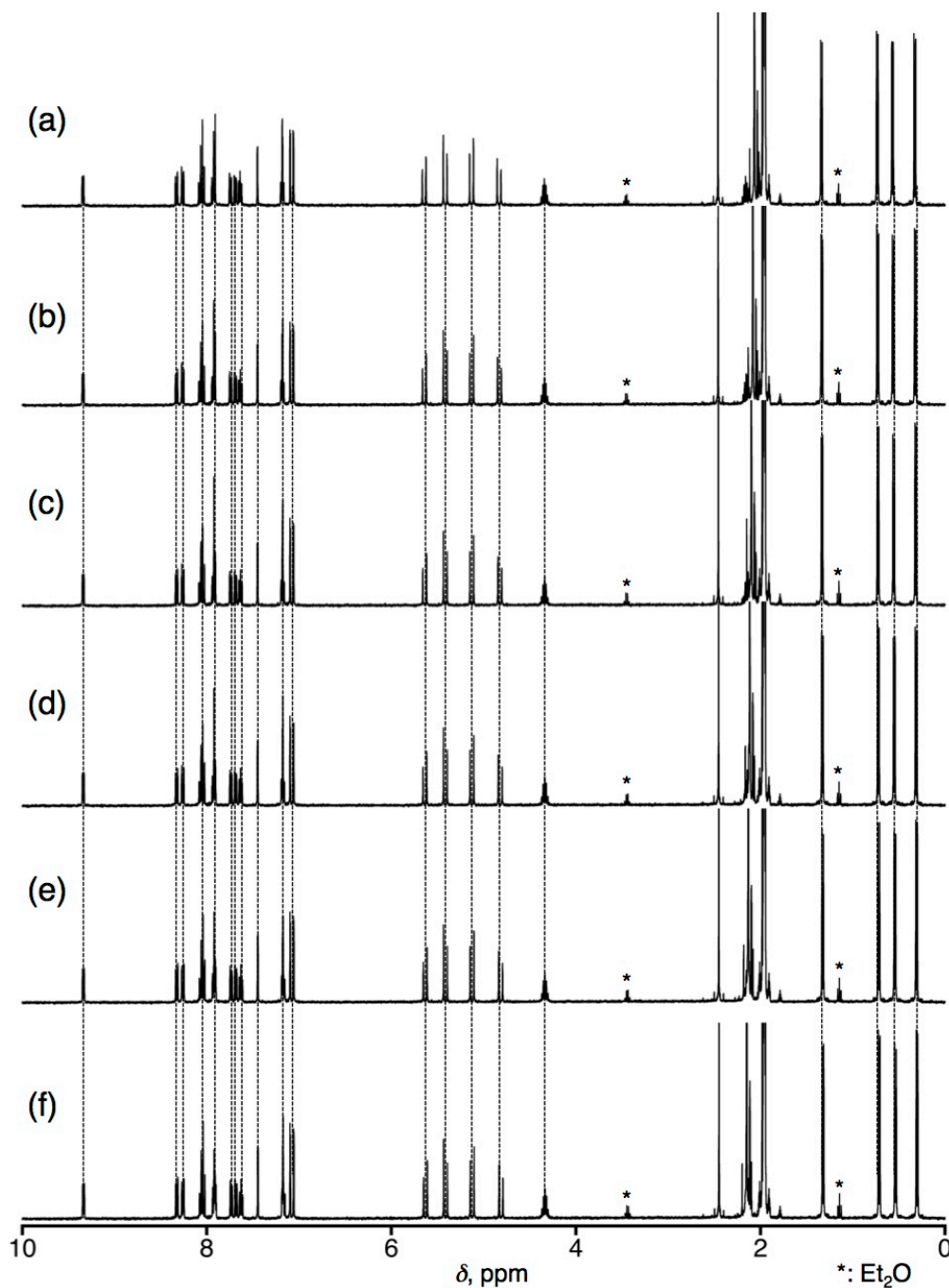


Figure 2-10. Variable temperature ^1H NMR spectra of **1**· $(\text{PF}_6)_2$ (2.0 mM) measured at 348 K (a), 338 K (b), 328 K (c), 318 K (d), 308 K (e), and 298 K (f) in acetonitrile- d_3 . No spectral change was observed in the temperature range as indicated by dashed lines.

2-4 Photochemical properties of $[\text{Ru}^{\text{II}}(\text{C}^{\wedge}\text{Py}^{\wedge}\text{C})(\text{bpy})(\text{L})](\text{PF}_6)_n$

In the UV/Vis spectra of **1** and **2** in acetonitrile, characteristic absorption bands were observed at 483 and 537 nm, respectively. On the basis of the TD-DFT calculations (Figure 2-11), these absorption bands are assigned to metal-to-ligand charge transfer (MLCT) bands ($d\pi$ of Ru^{II} to π^* of bpy). These wavelength values were larger (*ca.* 30 nm) compared to those for other related Ru^{II} complexes having bpy ligands.¹⁴

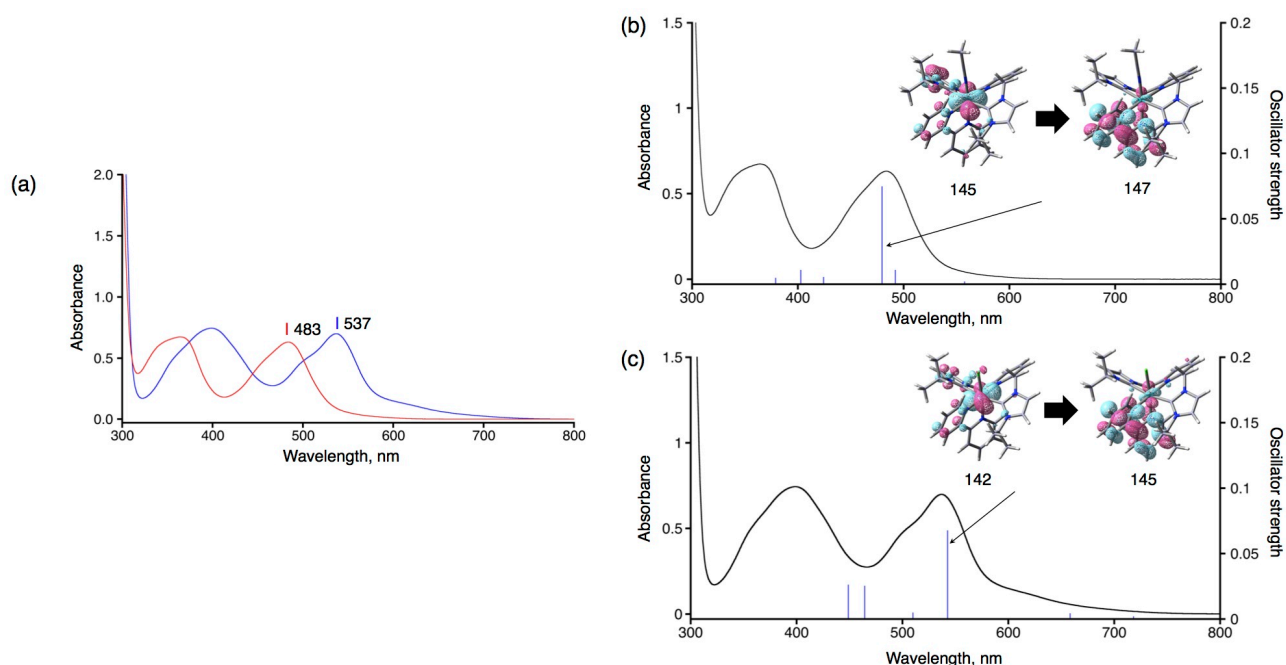


Figure 2-11. UV-Vis spectra of **1**·(PF₆)₂ (a, red) and **2**·(PF₆) (a, blue) in acetonitrile and UV-Vis spectra of **1**·(PF₆)₂ (b) and **2**·(PF₆) (c) and calculated oscillator strengths (blue sticks) obtained by the TD-DFT calculations at the B3LYP/SDD level of theory.

The emission and excitation spectra of **1** and **2** were measured in argon-purged butyronitrile at 77 K (Figure 2-12(a), (b)). The emission bands assigned to the phosphorescence from the ³MLCT excited states of **1** and **2** were observed at 608 and 732 nm, respectively. Phosphorescence derived from the ³MLCT excited state of **1** was partially quenched in an O₂-saturated butyronitrile solution measured at room temperature (Figure 2-12(c)). The quantum yields of the emissions of **1** and **2** were determined to be 0.41 and 1.5×10^{-3} , respectively, based on relative intensities to the reported quantum yield ($\Phi = 0.35$) for $[\text{Ru}^{\text{II}}(\text{bpy})_3]^{2+}$ in MeOH : EtOH = 1 : 4 (v/v) glass at 77 K.¹⁵

To compare the quantum yields of phosphorescence for **1** and **2** with those reported for other Ru^{II} -polypyridyl complexes, the phosphorescence measurements were also conducted at room temperature (Table 2-2). As a result, the phosphorescence quantum yields of **1** and **2** were determined as shown in Table 2-2. These values fall in the range of those reported for other Ru^{II} complexes. This lowering of the quantum yield for the phosphorescence of **2** can be explained by decreasing the lifetime of the ³MLCT excited state by thermal transition to a metal-centered triplet excited state (³MC); this is probably due to narrowing the ligand-field splitting in **2**, since the chloro ligand acts as a π donor to elevate the energy level of the $d\pi$ orbital in contrast to the acetonitrile ligand in **1**, which undergoes π -back bonding to lower that of the $d\pi$ orbital and to enlarge the splitting. Consequently, thermal transition from the ³MLCT excited state to the

^3MC excited state occurs easily in **2**. The effects of axial ligands on the photophysical properties of the Ru^{II} complexes have been also reported for Ru^{II} -porphyrin complexes.²¹

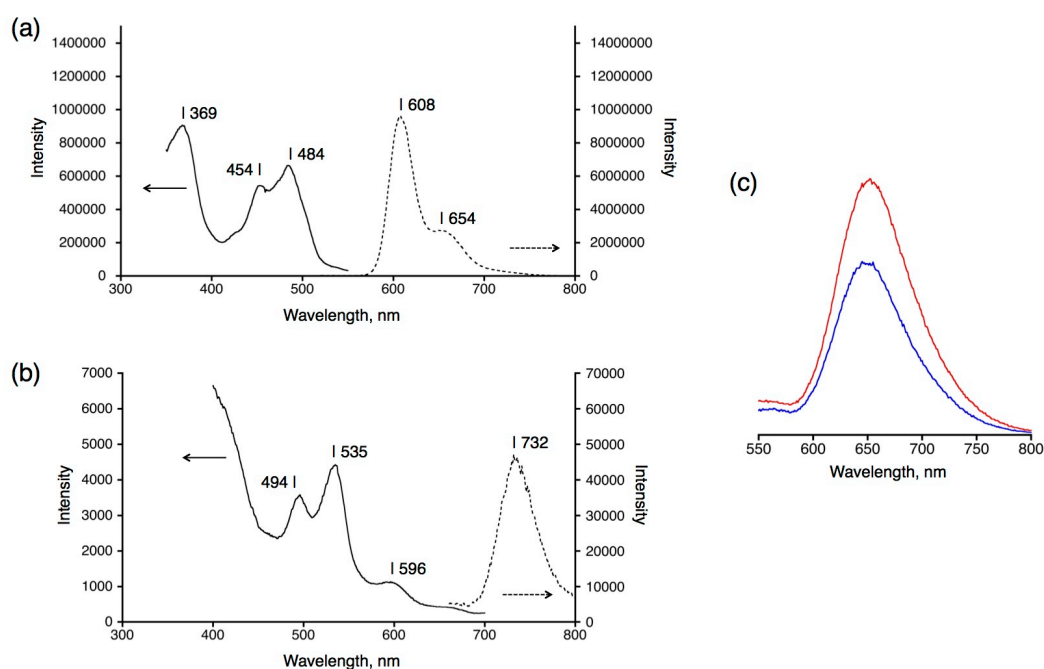
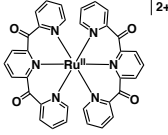
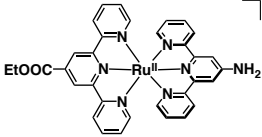


Figure 2-12. (a) Excitation (solid line) and emission spectra (dashed line) of **1** in the butyronitrile glass measured at 77 K under Ar: $[\mathbf{1}] = 0.1 \text{ mM}$, λ_{exc} : 486 nm, λ_{obs} for the excitation spectrum: 608 nm. (b) Excitation (solid line) and emission spectra (dashed line) of **2** in butyronitrile measured at 77 K under Ar: $[\mathbf{2}] = 0.1 \text{ mM}$, $\lambda_{\text{exc}} = 544 \text{ nm}$, λ_{obs} for the excitation spectrum: 732 nm. (c) Emission spectra of $\mathbf{1} \cdot (\text{PF}_6)_2$ in butyronitrile measured at RT under Ar (red) and O_2 (blue). $[\mathbf{1}] = 0.1 \text{ mM}$, λ_{exc} : 486 nm.

Table 2-2. Summary of quantum yields for emission of **1**, **2**, and ruthenium(II)-polypyridyl complexes in acetonitrile at RT.

Compound	Quantum yield (Φ)	Reference
$\mathbf{1} \cdot (\text{PF}_6)_2$	$7.0 \times 10^{-4}{}^a$	This work
$\mathbf{2} \cdot \text{PF}_6$	$<0.0001{}^a$	This work
$[\text{Ru}(\text{bpy})_3]^{2+}$	0.062	16
$[\text{Ru}(\text{tpy})_2]^{2+}$	5×10^{-6}	17
$[\text{Ru}(\text{tpy})(\text{bpy})(\text{NCMe})]^{2+}$	4.5×10^{-4}	18
	0.30	19
	3.4×10^{-4}	20

^a Quantum yields of $\mathbf{1} \cdot (\text{PF}_6)_2$ and $\mathbf{2} \cdot \text{PF}_6$ were determined with relative intensities to that for $[\text{Ru}^{\text{II}}(\text{bpy})_3](\text{PF}_6)_2$ as a standard ($\Phi = 0.062$ in MeCN, 25 °C).¹⁷ tpy = 2,2',6',2''-terpyridine. bpy = 2,2'-bipyridine.

2-5 Redox properties of $[\text{Ru}^{\text{II}}(\text{C}^{\wedge}\text{Py}^{\wedge}\text{C})(\text{bpy})(\text{L})](\text{PF}_6)_n$

Redox behavior of $1 \cdot (\text{PF}_6)_2$ and $2 \cdot \text{PF}_6$ in acetonitrile solutions was investigated by cyclic and differential-pulse voltammetries at room temperature (Figure 2-13). The cyclic voltammograms (CVs) showed reversible redox waves at $E_{1/2} = +1.01$ and -1.49 V vs SCE for $1 \cdot (\text{PF}_6)_2$ and

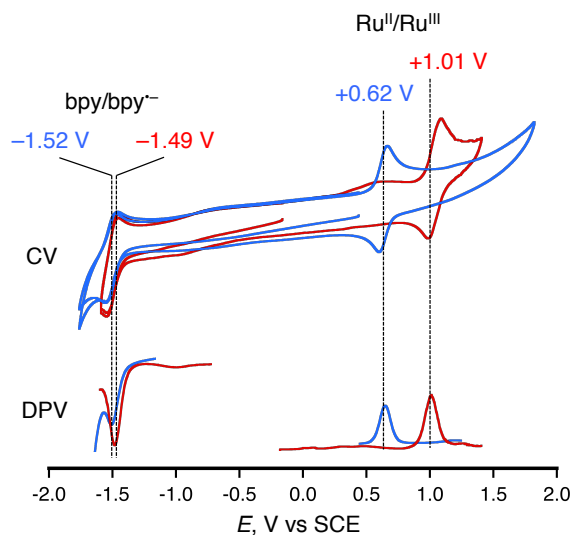


Figure 2-13. Cyclic and differential-pulse voltammograms (CV and DPV) of $1 \cdot (\text{PF}_6)_2$ (red) and $2 \cdot (\text{PF}_6)$ (blue) in acetonitrile at RT. $[1]$ or $[2] = 1.0$ mM. Electrolyte: 0.1 M $[(n\text{-Bu})_4\text{N}](\text{PF}_6)$. WE: Pt disk. CE: Pt wire. RE: Ag/AgCl. Scan rate for CV: 100 mV/s.

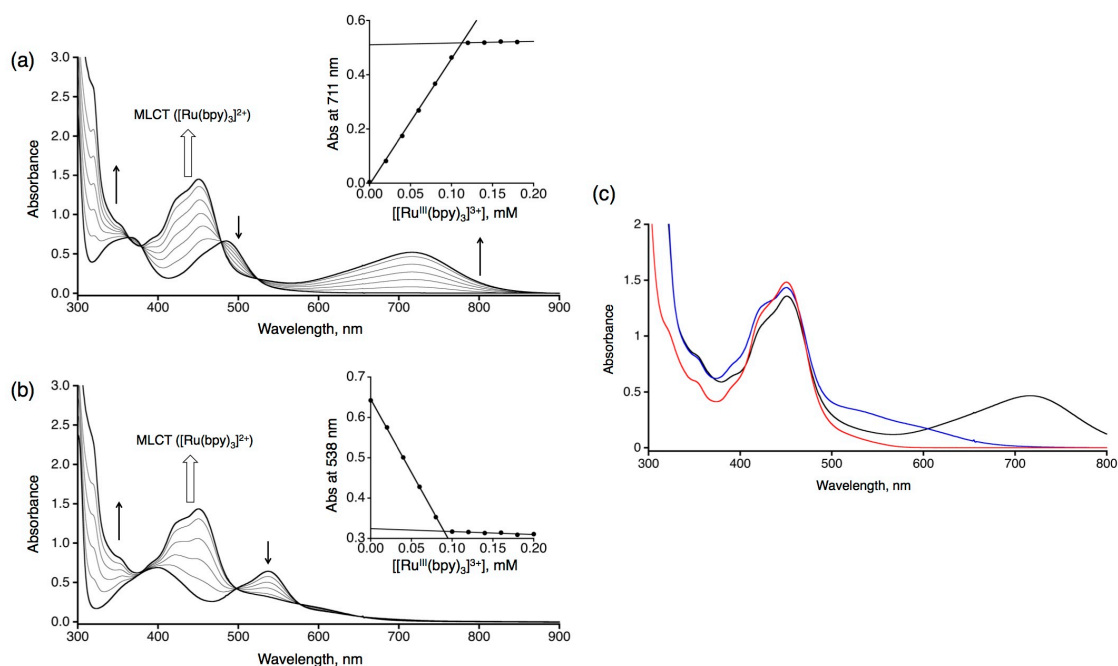


Figure 2-14. UV-Vis spectral changes upon addition of $[\text{Ru}^{\text{III}}(\text{bpy})_3]^{3+}$ to 1 (a) and 2 (b) at RT. $[1]$ and $[2]: 0.10$ mM. Solvent: acetonitrile. Inset shows the absorbance change at the selected wavelength against concentration of $[\text{Ru}^{\text{III}}(\text{bpy})_3]^{3+}$ added as an oxidant. (c) Overlaid UV-Vis spectra of 1 (0.1 mM, black) and 2 (0.1 mM, blue) upon addition of 1 equiv of $[\text{Ru}^{\text{III}}(\text{bpy})_3](\text{ClO}_4)_3$ to give 3 and 4 , respectively, and of $[\text{Ru}^{\text{II}}(\text{bpy})_3](\text{PF}_6)_2$ (0.1 mM, red) in acetonitrile at RT. The absorption bands around 450 nm for 3 and 4 were assigned to the MLCT transition of $[\text{Ru}^{\text{II}}(\text{bpy})_3]^{2+}$ produced by the oxidation reactions.

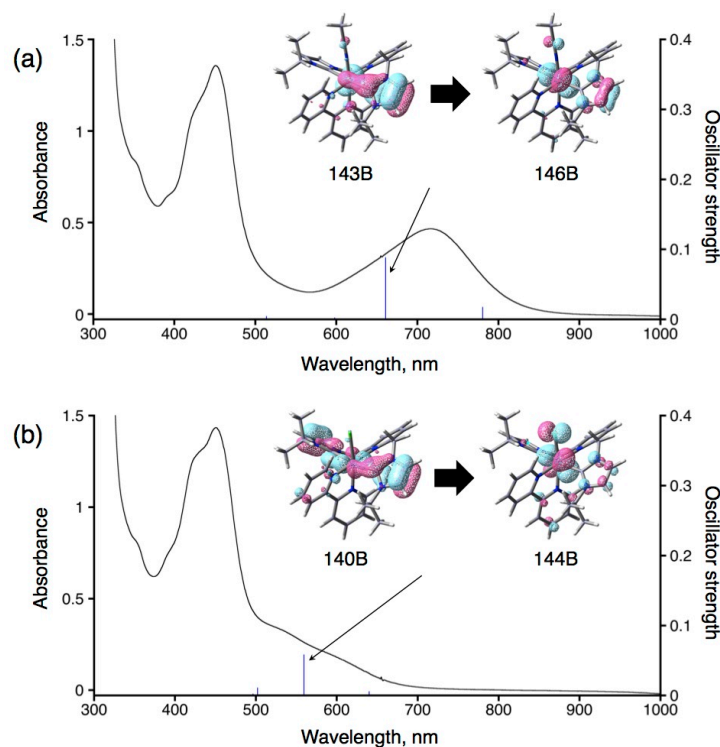


Figure 2-15. UV-Vis spectra (black line) of **1**·(PF₆)₂ (a) and **2**·PF₆ (b) in acetonitrile upon addition of 1 equiv of [Ru^{III}(bpy)₃](ClO₄)₃ at RT and the calculated oscillator strengths (blue sticks) of **3** (a) and **4** (b) obtained by the TD-DFT calculations at the B3LYP/SDD level of theory.

$E_{1/2} = +0.62$ and -1.52 V vs SCE for **2**·(PF₆). These potentials were relatively lower than those of other related Ru^{II} complexes having neutral polypyridyl ligands or alkylamine ligands.²² In particular, redox potentials of **1** and **2** were lower than Ru^{II} complexes having terpyridyl-like conjugated NHC ligands.⁶ This indicates that the σ -donating ability of the NHC moieties in C[^]Py[^]C ligand is stronger than the π -conjugated analog,⁶ and the strong σ -donating ability of the NHC moieties in the C[^]Py[^]C ligand makes the central Ru^{II} atom more electron-rich. Therefore, the Ru^{II} atom can be oxidized more easily than the π -conjugated counterparts.⁶ Upon addition of [Ru^{III}(bpy)₃](ClO₄)₃ ($E_{1/2} = +1.29$ V vs SCE)²³ to acetonitrile solutions of **1** and **2**, the absorption bands at 483 nm for **1** and 537 nm for **2** decreased and instead a new obvious absorption bands at 711 nm for **1** and 600 nm for **2** arose with an isosbestic point at 363 and 478 nm for **1** and 497 and 577 nm for **2**, respectively (Figure 2-14). The absorption increase around 450 nm was derived from the formation of [Ru^{II}(bpy)₃]²⁺, which matched to the absorption band of [Ru^{II}(bpy)₃](PF₆)₂. The changes were completed by addition of 1 equiv of [Ru^{III}(bpy)₃](ClO₄)₃; the solution color changed from orange to green for **1** in the formation of the 1e⁻-oxidized species (**3**) and from pink to red for **2** in that of the 1e⁻-oxidized species (**4**). Based on the TD-DFT calculations, the absorption band of 1e⁻-oxidized **1** at 711 nm was assigned to the ligand-to-metal charge transfer (LMCT) transition from the NHC ligand, having an isopropyl group forming the CH/ π interaction with the pyridine ring containing N7 atom, to the central Ru^{III} ion in **3** (Figure 2-15).

The ¹H NMR spectra of **3** and **4** showed relatively broad signals in the range of -74 to $+60$ ppm and -40 to $+20$ ppm, respectively, reflecting the paramagnetic characters of **3** and **4** (Figure 2-16).²⁴ On the other hand, in the diamagnetic region, only ¹H NMR signals derived from [Ru^{II}(bpy)₃]²⁺, formed through the reduction of [Ru^{III}(bpy)₃]³⁺ as the oxidant, were observed. This indicates that electron-transfer oxidation of **1** or **2** by [Ru^{III}(bpy)₃]³⁺ proceeded.

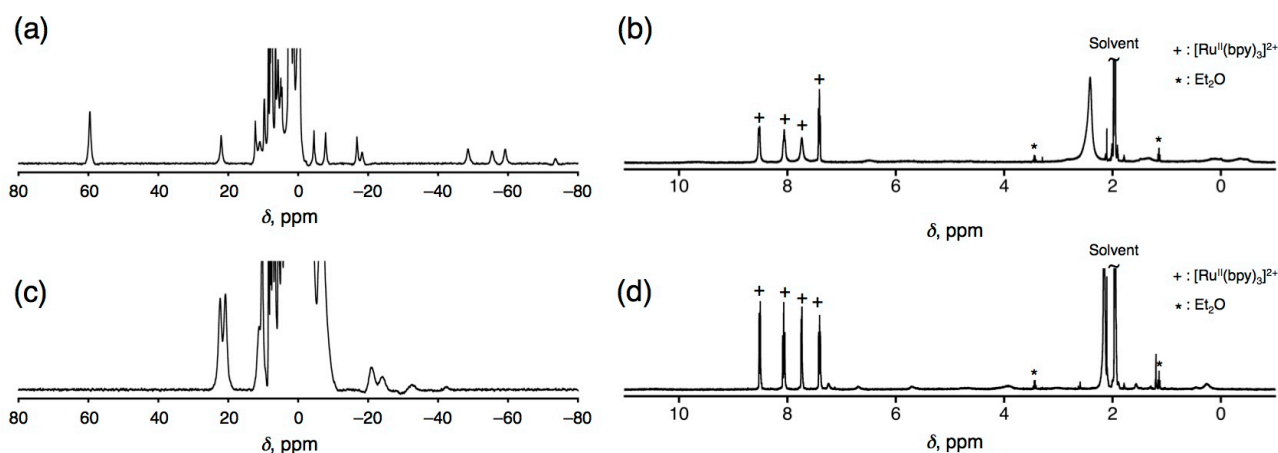


Figure 2-16. ^1H NMR spectra of **1** in paramagnetic region (a) and the diamagnetic region (b) upon addition of 1 equiv of $[\text{Ru}^{\text{III}}(\text{bpy})_3](\text{ClO}_4)_3$ at RT in acetonitrile- d_3 . ^1H NMR spectra of **2** in the paramagnetic (c) and diamagnetic regions (d) upon addition of 1 equiv of $[\text{Ru}^{\text{III}}(\text{bpy})_3](\text{ClO}_4)_3$ at RT in acetonitrile- d_3 .

The electron paramagnetic resonance (EPR) spectra recorded in acetonitrile at 5 K exhibited rhombic EPR signals²⁵ with $g_1 = 2.782$, $g_2 = 2.315$ and $g_3 = 1.980$ for **3**, and $g_1 = 2.984$, $g_2 = 2.116$ and $g_3 = 1.758$ for **4** (Figure 2-17). The root mean squares of the g values, $\langle g \rangle = ((|g_1|^2 + |g_2|^2 + |g_3|^2)/3)^{1/2}$, were calculated to be 2.382 and 2.343, respectively, which were comparable to typical $\langle g \rangle$ values for Ru^{III} complexes ($S = 1/2$), *ca.* 2.3.²⁶ Thus, the products of the first oxidation processes of **1** and **2** should be $[\text{Ru}^{\text{III}}(\text{C}^{\wedge}\text{Py}^{\wedge}\text{C})(\text{bpy})-(\text{NCMe})]^{3+}$ (**3**) and $[\text{Ru}^{\text{III}}\text{Cl}(\text{C}^{\wedge}\text{Py}^{\wedge}\text{C})(\text{bpy})]^{2+}$ (**4**), respectively.

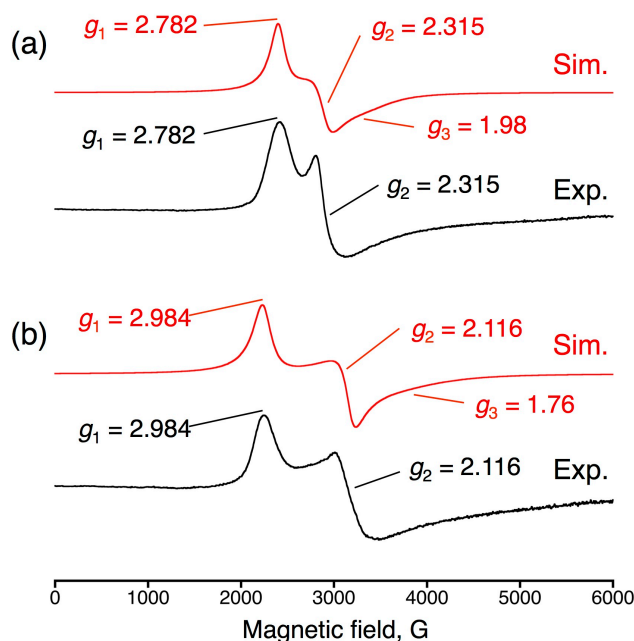


Figure 2-17. Experimental EPR spectra (black) and their simulations (red) for $1e^-$ -oxidized species of **1** (a) and **2** (b) measured at 5 K in helium-purged acetonitrile. $[\mathbf{1}]$ or $[\mathbf{2}] = 1$ mM, MW power: 5.024 mW, MW frequency: 9.398 GHz, Mod. frequency: 100.00 kHz, Mod. amplitude: 12.00 G. 1 equiv. of $[\text{Ru}^{\text{III}}(\text{bpy})_3](\text{ClO}_4)_3$ was used as the oxidant for $1e^-$ oxidation.

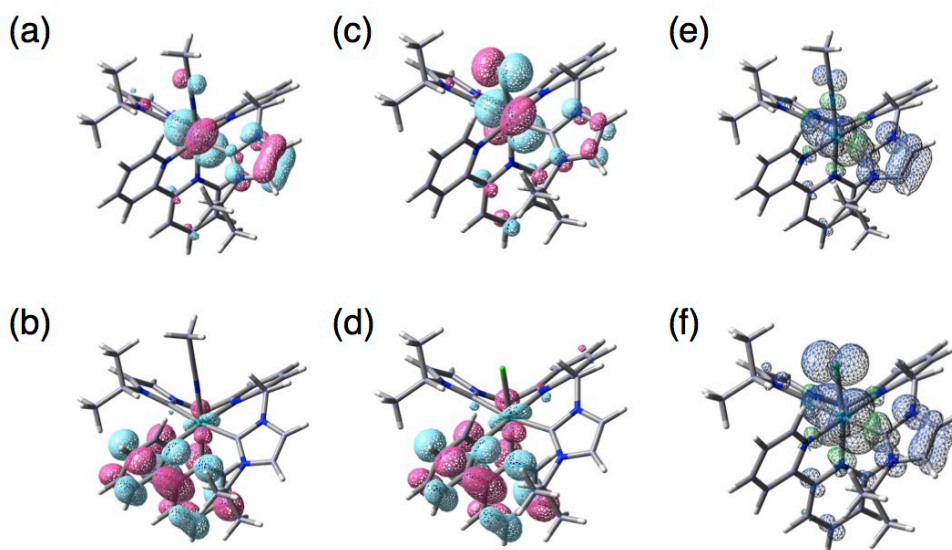


Figure 2-18. HOMO (a) and LUMO (b) orbitals of **1**, HOMO (c) and LUMO (d) orbitals of **2**, and Mulliken spin-density maps (blue and green meshes) of **3** (e) and **4** (f), calculated at the UB3LYP/SDD level of theory.

DFT-optimized structures of complexes **1** and **2** under vacuum were calculated and shown in Figure 2-18. The highest occupied molecular orbital (HOMO) of **1** mainly delocalized on the central Ru^{II} atom and also on the NHC ring forming CH/ π interaction with the pyridine ring. In contrast, that of **2** delocalized on the Ru^{II} atom, Cl ligand, and NHC rings. The lowest unoccupied molecular orbital (LUMO) of both of **1** and **2** located on the bpy ligands. These results indicate that the first oxidation of **1** and **2** should occur at the Ru^{II} center and the first reduction of them should proceed at the bpy ligand. In addition, the spin-density maps of **3** and **4** were obtained based on their DFT-optimized structures, and the unpaired electrons mainly located on the Ru center and NHC moiety in both **3** and **4**. The spin density on the Ru center was calculated to be 0.88 for **3** and 0.86 for **4**. Therefore, almost of all the unpaired electron localized on the Ru center, allowing us to conclude that the first oxidation should occur at the Ru^{II} center to afford formally Ru^{III} complexes. These results are consistent with the results of EPR measurements (Figure 2-17).

2-6 Conclusions

Novel two Ru^{II} complexes with pincer-type C^{Py}C ligands were successfully synthesized and characterized on the basis of crystallographic and spectroscopic analyses. The methylene-bridged NHC ligand (C^{Py}C) coordinated in a meridional manner and highly distorted. The coordination arrangement was maintained even in solution, where the intramolecular CH/ π interaction between the ^tPr group of the NHC moieties and the bpy ligand probably assists the fixation of the distorted structure of the C^{Py}C ligand. NHC ligands had a strong σ -donating ability to central Ru^{II} ions compared to pyridine or alkylamine ligands, which resulted in lowering oxidation potential of the Ru^{II}/Ru^{III} redox couple. In addition, these two Ru^{II} complexes were oxidized by using 1e⁻-oxidant in acetonitrile to afford the corresponding Ru^{III} complexes, which were revealed by ¹H NMR and EPR spectroscopic analyses and DFT calculations.

2-7 Experimental section

General.

NMR measurements were performed on a Bruker Avance 400 spectrometer (working frequency for ¹H: 400.0 MHz, for ¹³C: 100.0 MHz). Valuable-temperature NMR spectral measurements were conducted

with a valved-NMR tube, purchased from TCI chemicals. ESI-TOF-MS spectra were obtained on a JEOL JMS-T100CS mass spectrometer. UV-Vis absorption spectra were measured on a Shimadzu UV-2450 spectrophotometer and an Agilent 8453 photodiode-array spectrophotometer at room temperature. Cyclic and differential pulse voltammograms were recorded on a BAS Electrochemical Analyzer Model 660A. ESR spectroscopy was performed on a Bruker EMXPlus9.5/2.7 spectrometer. Simulations of the EPR spectra were conducted using “Hyperfine” (<http://wizard.chem.saga-u.ac.jp/program/hyperfine.html>) as a simulation program. Emission and excitation spectra were measured on a HORIBA FluoroMax-4 spectrofluorometer.

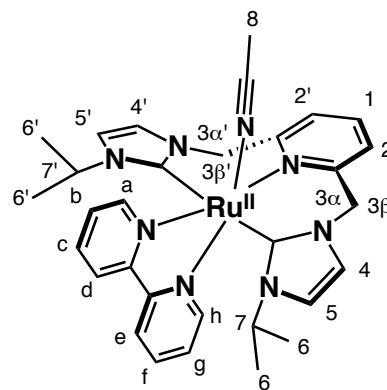
Materials.

All synthetic procedures were performed under Ar atmosphere. $[\text{Ru}^{\text{II}}\text{Cl}_2(\text{bpy})(\text{dmsO})_2]$ (bpy = 2,2'-bipyridyl, dmsO = dimethylsulfoxide) was synthesized from $[\text{Ru}^{\text{II}}\text{Cl}_2(\text{dmsO})_4]$ according to the literature method.²⁷ $\text{C}^{\wedge}\text{Py}^{\wedge}\text{C}^{\text{28}}$ and $[\text{Ru}^{\text{II}}\text{Cl}_2(\text{dmsO})_4]^{\text{29}}$ were synthesized according to the literature procedure. $\text{Ru}^{\text{III}}\text{Cl}_3 \cdot n\text{H}_2\text{O}$ was purchased from Furuya Metal Co. Ltd. and Ag_2O was purchased from Wako Pure Chemical Industries, Ltd.. All solvents used for the syntheses were dried over CaH_2 or magnesium powder and distilled before use.

Synthesis.

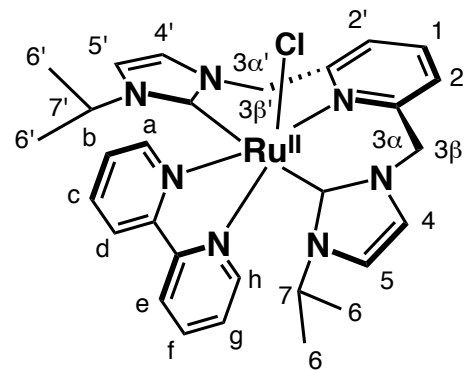
$[\text{Ru}^{\text{II}}(\text{C}^{\wedge}\text{Py}^{\wedge}\text{C})(\text{bpy})(\text{MeCN})(\text{PF}_6)_2 (\mathbf{1} \cdot (\text{PF}_6)_2)$.

A suspension of $[\text{Ru}^{\text{II}}\text{Cl}_2(\text{bpy})(\text{dmsO})_2]$ (153 mg, 315 μmol) in MeCN (10 mL) was degassed with freeze-pump-thaw cycles (3 times). Then, the solution of *in-situ*-generated $[\text{Ag}(\text{C}^{\wedge}\text{Py}^{\wedge}\text{C})]^+$ (330 μmol) in CH_2Cl_2 (2 mL) was added.³⁰ The suspension was refluxed for 24 h in the dark, and the white precipitate was filtered off on a Celite pad. The filtrate was evaporated to dryness under reduced pressure. To the obtained dark-red solid, MeOH (100 mL) was added to form gray precipitate, which was filtered off with use of a Celite pad. A saturated solution of NH_4PF_6 in MeOH (30 mL) was added to the filtrate, and the solution was concentrated to a small volume under reduced pressure. A few drops of distilled water were added to the solution, and then, the resulting brown precipitate formed was collected with filtration and washed with Et_2O . The brown solid was dried under vacuum and the crude solid was purified by column chromatography on alumina using MeCN as an eluent. The solvent of the collected orange solution was evaporated, and the crude product was recrystallized from MeCN/ Et_2O . Red solid (156 mg, 171 μmol , 47% yield) of the title compound was obtained. ^1H NMR (CD_3CN): δ 9.32 (dd, $J = 5.6, 0.8$ Hz, 1H, a-Py-H), 8.32 (dd, $J = 8.3, 0.8$ Hz, 1H, d-Py-H), 8.31 (m, 2H, c-Py-H, 1-Py-H), 8.25 (dd, $J = 7.3, 1.2$ Hz, 1H, h-Py-H), 7.91 (m, 2H, e-Py-H, f-Py-H), 7.73 (d, $J = 7.8$ Hz, 1H, 2'-Py-H), 7.68 (d, $J = 7.6$ Hz, 1H, 2-Py-H), 7.63 (td, $J = 6.6, 1.5$ Hz, 1H, b-Py-H), 7.44 (d, $J = 1.8$ Hz, 1H, 4-Im-H), 7.18 (m, 2H, 4'-Im-H, g-Ph-H), 7.10 (d, $J = 1.8$ Hz, 1H, 5'-Im-H), 7.06 (d, $J = 1.8$ Hz, 1H, 5-Im-H), 5.63 (ABq, $J = 16$ Hz, 1H, 3 α -CH), 5.41 (ABq, $J = 16$ Hz, 1H, 3 β -CH), 5.12 (ABq, $J = 16$ Hz, 1H, 3 β' -CH), 4.81 (ABq, $J = 16$ Hz, 1H, 3 α' -CH), 4.33 (sept, $J = 6.6$ Hz, 1H, 7'-CH₃), 2.45 (s, 3H, 8-CH₃), 2.1 (sept, $J = 6.6$ Hz, 1H, 7-CH), 1.32 (d, $J = 6.8$ Hz, 3H, 6'-CH₃), 0.71 (d, $J = 7.1$ Hz, 3H, 6-CH₃), 0.54 (d, $J = 6.8$ Hz, 3H, 6''-CH₃), 0.30 (d, $J = 7.1$ Hz, 3H, 6-CH₃). ^{13}C NMR (CD_3CN): δ 182.02, 180.25, 161.34, 160.20, 159.31, 155.34, 154.81, 139.87, 137.40, 137.05, 131.92, 127.85, 127.15, 126.69, 126.09, 124.76, 124.58, 124.11, 123.47, 55.73, 55.31, 51.31, 49.82, 23.59, 23.20, 21.91, 5.58. Anal. Calcd. for $\text{C}_{29}\text{H}_{35}\text{N}_7\text{ORu} \cdot 2\text{PF}_6 \cdot 0.25\text{C}_2\text{H}_3\text{N} \cdot 0.25\text{C}_4\text{H}_{10}\text{O}$: H 4.21, C 41.51, N



12.29. Found: H 4.03, C 41.71, N 12.48. UV-Vis: λ_{\max} [nm] = 363, 482. ESI-TOF-MS: m/z = 600.18 (calcd. for $[M - \text{MeCN} + \text{F}]^+$: 600.20).

[Ru^{II}Cl(C[^]Py[^]C)(bpy)](PF₆) (2·PF₆). A suspension of $[\text{Ru}^{\text{II}}\text{Cl}_2(\text{bpy})(\text{dmsO})_2]$ (372 mg, 769 μmol) in CH_2Cl_2 (50 mL) was degassed with freeze-pump-thaw cycles (3 times), and the solution of in-situ generated $[\text{Ag}(\text{C}^{\wedge}\text{Py}^{\wedge}\text{C})]^+$ (771 μmol) in CH_2Cl_2 (50 mL) was added. The solution was refluxed for 24 h in the dark and the resulting white precipitate was filtered off with a Celite pad, and the solvent of the filtrate was evaporated under reduced pressure. The obtained dark-red solid was added to acetone (100 mL) and the gray precipitate was filtered off on a Celite pad. A saturated solution of NH_4PF_6 in acetone (20 mL) was added to the reaction mixture and the mixture was dried up under reduced pressure. Distilled water was added to the residue, the resulting brown precipitate was filtered, and washed with Et_2O and dried under vacuum. Finally, the crude solid was purified by column chromatography on alumina using acetone as an eluent. The solvent of the collected red-purple solution was evaporated. The crude product was recrystallized from acetone/ Et_2O and red-purple solid (112 mg 147 μmol , 17% yield) of the title compound was obtained. ¹H NMR (CD_3CN): δ 9.97 (d, J = 5.1 Hz, 1H, a-Py-H), 8.22 (d, J = 8.4 Hz, 1H, d-Py-H), 8.12 (d, J = 8.1 Hz, 1H, h-Py-H), 7.92 (m, 3H, c-Py-H, 1-Py-H, e-Py-H), 7.70 (td, J = 8.2, 1.2 Hz, 1H, f-Py-H), 7.64 (d, J = 7.6 Hz, 1H, 2'-Py-H), 7.63 (d, J = 7.6 Hz, 1H, 2-Py-H), 7.55 (dt, J = 6.7, 1.3 Hz, b-Py-H), 7.34 (d, J = 1.8 Hz, 4-Im-H), 7.08 (d, J = 1.8 Hz, 1H, 4'-Im-H), 6.96 (m, 4H, 3 α -CH, 5-Im-H, 5'-Im-H, g-Py-H), 5.15 (AXd, J = 16 Hz, 1H, 3 β -CH), 5.05 (ABq, J = 16 Hz, 1H, 3 β' -CH), 4.93 (sept, J = 6.6 Hz, 1H, 7'-CH), 4.86 (ABq, J = 16 Hz, 1H, 3 α' -CH), 2.1 (sept, J = 6.6 Hz, 1H, 7-CH), 1.25 (d, J = 7.1 Hz, 3H, 6'-CH₃), 0.68 (d, J = 6.8 Hz, 3H, 6-CH₃), 0.44 (d, J = 7.1 Hz, 3H, 6'-CH₃), 0.28 (d, J = 6.8 Hz, 3H, 6-CH₃). ¹³C NMR (CD_3CN): δ 185.27, 183.54, 162.56, 161.04, 160.83, 160.24, 155.47, 155.45, 138.43, 134.88, 134.06, 126.88, 125.73, 125.63, 125.03, 123.87, 123.67, 123.44, 70.04, 56.21, 55.68, 55.29, 50.54, 49.26, 30.64, 29.57, 23.35, 23.05, 21.95, 15.37. Anal. Calcd. for $\text{C}_{29}\text{H}_{33}\text{N}_7\text{ClPF}_6\text{Ru}\cdot 0.25\text{C}_3\text{H}_6\text{O}$: H 4.48, C 46.07, N 12.64. Found: H 4.51, C 46.04, N 12.35. UV-Vis: λ_{\max} [nm] = 397, 537. ESI-TOF-MS: m/z = 616.20 (calcd. for $[\text{M}]^+$: 616.15).



X-ray crystallography.

Single crystals of $1\cdot(\text{PF}_6)_2$ and $2\cdot\text{PF}_6$, suitable for X-ray crystallography, were obtained by recrystallization with a vapor diffusion of Et_2O into the MeCN solution of $1\cdot(\text{PF}_6)_2$, with that of Et_2O into the solution of $2\cdot\text{PF}_6$ in acetone, respectively. The crystals were mounted using a mounting loop. All diffraction data were collected on a Bruker APEXII diffractometer at 120 K with a graphite monochromated Mo $\text{K}\alpha$ radiation source ($\lambda = 0.71073 \text{ \AA}$) by the 2θ scan. All structure refinements were performed using the Yadokari-XG crystallographic software package.³¹ The structures were solved by a direct method using SIR97³² and SHELX97.³² Crystallographic data for $1\cdot(\text{PF}_6)_2$ and $2\cdot\text{PF}_6$ are summarized in Table 2-3. CCDC-1830565 ($1\cdot(\text{PF}_6)_2$) and 1830567 ($2\cdot\text{PF}_6$) include supplementary crystallographic data, which are available free of charge from the Cambridge Crystallographic Data Center through www.ccdc.cam.ac.uk/data_request/cif.

Table 2-3. Crystallographic data for **1**·(PF₆)₂, **2**·PF₆

Compound	1 ·(PF ₆) ₂	2 ·PF ₆
MW	930.70	761.11
Formula	C ₃₂ H ₃₆ F ₁₂ N _{8.50} P ₂ Ru	C ₂₉ H ₃₃ ClF ₆ N ₇ PRu
Crystal system	Monoclinic	Monoclinic
Space group	<i>C2/c</i>	<i>P2₁/c</i>
<i>a</i> , Å	38.881(6)	8.7113(13)
<i>b</i> , Å	10.6280(16)	15.727(2)
<i>c</i> , Å	18.620(3)	22.211(3)
α , °	90	90
β , °	93.546(2)	92.2910(19)
γ , °	90	90
<i>V</i> , Å ³	7680(2)	3040.6(8)
<i>Z</i>	8	4
<i>R</i> ₁	0.0359	0.0270
<i>wR</i> ₂	0.0897	0.0613
GOF	1.031	1.040

DFT calculations.

Global minima on the potential energy surfaces were searched for obtaining optimized structures by using the restricted or unrestricted B3LYP method.³³ To reproduce the absorption and emission spectra, TD-DFT calculations³⁴ were performed on the basis of the optimized structures. For the all of atoms, we used the SDD basis sets.³⁵ The Gaussian 09 program package³⁶ was used for all DFT calculations.

References and notes.

- (1) (a) D. Pugh, A. A. Danopoulos, *Coord. Chem. Rev.* **2007**, *251*, 610–641. (b) F. E. Hahn, M. C. Jahnke, *Angew. Chem., Int. Ed.* **2008**, *47*, 3122–3172. (c) H. D. Velazquez, F. Verpoort, *Chem. Soc. Rev.* **2012**, *41*, 7032–7060.
- (2) S. Díez-González, N. Marion, S. P. Nolan, *Chem. Rev.* **2009**, *109*, 3612–3676.
- (3) (a) M. Poyatos, J. A. Mata, E. Falomir, R. H. Crabtree, E. Peris, *Organometallics* **2003**, *22*, 1110–1114. (b) M. Dakkach, X. Fontrodona, T. Parella, A. Atlamsani, I. Romero, M. Rodríguez, *Adv. Synth. Catal.* **2011**, *353*, 231–238. (c) L. Vaquer, P. Miró, X. Sala, F. Bozoglian, E. Masllorens, J. Benet-Buchholz, X. Fontrodona, T. Parella, I. Romero, A. Roglans, M. Rodríguez, C. Bo, A. Llobet, *ChemPlusChem.* **2013**, *78*, 235–243.
- (4) (a) R. Staehle, L. Tong, L. Wang, L. Duan, A. Fischer, M. S. G. Ahlquist, L. Sun, S. Rau, *Inorg. Chem.* **2014**, *53*, 1307–1319. (b) H.-J. Liu, M. Gil-Sepulcre, L. Francás, P. Nolis, T. Parella, J. Benet-Buchholz, X. Fontrodona, J. García-Antón, N. Romero, A. Llobet, L. Escriche, R. Bofill, X. Sala, *Dalton Trans.* **2017**, *46*, 2829–2843.
- (5) S. U. Son, K. H. Park, Y.-S. Lee, B. Y. Kim, C. H. Choi, M. S. Lah, Y. H. Jang, D.-J. Jang, Y. K. Chung, *Inorg. Chem.* **2004**, *43*, 6896–6898.

- (6) L.-H. Chung, K.-S. Cho, J. England, S.-C. Chan, K. Wieghardt, C.-Y. Wong, *Inorg. Chem.* **2013**, *52*, 9885–9896.
- (7) (a) S. C. Rasmussen, S. E. Ronco, D. A. Mlsna, M. A. Billadeau, W. T. Pennington, J. W. Kolis, J. D. Petersen, *Inorg. Chem.* **1995**, *34*, 821–829. (b) T. Kojima, K. Nakayama, M. Sakaguchi, T. Ogura, K. Ohkubo, S. Fukuzumi, *J. Am. Chem. Soc.* **2011**, *133*, 17901–17911. (c) K. Arora, J. White, R. Sharma, S. Mazumder, P. Martin, H. B. Schlegel, C. Turro, J. J. Kodanko, *Inorg. Chem.* **2016**, *55*, 6968–6979.
- (8) (a) H.-W. Tseng, R. Zong, J. T. Muckerman, R. Thummel, *Inorg. Chem.* **2008**, *47*, 11763–11773. (b) S. Ohzu, T. Ishizuka, H. Kotani, T. Kojima, *Chem. Commun.* **2014**, *50*, 15018–15021. (c) T. Kojima, T. Morimoto, T. Sakamoto, S. Miyazaki, S. Fukuzumi, *Chem. Eur. J.* **2008**, *14*, 8904–8915. (d) H. Mitome, T. Ishizuka, H. Kotani, Y. Shiota, K. Yoshizawa, T. Kojima, *J. Am. Chem. Soc.* **2016**, *138*, 9508–9520.
- (9) M. Dakkach, A. Atlamsani, T. Parella, X. Fontrodona, I. Romero, M. Rodríguez, *Inorg. Chem.* **2013**, *52*, 5077–5087.
- (10) The strain of the six-membered chelate rings might cause the elongation of the Ru–C coordination bonds; however, in Ru^{II} complexes, having a methylene-bridged NCN-type ligand and showing similar structural distortion as observed in **1** and **2** due to formation of the six-membered chelate rings, the Ru–N bond lengths were in the typical range of those for Ru^{II}-polypyridyl complexes. See: D. E. Prokopchuk, B. T. H. Tsui, A. J. Lough, R. H. Morris, *Chem. Eur. J.* **2014**, *20*, 16960–16968. Therefore, the elongation of the Ru–C bonds in **1** and **2** are probably derived from the mutual *trans*-influence.
- (11) J. Dinda, S. Liatard, J. Chauvin, D. Jouvenot, F. Loiseau, *Dalton Trans.* **2011**, *40*, 3683–3688.
- (12) (a) H. Suezawa, S. Ishihara, Y. Umezawa, S. Tsubonoya, M. Nishio, *Eur. J. Org. Chem.* **2004**, 4816–4822; (b) O. Sénèque, M. Giorgi, O. Renaud, *Chem. Commun.* **2001**, 984–985.
- (13) The steric strain around the CH₂ moieties of the C[∧]Py[∧]C ligand may contribute to the stabilization of the arrangement in **1**. However, Suárez and co-workers reported that Ru^{II} complexes, having a CNC type bis-NHC ligand with the meridional conformation, exhibited the seesaw-like motion to exchange the positions of the left and right NHC moieties above and below the equatorial plane even at room temperature. See: M. Hernández-Juárez, J. López-Serrano, P. Lara, J. P. Morales-Cerón, M. Vaquero, E. Álvarez, V. Salazar, A. Suárez, *Chem. Eur. J.* **2015**, *21*, 7540–7555. This kind of motions was not observed for **1** in the temperature range of 298–348 K in acetonitrile-*d*₃. Therefore, the strain of the CH₂ bridges forming six-membered chelate rings cannot explain the stabilization of the arrangement for **1**. The CH/π interaction between the methine CH of the ⁱPr groups and the bpy ligand plays an important role on the stabilization of the geometry.
- (14) A. Juris, V. Balzani, F. Barigelletti, S. Campagna, P. Belser, A. V. Zelewsky, *Coord. Chem. Rev.* **1988**, *84*, 85–277.
- (15) G. A. Crosby, W. H. Elfring Jr. *J. Phys. Chem.* **1976**, *80*, 2206–2211.
- (16) J. V. Casper, T. J. Meyer, *J. Am. Chem. Soc.* **1983**, *105*, 5583–5590.
- (17) M. Maestri, N. Armaroni, V. Balzani, E. C. Constable, A. M. W. C. Thompson, *Inorg. Chem.* **1995**, *34*, 2759–2767.
- (18) T. Moriuchi, J. Shiori, T. Hirao, *Tetrahedron Lett.* **2007**, *48*, 5970–5972.
- (19) F. Schramm, V. Meded, H. Fliegl, K. Fink, O. Fuhr, Z. Qu, W. Klopffer, S. Finn, T. E. Keyes, M. Ruben, *Inorg. Chem.* **2009**, *48*, 5677–5684.
- (20) K. Heinze, K. Hempel, M. Beckmann, *Eur. J. Inorg. Chem.* **2006**, 2040–2050.
- (21) L. M. A. Levine, D. Holten, *J. Phys. Chem.* **1988**, *92*, 714–720.

- (22) (a) C.-N. Tsai, M. M. Allard, R. L. Lord, D.-W. Luo, Y.-J. Chen, H. B. Schlegel, J. F. Endicott, *Inorg. Chem.* **2011**, *50*, 11965–11977. (b) L. Vaquer, A. Poater, J. D. Tovar, J. García-Antón, M. Solà, A. Llobet, X. Sala, *Inorg. Chem.* **2013**, *52*, 4985–4992.
- (23) J.-C. Chambron, J.-P. Sauvage, E. Amouyal, P. Koffi, *Nouv. J. Chim.* **1985**, *9*, 527–529.
- (24) Paramagnetic ^1H NMR spectra of Ru^{III} -NHC complexes are relatively rare. A few examples of ^1H NMR spectra of Ru^{III} complexes having polypyridyl ligands are shown below: (a) T. Kojima, K. Hayashi, S. Iizuka, F. Tani, Y. Naruta, M. Kawano, Y. Ohashi, Y. Hirai, K. Ohkubo, Y. Matsuda, S. Fukuzumi, *Chem. Eur. J.* **2007**, *13*, 8212–8222. (b) J. C. Dobson, B. P. Sullivan, P. Doppelt, T. J. Meyer, *Inorg. Chem.* **1988**, *27*, 3863–3866.
- (25) The rhombic g values ($g_1 - g_3$) for **3** and **4** were determined with the EPR simulation. In the EPR spectra of **3** and **4**, there are no obvious peaks derived from g_3 ; however, the spectra could not be well reproduced with g_{\parallel} and g_{\perp} as the axial EPR signals.
- (26) (a) K. Matsuura, L. Kevan, *J. Chem. Soc., Faraday Trans.* **1997**, *93*, 1763–1768. (b) Y. Pushkar, D. Moonshiram, V. Purohit, L. Yan, I. Alperovich, *J. Am. Chem. Soc.* **2014**, *136*, 11938–11945. (c) N. Gauthier, N. Tchouar, F. Justaud, G. Argouarch, M. P. Cifuentes, L. Toupet, D. Touchard, J.-F. Halet, S. Rigaut, M. G. Humphrey, K. Costuas, F. Paul, *Organometallics* **2009**, *28*, 2253–2266.
- (27) M. Toyama, K. Inoue, S. Iwamatsu, N. Nagao, *Bull. Chem. Soc. Jpn.* **2006**, *79*, 1525–1534.
- (28) J. R. Miecznikowski, W. Lo, M. A. Lynn, S. Jain, L. C. Keilich, N. F. Kloczko, B. E. O’Loughlin, A. P. DiMarzio, K. M. Foley, G. P. Lisi, D. J. Kwiecien, E. E. Butrick, E. Powers, R. Al-Abbasee, *Inorg. Chim. Acta* **2012**, *387*, 25–36.
- (29) I. P. Evans, A. Spencer, G. Wilkinson, *J. Chem. Soc., Dalton Trans.* **1973**, 204–209.
- (30) L. Canovese, F. Visentin, C. Levi, C. Santo, V. Bertolasi, *Inorg. Chim. Acta* **2012**, *390*, 105–118.
- (31) C. Kabuto, S. Akine, T. Nemoto, E. Kwon, Release of software (Yadokari-XG 2009) for crystal structure analyses. *J. Cryst. Soc. Jpn.* **2009**, *51*, 218–224.
- (32) G. M. Sheldrick, SIR97 and SHELX97, Programs for Crystal Structure Refinement, University of Göttingen, Göttingen (Germany), 1997.
- (33) a) A. D. Becke, *Phys. Rev. A* **1988**, *38*, 3098–3100. b) C. Lee, W. Yang, R. G. Part, *Phys. Rev. B* **1988**, *37*, 785–789.
- (34) M. E. Casida, C. Jamorski, K. C. Casida, D. R. Salahub, *J. Chem. Phys.* **1998**, *108*, 4439–4449.
- (35) M. Dolg, H. Stoll, H. Preuss, *Theor. Chim. Acta* **1993**, *85*, 441–450.
- (36) Gaussian 09, Revision D.01, M. J. Frisch, G. W. Trucks, H. B. Schlegel, G. E. Scuseria, M. A. Robb, J. R. Cheeseman, G. Scalmani, V. Barone, B. Mennucci, G. A. Petersson, H. Nakatsuji, M. Caricato, X. Li, H. P. Hratchian, A. F. Izmaylov, J. Bloino, G. Zheng, J. L. Sonnenberg, M. Hada, M. Ehara, K. Toyota, R. Fukuda, J. Hasegawa, M. Ishida, T. Nakajima, Y. Honda, O. Kitao, H. Nakai, T. Vreven, J. A. Montgomery, Jr., J. E. Peralta, F. Ogliaro, M. Bearpark, J. J. Heyd, E. Brothers, K. N. Kudin, V. N. Staroverov, R. Kobayashi, J. Normand, K. Raghavachari, A. Rendell, J. C. Burant, S. S. Iyengar, J. Tomasi, M. Cossi, N. Rega, J. M. Millam, M. Klene, J. E. Knox, J. B. Cross, V. Bakken, C. Adamo, J. Jaramillo, R. Gomperts, R. E. Stratmann, O. Yazyev, A. J. Austin, R. Cammi, C. Pomelli, J. W. Ochterski, R. L. Martin, K. Morokuma, V. G. Zakrzewski, G. A. Voth, P. Salvador, J. J. Dannenberg, S. Dapprich, A. D. Daniels, Ö. Farkas, J. B. Foresman, J. V. Ortiz, J. Cioslowski, D. J. Fox, Gaussian, Inc., Wallingford CT, 2009.

Chapter 3

A ruthenium(III)-oxyl complex bearing strong radical character

3-1 Introduction

High-valent metal-oxo complexes are an important class of compounds, because they are found as reactive intermediates in oxidation by metalloenzymes and synthetic oxidation reactions.^{1,2}

Among metal-oxo ($M^{n+}=O$) complexes, $Ru^{IV}=O$ complexes have been a category of the most intensively investigated, owing to the high performance in catalytic oxidation reactions not only of organic substrates but also of water.³⁻⁶ $Ru^{IV}=O$ complexes are formed through proton-coupled electron-transfer (PCET) oxidation of the corresponding Ru^{II} -aqua complexes and they also oxidize C-H bonds of substrates through a PCET mechanism.^{6,7}

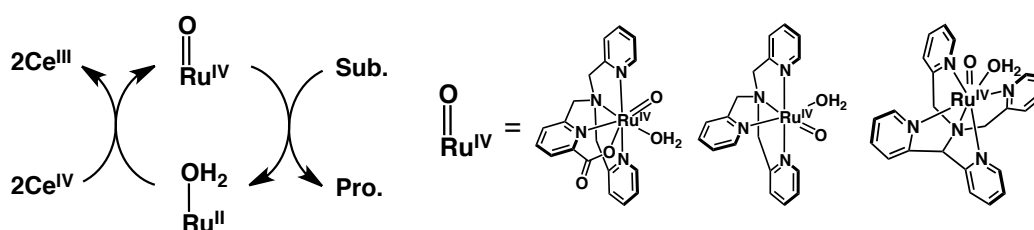


Figure 3-1. Catalytic substrate oxidation through a PCET oxidation mechanism by Ru^{II} -aqua complexes.⁶

In studies on the metal-oxo complexes, a very important question is whether a double bond is formed between the metal center and the oxo ligand or if the oxo ligand has a radical character in a metal-oxyl ($M^{(n-1)+}-O\bullet$) electronic structure.^{8,9} The radical character of the oxo ligand is crucial to evaluate the reactivity in hydrogen-atom abstraction from a substrate.^{9,10} In light of the “oxo-wall”, which resides between Groups 8 and 9 on the periodic table as proposed and elucidated by Gray and co-workers,^{8b} an octahedral d^4 Ru^{IV} or d^3 Ru^V ion should have an oxo ligand connected by a double bond, in other words, $Ru^{IV}=O$ or $Ru^V=O$ species are generally stable than electronically equivalent Ru^{III} -oxyl ($Ru^{III}-O\bullet$) or Ru^{IV} -oxyl ($Ru^{IV}-O\bullet$) species as the corresponding resonance forms, respectively. Despite plenty of studies on the properties and reactivity of $Ru^{n+}=O$ complexes,¹¹ $Ru^{(n-1)+}-O\bullet$ complexes have yet to be well characterized and elucidated on the reactivity in oxidation catalysis.¹²

Recently, radical characters of terminal oxo ligand have been considered in $Ru^V=O$ species for water oxidation catalyst on the basis of theoretical studies.¹³ Pushkar and co-workers reported the experimental evidence of a radicaloid character of $Ru^V=O$ intermediates in a diruthenium complex, $[4,5]^{4+}$ (Figure 3-2), based on the EPR measurements in ^{17}O -enriched water.¹⁴ $[4,5]^{4+}$ also has been considered as a reactive intermediate in water oxidation by the “blue dimer” catalyst.¹⁵ The EPR spectrum of $[4,5]^{4+}$ in $H_2^{16}O$ showed an EPR signal derived from the $S = 1/2$ spin state with the g -tensors of $g_{xx} = 2.03$, $g_{yy} = 1.98$, and $g_{zz} = 1.87$. The simulated EPR spectrum clarified the Ru hyperfine splitting (hfs) of $A_{yy} = 40 \pm 5$ G and $A_{zz} = 25 \pm 5$ G, reflecting the isotopic composition for $^{99,101}Ru$ ($I = 5/2$). The A values were consistent with the reported apparent $^{99,101}Ru$ hfs ($A \sim 40$ G).¹⁶ In 50 – 60% ^{17}O -enriched water, the $[4,5]^{4+}$ intermediate has terminal Ru-O groups labeled with ^{17}O atoms, whereas the bridging oxygen is not exchangeable under the reaction conditions. An EPR spectrum for $[4,5]^{4+}$ in $H_2^{17}O$ was extracted by subtracting the contribution of $[3,4]^{4+}$ -prime, and the spectrum showed a significant broadening of the EPR signals and hfs due to the ^{17}O nuclei ($I = 5/2$) was clearly observed on the low field side of the signal at $g \sim 2.1$ with a splitting of 60 G.

These experiments showed a high spin density on the oxygen in the d^3 $\text{Ru}^{\text{V}}=\text{O}$ moiety of the $[4,5]^{4+}$ intermediate, which was considered as a reactive species of the water oxidation.

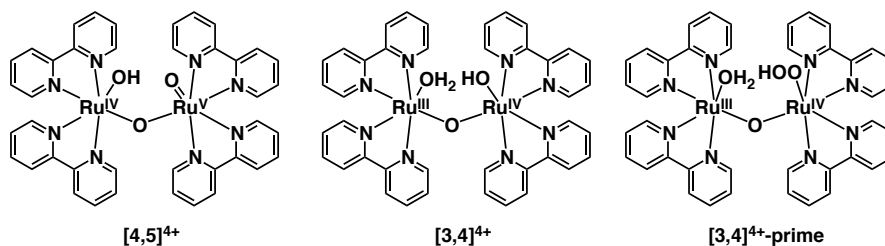


Figure 3-2. Structures of $[4,5]^{4+}$ (left), $[3,4]^{4+}$ (center) and $[3,4]^{4+}$ -prime (right).¹⁴

Tanaka and co-workers have reported the first example of metal-bound oxyl radical species, $\text{Ru}^{\text{II}}\text{-O}\cdot$ ($\text{Ru}^{\text{II}}\text{-O}\cdot$) complexes, formed from ruthenium complexes having polypyridyl and semiquinonato ligands, $[\text{Ru}^{\text{III}}(\text{trpy})(4\text{ClSQ})(\text{OH}_2)]^{2+}$ ($\text{Ru}^{\text{III}}_{\text{ClSQ-OH}_2}$, $\text{trpy} = 2,2':6',2''\text{-terpyridyl}$, $4\text{ClSQ} = 4\text{-chloro-1,2-benzo-semiquinonato}$) and $[\text{Ru}^{\text{III}}(\text{trpy})(\text{DBSQ})(\text{OH}_2)]$ ($\text{Ru}^{\text{III}}_{\text{DBSQ-OH}_2}$, $\text{DBSQ} = 3,5\text{-di-tert-1,2-benzo-semiquinonato}$) (Figure 3-3).¹⁷ Upon addition of a strong base such as KO^tBu into a CH_2Cl_2 solution of $\text{Ru}^{\text{III}}_{\text{ClSQ-OH}_2}$ or $\text{Ru}^{\text{III}}_{\text{DBSQ-OH}_2}$, UV-Vis spectral changes due to the deprotonation from the aqua ligand of the corresponding $\text{Ru}^{\text{III}}\text{-OH}_2$ complexes have been observed. Based on EPR, resonance Raman, and X-ray photoelectron spectroscopic analyses, the deprotonated products have been revealed to be $[\text{Ru}^{\text{II}}(\text{trpy})(\text{DBSQ})(\text{O}^{\cdot-})]$ ($\text{Ru}^{\text{II}}_{\text{DBSQ-O}^{\cdot-}}$) and $[\text{Ru}^{\text{II}}(\text{trpy})(4\text{ClSQ})(\text{O}^{\cdot-})]$ ($\text{Ru}^{\text{II}}_{\text{ClSQ-O}^{\cdot-}}$). The $\text{Ru}^{\text{II}}\text{-O}\cdot$ complexes can be reversibly protonated with addition of 2.0 eq of HClO_4 to recover the corresponding $\text{Ru}^{\text{III}}\text{-OH}_2$ complexes.¹⁴ The $\text{Ru}^{\text{II}}\text{-O}\cdot$ species, $\text{Ru}^{\text{II}}_{\text{DBSQ-O}^{\cdot-}}$, has been reported to be quite stable enough to form single crystals suitable for X-ray crystallography. In the crystal structure of $\text{Ru}^{\text{II}}_{\text{DBSQ-O}^{\cdot-}}$, the $\text{Ru-O}\cdot$ bond length was 2.043(7) Å, indicating a single-bond character of the Ru-O bond.^{17a} A reaction of $\text{Ru}^{\text{II}}_{\text{DBSQ-O}^{\cdot-}}$ with a spin-trapping reagent, 5,5-dimethyl-1-pyrroline *N*-oxide (DMPO), affords a spin adduct showing an EPR signal with hyperfine splitting derived from N and H nuclei at $g = 2.006$ at 193 K in CH_2Cl_2 . This result supports the strong radical character of the $\text{Ru}^{\text{II}}\text{-O}\cdot$ complex.¹⁷

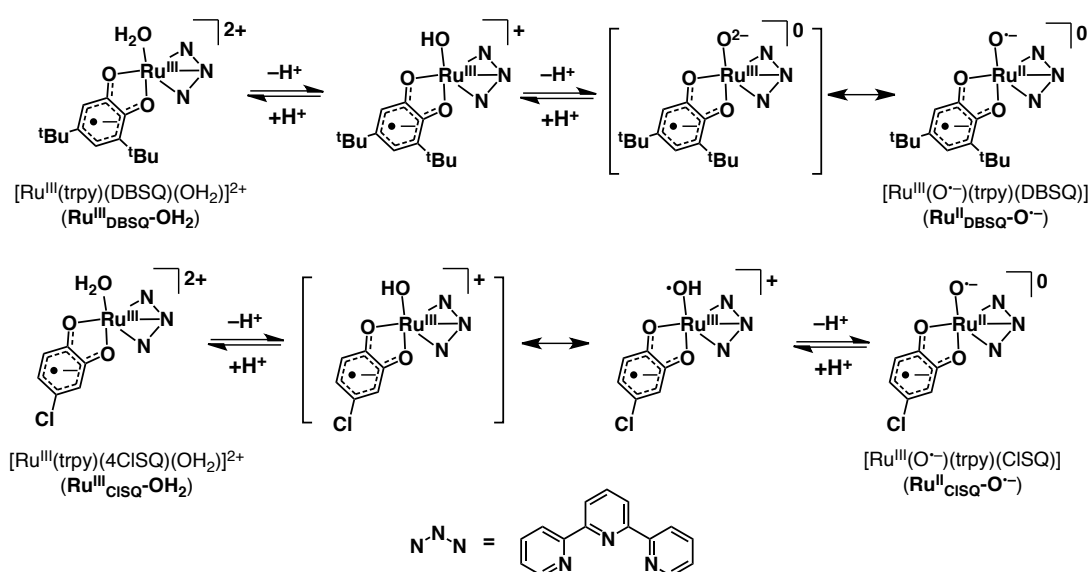


Figure 3-3. Deprotonation of $\text{Ru}^{\text{III}}\text{-OH}_2$ complexes to generate corresponding $\text{Ru}^{\text{II}}\text{-O}\cdot$ species.¹⁷

Reactivity of $\text{Ru}^{\text{II}}\text{-O}^{\ominus}$ species in substrate oxidation has been compared with $\text{Ru}^{\text{II}}\text{-O}^{\ominus}$ species formed by oxidation of a dinuclear complex, $[\text{Ru}^{\text{II}}_2(\text{OH})_2(\text{Q})(\text{btpyan})]^{2+}$ ($\text{Q} = 3,6\text{-di-}t\text{-tert-butyl-1,2-bezoquinone}$, $\text{btpyan} = 1,8\text{-bis}(2,2':6',2'')\text{-terpyridylanthracene}$, Ru_2Q), and a mononuclear complex, $[\text{Ru}^{\text{II}}(\text{OH})_2(\text{Q})\text{-}(\text{Ph-terpy})]^{2+}$ ($\text{Ph-terpy} = 4'\text{-phenyl-2,2':6',2'')\text{-terpyridyl}$, RuQ).¹⁸ Reactive species can be formed from both complexes with Ag^+ ion as a mild oxidant and KO^tBu as a base, as shown in Figure 3-4. Ru_2Q oxidized 1,3-cyclohexadiene and 1,2-dihydronaphthalene completely within one minute to afford benzene and naphthalene, whereas RuQ oxidized these substrates in low yields. On the other hand, Ru_2Q cannot oxidize 9,10-dihydroanthracene (DHA) at all, whereas RuQ shows relatively high reactivity in the DHA oxidation to afford anthracene in 42% yield. Low reactivity of Ru_2Q toward oxidation of DHA can be explained by the steric hindrance upon the approach of the substrate to the oxo group.¹⁸ As mentioned above, there are several reports on ruthenium-bound oxyl species in water oxidation and substrate oxidation. However, a “reactive” $\text{Ru}^{(\text{n}-1)+}\text{-O}\cdot$ species toward oxidation of organic substrates have never been reported yet.

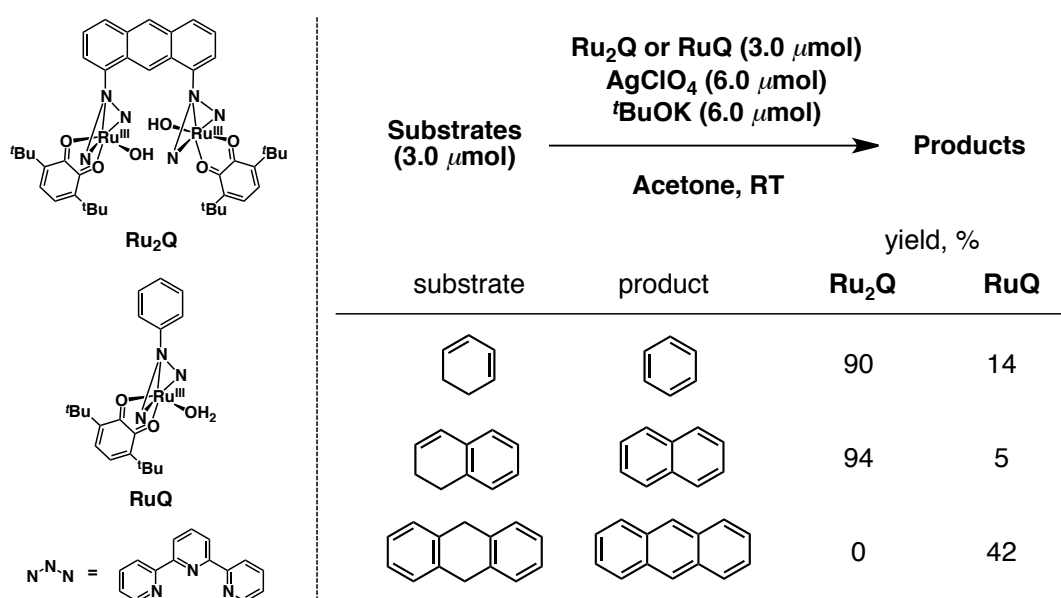


Figure 3-4. Oxidation of hydrocarbons by di- and mononuclear ruthenium-quinone complexes (Ru_2Q , RuQ) in the presence of AgClO_4 and KO^tBu .¹⁸

On the other hand, Solomon and co-workers reported elongation of an Fe-O bond in the transition state of benzene-ring hydroxylation to form an $\text{Fe}^{\text{III}}\text{-O}\cdot$ species (details are shown in Chapter 1.3.3).¹⁹ This work has indicated that oxidation of aromatics with lower activation barriers probably requires formation of $\text{M-O}\cdot$ species as the reactive intermediates and elongation of M-O bonds by *trans* influence of auxiliary ligands should be effective for the purpose. Therefore, introduction of strong σ -donating ligands at the *trans* position of the oxo ligand is required to elongate M-O bonds to afford $\text{M-O}\cdot$ species.²⁰ To exert strong *trans* influence to metal-oxygen bonds, *N*-heterocyclic carbene (NHC) ligands is a promising candidate, since the pyridine ligand at the *trans* position of an NHC ligand in a palladium-NHC complex was reported to be labile due to its *trans* influence.²¹

In this chapter, the author describes the formation and characterization of a $\text{Ru}^{\text{III}}\text{-O}\cdot$ complex with use of a tridentate ligand (H-BPIIm),²² including an NHC moiety as an auxiliary ligand, which exerts strong σ -donation and *trans* influence. Is also described the reactivity of the $\text{Ru}^{\text{III}}\text{-O}\cdot$ complex in oxidation of organic substrates in acidic water.

3-2 Synthesis and characterization of $[\text{Ru}^{\text{II}}(\text{BPIIm})(\text{bpy})(\text{L})]^{\text{n}+}$ ($\text{L} = \text{Cl}$, $\text{n} = 1$ (**5**); $\text{L} = \text{OH}_2$, $\text{n} = 2$ (**6**))

Syntheses of $[\text{Ru}^{\text{II}}\text{Cl}(\text{BPIIm})(\text{bpy})]^+$ (**5**) and $[\text{Ru}^{\text{II}}(\text{BPIIm})(\text{bpy})(\text{OH}_2)]^{2+}$ (**6**) (BPIIm = 1,3-bis(2-pyridylmethyl)imidazole-2-ylidene, bpy = 2,2'-bipyridyl) are described in Figure 3-5. **5**·Cl was synthesized by refluxing of a CH_2Cl_2 solution of *in-situ* generated $[\text{Ag}^{\text{I}}(\text{BPIIm})]^+$ and $[\text{Ru}^{\text{II}}\text{Cl}_2(\text{bpy})(\text{dmsO})_2]$ in the dark. **6**·(ClO_4)₂ was formed by dissociation of the chloro ligand from **5**·Cl with 2 equiv of silver(I) trifluoromethanesulfonate in water, followed by exchanging the counter anion with perchlorate ion. Characterization of **5** and **6** was conducted with ^1H NMR spectroscopy (Figure 3-6(a), (b)), ESI-TOF-MS spectrometry (Figure 3-6(c), (d)), elemental analysis, and X-ray crystallography (Figure 3-7). ^1H NMR spectra of **5**·Cl in methanol- d_4 and **6**·(ClO_4)₂ in D_2O showed distinctive signals and the signal patterns reflected the C_s symmetry. Additionally, the methylene protons were observed as an AB quartet at 5.37 and 5.00 ppm for **5** and 5.25 and 5.07 ppm for **6**, respectively. This indicates that the BPIIm ligand is coordinated to the Ru^{II} center with the facial manner both in **5** and **6**. The ESI-TOF-MS spectra of **5**·Cl and **6**·(ClO_4)₂ in MeOH exhibited a monocationic peak cluster at $m/z = 542.99$ and a dicationic peak cluster at $m/z = 254.01$, respectively, which were well matched with the simulation for $[\text{5}]^+$ and $[\text{6} - \text{OH}_2]^{2+}$ (Figure 3-6).

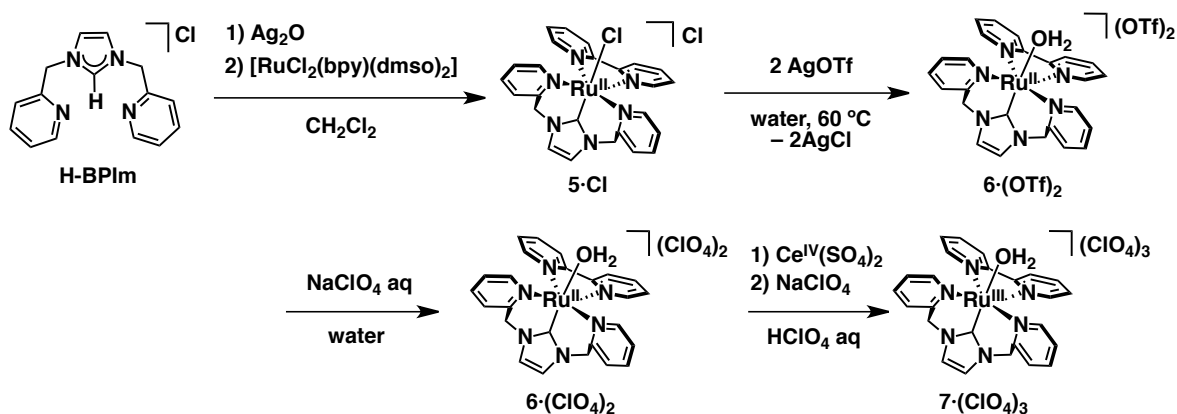


Figure 3-5. Synthetic procedure of **5**·Cl, **6**·(OTf)₂, **6**·(ClO_4)₂ and **7**·(ClO_4)₃.

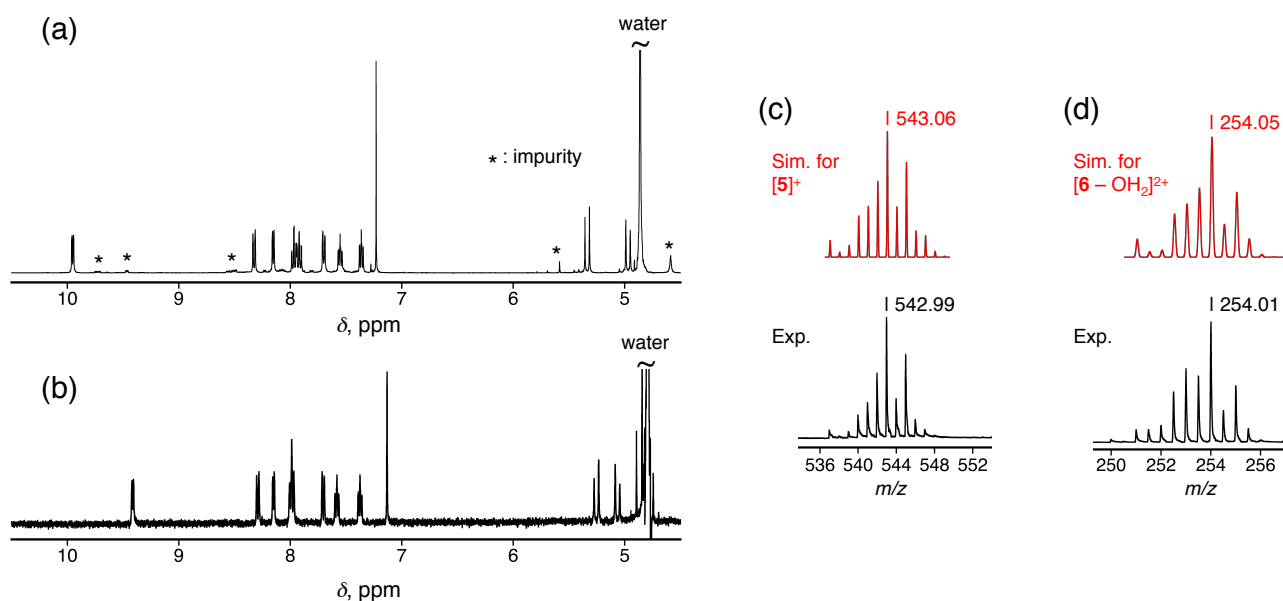


Figure 3-6. ^1H NMR spectra of **5**·Cl in methanol- d_4 (a) and **6**·(ClO_4)₂ in D_2O (b). ESI-TOF-MS spectra of **5**·Cl in acetone (c) and **6**·(ClO_4)₂ in methanol (d).

The crystal structures of **5**·Cl (Figure 3-7(a)) and **6**·(ClO₄)₂ (Figures 3-7(b)) indicate that the coordination manner of the BPIIm ligand is not meridional but facial, which is consistent with the ¹H NMR spectra (Figure 3-6). Due to the facial coordination, the BPIIm ligand exhibited structural distortion. For example, the bond angles around the methylene carbons of the NHC-pincer ligands became wider than normal 109.5°: ∠N2-C6-C5 = 112.8(4)° for **5**·Cl and 112.6(3)° for **6**·(ClO₄)₂, and ∠N3-C10-C11 = 110.5(4)° for **5**·Cl and 111.5(3)° for **6**·(ClO₄)₂, respectively. Additionally, the methylene protons were

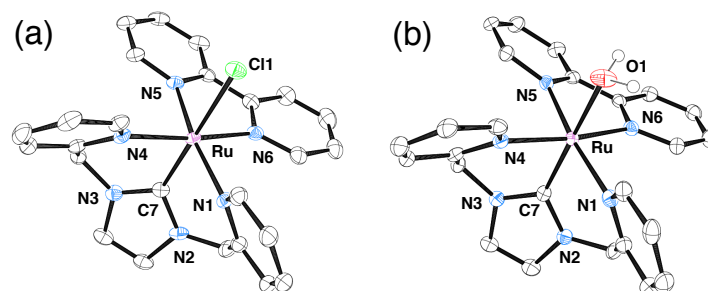


Figure 3-7. ORTEP drawings of **5**·Cl, **6**·(ClO₄)₂. with 50% thermal ellipsoids. Counter anions and hydrogen atoms except for an aqua ligand were omitted for clarity.

distorted from the least-square plane of the imidazole ring of the NHC-pincer ligand: the distance of C6 from the imidazole plane was 0.234 Å for **5**·Cl and 0.261 Å for **6**·(ClO₄)₂ and that of C10 was 0.254 Å for **5**·Cl and 0.308 Å for **6**·(ClO₄)₂, respectively. The reason why the BPIIm ligand takes the facial coordination in spite of the disadvantage of the severe distortion is π -acceptability of the NHC ligand.²³ As a result of the facial coordination, the ligand at the *trans*-position of the π -donating axial ligand, a chloro ligand for **5** and an aqua ligand for **6**, is the π -accepting NHC moiety, and thus, the electronic requirement controls the facial configuration. The strong *trans*-influence of the NHC ligand²¹ is also clearly reflected on the crystal structures of **5**. The bond distance of Ru-Cl in **5** is 2.5250(12) Å, which is longer than those of other complexes: 2.39 – 2.41 Å for Ru-Cl complexes, having a pyridine ligand at the *trans*-position of the Cl ligand,²⁴ 2.42 – 2.44 Å for ones having an anionic phenyl ligand,²⁵ and 2.469(2) Å for one having an NHC ligand.²⁶ In contrast, the *trans*-influence of the NHC ligand is not obvious in the crystal structure of **6**·(ClO₄)₂, because the aqua ligand forms hydrogen bonds with the counter anions or solvent molecules of crystallization and the hydrogen bonds affect the bond lengths between Ru and O significantly. In fact, the

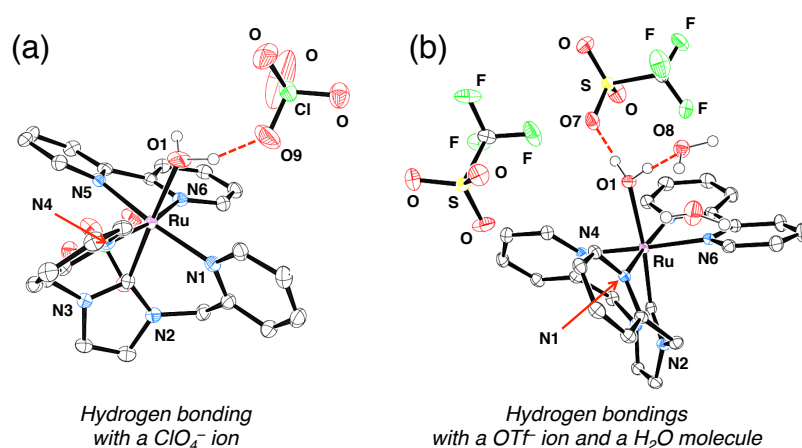


Figure 3-8. ORTEP drawings for crystal structures of **6**·(ClO₄)₂ (a) and **6**·(OTf)₂ (b).

Ru-O bond length of **6** is strongly dependent on the counter anion: 2.119(3) Å for **6**·(ClO₄)₂ and 2.1953(10) Å for **6**·(OTf)₂, the latter of which contains a hydrogen-bonded water molecule of crystallization (Figure 3-8).

The redox behavior of **6**·(ClO₄)₂ in an aqueous solution was investigated by cyclic and square-wave voltammetries (CV and SWV, respectively) at room temperature. At pH 2.5, which was controlled with addition of HClO₄ to the aqueous solution of **6**·(ClO₄)₂, the CV showed a reversible redox wave at +0.86 V vs NHE and a broad irreversible oxidation wave at +1.6 V vs NHE (Figure 3-9(a)). In the Pourbaix diagram, the potential of the first redox process showed no dependence on the solution pH (Figure 3-9(b)), whereas

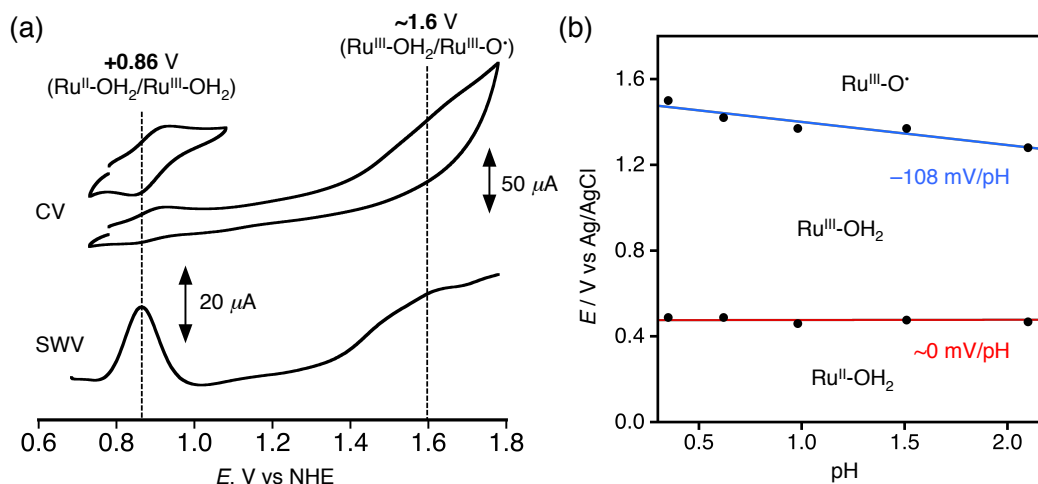


Figure 3-9. (a) Cyclic and square-wave voltammograms (CV and SWV) of **6**·(ClO₄)₂ in water (pH 2.5). 0.9 mM **6**, electrolyte: 0.1 M KNO₃, working electrode: glassy carbon, counter electrode: Pt wire, reference electrode: Ag/AgCl, scan rate for CV: 100 mV/s. The pH of the sample solution was controlled by addition of HClO₄. (b) Pourbaix diagram of **6** in pH-controlled H₂SO₄ aq. The oxidation potentials of **6** were determined by square-wave voltammetry. Conditions: 1.0 mM **6**, working electrode: glassy carbon, counter electrode: Pt wire, reference electrode: Ag/AgCl, temperature: 277 K.

the potential of the second oxidation step was lowered as the solution pH increased, with a slope of -108 mV/pH in the acidic region, indicating that the first redox step should be a 1e⁻ process and the second oxidation should be a 1e⁻/2H⁺ process. Therefore, the first wave was assigned to the oxidation of **6** to form [Ru^{III}(BPIIm)(bpy)(OH₂)]³⁺ (**7**) (Figure 3-5). The assignment was confirmed by a UV-Vis titration experiment of **6** with (NH₄)₂[Ce^{IV}(NO₃)₆] (CAN) (Figure 3-9(a)), ¹H NMR and EPR spectroscopies, and single-crystal X-ray crystallography (see below).

3-3 Synthesis and characterization of [Ru^{III}(BPIIm)(bpy)(OH₂)](ClO₄)₃ (**7**·(ClO₄)₃)

Upon addition of CAN to an aqueous solution of **6**·(ClO₄)₂, whose pH was set to 0.6 with addition of nitric acid, the absorption band at 490 nm decreased and instead a new absorption band at 627 nm arose with an isosbestic point at 547 nm, as shown in Figure 3-10(a). The change was saturated by addition of 1 equiv of CAN; the solution color changed from orange to blue. The absorption band at 627 nm was assigned to the LMCT transition from the NHC ligand to the Ru^{III} center in **7** using TD-DFT calculations (Figure 3-10(b)).

The ¹H NMR spectrum of **7** showed relatively broad signals in the range from -25 to 20 ppm, reflecting the paramagnetic character of **7** (Figure 3-11(a)). The EPR spectrum of **7** in water at 5 K exhibited

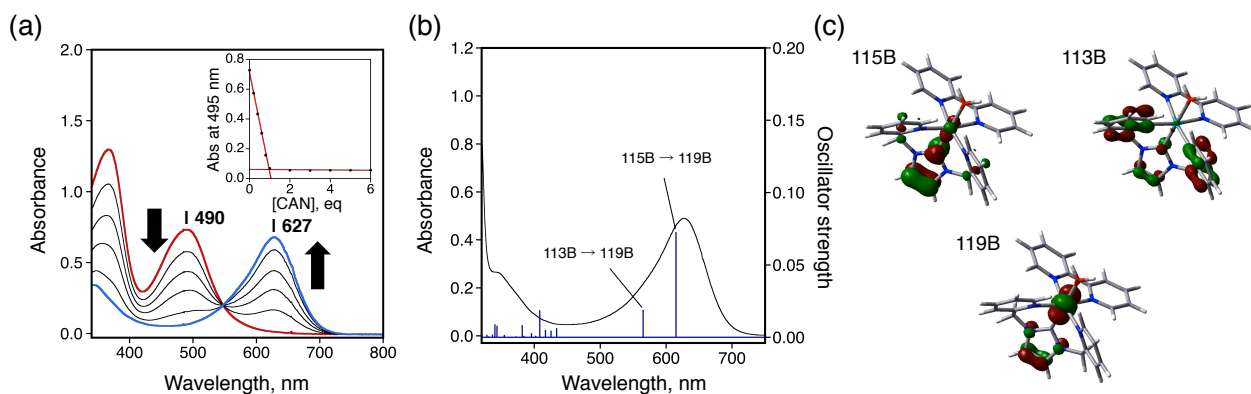


Figure 3-10. (a) UV-Vis spectral titration of $6 \cdot (\text{ClO}_4)_2$ with CAN (0–1 equiv) in HNO_3 aq (pH 0.6) at 277 K. (b) Calculated oscillator strengths by TD-DFT methods and observed spectrum of **7** (black trace). (c) Calculated molecular orbitals (113B, 115B, 119B) for **7**. TD-DFT calculations were performed at the UB3LYP/SDD (Ru) and D95** (C, H, N, O) level of theory.

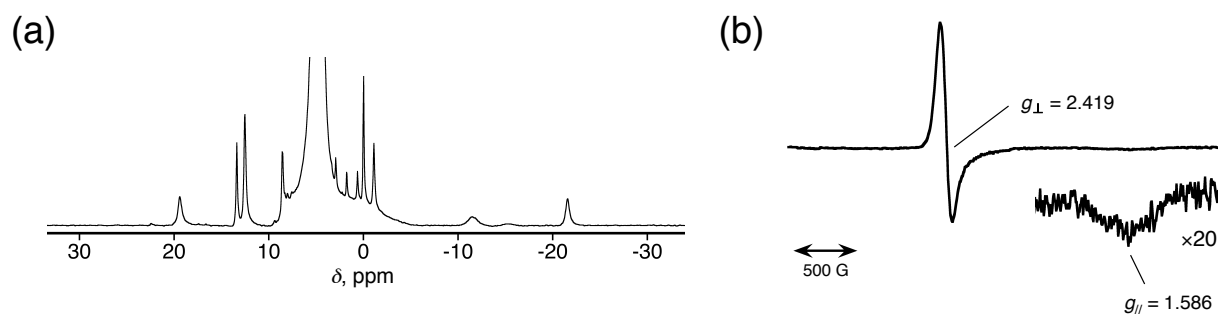


Figure 3-11. (a) ^1H NMR spectrum of $6 \cdot (\text{ClO}_4)_2$ in an acidic D_2O solution (pD 1.0) upon addition of 1 equiv of CAN. (b) An EPR spectrum of **7** in water at 5 K. MW power: 10 mW, MW frequency: 9.394 GHz, mod. frequency: 100 kHz, mod. amplitude: 6.00 G. The root-mean square of g -values was determined to be 2.177.

Table 3-1. Selected bond lengths (\AA) and angles ($^\circ$) of the crystal structures for $5 \cdot \text{Cl}$, $6 \cdot (\text{ClO}_4)_2$, $6 \cdot (\text{OTf})_2$ and $7 \cdot (\text{ClO}_4)_3$.

	Bond length, \AA			
	$5 \cdot \text{Cl}$	$6 \cdot (\text{ClO}_4)_2$	$6 \cdot (\text{OTf})_2$	$7 \cdot (\text{ClO}_4)_3$
Ru-X	2.5250(12) (X = Cl)	2.119(3) (X = O)	2.1953(10) (X = O)	2.099(4) (X = O)
Ru-C7	1.973(4)	1.961(4)	1.8362(16)	2.001(4)
Ru-N1	2.126(4)	2.126(3)	1.9453(15)	2.143(4)
Ru-N4	2.138(4)	2.110(3)	1.9476(15)	2.132(3)
Ru-N5	2.062(4)	2.051(3)	2.0743(11)	2.078(4)
Ru-N6	2.071(4)	2.084(3)	2.0663(11)	2.079(5)
	Bond angle, $^\circ$			
X-Ru-C7	175.41(13) (X = Cl)	174.63(13) (X = O)	172.64(4) (X = O)	171.77(17) (X = O)
C7-Ru-N1	84.67(16)	85.08(13)	83.91(5)	83.83(18)
N2-C6-C5	112.8(4)	112.6(3)	111.26(11)	111.6(4)
N1-Ru-N4	94.32(13)	94.82(12)	94.89(4)	95.09(16)

a signal at $g_{\parallel}=2.419$ and $g_{\perp}=1.586$ (Figure 3-11(b)). Thus, the root mean square of g -values, $\langle g \rangle$, was determined to be 2.177, which was a typical $\langle g \rangle$ value for Ru^{III} complexes ($S = 1/2$): approximately 2.2.²⁷

Single crystals of $7 \cdot (\text{ClO}_4)_3$ were obtained as the monohydrate form by recrystallization from an aqueous HClO_4 solution of the complex at 255 K. In the crystal structure of $7 \cdot (\text{ClO}_4)_3$ (Figure 3-12), three perchlorate ions were included as counter anions. In the crystal, the water molecule of crystallization formed hydrogen bonding with the aqua ligand with the $\text{O} \cdots \text{O}$ distance of 2.606 Å. The bond length between the Ru center and the oxygen atom of the aqua ligand was shortened in $7 \cdot (\text{ClO}_4)_3$ (2.099(4) Å) as compared to that in $6 \cdot (\text{ClO}_4)_2$ (2.119(3) Å), reflecting the increase in the valence number of the Ru center from +2 to +3 (Table 3-1).

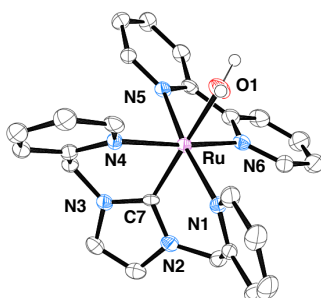


Figure 3-12. ORTEP drawing of $7 \cdot (\text{ClO}_4)_3$ with 50% thermal ellipsoid. Three ClO_4^- ions were omitted for clarity.

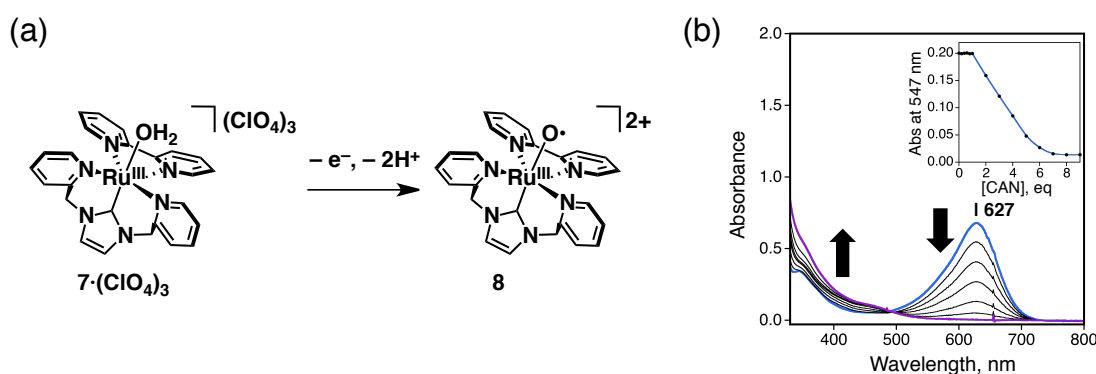


Figure 3-13. (a) Schematic representation of PCET oxidation of **7** to afford **8**. (b) UV-Vis spectral titration of $7 \cdot (\text{ClO}_4)_2$ with CAN (1–9 equiv) in HNO_3 aq (pH 0.6) at 277 K.

3-4 Formation and characterization of $[\text{Ru}^{\text{III}}(\text{O}^{\bullet})(\text{BPIIm})(\text{bpy})]^{2+}$ (**8**)

Further addition of CAN to the aqueous solution of **7** induced decrease of the absorption band at 627 nm with an isosbestic point at 495 nm. The absorbance change was completed with addition of over 7 equiv of CAN (Figure 3-13(b), inset). This can be ascribed to the high second-oxidation potential of **6** at +1.6 V vs NHE, which is comparable to the reduction potential of CAN in an acidic aqueous solution (+1.61 V vs NHE);²⁸ thus, due to the electron-transfer equilibrium between **7** and CAN, the oxidation of **7** with CAN to give complex **8** requires addition of excess CAN to complete the reaction. According to the Pourbaix diagram of **6** (Figure 3-9), the oxidation of **7** to afford **8** should be a $1e^-/2H^+$ process. ^1H NMR spectral titration of **7** with CAN exhibited signals ascribable to a different paramagnetic species from **7** (Figure 3-14(a)) in a wider range of -35 to 30 ppm as compared to those of **7** ($S = 1/2$), suggesting that complex **8**

should be in the $S = 1$ spin state. The $S = 1$ spin state was also confirmed by EPR spectroscopy to observe spin-forbidden ($\Delta m_s = \pm 2$) transition at $g = 4.31$ (Figure 3-14(b)).

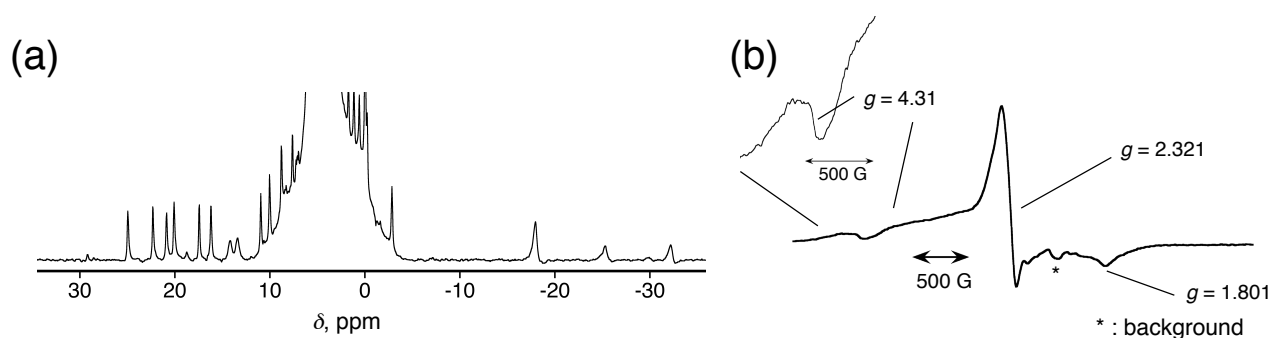


Figure 3-14. (a) ^1H NMR spectrum of $6 \cdot (\text{ClO}_4)_2$ in an acidic D_2O solution (pD 1.0) upon addition of 10 equiv of CAN. (b) An EPR spectrum of **8** in water at 5 K. MW power: 10 mW, MW frequency: 9.394 GHz, mod. frequency: 100 kHz, mod. amplitude: 6.00 G.

Further characterization of **8** was performed with ESI-TOF-MS spectrometry and resonance-Raman (rR) spectroscopy. The ESI-TOF-MS spectrum of **8**, which was derived from the oxidation of **6** by CAN in H_2^{16}O and diluted with CH_3CN , showed a peak cluster of a divalent cation at $m/z = 262.01$, which was assigned to $[\text{Ru}^{16}\text{O}(\text{BPIIm})(\text{bpy})]^{2+}$ (calcd. 262.04); with use of H_2^{18}O as the solvent in place of H_2^{16}O , the peak cluster shifted to $m/z = 263.02$ by substitution of ^{16}O with ^{18}O (Figure 3-15).

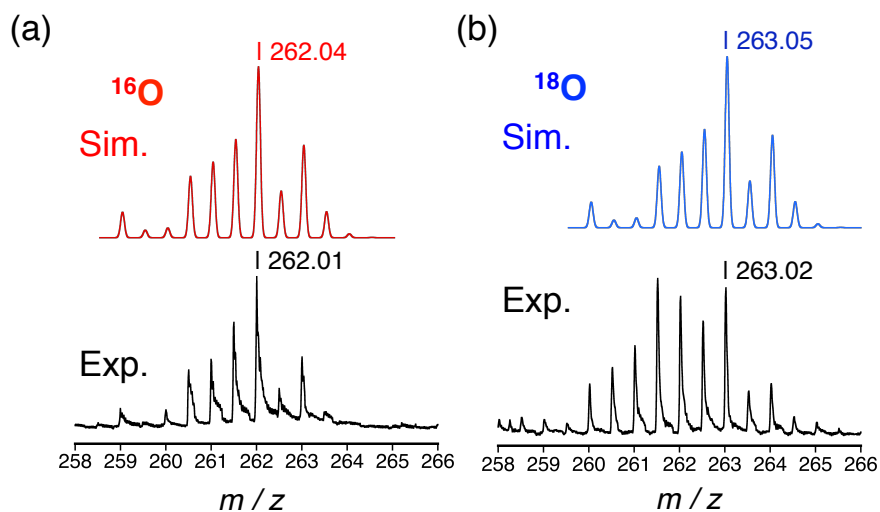


Figure 3-15. ESI-TOF-MS spectra of **8** and their simulations in the positive mode. 2.3 equiv of CAN was used for generating **8** from $6 \cdot (\text{ClO}_4)_2$ in 200 μL of H_2^{16}O (top) or H_2^{18}O (bottom), and then diluted by addition of 1 mL of MeCN or a MeCN- H_2^{18}O mixed solvent (49:1, v/v), respectively. Orifice voltage: 30 V.

The rR spectrum of **8** in an acidic aqueous solution (pH 4.0) at 276 K exhibited a Raman scattering derived from the Ru-O bond a 732 cm^{-1} ; the use of H_2^{18}O caused a low-energy shift of the signal to 696 cm^{-1} (Figure 3-16). The isotope shift ($\Delta\nu$) was 36 cm^{-1} , which was consistent with the theoretical value ($\Delta\nu_{\text{calc}} = 36\text{ cm}^{-1}$). The energy value of the stretching band of the Ru-O bond was significantly lower than those of $\text{Ru}^{\text{IV}}=\text{O}$ bonds reported to date ($\nu = 780\text{--}833\text{ cm}^{-1}$).^{6,11} Additionally, the experimental value is close to that

obtained from the DFT calculations on the Ru^{III}-O• structure of **8** in the triplet state ($\nu = 767 \text{ cm}^{-1}$; Figure 3-17(a)). Single-point energy calculations were performed on the open-shell triplet, open-shell singlet, and closed-shell singlet states for the DFT-optimized structures of **8**, which showed that the triplet state was more stable by 7.3 kcal mol⁻¹ than the singlet states (Figure 3-17(b)). The bond order of the Ru^{III}-O• bond was also estimated to be 1.3 by DFT calculations (Figure 3-18). Therefore, the electronic structure of **8** can be assigned to the triplet Ru^{III}-O• state, rather than a Ru^{IV}=O state.

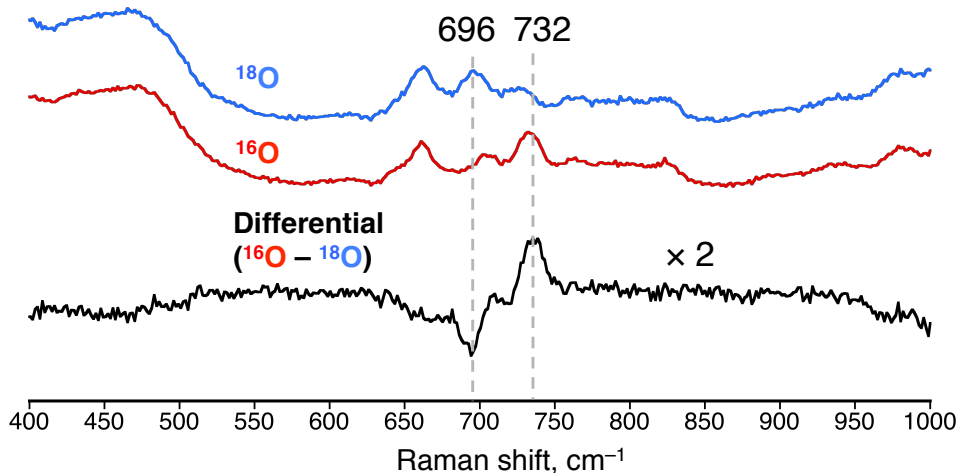


Figure 3-16. rR spectra of **8** in H₂¹⁶O (red) and in H₂¹⁸O (blue) at 276 K and the differential spectrum (black). Excitation wavelength: 441.6 nm.

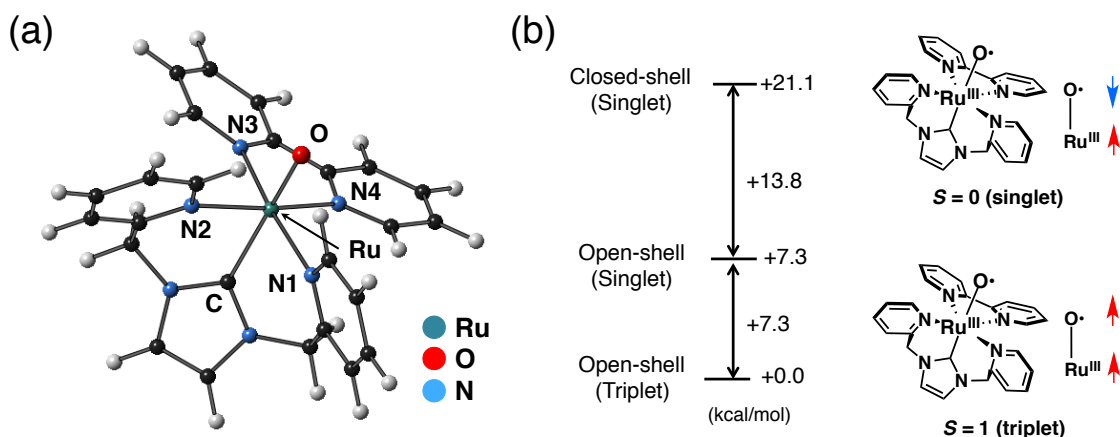


Figure 3-17. (a) A DFT-optimized structure of the Ru^{III}-O• state of **8** ($S = 1$) calculated by UB3LYP as a functional, SDD (Ru) and D95** (C, H, N, O) as basis sets. The bond order of the Ru-O bond was determined to be 1.3 and the Ru-O bond length was estimated to be 1.801 Å. Other bond lengths around the ruthenium center: Ru-N1, 2.211 Å; Ru-N2, 2.211 Å; Ru-N3, 2.101 Å; Ru-N4, 2.101 Å; Ru-C, 2.155 Å. (b) Single-point calculations on the energy of the open-shell triplet, open-shell singlet, and closed-shell singlet states for the DFT-optimized structure of **8**, calculated at the B3LYP/SDD(Ru) and D95** (C, H, N, O) level of theory.

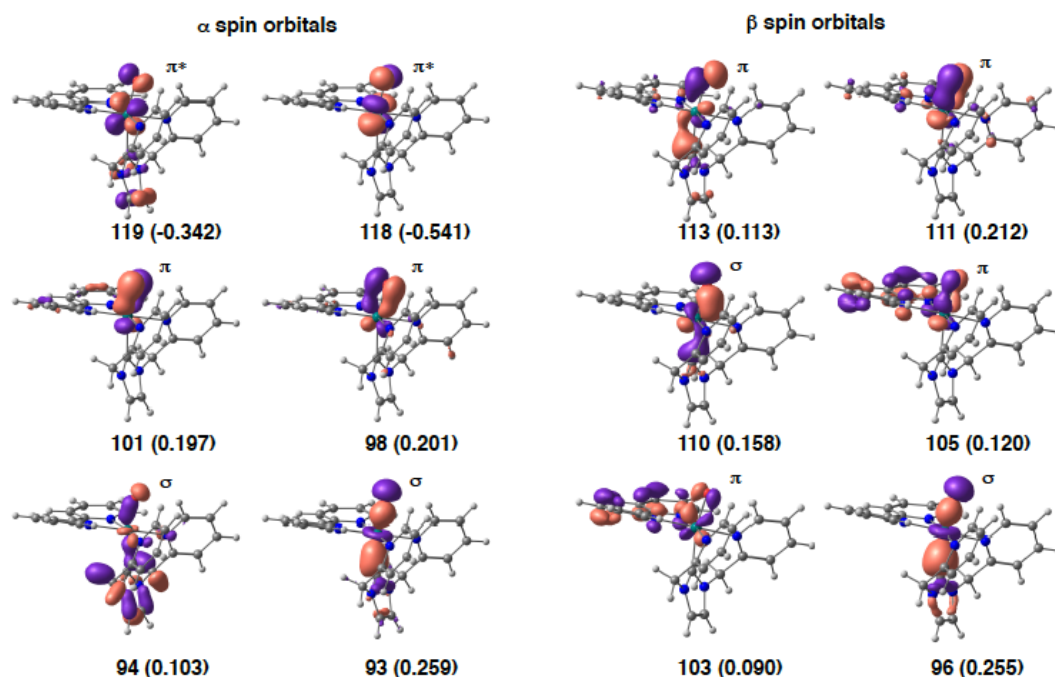


Figure 3-18. Selected molecular orbitals of **8** corresponding to the bonding and antibonding orbitals of the Ru-O bond. Values in parentheses are the Mayer bond-order contribution from the corresponding MOs. The DFT calculations were performed at the UB3LYP/SDD(Ru) and D95** (C, H, N, O) level of theory. The overall bond order was calculated to be 1.3 as follows: [(0.77 (σ -bonding orbitals) + {0.93 (π -bonding orbitals) - 0.88 (π -antibonding orbitals)} + 0.38 ($\alpha 80 \sim \alpha 110$ and $\beta 80 \sim \beta 110$ orbitals contribution to the bond order except the orbitals depicted above) + 0.10 (others))].

The oxidation state of the Ru center in **8** was elucidated using X-ray absorption near-edge structure (XANES) spectroscopy. The XANES spectra of **6**, **7**, and **8** at the Ru-K edge are shown in Figures 3-19.

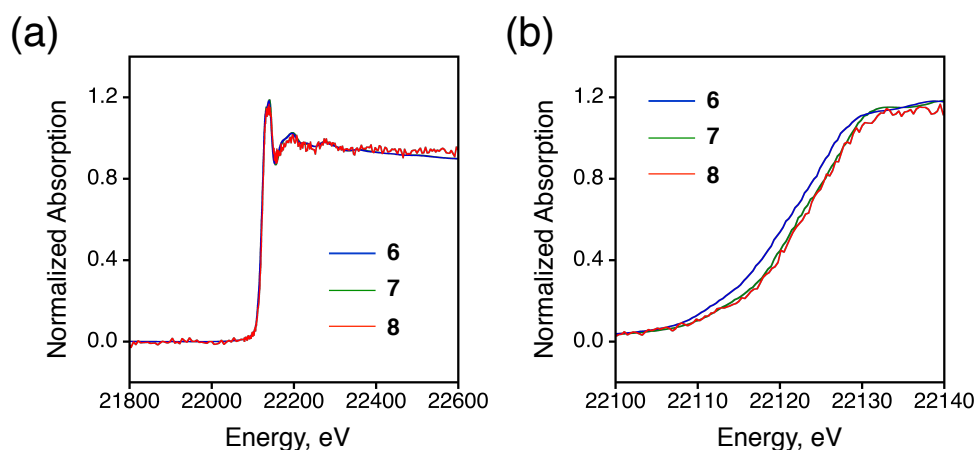


Figure 3-19. (a) X-ray absorption spectra of **6** (blue), **7** (green) and **8** (red) at the Ru-K edge. (b) Expanded plots in the near-edge region. The spectra of **6** and **7** were recorded by a transmission method with sample pellets of $6 \cdot (\text{ClO}_4)_2$ and $7 \cdot (\text{ClO}_4)_3$ diluted with boron nitride powder in a 1:36 molar ratio. The spectrum of **8** was recorded by a fluorescence method. The details of sample preparation were described in Experimental section.

The energy at the half-height (E_{hh}) was gradually shifted to the higher region in the order of **6** < **7** < **8**; 22120.6 eV for **6**, 22122.1 eV for **7**, and 22122.6 eV for **8**. Comparing the E_{hh} values between **6** and **7**, the shift width is 1.5 eV and thus the increase of the valence number of the Ru center from +2 to +3 is adequately confirmed.^{10c} In contrast, the shift width of the E_{hh} value from **7** to **8** is only 0.5 eV, and thus, the valence number of the Ru center in **8** should be close to +3, not to +4. Extended X-ray absorption fine structure (EXAFS) analysis on the aqueous solution of **8** allowed us to estimate the Ru-O bond of **8** to be 1.77(1) Å (Figure 3-20). Although the bond length is in the range of Ru^{IV}=O bonds reported so far, it should be noted that the Ru-O bond distances in Ru-oxo complexes show no clear relationship with the oxidation states of the Ru centers.¹¹ Thus, in light of spectroscopic data and results of DFT calculations, we concluded that the electronic structure of **8** should be described as a Ru^{III}-O• complex, rather than a Ru^{IV}=O complex.

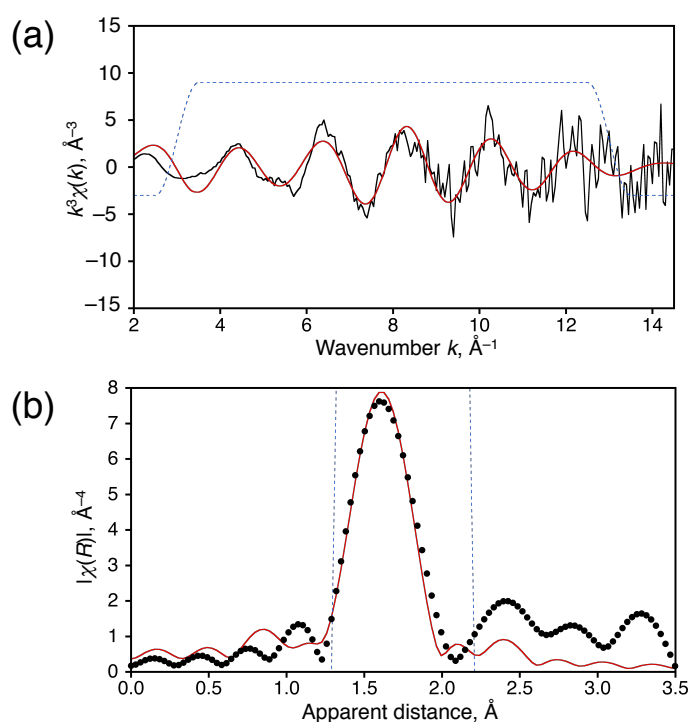


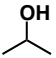
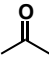
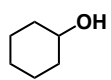
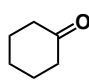
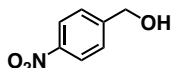
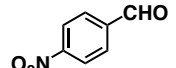
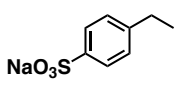
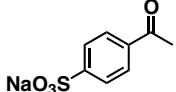
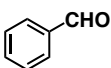
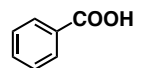
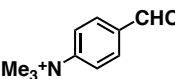
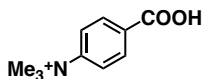
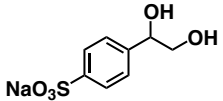
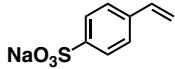
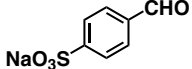
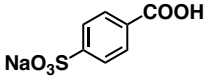
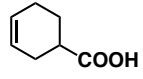
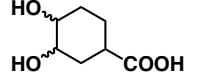
Figure 3-20. The k^3 -weighted EXAFS spectrum of the Ru-K edge of **8** in an acidic aqueous solution at 223 K (a) and the corresponding Fourier transform (b). The experimental data are shown with a solid black line in (a) and with filled black circles in (b). The fitting curves to the data are shown with red lines in (a) and (b). The Hanning windows were shown with a blue dashed line in (a) and (b). The fitting analysis of the EXAFS data was performed on the basis of the DFT-optimized structure of **8**. The fitting parameters are as follows: Coordination number: 6, Debye-Waller factor: 0.00020(15) Å², R-factor: 0.0120. The bond lengths obtained by the fitting analysis were Ru-N: 2.17(1) Å (× 2), Ru-N: 2.06(1) Å (× 2), Ru-C: 2.12(1) Å (× 1), and Ru-O: 1.77(1) Å (× 1).

3-5 Catalytic reactivity for substrate oxidation by **8** as reactive species

Catalytic reactivity of **6** in oxidation of organic substrates was examined using CAN as a sacrificial oxidant in acidic water (pH 0.6) at 278 K. The yields of oxidation products after stirring for 24 h were determined by ¹H NMR spectroscopy (Tables 3-2).^{29,30} In the case of oxidation of 2-propanol and cyclohexanol, the 2e⁻ oxidation proceeded to give acetone and cyclohexanone in 96% and 82% yields,

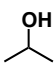
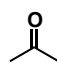
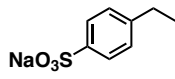
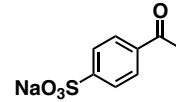
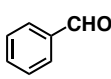
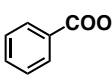
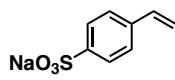
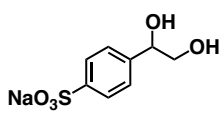
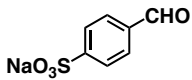
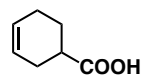
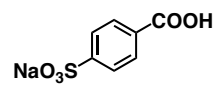
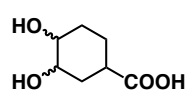
respectively (entries 1 and 2). 4-Nitrobenzyl alcohol was also oxidized to 4-nitrobenzaldehyde (entry 3).³¹ Sodium ethylbenzene sulfonate underwent 4e⁻ oxidation to afford the corresponding acetophenone derivative with a relatively low yield (entry 4). It should be noted that benzaldehyde and the derivative were also oxidized to give the corresponding benzoic acids (entries 5 and 6); however, benzaldehyde and the derivatives are generally difficult to be oxidized with Ru^{IV}=O complexes.^{6,32} This indicates the higher reactivity of the electronically equivalent Ru^{III}-O• species **8** as the active species in C-H oxidation than Ru^{IV}=O species. Terminal and internal alkenes gave the corresponding diols, which should be derived from cleavage of the corresponding epoxides as the primary products under the strongly acidic conditions (entries 7 and 8).

Table 3-2. Summary of product yields and turnover numbers of the catalytic oxidation reactions with **6**.^a

Entry	Substrate	Product	Yield, %	Efficiency, % ^b	TON ^c	Conversion, %
1			96	87	230	96
2			82	76	206	97
3 ^d			28 ^e	25	69	— ^f
4			33	60	75	33
5			42	39	102	42 ^g
6			37	34	69	38
			63	58	116	
7			11	20	28	75
			1	3	3	
8			11 : 4 ^h	10 : 3	27 : 8	48

^a Conditions: 0.14 mM **6**, 75 mM CAN, 34 mM substrate. ^b Efficiency = ([product] × n / [CAN]); n denotes the number of electron removed from the substrate to obtain the product. ^c TON = [Product]/[Catalyst]. ^d The reaction time was 1 h. ^e As a byproduct, 4-nitro-benzoic acid was also obtained in 5% yield. ^f The conversion could not be correctly calculated due to the insolubility of the substrate. ^g The amounts of the products and the remaining substrate were determined with ¹H NMR spectra of the reaction mixture in D₂O (pD ~ 1), which was diluted with the same volume of acetonitrile-*d*₃ after oxidation reaction to completely dissolve DSS as the internal standard. ^h Product ratio of *cis:trans* diols.

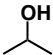
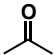
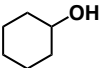
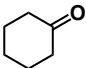
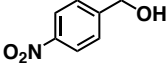
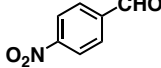
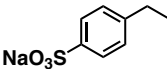
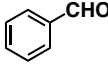
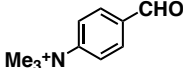
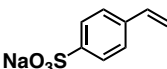
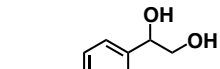
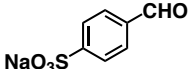
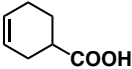
Table 3-3. Summary of the catalytic oxidation reactions of substrates with use of $\text{Ce}^{\text{IV}}(\text{SO}_4)_2$ in the presence of **6** as a catalyst at 278 K under air for 24 h.^a

Entry	Substrate	Product	Yield, %	Efficiency, % ^b	TON ^c	Conversion, %
1			82	73	192	82
2			24	44	58	24
3			70	63	166	70
4			19	17	45	40
			12	22	29	
5			3	9	8	84 ^[d]
			0 : 45	0 : 41	0 : 111	

^a Conditions: 0.14 mM **6**, 75 mM $\text{Ce}^{\text{IV}}(\text{SO}_4)_2$, 34 mM substrate. ^b Efficiency = $([\text{product}] \times n / [\text{CAN}])$; n denotes the number of electron removed from the substrate to obtain the product. ^c TON = $[\text{Product}]/[\text{Catalyst}]$. ^d Product ratio of *cis:trans* diols.

To gain mechanistic insights into the oxidation process of benzaldehyde, kinetic studies were performed. The catalytic oxidations of benzaldehyde were performed in D_2O (pD ~ 1) in the presence of CAN (0.31 M) and various concentration of $\text{6} \cdot (\text{ClO}_4)_2$ (0.014–0.28 mM) at 283 K. The progress of the reaction was monitored by the ^1H NMR spectroscopy (Figure 3-21(a), (b)). The initial rates, v_0 (M s^{-1}), were determined on the basis of the slope of time-course of benzoic acid formation. The observed dependence of v_0 on the concentration of **6** allowed us to determine the rate constant of the catalysis, $k_{\text{cat}}^{\text{H}}$, to be $1.2 \text{ M}^{-1} \text{ s}^{-1}$ (Figure 3-21(c), red). The kinetic isotope effect (KIE) was also examined using deuterated benzaldehyde, PhCDO, as a substrate under the same catalytic conditions (Figure 3-21(b)). The $k_{\text{cat}}^{\text{D}}$ value was also determined to be $0.15 \text{ M}^{-1} \text{ s}^{-1}$ (Figure 3-21(c), blue). Thus, the KIE value ($k_{\text{cat}}^{\text{H}}/k_{\text{cat}}^{\text{D}}$) was 8.0, indicating that hydrogen atom abstraction from the formyl group is involved in the rate-determining step of the benzaldehyde oxidation reaction. A Hammett plot was provided by using other four benzaldehyde derivatives having various substituents at the *para* position to demonstrate that there was no dependence of the initial rate on the substituents ($\rho = -0.07$; Figure 3-22). Such large KIE and small ρ values have also been observed in galactose oxidase³⁴ and its model complex,³⁵ in which a phenoxyl radical bound to a copper center is responsible for the substrate oxidation.³⁶ The results indicate that any polarized transition state, which has been suggested for the benzaldehyde oxidation with a $\text{Ru}^{\text{IV}}=\text{O}$ complex ($\rho = -0.65$),³⁷ is not involved in the hydrogen-atom-abstraction process by **8** and the oxidation of benzaldehyde does not proceed through a nucleophilic pathway. In the present catalytic reactions, benzaldehyde derivatives are oxidized through a pure hydrogen-atom-transfer mechanism. Therefore, we conclude that the $\text{Ru}^{\text{III}}-\text{O}\cdot$ complex (**8**) bears a strong oxyl radical character.

Table 3-4. Summary of the control experiments of the catalytic oxidation reactions of substrates with use of CAN in D₂O (pD ~ 1) in the **absence** of the catalyst, **6** at 278 K. ^a

Entry	Substrate	Product	Efficiency, % ^b
1			11
2			10
3			4
4		none	N. A.
5		none	N. A.
6		none	N. A.
7		 	6 88
8 ^c		none	N. A.

^a Conditions: 75 mM CAN, 34 mM substrate. time: 24 h. ^b Efficiency (%) = 100[(product] × n / [CAN]); n denotes the number of electron removed from the substrate to obtain the product. ^c Reaction time: 22 h.

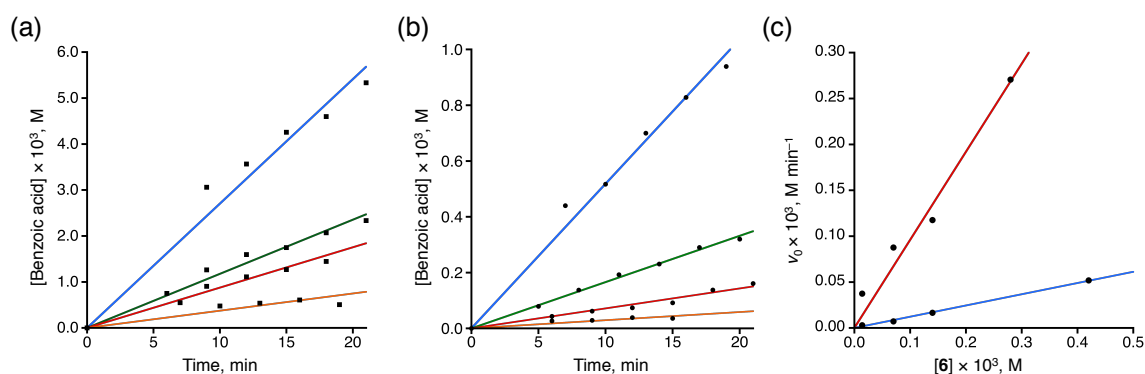


Figure 3-21. Time-profiles of benzoic acid formation in catalytic oxidation of benzaldehyde (14 mM) (a) and benzaldehyde-*d*₁ (b) in D₂O (pD ~ 1) at 278 K in the presence of CAN (0.31 M) as a sacrificial oxidant and **6** as a catalyst. [6]: 0.28 (blue), 0.14 (green), 0.07 (red), and 0.014 mM (orange). (c) An overlaid plot of dependence of the initial rates on the catalyst concentration for oxidation of benzaldehyde (red) and benzaldehyde-*d*₁ (blue) catalyzed by **6**. The concentration of benzoic acid was calculated by integral values of the ¹H NMR signal using DSS as an internal standard.

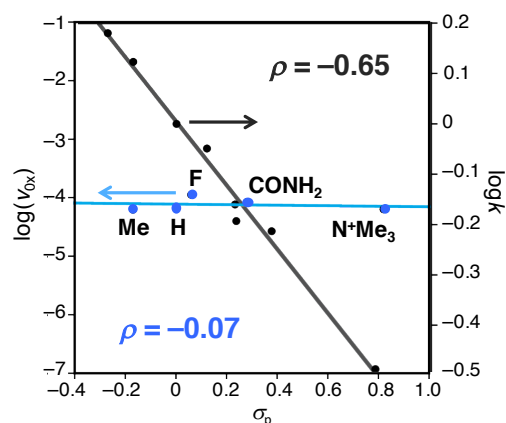


Figure 3-22. A Hammett plot of $\log(v_{0x})$ against σ_p for the oxidation of benzaldehyde derivatives in D_2O ($pD \sim 1$) under 283 K in the presence of **6** (0.15 mM) as a catalyst. v_{0x} refers to the initial rate for the oxidation of a benzaldehyde derivative having a substituent X at the *para* position. Concentration of a benzoic acid derivative was determined by integration values of the 1H NMR signal for the *o*-H, based on an internal standard, DSS. The initial rates obtained, v_{0x} , were $8.1 \times 10^{-5} \text{ M min}^{-1}$ for X = H ($\sigma_p = 0.0$), $6.3 \times 10^{-5} \text{ M min}^{-1}$ for X = Me ($\sigma_p = -0.17$), $1.1 \times 10^{-4} \text{ M min}^{-1}$ for X = F ($\sigma_p = 0.06$), $8.4 \times 10^{-5} \text{ M min}^{-1}$ for X = $CONH_2$ ($\sigma_p = 0.36$), and $6.4 \times 10^{-5} \text{ M min}^{-1}$ for X = N^+Me_3 ($\sigma_p = 0.82$), respectively. The Hammett parameters were obtained from the literature.³³

3-6 Conclusions

The formation and characterization of a $Ru^{III}\text{-O}\cdot$ complex, electronically equivalent to the corresponding $Ru^{IV}\text{=O}$ species, have been successfully achieved with use of a tridentate NHC ligand. The $Ru^{III}\text{-O}\cdot$ complex exhibits high reactivity in catalytic oxidation of organic substrates, including benzaldehyde derivatives in the presence of a Ce^{IV} complex as a sacrificial oxidant. In addition, the oxidation reaction includes hydrogen-atom abstraction from the substrates in a pure radical manner as the rate-determining step. The strategy to elongate the metal-oxo bond by the strong *trans* influence of NHC ligands to reduce the π -bonding interaction between the metal center and the oxo ligand can provide a new category of metal-oxyl complexes with strong radical character toward efficient catalytic oxidation reactions of organic compounds.

3-7 Experimental section

General.

NMR measurements were performed on a Bruker Avance 400 spectrometer (working frequencies for 1H : 400.0 MHz, and for ^{13}C : 100.0 MHz). DSS (= 3-(trimethylsilyl)propanesulfonate sodium salt) was used as an internal standard for 1H NMR spectral measurements in D_2O . ESI-TOF-MS spectra were obtained on a JEOL JMS-T100CS mass spectrometer. UV-Vis absorption spectra were measured on a Shimadzu UV-2450 spectrophotometer and an Agilent 8453 photodiode-array spectrophotometer at 277 K. Cyclic and square-wave voltammograms were recorded on a BAS electrochemical analyzer model 660A. ESR spectroscopy was performed on a Bruker EMXPlus9.5/2.7 spectrometer. Gas chromatography was performed using a Shimadzu GC-2014 equipped with a thermal conductivity detector (TCD) and a capillary column packed with molecular sieves 5A.

Materials.

All syntheses were performed under Ar atmosphere. H-BPIm was synthesized according to the literature procedure.²² $[\text{Ru}^{\text{II}}\text{Cl}_2(\text{bpy})(\text{dmsO})_2]$ (bpy = 2,2'-bipyridyl, dmsO = dimethylsulfoxide) was synthesized from $[\text{Ru}^{\text{II}}\text{Cl}_2(\text{dmsO})_4]$ according to the literature method.³⁸ $[\text{Ru}^{\text{II}}\text{Cl}_2(\text{dmsO})_4]$ was synthesized from $\text{Ru}^{\text{III}}\text{Cl}_3 \cdot n\text{H}_2\text{O}$ purchased from Furuya metal Co. Ag_2O and $\text{NaClO}_4 \cdot \text{H}_2\text{O}$ were purchased from Wako Co. All solvents used for the syntheses were dried over CaH_2 and distilled before use. Benzaldehyde- d_1 (PhCDO) was synthesized according to the literature procedure.³⁹ $(\text{NH}_4)_2[\text{Ce}^{\text{IV}}(\text{NO}_3)_6]$ (CAN; Aldrich) and $\text{Ce}^{\text{IV}}(\text{SO}_4)_2 \cdot 4\text{H}_2\text{O}$ (Wako Chemicals) were purchased and used without further purification. $[\text{Ag}(\text{BPIm})]^+$ was prepared according to the literature procedure.⁴⁰

Synthesis.

$[\text{Ru}^{\text{II}}\text{Cl}(\text{BPIm})(\text{bpy})]\text{Cl}$ (5·Cl**).** A solution of $[\text{Ag}(\text{BPIm})]^+$ (0.74 mmol) in CH_2Cl_2 (30 mL) was prepared by mixing H-BPIm (211 mg, 0.74 mmol) and excess amount of Ag_2O (223 mg, 0.96 mmol) in CH_2Cl_2 (30 mL) for 67 h under Ar in the dark and subsequent filtration to remove insoluble Ag_2O . The solution was added to a degassed suspension of $[\text{Ru}^{\text{II}}\text{Cl}_2(\text{bpy})(\text{dmsO})_2]$ (359 mg, 0.74 mmol) in CH_2Cl_2 (20 mL), whose degassing was done by three freeze-pump-thaw cycles. The mixture was refluxed for 24 h in the dark. After cooling to room temperature, a mixture of white and purple solids was filtered from the reaction mixture with a glass filter. The solids were washed with CH_2Cl_2 to remove CH_2Cl_2 -soluble materials until the orange-red color of the filtrate disappeared. Then, the purple solid on the glass filter was extracted with acetone to remove the white solid from the solid mixture. The purple filtrate was evaporated to dryness under reduced pressure to obtain a purple solid of **5·Cl** (161 mg, 0.28 mmol, 34% yield). ^1H NMR (methanol- d_4): δ 9.99 (d, $J = 8.0$ Hz, 2H, $\text{Py}_{\text{pin-6}}$), 8.36 (d, $J = 8.0$ Hz, 2H, $\text{Py}_{\text{bpy-6}}$), 8.18 (dd, $J = 5.6, 0.8$ Hz, 2H, $\text{Py}_{\text{bpy-3}}$), 8.00 (td, $J = 7.6, 1.2$ Hz, 2H, $\text{Py}_{\text{pin-4}}$), 7.95 (td, $J = 7.8, 1.2$ Hz, 2H, $\text{Py}_{\text{bpy-5}}$), 7.73 (dd, $J = 5.2, 0.8$ Hz, 2H, $\text{Py}_{\text{pin-3}}$), 7.58 (td, $J = 6.6, 1.2$ Hz, 2H, $\text{Py}_{\text{pin-5}}$), 7.39 (td, $J = 6.6, 1.2$ Hz, 2H, $\text{Py}_{\text{bpy-4}}$), 7.26 (s, 2H, Im-4&Im-5), 5.37 (ABq, $J = 16$ Hz, 2H, Py- CH_2 -Im), 5.00 (ABq, $J = 16$ Hz, 2H, Py- CH_2 -Im). ^{13}C NMR (methanol- d_4): δ 186.02, 160.94, 158.85, 157.98, 154.04, 138.91, 137.32, 127.80, 126.61, 125.49, 123.83, 123.51, 55.27. ESI-TOF-MS (acetone): $m/z = 542.99$ (calcd. for $[\text{M} - \text{Cl}]^+$: 543.06). Anal. Calcd. for $\text{C}_{25}\text{H}_{22}\text{N}_6\text{Cl}_2\text{Ru} \cdot 2\text{H}_2\text{O}$: H 4.26, C 48.87, N 13.68; Found: H 4.10, C 49.01, N 13.64.

$[\text{Ru}^{\text{II}}(\text{BPIm})(\text{bpy})(\text{OH}_2)](\text{ClO}_4)_2$ (6·(ClO₄)₂**).** A solution of AgOTf (693 mg, 2.69 mmol) in water (10 mL) was added to the suspension of **5·Cl** (396 mg, 0.684 mmol) in water (10 mL), and then, the reaction mixture was heated at 60 °C for 10 h in the dark. The reaction mixture was filtered through a membrane filter by hot filtration. Then, the solution of $\text{NaClO}_4 \cdot \text{H}_2\text{O}$ (2.000 g, 14.2 mmol) in water (5 mL) was added to the hot filtrate. The solution was kept in a refrigerator overnight to form orange-red precipitate. The precipitate was filtered with a membrane filter and washed with water. The red solid was dried under vacuum to obtain **6·(ClO₄)₂** (384 mg, 0.53 mmol, 78% yield). ^1H NMR (D_2O): δ 9.42 (d, $J = 5.6$ Hz, 2H, $\text{Py}_{\text{pin-6}}$), 8.29 (d, $J = 8.0$ Hz, 2H, $\text{Py}_{\text{bpy-6}}$), 8.15 (d, $J = 6.0$ Hz, 2H, $\text{Py}_{\text{bpy-3}}$), 8.00 (t, $J = 8.0$ Hz, 4H, $\text{Py}_{\text{bpy-5}}$ & $\text{Py}_{\text{pin-4}}$), 7.70 (d, $J = 8.0$ Hz, 2H, $\text{Py}_{\text{pin-3}}$), 7.58 (t, $J = 8.0$ Hz, 2H, $\text{Py}_{\text{pin-5}}$), 7.38 (t, $J = 7.2$ Hz, 2H, $\text{Py}_{\text{bpy-4}}$), 7.13 (s, 2H, Im-4 & Im-5), 5.25 (ABq, $J = 16$ Hz, 2H, Im- CH_2 -Py), 5.07 (ABq, $J = 16$ Hz, 2H, Im- CH_2 -Py). ESI-TOF-MS (MeOH): $m/z = 254.01$ (calcd. for $[\text{M} - \text{OH}_2 - 2\text{ClO}_4]^{2+}$: 254.05). UV-Vis (HNO_3 aq, pH 0.6): λ_{max} [nm] = 353, 490. Anal. Calcd. for $\text{C}_{25}\text{H}_{24}\text{N}_6\text{O}_9\text{Cl}_2\text{Ru} \cdot \text{H}_2\text{O}$: H 3.53, C 40.44, N 11.32; Found: H 3.43, C 40.27, N, 11.24.

[Ru^{III}(BPIIm)(bpy)(OH₂)](ClO₄)₃ (7·(ClO₄)₃). A suspension of Ce^{IV}(SO₄)₂·4H₂O (13.46 mg, 33.3 μmol) in 3 M HClO₄ aq (0.5 mL) was added to a suspension of **6·(ClO₄)₂** (19.06 mg, 26.3 μmol) in 3 M HClO₄ aq (2 mL). After the solution color changed from red to deep blue, a solution of NaClO₄·H₂O (2.392 g, 17.0 mmol) in 3 M HClO₄ aq (1 mL) was added to the blue solution. The reaction mixture was kept in a refrigerator overnight to form black crystals of **7·(ClO₄)₃** (2.44 mg, 3.0 μmol, 9% yield). ¹H NMR (D₂O): δ 19.41, 13.40, 12.52, 8.56, -1.10, -11.52, -15.32, -21.56. UV-Vis (HNO₃ aq, pH 0.6): λ_{max} [nm] = 627. Anal. Calcd. for C₂₅H₂₄N₆O₁₃Cl₃Ru·3H₂O: H 3.44, C 34.20, N 9.57; Found: H 3.38, C 34.29, N 9.51.

[Ru^{III}(O⁻)(BPIIm)(bpy)]²⁺ (8). ¹H NMR (D₂O): δ 25.02, 22.35, 20.92, 20.15, 17.48, 16.25, -2.80, -17.88, -25.22, -32.13. rR (H₂¹⁶O or H₂¹⁸O): ν [cm⁻¹] = 732 (Ru-¹⁶O), 696 (Ru-¹⁸O). ESI-TOF-MS (MeCN): *m/z* = 262.01 ([M(¹⁶O) - 2ClO₄]²⁺), 263.02 ([M(¹⁸O) - 2ClO₄]²⁺).

X-ray crystallography.

Single crystals of **5·Cl**, **6·(ClO₄)₂**, **6·(OTf)₂·2H₂O** and **7·(ClO₄)₃·H₂O**, suitable for X-ray crystallography, were obtained by recrystallization with a vapor diffusion of AcOEt into the MeOH solution of **5·Cl**, with that of AcOEt into the solution of **6·(ClO₄)₂** in EtOH : water = 2 : 1 (v/v) mixed solvent, with slow condensation of the solution of **6·(OTf)₂** in a reaction mixture, and recrystallization from an HClO₄ solution of **7·(ClO₄)₃·H₂O** at 255 K, respectively. The crystals were mounted using a mounting loop. All diffraction data were collected on a Bruker APEXII diffractometer at 120 K with a graphite-monochromated

Table 3-5. Crystallographic data for **5·Cl**, **6·(ClO₄)₂**, **6·(OTf)₂·2H₂O** and **7·(ClO₄)₃·H₂O**

Compound	5·Cl	6·(ClO₄)₂	6·(OTf)₂·2H₂O	7·(ClO₄)₃·H₂O
MW	578.45	724.47	859.74	841.94
Formula	C ₂₅ H ₂₂ Cl ₂ N ₆ Ru	C ₂₅ H ₂₄ Cl ₂ N ₆ O ₉ Ru	C ₂₇ H ₂₄ F ₆ N ₆ O ₇ RuS ₂ ·2H ₂ O	C ₂₅ H ₂₄ Cl ₃ N ₆ O ₁₃ Ru ·H ₂ O
Crystal system	Monoclinic	Monoclinic	Monoclinic	Triclinic
Space group	<i>Pa</i>	<i>P2₁/c</i>	<i>P2₁/n</i>	<i>P</i> $\bar{1}$
<i>a</i> , Å	9.0685(16)	16.042(4)	12.2014(15)	10.872(5)
<i>b</i> , Å	19.722(4)	10.410(3)	17.646(2)	11.488(5)
<i>c</i> , Å	13.712(2)	17.014(4)	15.1836(19)	13.974(5)
α, °	90	90	90	91.803(5)
β, °	94.618(2)	92.196(12)	95.4380(10)	98.179(5)
γ, °	90	90	90	90.053(5)
<i>V</i> , Å ³	2444.4(7)	2839.0(12)	3254.4(7)	1726.7(13)
<i>Z</i>	4	4	4	2
<i>R</i> 1, %	2.72	4.44	2.26	6.23
<i>wR</i> 2, %	6.21	10.84	9.40	15.49
GOF	1.031	1.074	0.890	1.056

Mo $K\alpha$ radiation source ($\lambda = 0.71073 \text{ \AA}$) by the 2θ scan. All structure refinements were performed using the Yadokari-XG crystallographic software package.⁴¹ The structures were solved by a direct method using SIR97 and SHELX97.⁴² Crystallographic data for **5**·Cl, **6**·(ClO₄)₂, **6**·(OTf)₂·2H₂O and **7**·(ClO₄)₃·H₂O are summarized in Table 3-5.

Resonance Raman spectroscopy.

The sample solution of **8** was prepared by the following procedure: Complex **6**·(ClO₄)₂ (1.62 mg, 2.24 μmol) was suspended into water (pH 3.99, 500 μL). Then, CAN (3.42 mg, 6.24 μmol) was added as a solid to the suspension to afford a dark-blue solution. Resonance Raman spectroscopic measurements were conducted on the dark-blue solution. An ¹⁸O-labeling experiment was made by the following procedure: Complex **6**·(ClO₄)₂ (1.05 mg, 1.45 μmol) was suspended in H₂¹⁸O (300 μL) and CAN (2.41 mg, 4.40 μmol) was added to the suspension. The solution obtained was submitted to resonance Raman spectroscopic measurements. Resonance Raman scattering was made by excitation at 441.6 nm with a He-Cd laser (Kimmon Koha, IK5651R-G), dispersed by a single polychromator (Chromex, 500IS) and detected by a liquid-nitrogen-cooled CCD detector (Roper Scientific, Spec10:400B/LN). The resonance Raman measurements were carried out at 276 K using a spinning cell (outer diameter = 5 mm, wall thickness = 0.2 mm) at 135° scattering geometry.

X-ray absorption near edge structure (XANES) spectroscopy.

XANES spectra at the Ru K-edge were collected on the superconducting wiggler beamline BL07 at SAGA Light Source.⁴³ The X-rays were monochromated by a Si(220) double crystal monochromator and were focused by a rhodium coated bent cylindrical mirror. The intensity of the X-rays was monitored by an ionization chamber filled with a mixed gas of 50% nitrogen and 50% argon. The solid samples of **6**·(ClO₄)₂ and **7**·(ClO₄)₃ were diluted with boron nitride (BN) powder in a 1 : 36 molar ratio, pressed by a hydraulic press to obtain sample pellets, and measured in transmission mode at room temperature. The intensity of transmitted X-rays from the sample was monitored by an ionization chamber filled with a mixed gas of 75% argon and 25% krypton. A solution sample of **8** was prepared by the following procedure; **6**·(ClO₄)₂ (1.0 mg, 1.4 μmol) was dissolved in HNO₃ aq (pH 0.6, 1.4 mM) at 263 K, and CAN (7.8 mg, 14 μmol) was added to the solution of **6**·(ClO₄)₂ and the mixture was stirred for 5 min at -10 °C. When the color of solution turned from blue to pale yellow, the XANES spectrum of **8** was recorded with a fluorescence mode using a silicon drift detector. During the measurements, the samples were kept at -25 °C under nitrogen atmosphere at ambient pressure. The energy calibration was performed for the XANES spectrum of **6**·(ClO₄)₂ with use of Pd (24350 eV) and Rh foils (23220 eV).

Extended X-ray absorption fine structure (EXAFS) analysis on **8**.

EXAFS spectrum at the Ru K-edge of **8** was collected at the beamline BL-NW10A of PF-AR in High Energy Accelerator Research Organization with an acidic solution of **8** in a fluorescent method using a 21-element Ge solid-state array detector (CANBERRA, USA). The solution sample of **8** was prepared by the following procedure; **6**·(ClO₄)₂ (2.0 mg, 2.8 μmol) was dissolved in HNO₃ aq (2 mL, pH 0.6, 1.4 mM) at room temperature, and CAN (15 mg, 28 μmol) was added to the solution. When the color of the solution turned from blue to yellow, the solution was transferred to an Eppendorf tube, and frozen with liquid nitrogen. The frozen sample was mounted on a cryostat placed in front of the detector, and then, the cryostat was cooled to 223 K. k^3 -Weighted EXAFS function, $k^3\chi(k)$, was extracted from the raw X-ray absorption

data of **8**, which were obtained by using the ATHENA software.⁴⁴ Fourier transform of the EXAFS function was performed in the k range of 3 – 13 Å⁻¹ by using the Hanning window and its fitting to the theoretical curve calculated for the DFT-optimized structural model (Figure 3-17(a)) was carried out with use of the ARTEMIS software⁴⁴ in the R range of 1.3 – 2.2 Å corresponding to the first shell. In this fitting, the amplitude and phase shift for all scattering paths were also calculated using FEFF6L software in the ARTEMIS software.⁴⁵

DFT calculations.

Global minima on the potential energy surfaces using the B3LYP method.⁴⁶ To estimate excited states TD-DFT calculations⁴⁷ were performed using optimized structures. For the Ru atom, we used the SDD basis sets,⁴⁸ and for the H, C, N, and O atoms, we used the D95** basis set.⁴⁹ Vibration frequencies were systematically computed to ensure that on a potential energy surface each optimized geometry corresponds to a local minimum that has no imaginary frequency. The Gaussian 09 program package⁵⁰ was used for all DFT calculations.

Determination of rate constants (k_{cat}) for the catalytic oxidation with **6**.

The ¹H NMR signals of benzoic acid derivatives derived from oxidation of benzaldehyde derivatives were observed to monitor the reaction progress in D₂O (pD ~ 1). The amounts of the benzoic acid derivatives were determined using DSS as an internal standard. Least-square linear fitting was conducted for the time-profile plots between 0 to *ca.* 40 min. The slope of the fitting line obtained was used as the initial rate of the benzaldehyde oxidation. The $k_{\text{cat}}^{\text{H}}$ value was determined by using Eq. 1 (Figure 3-21).

$$v_0 = k_{\text{cat}}^{\text{H}}[\text{Substrate}][\mathbf{6}] \quad (\text{Eq. 1})$$

Pourbaix diagram of **6**.

To prepare the Pourbaix diagram of **6** (Figure 3-9), a pH-controlled H₂SO₄ aq was used as a solvent and the voltammograms at a different pH were measured by square-wave voltammetry with a different sample solution, whose pH was adjusted by addition of 0.1 M NaOH aq. The sample solution (1.0 mM) of **6** was prepared by dissolving **6**·(ClO₄)₂ (1.0 mg, 1.4 μmol) into a pH-controlled H₂SO₄ aq (1.4 mL) just before the measurements and kept cooled in an ice bath at 277 K. The voltammetric measurements were also performed at 277 K.

Reference and notes.

- (1) (a) M. Costas, M. P. Mehn, M. P. Jensen, L. Que, Jr., *Chem. Rev.* **2004**, *104*, 939–986. (b) B. Meunier, S. P. de Visser, S. Shaik, *Chem. Rev.* **2004**, *104*, 3947–3980.
- (2) (a) A. Kohen, J. P. Klinman, *Acc. Chem. Res.* **1998**, *31*, 397–404. (b) W. Nam, *Acc. Chem. Res.* **2007**, *40*, 522–531.
- (3) (a) R. A. Binstead, M. E. McCuire, A. Dovletoglou, W. K. Seok, L. E. Roecker, T. J. Meyer, *J. Am. Chem. Soc.* **1992**, *114*, 173–186. (b) J. J. Concepcion, J. W. Jurss, J. L. Templeton, T. J. Meyer, *J. Am. Chem. Soc.* **2008**, *130*, 16462–16463.
- (4) (a) E. Masllorens, M. Rodríguez, I. Romero, A. Roglans, T. Parella, J. Benet-Bichholz, M. Poyatos, A. Llobet, *J. Am. Chem. Soc.* **2006**, *128*, 5306–5307, (b) R. Staehle, L. Tong, L. Wang, L. Duan, A. Fischer, M. S. G. Ahlquist, L. Sun, S. Rau, *Inorg. Chem.* **2014**, *53*, 1307–1319.

- (5) (a) M. Dakkach, A. Atlamsani, T. Parella, X. Fontrodona, I. Romero, M. Rodríguez, *Inorg. Chem.* **2013**, *52*, 5077–5087, (b) M. Dakkach, X. Fontrodona, T. Parella, A. Atlamsani, I. Romero, M. Rodríguez, *Adv. Synth. Catal.* **2011**, *353*, 231–238.
- (6) (a) Y. Hirai, T. Kojima, Y. Mizutani, Y. Shiota, K. Yoshizawa, S. Fukuzumi, *Angew. Chem. Int. Ed.* **2008**, *47*, 5772–5776. (b) S. Ohzu, T. Ishizuka, Y. Hirai, H. Jiang, M. Sakaguchi, T. Ogura, S. Fukuzumi, T. Kojima, *Chem. Sci.* **2012**, *3*, 3421–3431.
- (7) (a) J. J. Warren, T. A. Tronic, J. M. Mayer, *Chem. Rev.* **2010**, *110*, 6961–7001. (b) D. R. Weinberg, C. J. Gagliardi, J. F. Hull, C. F. Murphy, C. A. Kent, B. C. Westlake, A. Paul, D. H. Ess, D. G. McCafferty, T. J. Meyer, *Chem. Rev.* **2012**, *112*, 4016–4093.
- (8) (a) W. A. Nugent, J. M. Mayer, *Metal-Ligand Multiple Bonds*, Wiley, New York, **1988**. (b) J. R. Winkler, H. B. Gray, *Struct. Bonding* (Berlin) **2012**, *142*, 17–28.
- (9) (a) I. Kretzschmar, A. Fiedler, J. N. Harvey, D. Schröder, H. Schwarz, *J. Phys. Chem. A* **1997**, *101*, 6252–6264. (b) M. Baik, X. Yang, *J. Am. Chem. Soc.* **2006**, *128*, 7476–7485.
- (10) (a) T. Kojima, K. Hayashi, S. Iizuka, F. Tani, Y. Naruta, M. Kawano, Y. Ohashi, Y. Hirai, K. Ohkubo, Y. Matsuda, S. Fukuzumi, *Chem. Eur. J.* **2007**, *13*, 8212–8222. (b) F. Neese, S. Ye, *Proc. Natl. Acad. Sci. USA.* **2011**, *108*, 1228–1233. (c) N. Planas, L. Vigara, C. Cady, P. Mirl, P. Huang, L. Hammarström, S. Styring, N. Leidel, H. Dau, M. Haumann, L. Gagliardi, C. J. Cramer, A. Llobet, *Inorg. Chem.* **2011**, *50*, 11134–11142.
- (11) T. Ishizuka, H. Kotani, T. Kojima, *Dalton Trans.* **2016**, *45*, 16727–16750.
- (12) Y. Shiota, J. M. Herrera, G. Juhász, T. Abe, S. Ohzu, T. Ishizuka, T. Kojima, K. Yoshizawa, *Inorg. Chem.* **2011**, *50*, 6200–6209.
- (13) X. Yang, M.-H. Baik, *J. Am. Chem. Soc.* **2006**, *128*, 7476–7485.
- (14) D. Moonshiram, I. Alperovich, J. J. Conception, T. J. Meyer, Y. Pushkar, *Proc. Natl. Acad. Sci. USA.* **2013**, *110*, 3765–3770.
- (15) S. W. Gersten, G. J. Samuels, T. J. Meyer, *J. Am. Chem. Soc.* **1982**, *104*, 4029–4030.
- (16) J. K. Hurst, J. L. Cape, A. E. Clark, S. Das, C. Y. Qin, *Inorg. Chem.* **2008**, *47*, 1753–1764.
- (17) (a) K. Kobayashi, H. Ohtsu, T. Wada, T. Kato, K. Tanaka, *J. Am. Chem. Soc.* **2003**, *125*, 6729–6739. (b) K. Kobayashi, H. Ohtsu, T. Wada, T. Kato, K. Tanaka, *Chem. Lett.* **2002**, 868–869.
- (18) T. Wada, K. Tsuge, K. Tanaka, *Chem. Lett.* **2000**, *29*, 910–911.
- (19) M. L. Neidig, A. Decker, O. W. Choroba, F. Huang, M. Kavana, G. R. Moran, J. B. Spencer, E. I. Solomon, *Proc. Natl. Acad. Sci. U. S. A.* **2006**, *103*, 12966–12973.
- (20) Introduction of a strongly σ -donating ligand at the *trans* position to an oxo ligand is known to weaken the M=O bond and increase the spin density of the terminal oxygen atom. See: Ref. 10b.
- (21) A. Kumar, K. Madanakrishna, P. Ghosh, *Polyhedron* **2013**, *52*, 524–529.
- (22) A. M. Magill, D. S. McGuinness, K. J. Cavell, G. J. P. Britovsek, V. C. Gibson, A. J. P. White, D. J. Williams, A. H. White, B. W. Skelton, *J. Organomet. Chem.* **2001**, *617*, 546–560.
- (23) (a) M. N. Hopkinson, C. Richter, M. Schedler, F. Glorius, *Nature* **2014**, *510*, 485–496. (b) H. Jacobsen, A. Correa, A. Poater, C. Costabile, L. Cavallo, *Coord. Chem. Rev.* **2009**, *253*, 687–703. (c) D. M. Khramov, V. M. Lynch, C. W. Bielawski, *Organometallics* **2007**, *26*, 6042–6049. (d) H. Jacobsen, A. Correa, C. Costabile, L. Cavallo, *J. Organomet. Chem.* **2006**, *691*, 4350–4358. (e) L. Merces, G. Labat, A. Neels, A. Ehlers, M. Albrecht, *Organometallics* **2006**, *25*, 5648–5656.
- (24) (a) S. Ohzu, T. Ishizuka, H. Kotani, T. Kojima, *Chem. Commun.* **2014**, *50*, 15018–15021. (b) H. Tseng, R. Zong, J. T. Muchkerman, R. Thummel, *Inorg. Chem.* **2008**, *47*, 11763–11773.

- (25) (a) S. Aiki, Y. Kijima, J. Kuwabara, A. Taketoshi, T. Koizumi, S. Akine, T. Kanbara, *ACS. Catal.* **2013**, *3*, 812–816. (b) H. Hadadzadeh, M. C. DeRosa, G. P. A. Yap, A. R. Rezvani, R. J. Crutchley, *Inorg. Chem.* **2002**, *41*, 6521–6526.
- (26) M. Dakkach, X. Fontrodona, T. Parella, A. Atlamsani, I. Romero, M. Rodríguez, *Adv. Synth. Catal.* **2011**, *353*, 231–238.
- (27) Y. Pushkar, D. Moonshiram, V. Purohit, L. Yan, I. Alperovich, *J. Am. Chem. Soc.* **2014**, *136*, 11938–11945.
- (28) V. Nair, A. Deepthi, *Chem. Rev.* **2007**, *107*, 1862–1891.
- (29) There is a report about a nitrate effect on the oxidation reactions (J. A. Stull, R. D. Britt, J. L. McHale, F. J. Knorr, S. V. Lyman, J. K. Hurst, *J. Am. Chem. Soc.* **2012**, *134*, 19973); however, the catalytic reactivity of **6** in the substrate oxidation, in which cerium(IV) sulfate was used as a sacrificial oxidant in the aqueous solution acidified with H₂SO₄, was almost the same as that with CAN in HNO₃ aq. Therefore, the nitrate effect was not found in the present catalytic system. See Table 3-3.
- (30) As control experiments, the reactions of the substrates listed in Table 3-4 with CAN under the same reaction conditions except in the absence of **6**. See Table 3-4.
- (31) After 24 h, most of 4-nitrobenzyl alcohol was oxidized by CAN even in the absence of a catalyst. Therefore, the catalytic oxidation of 4-nitrobenzyl alcohol was performed for 1 h.
- (32) A. Gerli, J. Reedijk, M. T. Lakin, A. L. Spek, *Inorg. Chem.* **1995**, *34*, 1836–1843.
- (33) A. Hansch, A. Leo, R. W. Taft, *Chem. Rev.* **1991**, *91*, 165–195.
- (34) M. M. Whittaker, J. W. Whittaker, *Biochemistry* **2001**, *40*, 7140–7148.
- (35) Y. Wang, J. L. DuBois, B. Hedman, K. O. Hodgson, T. D. P. Stack, *Science* **1998**, *279*, 537–540.
- (36) F. Thomas, *Eur. J. Inorg. Chem.* **2007**, 2379-2404.
- (37) W. K. Seok, T. J. Meyer, *Inorg. Chem.* **2005**, *44*, 3931–3941.
- (38) M. Toyama, K. Inoue, S. Iwamatsu, N. Nagao, *Bull. Chem. Soc. Jpn.* **2006**, *79*, 1525–1534.
- (39) P. L. Polavarapu, L. P. Fontana, H. E. Smith, *J. Am. Chem. Soc.* **1986**, *108*, 94–99.
- (40) L. Canovese, F. Visentin, C. Levi, C. Santo, V. Bertolasi, *Inorg. Chim. Acta* **2012**, *390*, 105–118.
- (41) C. Kabuto, S. Akine, T. Nemoto, E. Kwon, Release of software (Yadokari-XG 2009) for crystal structure analyses. *J. Cryst. Soc. Jpn.* **2009**, *51*, 218–224.
- (42) G. M. Sheldrick, SIR97 and SHELX97, Programs for Crystal Structure Refinement, University of Göttingen, Göttingen (Germany), 1997.
- (43) M. Kawamoto, K. Sumitani, T. Okajima, *AIP Conf. Proc.* **2010**, *1234*, 355–358.
- (44) B. Ravel, M. Newville, *J. Synchrotron. Rad.* **2005**, *12*, 537–541.
- (45) S. I. Zabinsky, J. J. Rehr, A. Ankudinov, R. C. Albers, M. J. Eller, *Phys. Rev. B* **1995**, *52*, 2995–3009.
- (46) (a) A. D. Becke, *Phys. Rev. A* **1988**, *38*, 3098. (b) C. Lee, W. Yang, R. G. Parr, *Phys. Rev. B* **1988**, *37*, 785–789.
- (47) M. E. Casida, C. Jamorski, K. C. Casida, D. R. Salahub, *J. Chem. Phys.* **1998**, *108*, 4439–4449.
- (48) M. Dolg, H. Stoll, H. Preuss, *Theor. Chim. Acta* **1993**, *85*, 441–450.
- (49) T. H. Dunning, P. J. Hay, In *Modern Theoretical Chemistry*; Schaefer, H. F., III, Ed.; Plenum: New York, **1976**; Vol. 3, pp 1–27.
- (50) Gaussian 09, Revision D.01, M. J. Frisch, G. W. Trucks, H. B. Schlegel, G. E. Scuseria, M. A. Robb, J. R. Cheeseman, G. Scalmani, V. Barone, B. Mennucci, G. A. Petersson, H. Nakatsuji, M. Caricato, X. Li, H. P. Hratchian, A. F. Izmaylov, J. Bloino, G. Zheng, J. L. Sonnenberg, M. Hada, M. Ehara, K. Toyota, R. Fukuda, J. Hasegawa, M. Ishida, T. Nakajima, Y. Honda, O. Kitao, H. Nakai, T. Vreven, J. A. Montgomery, Jr., J. E. Peralta, F. Ogliaro, M. Bearpark, J. J. Heyd, E. Brothers, K. N. Kudin, V. N.

Staroverov, R. Kobayashi, J. Normand, K. Raghavachari, A. Rendell, J. C. Burant, S. S. Iyengar, J. Tomasi, M. Cossi, N. Rega, J. M. Millam, M. Klene, J. E. Knox, J. B. Cross, V. Bakken, C. Adamo, J. Jaramillo, R. Gomperts, R. E. Stratmann, O. Yazyev, A. J. Austin, R. Cammi, C. Pomelli, J. W. Ochterski, R. L. Martin, K. Morokuma, V. G. Zakrzewski, G. A. Voth, P. Salvador, J. J. Dannenberg, S. Dapprich, A. D. Daniels, Ö. Farkas, J. B. Foresman, J. V. Ortiz, J. Cioslowski, D. J. Fox, Gaussian, Inc., Wallingford CT, 2009.

Chapter 4

Catalytic oxidative cracking of benzene rings in water

4-1 Introduction

Benzene has been widely used not only as solvents for organic synthesis but also as starting materials for industrial production of aromatic compounds. Vapor concentration of benzene, however, is strictly restricted due to its high carcinogenicity and noxiousness.^{1,2} Once discharged to the environment, benzene and the derivatives are difficult to be decomposed due to their high stability derived from its resonance stabilization and strong C-H and C-C bonds; therefore, cracking reactions of benzene rings require large thermal energy³⁻⁵ or strictly limited conditions.^{6,7} For example, catalytic cracking reactions of benzene derivatives into C1 compounds using Pd catalysts,³ Fe oxide⁴ or microbes^{6,7} have been reported; however, the products are CH₄ or CO₂, which are too stable to be used as starting materials for syntheses of useful chemicals and even known to exert strong greenhouse effects.⁸ Thus, the utility of the reactions reported so far is quite limited. It has been also demonstrated that the activation of benzene rings can be achieved at ambient temperature with reactive organic molecules^{9,10} or transition-metal complexes (Figure 4-1).^{11,12}

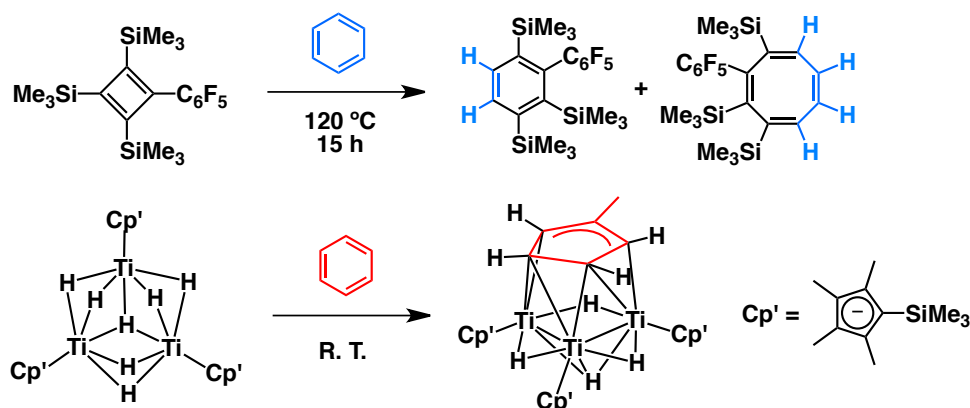


Figure 4-1. Examples of an organic molecule (top)⁹ and a transition-metal complex (bottom)¹¹ that can activate benzene rings stoichiometrically at ambient temperature.

These reactions, however, are limited to stoichiometric reactions and not applicable to catalytic reactions. Under the situation referred above, the development of efficient catalysts, capable of cracking benzene rings into useful C1 compounds at ambient temperature, should be strongly required for solving environmental issues derived from benzene derivatives and also for gaining industrial benefits. Catalytic oxidative cracking reactions of monosubstituted benzene derivatives at ambient temperature have been reported with use of ruthenium(VIII) tetraoxide (Ru^{VIII}O₄) as a reactive oxidant,¹³⁻¹⁵ formed *in situ* from a reaction between ruthenium(III) trichloride and sodium periodate (NaIO₄), in water/organic solvents biphasic

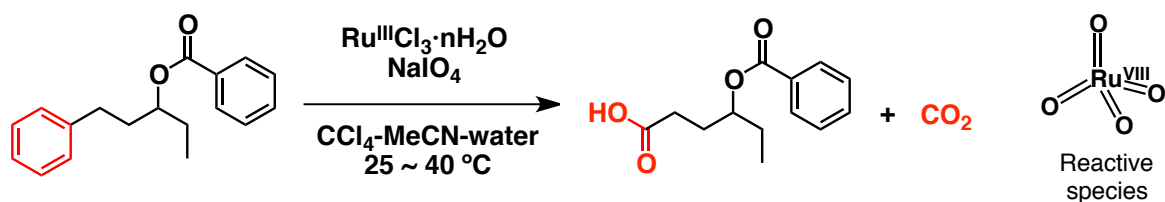


Figure 4-2. Catalytic oxidative cracking reactions of monosubstituted benzene derivatives by Ru^{VIII}O₄ as a reactive oxidant.^{13,14}

media (Figure 4-2).^{13, 14}

In the reported oxidative benzene cracking (OBC) reactions of mono-substituted benzene derivatives, the products have been the corresponding carboxylic acids having the substituents on the benzene rings of the substrates and the other five carbons were oxidized to CO₂.¹³ Therefore, only one carbon among six of the benzene ring was available to produce a useful compound. A strategy to develop more useful OBC reactions can be attained on the basis of the fact that metal-bound oxygen-centered radical (metal-oxyl) species can react with benzene derivatives through addition of the oxyl radical to a double bond of the benzene derivative to afford phenol derivatives in high selectivity.^{16, 17}

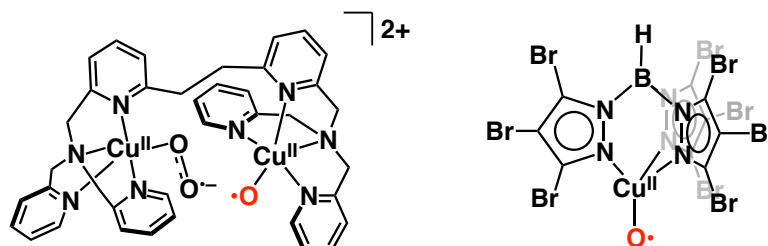


Figure 4-3. Copper-bound oxygen-centered radical species that react with benzene derivatives.^{16, 17}

As described in Chapter 3, the author has achieved the formation and characterization of a ruthenium(III)-oxyl (Ru^{III}-O•) complex bearing a single bond character between the Ru and O atoms and the application to catalytic oxidation of organic substrates in water.¹⁸ The Ru^{III}-O• complex as the active species in the catalytic oxidation can be formed through proton-coupled electron transfer (PCET) oxidation of a ruthenium(II)-aqua complex, bearing a tridentate NHC ligand, [Ru^{II}(BPIIm)(bpy)(OH₂)]²⁺ (**6**) (Chapter 3 in this thesis), using (NH₄)₂[Ce^{IV}(NO₃)₆] (CAN) as a sacrificial oxidant in acidic water.¹⁸ Inspired by the oxidation reactions of benzene derivatives with the metal-oxyl species mentioned above,^{16, 17} the Ru^{III}-O• species has been applied to OBC reactions in aqueous media. In this Chapter, the author describes catalytic conversion of benzene and the derivatives into carboxylic acids such as formic acid, which can serve as a hydrogen reservoir,¹⁹ by using the Ru^{III}-O• complex as an active species and dihydrogen evolution from the reaction solution with use of a rhodium(III) catalyst.²⁰ The kinetic studies revealed that the OBC reaction in this work proceeds through an electrophilic addition of Ru^{III}-O• species on a benzene ring in the substrate followed by benzene-ring cleavage reaction to afford formic acid and carbon dioxide.

4-2 Catalytic oxidative cracking of benzene rings (OBC) in acidic water

An OBC reaction was performed at 283 K under Ar in D₂O (pD 1.2, 1 mL) using CAN (75 mM) as a sacrificial oxidant and **6**·(ClO₄)₂ (0.14 mM) as a catalyst, which was prepared according to the literature procedure.¹⁸ A substrate (1 mL) was added to the D₂O solution of **6**, followed by addition of CAN and the biphasic reaction mixture was stirred vigorously.²¹ The color of the mixture turned from yellow to pale red-brown in the course of the reaction time (24 h). The aqueous phase of the reaction mixture was analyzed spectroscopically to identify the products (Figure 4-4). In the ¹H NMR spectrum of the reaction mixture, a signal assigned to ¹HCOOH was observed at δ 8.29 ppm (Figure 4-4(a)) and a ¹³C NMR signal for H¹³COOH was observed at δ 168 ppm in the ¹H-decoupled ¹³C NMR spectrum (Figure 4-4(b)). The two-dimensional heteronuclear single-quantum coherence (HSQC) spectrum of the reaction mixture exhibited a correlation cross peak between the ¹H NMR signal at δ 8.29 ppm and the ¹³C NMR signal at δ 168 ppm (Figure 4-4(c)).

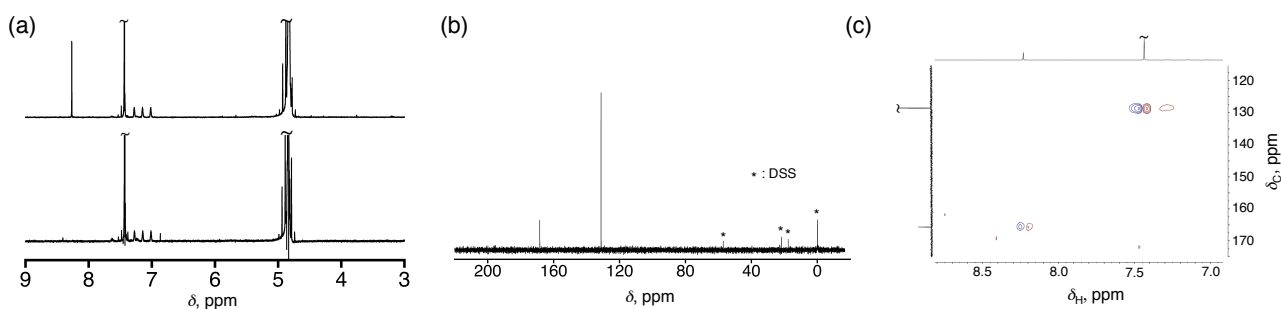


Figure 4-4. (a) ^1H NMR spectra of the aqueous phase of the reaction mixture after it had been stirred for 24 h in the presence (top; 0.14 mM) and absence (bottom) of catalyst **6**. The reactions were performed at 283 K in D_2O ; the pH was set at pD 1.2, and the mixture included CAN (75 mM).²¹ (b) ^{13}C NMR spectrum of the aqueous phase of the reaction mixture described above in the presence of **6** after the mixture had been stirred for 24 h. (c) HSQC spectrum of the aqueous phase of the reaction mixture in the presence of **6** after the mixture had been stirred for 24 h. ^1H NMR, ^{13}C NMR, and HSQC spectra were measured at 298 K.

Thus, the main product of the OBC reaction of benzene, observed in the NMR spectra, was assigned to formic acid. The concentration of formic acid in the aqueous phase of the reaction mixture was determined by ^1H NMR spectroscopy with use of DSS (= sodium 4,4-dimethyl-4-silapentane-sulfonate) as an internal standard, and the turnover number (TON) of the catalysis was determined to be 55 ± 5 . This catalytic OBC reaction proceeded without any induction period as seen in the time profile of TON for the formic acid production measured at 283 K (Figure 4-5). This suggests that the active species in the OBC reaction is not decomposed products of the catalyst. In addition, the author examined a catalytic OBC reaction with the black precipitate, adhered on a stirrer chip after the OBC reaction, under the same conditions. As the result, formic acid was observed in the aqueous phase with very lower efficiency (4%) than that of **6** used as a

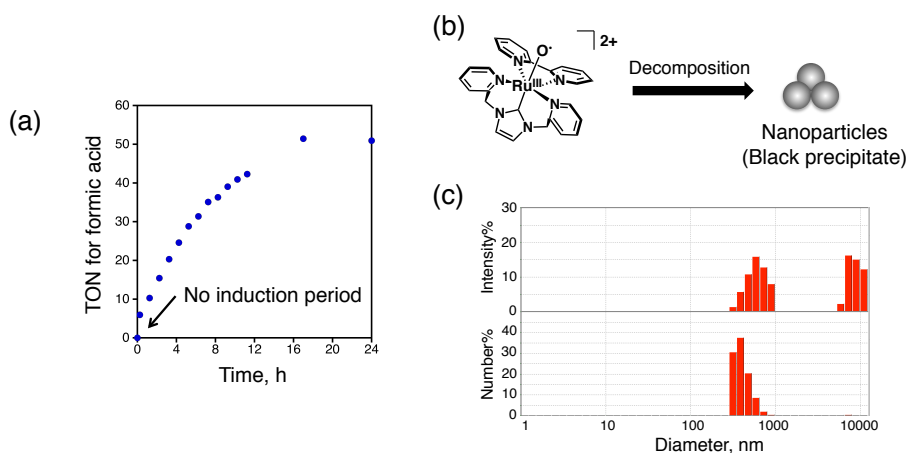


Figure 4-5. (a) A time-profile of the turnover number (TON) for the formic acid production in the catalytic OBC reaction by **6** performed at 283 K. $\text{TON} = [\text{formic acid}]/[\mathbf{6}]$. (b) A schematic representation for decomposition of the Ru(III)-oxyl complex under the reaction conditions. (c) Size distributions of nanoparticles based on the intensity% (top) and number% (bottom) observed in the DLS measurements for the aqueous phase of the catalytic OBC reaction. Irradiation wavelength for the DLS measurement: 532 nm, Temp.: 298 K, Solvent: D_2O (pD 1.2). Nanoparticles having diameters of $(3.8 \pm 0.9) \times 10^2$ nm were observed. The OBC reaction was performed in the mixture of benzene (1 mL) and D_2O (4 mL, pD 1.2), including **6** (0.14 mM) and CAN (75 mM).

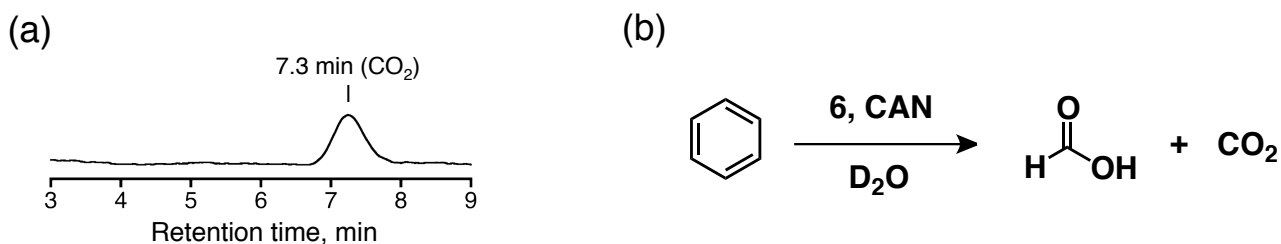


Figure 4-6. (a) GC chart of the gaseous phase in the experimental setup. (b) Schematic representation of the OBC reaction of benzene as a substrate.

catalyst (30%).

In the gas chromatogram of the gaseous phase of the reaction mixture, a peak derived from CO₂ was observed at 7.3 min of the retention time (Figure 4-6(a)). Therefore, the overall reaction of catalytic OBC reaction can be described as shown in Figure 4-6(b). The amount of CO₂ formed was determined by GC and the TON based on the amount of the catalyst was calculated to be 17 ± 6 . Carbon monoxide and formaldehyde were not observed both in the gaseous or liquid phase (Figure 4-7).

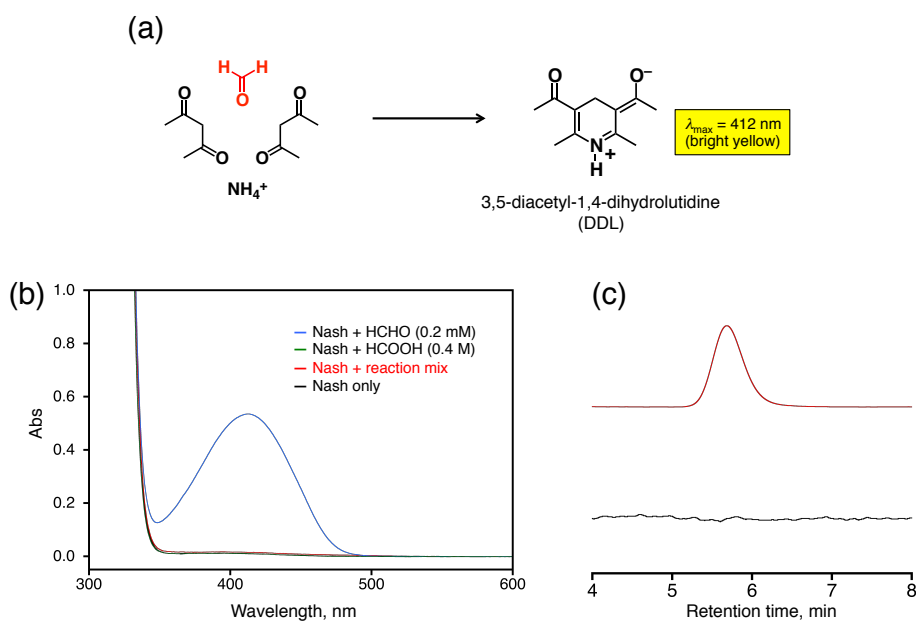


Figure 4-7. (a) Schematic representation for the reaction of formaldehyde with the Nash reagent to form yellow-colored DDL.²² The Nash reagent was prepared by mixing NH₄OAc (15 g), acetic acid (300 μL), acetylacetone (200 μL) in distilled water (100 mL). (b) UV-Vis spectra of the Nash reagent (200 μL; black) and mixtures of the Nash reagent (200 μL) and an aqueous solution of formaldehyde (0.2 mM; blue), formic acid (0.4 M; green), or the reaction mixture obtained from the OBC reaction of benzene with **6** (0.14 mM) as the catalyst and CAN (75 mM) (red). (c) A GC chart of authentic carbon monoxide (red) and gaseous phase in the experimental setup (black).

Other sacrificial oxidants were also used for these catalytic OBC reactions. Comparing the TON values and efficiencies, Ce^{IV} salts (CAN and Ce^{IV}(SO₄)₂) were relatively efficient for catalytic OBC reactions than other oxidants such as Oxone; in particular, CAN gave the best results (Table 4-1). Despite the fact that

the other oxidants, Oxone, and NaIO₄, have higher reduction potentials, formic acid and CO₂ were obtained in very low yields upon using the oxidants.

Table 4-1. Effects of water-soluble oxidants on the TON of the OBC reaction using benzene as a substrate^a

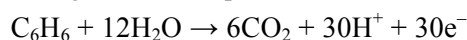
Entry	Oxidant	TON(HCOOH)	Efficiency(HCOOH)	TON(CO ₂)	Efficiency(CO ₂)
1	CAN (75 mM)	53	30	17	16
2	Ce ^{IV} (SO ₄) ₂ ·4H ₂ O (75 mM) ^b	26	15	20	19
3	Oxone [®] triple salt (75 mM)	1.1	<1	N. D.	N. D.
4	Na ₂ S ₂ O ₈ (38 mM) ^c	2	1	N. D.	N. D.
5	NaIO ₄ (38 mM) ^d	N. D.	N. D.	5	5

Reduction potentials of the sacrificial oxidants in the table have been summarized in literature^{23, 24}: $E_{\text{red}} = +1.37$ V (vs SCE) for CAN,²³ $+1.20$ V for Ce^{IV}(SO₄)₂·4H₂O,²³ $+1.58$ V for Oxone[®] (K₂SO₄·KHSO₄·2KHSO₅),²³ $+0.4$ V for Na₂S₂O₈,²⁴ and $+1.36$ V for NaIO₄.²³ ^a Reaction conditions are as follows: [6] = 0.14 mM, $T = 283$ K. Reaction time: 24 h. Benzene (1 mL) was used as the substrate. ^b H₂SO₄ in D₂O (pD 1.0) was used as a solvent for increasing solubility of the cerium salt. ^c pD 1.4. Phenol was observed as the main product with the TON value of 16 and efficiency of 6. ^d pD of the reaction mixture was not adjusted.

To produce formic acid from benzene, the theoretical equivalent number of the oxidant is calculated to be three molecules of the oxidant against one molecule of HCOOH based on the following chemical equation:



On the other hand, to produce CO₂ from benzene, 5e⁻ removal from a benzene carbon per one molecule of CO₂ is required in light of the following chemical equation:



Therefore, the efficiencies (*Eff*) of these oxidation processes can be calculated using the following equations:

$$\text{Eff for formic acid} = 100 \left[\frac{([\text{HCOOH}] \times 3)}{[\text{Ce}^{\text{IV}}]} \right]$$

$$\text{Eff for CO}_2 = 100 \left[\frac{([\text{CO}_2] \times 5)}{[\text{Ce}^{\text{IV}}]} \right]$$

Thus, the efficiencies were determined to be (32 ± 2)% for formic acid and (16 ± 5)% for CO₂. CO₂ can be also produced by overoxidation of formic acid obtained. The stoichiometry of the OBC reaction was discussed in detail in the part of mechanistic investigation (see below).

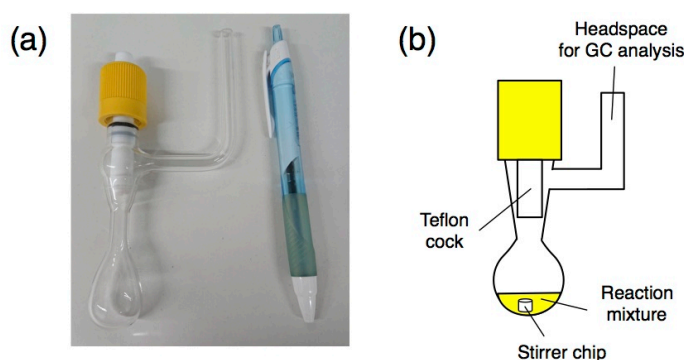


Figure 4-8. A photo (a) and the simplified cartoon (b) of the reaction equipment. This equipment was manufactured from an angled glass tube (purchased from Furukawa Riko Co.), equipped with a grease-less J. Young stopcock to endure high vacuum conditions. The apparatus shown in (a) was provided by the manufacturing branch of University of Tsukuba. The reaction conditions are shown below: [6] = 0.14 mM, [CAN] = 75 mM, $T = 283$ K. Time: 24 h.

The author has also conducted the OBC reaction of benzene in a benzene-saturated aqueous solution (~20 mM), not under biphasic conditions. As a result, formic acid and CO₂ were obtained with TON values of 50 and 9, respectively; however, the accurate conversion of benzene could not be determined due to the high volatility of benzene. The details of the reaction setup for this experiment are shown in Figure 4-8. In addition, to improve the TON, the OBC reaction of benzene was performed with lower concentration of the catalyst **6** (0.1 μM) at a higher temperature (303 K) for a longer reaction time (48 h); as a result, the TON value for formic acid reached ~15300.

To confirm the origin of formic acid, deuterium-labeled benzene-*d*₆ was used as a substrate for the catalytic OBC reaction in H₂O (pH 0.8). In the ²H NMR spectrum of the reaction mixture, a ²H NMR signal assigned to DCOOH was observed at δ 8.2 ppm (Figure 4-9). Thus, the observed formic acid was definitely derived from benzene as the substrate in the OBC reaction.

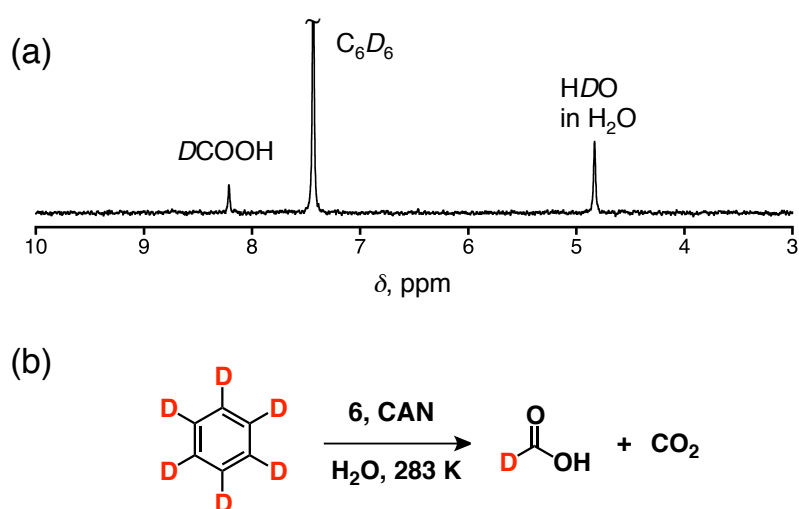


Figure 4-9. (a) ²H NMR spectra of the reaction mixture for the OBC reaction of benzene-*d*₆ in the presence of CAN (75 mM) and **6** (0.14 mM) at pH 0.8. (b) Schematic representation of the catalytic OBC reactions of benzene-*d*₆ in H₂O.

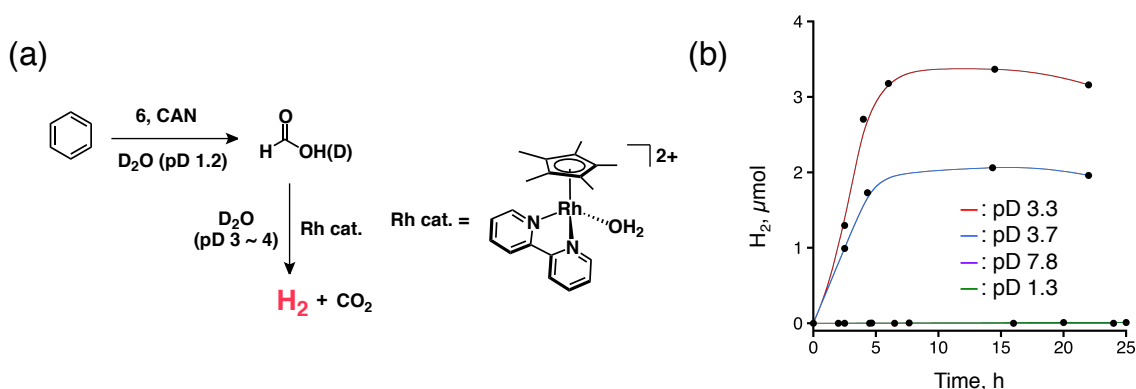


Figure 4-10. (a) Schematic representation of the catalytic decomposition of formic acid to evolve dihydrogen after the catalytic OBC reaction. (b) Time profiles of dihydrogen evolution from the reaction mixture of the OBC reaction, whose pD was adjusted by adding aqueous NaOH as shown in the figure after the OBC reaction, at room temperature in the presence of a rhodium catalyst (3.1 mM).

The OBC reaction presented here is the first example affording formic acid as a product from benzene, in sharp contrast to other benzene oxidation reactions,^{13, 14} which do not afford formic acid but CO₂ as a product as mentioned above. Furthermore, formic acid formed in the OBC reaction was efficiently converted to dihydrogen as a mixture of H₂, HD, and D₂ upon addition of a Rh^{III} catalyst, [Rh^{III}(Cp*)(bpy)(H₂O)]²⁺ (Cp* = pentamethylcyclopentadienyl),²⁵ to the reaction solution of OBC by adjusting the pH to 3.3 with addition of an aqueous NaOH solution (Figure 4-10). Thus, it should be emphasized that catalytic conversion of harmful benzene into useful formic acid as a H₂ source^{19, 20, 25} has been accomplished efficiently at ambient temperature in this study.

Table 4-2. Effects of reaction atmosphere on the OBC reaction of benzene^a

Atmosphere	TON(HCOOH)	Efficiency(HCOOH)	TON(CO ₂)	Efficiency(CO ₂)
under Ar	53	30	17	16
under air	55	31	12	13
under O ₂	57	33	20	19

^a Reactions were performed under the same conditions²¹ except the atmosphere.

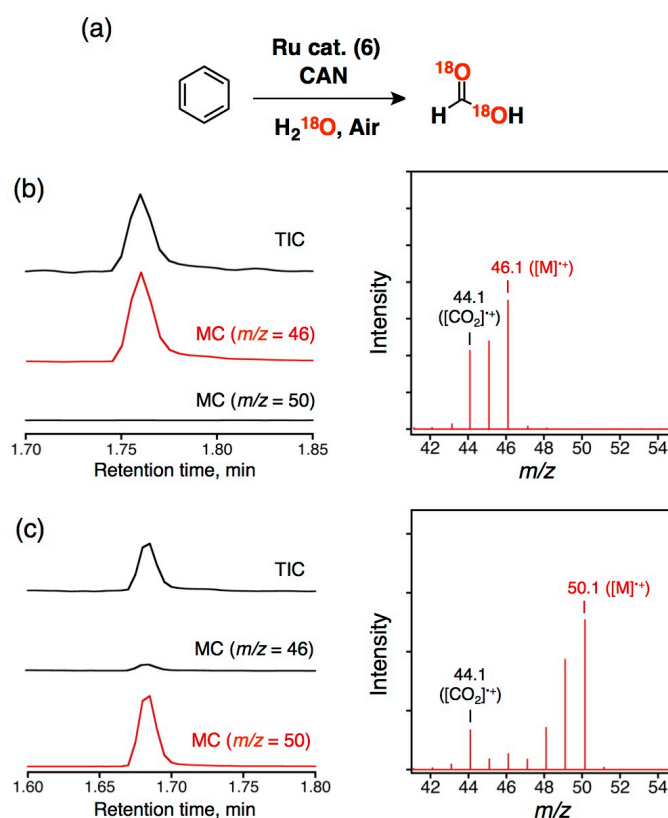


Figure 4-11. (a) Schematic representation for the catalytic OBC reaction of benzene in H₂¹⁸O. (b) Total-ion chromatogram (TIC) chart, and mass chromatogram (MC) charts at $m/z = 46$ and 50 (left) of the reaction mixture in H₂¹⁶O and EI-MS spectrum (right) of the fraction eluted at the retention time of 1.76 min. (c) TIC chart and MC charts at $m/z = 46$ and 50 (left) of the reaction mixture in H₂¹⁸O and EI-MS spectrum (right) of the fraction eluted at the retention time of 1.68 min. Reaction conditions are as follows: [6] = 0.14 mM, [CAN] = 75 mM, $T = 283$ K. The reactions were conducted under air for 24 h. Parameters on GC-MS measurements are as follows: split mode (split ratio: 1/50); $T(\text{interface}) = 240$ °C, $T(\text{detector}) = 200$ °C. The temperature program was set as follows: 40 °C (2 min) – 20 °C/min – 200 °C (5 min). SH-Rxi-5ms capillary column (30 meter) was employed and He was used as the carrier gas.

To assess the influence of dioxygen on the reaction, catalytic OBC reactions were performed under air, Ar, and O₂. The results indicate that the atmosphere does not affect the TON values of formic acid production (Table 4-2), demonstrating that the OBC reaction catalyzed by **6** proceeds without the influence of dioxygen, which can participate in radical chain reactions. In addition, to confirm the origin of the oxygen atoms of formic acid obtained from the OBC reaction under air, ¹⁸O-labeled water (H₂¹⁸O) was used as a solvent. A peak was observed at *m/z* = 50 for HC¹⁸O¹⁸OH, not at *m/z* = 46 for HC¹⁶O¹⁶OH, in the GC-MS spectra (Figure 4-11). These results indicate that the origin of the oxygen atoms in formic acid obtained should be water as a solvent and the OBC reaction does not involve any free radical species that can react with dioxygen as intermediates. Other ruthenium(II)-aqua complexes and metal salts were also employed as catalysts for the OBC reactions in place of **6**; however, they could not catalyze the OBC reactions so efficiently under the same conditions in comparison with **6** (Tables 4-3 and 4-4). These results indicate that the strong radical character of the Ru^{III}-O• species formed from **6** as a catalyst (see Chapter 3)¹⁸ should be responsible for the OBC reactions.

Table 4-3. Comparison of the catalytic reactivity in the OBC reaction of benzene among ruthenium complexes as catalysts^a

Catalyst	TON(HCOOH)	Efficiency(HCOOH) ^b
6 ·2ClO ₄	55	32
[Ru ^{II} (PY5Me ₂)(OH ₂)](PF ₆) ₂ ²⁶	3	2
[Ru ^{II} (N4Py)(OH ₂)](PF ₆) ₂ ²⁷	18	10
Ru ^{III} Cl ₃ ·nH ₂ O ^c	5	3
Ru ^{IV} O ₂ (1 mg dispersed)	–	4
none	–	<1

^a [catalyst] = 0.14 mM, [CAN] = 75 mM, *T* = 283 K. Time: 24 h. ^b [efficiency] = 100[(HCOOH) × 3 / [CAN]]. ^c The TON value was calculated assuming the number of hydrated water molecules as 3 (*n* = 3).

Table 4-4. Catalytic OBC reactions of benzene catalyzed by various metal salts in D₂O^a

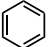
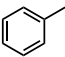
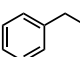
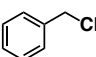
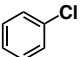
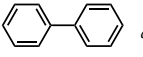
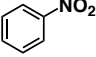
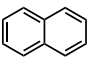
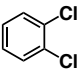
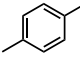
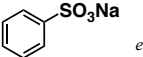
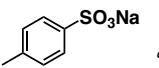
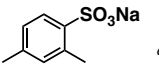
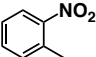
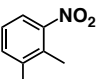
Catalyst	TON(HCOOH)	Efficiency(HCOOH)
Mn ^{II} Cl ₂ ·6H ₂ O	9	5
Fe ^{II} Cl ₂ ·4H ₂ O	3	2
Co ^{II} Cl ₂	4	2
Ni ^{II} Cl ₂ ·6H ₂ O	2	1
Cu ^{II} Cl ₂ ·2H ₂ O	4	2
Ru ^{III} Cl ₃ ·nH ₂ O ^b	5	3
Rh ^{III} Cl ₂ ·nH ₂ O ^b	3	1
Pd ^{II} Cl ₂	4	2
Cr ^{III} (ClO ₄) ₃ ·6H ₂ O ^c	2	1

^a [catalyst] = 0.14 mM, [CAN] = 75 mM, solvent: D₂O (pD 1.2), *T* = 283 K. Time: 24 h. Benzene (1 mL) was used as a substrate. ^b The TON values were calculated assuming the number of hydrated water molecules as 3. ^c Since Cr^{III}Cl₃ was not soluble in water, the perchlorate salt was employed instead.

4-3 Scope and limitation of the catalytic OBC reactions

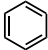
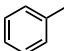
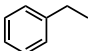
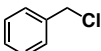
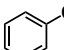
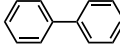
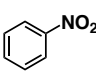
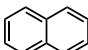
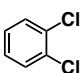
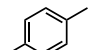
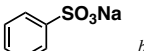
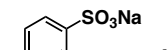
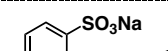
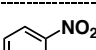
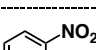
The OBC reaction catalyzed by **6** was also applied to other aromatic compounds as listed in Table 4-5. The OBC reaction can be applied not only to benzene derivatives that have electron-donating groups such as

Table 4-5. Catalytic OBC reactions of various benzene derivatives with **6** as the catalyst and CAN as the sacrificial oxidant in D₂O at 283 K.

Entry	Substrate	Product	TON	Efficiency ^b
1		Formic acid	53	30
2		Formic acid	39	22
		Acetic acid	20	11
3		Formic acid	28	16
		Propionic acid	13	7
		Acetic acid	5	7
		Phenylethanol	1	<1
		Acetophenone	3	2
4		Formic acid	14	8
		Chloroacetic acid	2	1
		Benzaldehyde	1	1
		Benzoic acid	6	7
5		Formic acid	8	4
6		Formic acid	38	21
		Benzoic acid	14	8
7		Formic acid	4	2
8		Formic acid	9	5
		Naphthoquinone	14	11
		Naphthoquinonediol	10	12
		Phthalic acid	17	38
9		Formic acid	6	3
10		Formic acid	20	11
		Acetic acid	27	14
11		Formic acid	3	2
12		Formic acid	8	5
		Acetic acid	6	3
13		Formic acid	16	9
		Acetic acid	38	21
14		Formic acid	7	4
		Acetic acid	5	3
15		Formic acid	27	15
		Acetic acid	54	30

^a The results of the control experiments in the absence of catalyst **6** are shown in the Table 4-6. As for the detailed reaction conditions, see ref. 21. ^b The values were based on the NMR yield determined with DSS as the internal standard. ^c Acetic acid was probably formed by C-C bond cleavage of pyruvic acid derived from cracking of acetophenone obtained by the C-H oxidation of ethylbenzene. ^d 10 mg of biphenyl was added. ^e [substrate] = 13 mM.

Table 4-6. Catalytic OBC reactions in the absence of catalyst **6**.

Entry	Substrate	Product	Efficiency ^a
1		Formic acid	<1
2		Formic acid Acetic acid	<1 <1
3		Formic acid Propionic acid Phenylethanol Acetophenone	1 <1 3 4
4		Formic acid Chloroacetic acid Benzoic acid	<1 <1 3
5		Formic acid	1
6		Formic acid Biphenoquinone	<1 4
7		Formic acid	1
8		Formic acid Naphthoquinone Phthalic acid	<1 15 <1
9		Formic acid	<1
10		Formic acid Acetic acid	3 4
11	 ^b	Formic acid	<1
12	 ^c	Formic acid Acetic acid	<1 <1
13	 ^d	Formic acid Acetic acid	2 <1
14		Formic acid Acetic acid	2 <1
15		Formic acid Acetic acid	2 4

^a Efficiency (%) = 100[$\{([Product] \times n) / [CAN]\}$]. n: the number of electrons (n = 2 for phenylethanol, n = 3 for formic, acetic, propionic and monochloroacetic acids, n = 4 for benzoic acid, n = 6 for biphenoquinone and naphthoquinone, n = 8 for phthalic acid). ^b [substrate] = 17.7 mM. ^c [substrate] = 5.3 mM. ^d [substrate] = 13.0 mM, T = 283 K, [CAN] = 75 mM. Time: 24 h.

ethylbenzene and xylene, but also to those that have electron-withdrawing groups such as chloro- and nitrobenzenes. In addition, polyaromatic substrates such as naphthalene were also oxidized under the same conditions to afford formic acid as a product. When toluene was employed as a substrate under the same

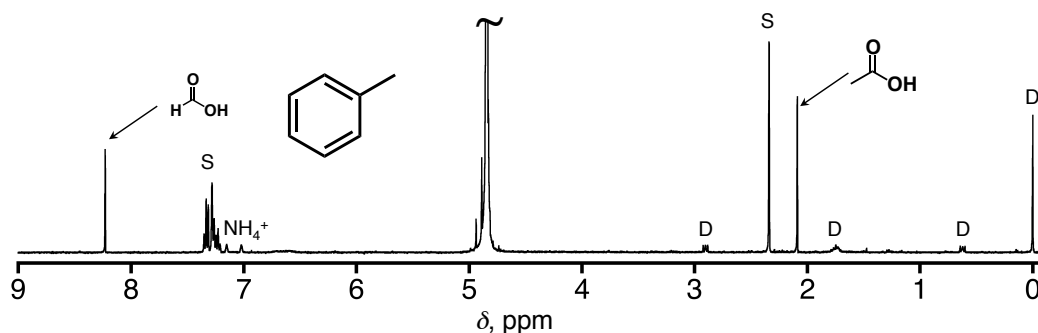


Figure 4-12. ^1H NMR spectrum of the reaction mixture for the OBC reaction of toluene in the presence of CAN (75 mM) and **6** (0.14 mM) at pD 1.2.

conditions as mentioned above, the ^1H NMR spectrum of the aqueous phase of the reaction mixture showed a signal assigned to acetic acid as a product at δ 2.09 ppm as well as that of formic acid (Figure 4-12). In the reaction of toluene- d_8 as a substrate in distilled water, the signals assigned to DCOOH and CD_3COOH were observed at δ 8.2 and 1.9 ppm, respectively, in the ^2H NMR spectrum (Figure 4-13). Thus, the origin of the formic and acetic acids was explicitly confirmed to be toluene as the substrate. In contrast, oxidation reactions of toluene and the derivatives by ruthenium(IV)-oxo complexes generally afford benzyl alcohol, benzaldehyde, and benzoic acid as products of the C-H oxidation reactions at the methyl group.^{28, 29} This exemplifies the uniqueness of the OBC reaction by the $\text{Ru}^{\text{III}}\text{-O}\cdot$ complex, in which oxidation of the aromatic ring primarily proceeds rather than the C-H oxidation at the benzylic position of toluene. The reactivity of the $\text{Ru}^{\text{III}}\text{-O}\cdot$ complex was also found in the case of ethylbenzene as a substrate; formic and propionic acids were observed as the main products in the ^1H NMR spectrum (Figure 4-14(a)) and high-performance liquid chromatography (HPLC) analysis (Figure 4-14(b)). In the case of benzyl chloride as a substrate, formic and chloroacetic acids were obtained as products (Figure 4-15(a)). Biphenyl employed as a substrate was oxidized to give formic and benzoic acids in this OBC system (Figure 4-15(b)).

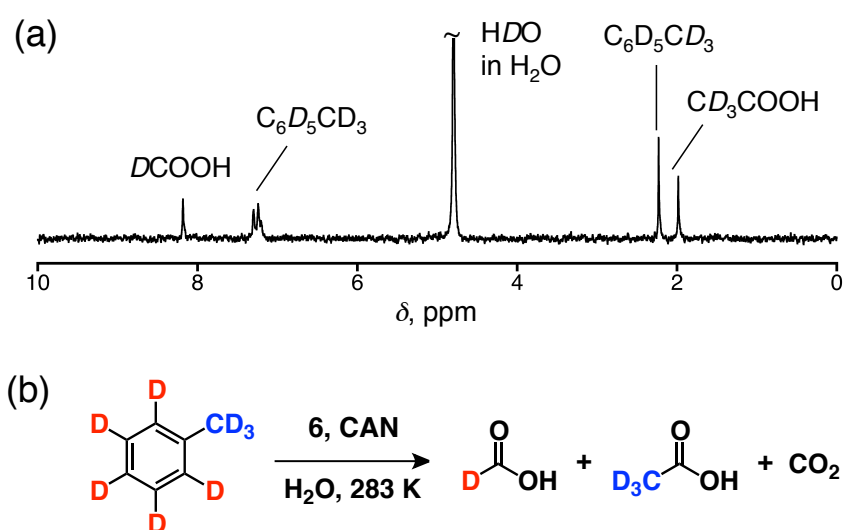


Figure 4-13. (a) ^2H NMR spectra of the reaction mixture for the OBC reaction of toluene- d_8 in the presence of CAN (75 mM) and **6** (0.14 mM) at pH 0.8. (b) Schematic representation of the catalytic OBC reactions of toluene- d_8 in H_2O .

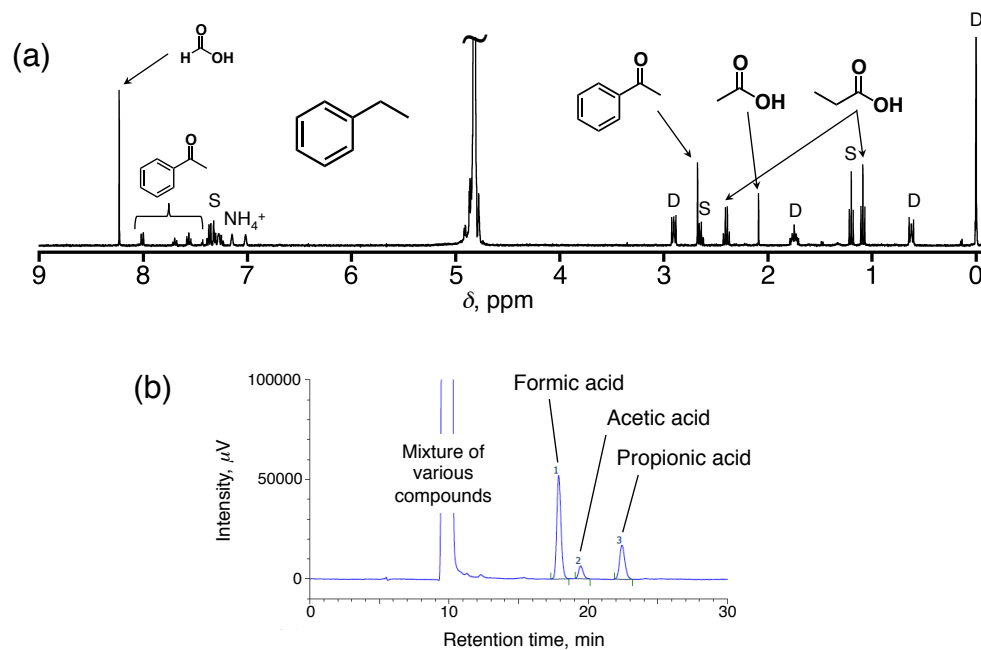


Figure 4-14. (a) ^1H NMR spectrum of the reaction mixture of the OBC reaction of ethylbenzene as a substrate in D_2O . D: DSS, S: Substrate. (b) An HPLC chromatogram obtained for the aqueous phase of the OBC reaction of ethylbenzene catalyzed by **6**. The injected sample was prepared by treatment of the reaction mixture with 0.2 mM bromothymol blue solution in 15 mM Na_2HPO_4 aq. Column: Shodex Rspak KC-G, KC-811. Eluent: 3 mM HClO_4 aq. Column temp.: 60 $^\circ\text{C}$. Monitoring wavelength: 445 nm. Injected amount of the sample: 50 μL .

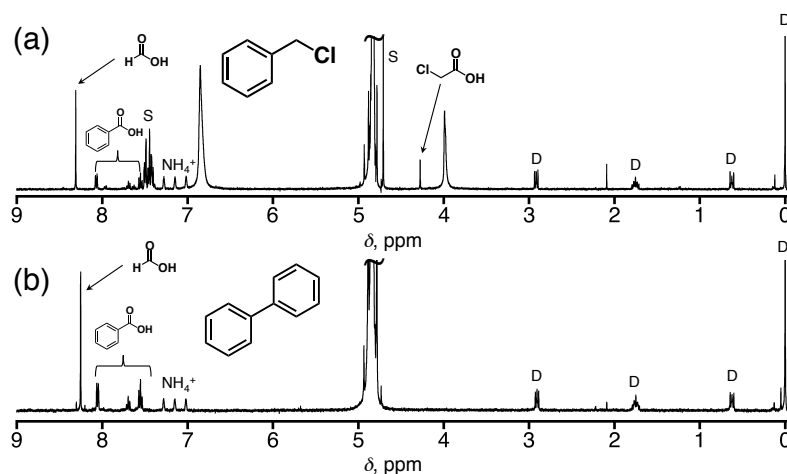


Figure 4-15. ^1H NMR spectra of reaction mixtures of the OBC reactions for benzyl chloride (a) and biphenyl (10 mg added, b). $[\mathbf{6}] = 0.14$ mM, $[\text{CAN}] = 75$ mM, $T = 283$ K. Time: 24 h. D: DSS, S: Substrate.

4-4 Mechanistic insights into the catalytic OBC reactions

As mentioned in Chapter 3, the author has revealed that an acetophenone derivative was obtained in a 33% yield (TON: 75) from the oxidation reaction of sodium *p*-ethylbenzenesulfonate as a substrate catalyzed by complex **6** (Figure 4-16(a)).¹⁸ The sharp contrast to the result using ethylbenzene as the substrate (see above) indicates that the C-H oxidation at the benzylic position proceeds primarily for the aromatic substrate having an electron-withdrawing group such as the sulfonate ($-\text{SO}_3^-$) group on the aromatic ring rather than

the cracking of the benzene ring. The OBC reactions of other substrates having electron-withdrawing groups also resulted in low yields of formic acid as the product of the OBC reactions (Table 4-5; entries 5, 7, 9, 11~15). Therefore, the OBC reaction is expected to proceed through an electrophilic attack on an aromatic ring, and thus, the electron-withdrawing substituents lower the reaction efficiencies in the aromatic ring oxidation. Further scrutiny was applied to the electronic effects of the substituents on the aromatic ring oxidation. The one-electron oxidation potentials of benzene (+2.48 V vs SCE)³⁰ and chlorobenzene (+2.46 V)³⁰ are comparable. The TON values, however, based on the amount of formic acid obtained were largely different between these substrates; the TON value for the oxidation of chlorobenzene having the electron-withdrawing chloro substituent was apparently lower than that of benzene. The result indicates that the OBC reaction does not proceed through electron transfer from a substrate to the Ru^{III}-O• complex, whereas Fujii and co-workers proposed an electron-transfer mechanism for an oxidation reaction of benzene with an iron(IV)-oxo complex having a porphyrin π -radical cation ligand.³¹

Furthermore, the total efficiencies of the OBC reactions are dependent on the Hammett parameters (σ) of the substituents of the substrates (Figure 4-16). The σ_p values for the electron-donating substituents were employed as the Hammett parameters,³² whereas the σ_m values for the electron-withdrawing substituents were applied, because the OBC reactions were considered to proceed through the electrophilic mechanism as mentioned above. The total efficiencies were calculated by summations of yields of products, HCOOH, XCOOH (X = CH₃, C₆H₅, or CF₃), and CO₂ (Figure 4-16);³³ the values were divided by 3 in the case of substituents having an electron-donating substituent, and those were divided by 2 in the case of substituents having an electron-withdrawing substituent for normalization (see right panel of Figure 4-16(b)). Logarithm

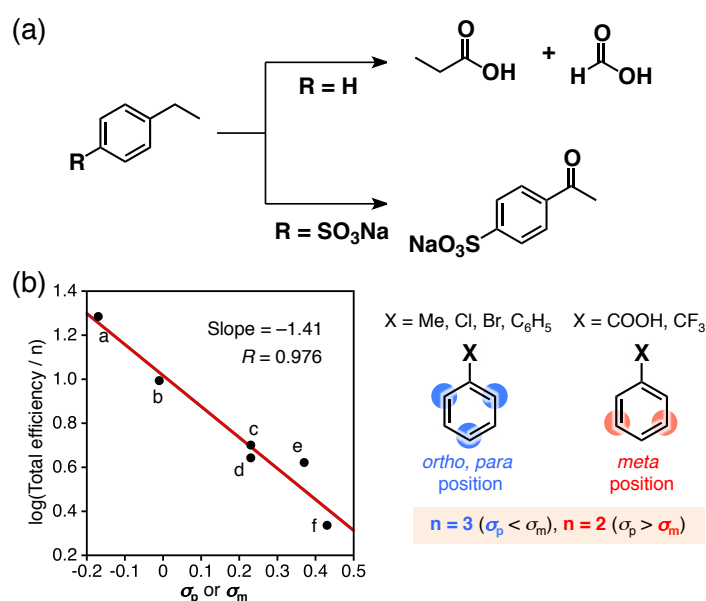


Figure 4-16. Reaction of ethylbenzene derivatives under the OBC conditions (a) and a Hammett plot of the efficiencies for the OBC reactions of benzene derivatives, C₆H₅X (b). In the Hammett plot, substituents of the substrates used are as follows: X = CH₃ (a, $\sigma_p = -0.17$), C₆H₅ (b, $\sigma_p = -0.01$, normalized by division of total efficiency by $n = 6$), Cl (c, $\sigma_p = +0.23$), Br (d, $\sigma_p = +0.23$), COOH (e, $\sigma_m = +0.37$), CF₃ (f, $\sigma_m = +0.43$). Conditions: [6] = 0.14 mM, [CAN] = 75 mM, [Substrate] = 1 mM (the concentration of substrates is not accurate due to their insolubility in water and thus cannot be controlled.), $T = 283$ K, reaction time = 24 h. Hammett parameters were obtained from ref. 32.

values of the normalized total efficiencies were plotted against the Hammett parameters (Figure 4-16(b)). A linear correlation was observed with a slope of -1.41 , confirming that the OBC reactions proceed through electrophilic attack of the $\text{Ru}^{\text{III}}\text{-O}\cdot$ complex as the active species¹⁸ to the aromatic rings. Negative ρ values have been also observed for benzene hydroxylation by high-valent iron-oxo complexes.³⁴⁻³⁶

In the case of benzene or other benzene derivatives, having relatively low boiling points, used as substrates, the stoichiometry of the OBC reaction was difficult to determine due to the volatility and adsorption by rubber septums. The kinetics of the OBC reactions was also difficult to investigate due to the low solubility of the substrates in water. Thus, substituents such as the sulfonate group was introduced to the benzene ring to increase the boiling points and improve the solubility of the substrate in water; however, the reactivity of those substrates in the OBC reaction was decreased due to the electron-withdrawing nature of the substituent. Therefore, sodium *m*-xylene sulfonate (*m*XS) was employed as a nonvolatile substrate to calculate the conversion yields (Figure 4-17); the two electron-donating methyl groups of *m*XS are expected to suppress the negative effect of the electron-withdrawing sulfonate group on the reactivity. The conversion of *m*XS was determined to be 84%,³⁷ and yields of formic and acetic acids, and CO_2 were estimated to be 77, 151, and 211%, respectively, based on *m*XS. This result indicates that all of the aromatic C-H bonds on the benzene ring are not involved in formic acid, but one of the three aromatic C-H bonds of *m*XS is involved in formic acid. In addition, the obtained formic acid was partially converted to CO_2 by the $\text{Ru}^{\text{III}}\text{-O}\cdot$ complex

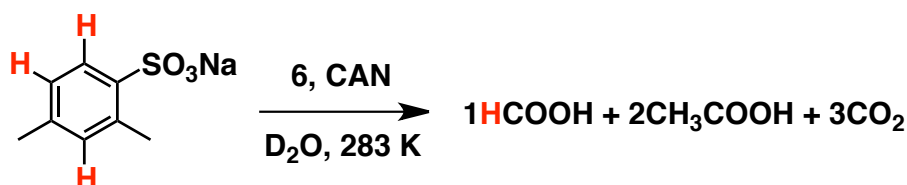


Figure 4-17. Schematic representation of the OBC reaction of *m*XS catalyzed by **6** in D_2O .

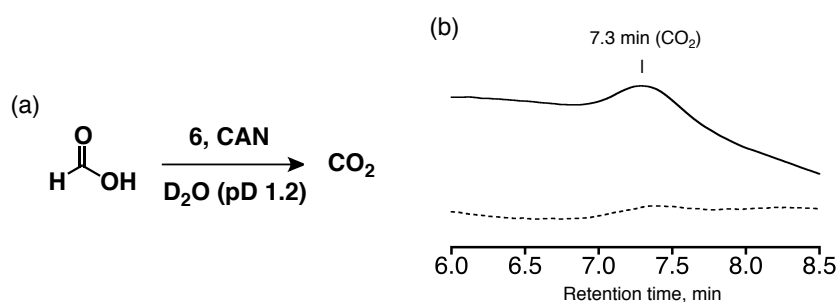


Figure 4-18. (a) Schematic representation of catalytic formic acid oxidation in D_2O (pD 1.2) by **6** as a catalyst and CAN as a sacrificial oxidant. (b) GC charts of the gaseous phase in formic acid oxidation in the presence (black solid line) and absence (black dashed line) of catalyst **6** (0.14 mM). CAN (75 mM), formic acid (27 mM), $T = 283 \text{ K}$, reaction time: 24 h. Conversion yields of formic acid were calculated to be 41% in the presence of **6** and 0% in the absence of **6** based on the ^1H NMR spectra of the aqueous phases.

under the reaction conditions, as confirmed by a separate experiment (Figure 4-18). To consider the product ratio mentioned above, one *m*XS molecule is assumed to afford one formic acid, two acetic acids and three CO_2 molecules (Figure 4-17). On the basis of this assumption, the conversion and the product yields match well within the experimental errors. This is a very important clue for discussing the reaction mechanism (see below).

4-5 Kinetic analysis on the catalytic OBC reactions

Kinetic analysis has been also performed on the OBC reaction using *mXS* as a substrate by ^1H NMR spectroscopy (Figure 4-19). In particular, the author has investigated the dependence of the rate constants on the concentrations of the substrate and catalyst. Time-courses of the concentrations of formic and acetic acids in the initial stage of the reaction showed a linear correlation to determine the reaction rate (v_0) (Figure 4-19(a) and (b)). The dependence of the v_0 values for acetic acid formation on the *mXS* concentration exhibited saturation behavior at higher concentrations, which was analyzed on the basis of the Michaelis-Menten equation (Figure 4-19(c)).³⁸ The Michaelis constant, K_m , and the V_{\max} value were determined to be 1.4 mM and $7.3 \times 10^{-4} \text{ mM s}^{-1}$, respectively. This small K_m value indicates that there are relatively strong interactions between the substrate and the reactive species prior to the oxidation reaction. The dependence of the v_0 value on the catalyst concentration was investigated to determine the catalytic rate constants (k_{cat}) under the conditions, where the substrate concentration was high enough to show the saturation of the v_0 value. As a result, k_{catF} for the formic acid formation and $k_{\text{catA}}^{\text{H}}$ for the acetic acid formation in the OBC reaction of *mXS* were determined to be 1.5×10^{-3} and $4.2 \times 10^{-3} \text{ s}^{-1}$, respectively (Figure 4-19(d)).³⁹ With deuterated *mXS* (*mXS-d*₃) as a substrate, whose three protons on the aromatic ring were selectively labeled with deuterium, $k_{\text{catA}}^{\text{D}}$ values for the obtained deuterated acetic acid were determined to be $4.1 \times 10^{-3} \text{ s}^{-1}$. Therefore, the kinetic isotope effect ($\text{KIE} = k_{\text{catA}}^{\text{H}}/k_{\text{catA}}^{\text{D}}$) was calculated to be 1.0 (Figure 4-20). This indicates that hydrogen-atom transfer (HAT) from C-H bonds of the aromatic rings

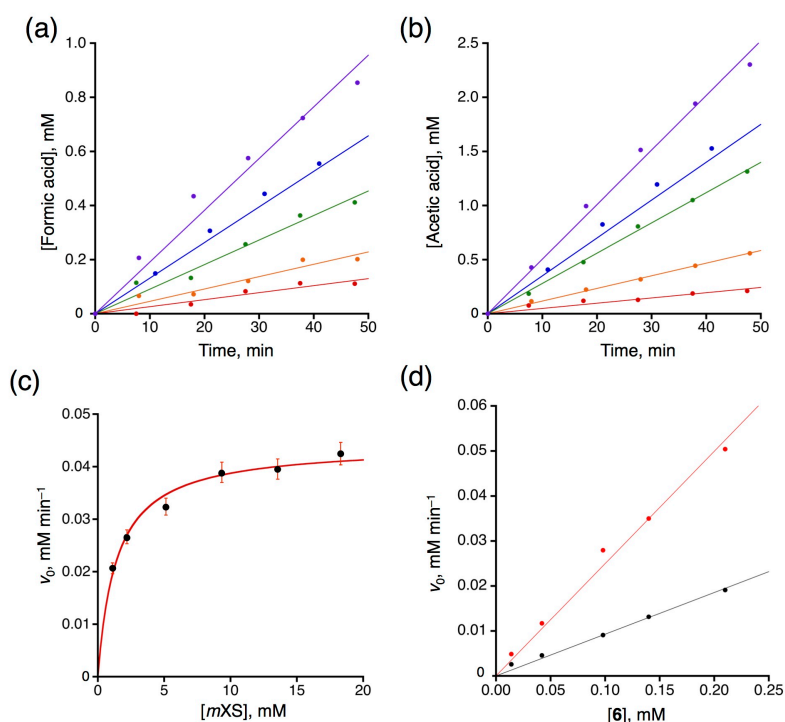


Figure 4-19. Time-profiles of formic acid (a) and acetic acid (b) formation in the catalytic oxidation of *mXS* (8.4 mM) in D_2O (pD 1.2) at 283 K in the presence of CAN (75 mM) as a sacrificial oxidant and **6** as a catalyst, whose concentration was varied as 0.21 (purple), 0.14 (blue), 0.098 (green), 0.042 (orange), and 0.014 mM (red). (c) Dependence of the initial rates (black filled circles) of acetic acid formation in OBC on the concentration of *mXS* and the fitting curve based on the Michaelis-Menten equation (red solid line). (d) Dependence of the initial rates of formic acid (black) and acetic acid (red) production on the catalyst concentration in the OBC reaction of *mXS* catalyzed by **6**.

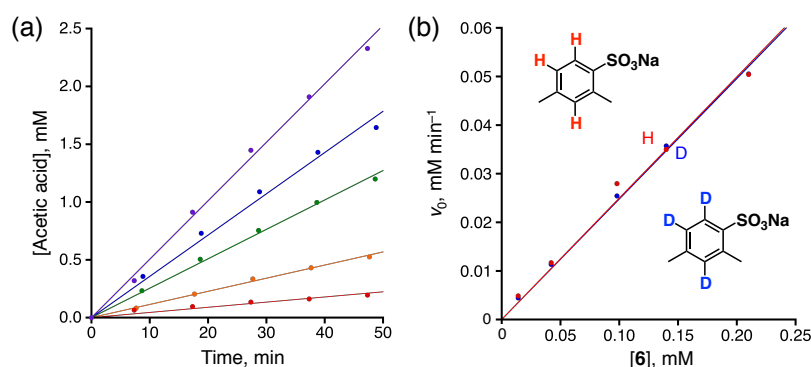


Figure 4-20. (a) Time-profiles of acetic acid formation in the OBC reaction of *mXS-d*₃ (8.4 mM) in D₂O (pD 1.2) at 283 K in the presence of CAN (75 mM) as a sacrificial oxidant and **6** as a catalyst, whose concentration was varied as 0.21 (purple), 0.14 (blue), 0.098 (green), 0.042 (orange), and 0.014 (red) mM. The concentration of acetic acid was calculated on the basis of the integral values of the ¹H NMR signal using DSS as an internal standard. (b) Dependence of the initial rates (red filled circles for *mXS* and blue filled circles for *mXS-d*₃) of acetic acid formation in OBC on a lower range of concentrations of *mXS* and *mXS-d*₃ and the fitting curves based on the second-order dependence (red and blue solid lines). Conditions: [*mXS*] = 8.5 mM or [*mXS-d*₃] = 8.4 mM, [CAN] = 75 mM, *T* = 283 K. Concentrations of the products were determined by ¹H NMR spectroscopy with DSS as an internal standard.

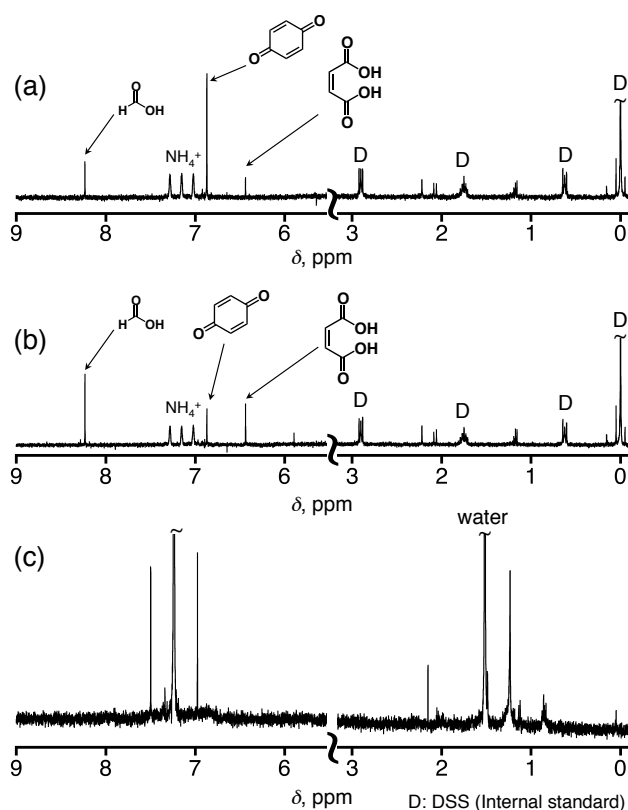


Figure 4-21. (a) ¹H NMR spectrum of the reaction solution of the phenol oxidation in the absence of catalysts: [CAN] = 75 mM, [phenol] = 21 mM. (b) ¹H NMR spectrum of the reaction solution of phenol oxidation in the presence of catalyst **6**: [**6**] = 0.14 mM, [CAN] = 75 mM, [phenol] = 21 mM. (c) ¹H NMR spectrum in CDCl₃ for brown precipitate obtained from the reaction of phenol with CAN in D₂O.

to the $\text{Ru}^{\text{III}}\text{-O}\cdot$ complex is not involved in the rate-limiting step of the OBC reactions. A similar KIE value (1.04) has been also reported by Kodera and co-workers for benzene oxidation that afforded phenol as the product.¹⁶ The obtained KIE value also suggests that the active species of the OBC reaction in this study is not the hydroxyl radical, because the KIE values of a Fenton-type benzene oxidation reaction reported so far, using hydroxyl radical as the active species and giving CO_2 as the product, are in the range of 1.7 – 1.8.^{40,41} In the Fenton-type reaction, the rate-determining step is assumed to be the abstraction of hydrogen atom from aromatic C-H bonds by hydroxyl radical or deprotonation from C-H bonds of oxidized intermediates.⁴¹ The assumption that HAT from the C-H bond of benzene does not occur in the present OBC reaction is consistent with the large bond-dissociation energy of the C-H bond of benzene ($113 \text{ kcal mol}^{-1}$).⁴²

In addition, as one of the possible candidates for intermediates derived from benzene in the course of the OBC reaction, phenol was subjected to the OBC reaction as a substrate (Figure 4-21), because there have been plenty of reports of benzene oxidation affording phenol as a product.^{16, 17, 43-45} In the phenol oxidation under the same conditions that were used for the OBC reactions, a complicated mixture of aromatic compounds was obtained as brown precipitate. Moreover, a rapid reaction of phenol with CAN proceeded even in the absence of **6** (Figure 4-21(a)), indicating that phenol can be excluded as an intermediate of the OBC reaction. To obtain further information about organic intermediates in the catalytic OBC reaction, time-dependent product analysis have been performed by ^1H NMR measurements for the catalytic OBC reaction of benzene (Figure 4-22). A ^1H NMR signal derived from 1,4-benzoquinone was observed at 6.9

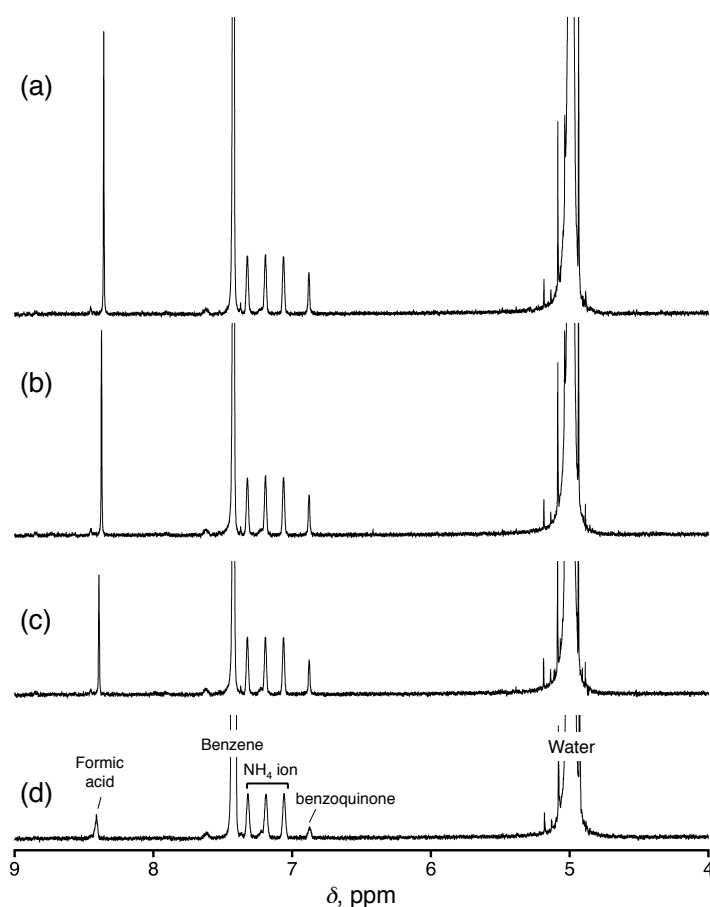


Figure 4-22. Time-course of the ^1H NMR spectra of a catalytic OBC reaction mixture including benzene as a substrate in D_2O . Conditions: [**6**] = 0.14 mM, [CAN] = 75 mM, $T = 283 \text{ K}$. Reaction time: 100 (a), 70 (b), 40 (c), and 10 min (d).

ppm in the time range of 1 – 3 h. To confirm whether 1,4-benzoquinone can be involved as an intermediate in the catalytic OBC reaction, catalytic oxidation of 1,4-benzoquinone was conducted using **6** as a catalyst; both formic acid and CO₂ were obtained and the TON values were determined to be 39 and 52, respectively. ¹H NMR spectroscopic analysis of the OBC reaction mixture was also performed with lower concentration

Table 4-7. Catalytic oxidation reactions of *trans,trans*-muconic acid

Entry	Catalyst	TON (efficiency, %) ^a	
		Formic acid	CO ₂
1	6	122 (68)	45 (8)
2	None	– (21)	– (3)

Reaction conditions: [**6**] = 0.14 mM (entry 1), [CAN] = 75 mM, *T* = 283 K. Reaction time: 24 h. Concentration of *trans,trans*-muconic acid was not able to be determined due to its low solubility in acidic water. ^a TON = [Product]/[**6**], Efficiency (%) = [([Product] × n) / [CAN]] (n = 3 for formic acid, n = 1 for CO₂).

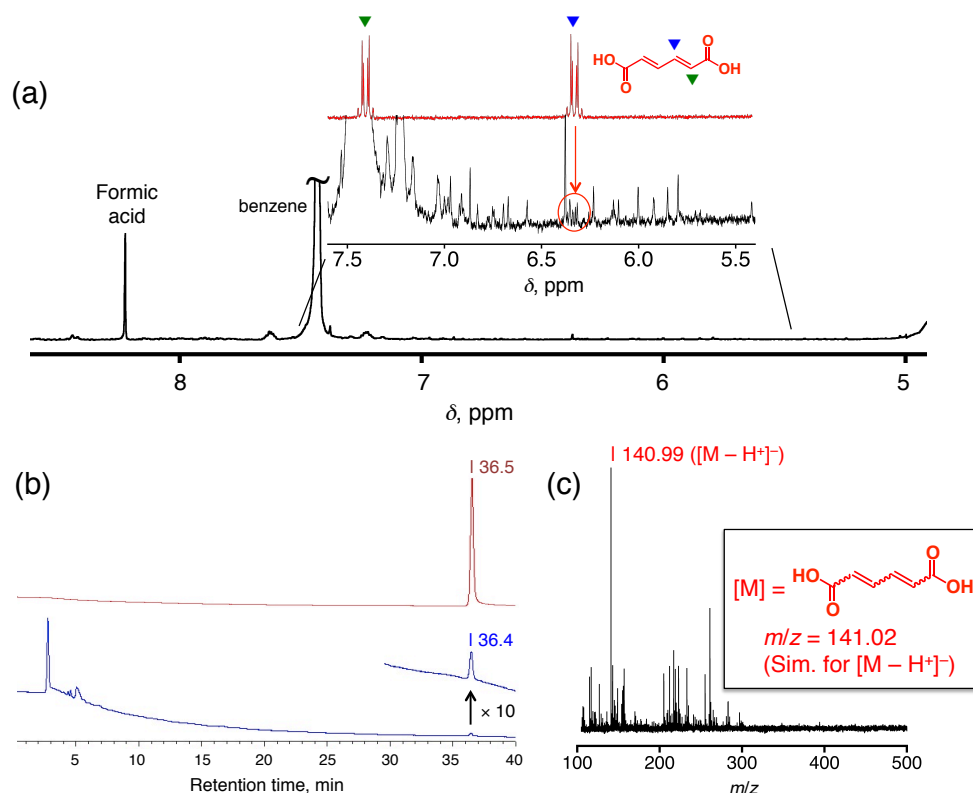


Figure 4-23. Detection of muconic acid as a product. (a) ¹H NMR spectrum of a reaction mixture of the catalytic OBC reaction of benzene in D₂O (black) and that of authentic *trans,trans*-muconic acid in D₂O (red), measured at 298 K. (b) HPLC charts of the reaction mixture after the catalytic OBC reaction of benzene in H₂O (blue) and of authentic *trans,trans*-muconic acid in H₂O (red), monitored at 265 nm. (c) ESI-TOF-MS spectrum of a fraction (retention time: 36 – 38 min), separated by HPLC and diluted with MeOH. Reaction conditions: [**6**] = 0.14 mM, [CAN] = 19 mM, *T* = 283 K. Reaction time: 40 min. The remaining oxidants were quenched by addition of excess sodium oxalate (22 mM) into the reaction mixture. The HPLC analyses were conducted at 40 °C with a gradient program for the eluent (0 min; 100% HClO₄ aq (pH 2.0), 30 min: 100 % distilled water). Flow rate: 1.0 mL/min. Pressure: 6.7 MPa. An orifice voltage in the ESI-TOF-MS measurements, operating in a negative mode, was regulated to be –105 V.

of CAN (19 mM) to suppress overoxidation of the organic intermediates. The reaction mixture was treated with an excess of sodium oxalate at the reaction time of 40 min to quench the remaining oxidants;⁴⁶ ¹H NMR signals assigned to muconic acid were observed (Figure 4-23(a)). The products of the OBC reaction, which was also treated with an excess of sodium oxalate at a reaction time of 40 min, were separated by HPLC (Figure 4-23(b)). The ESI-TO-MS measurement of the HPLC fraction at a retention time of 36.4 min exhibited a MS peak derived from muconic acid at $m/z = 140.99$ (simulation for $[M - H]^+$: $m/z = 141.02$) (Figure 4-23(c)). In addition, catalytic oxidation of *trans,trans*-muconic acid also gave formic acid and CO₂ as products (Table 4-7), and formic acid and CO₂ were obtained very fast through the oxidation with CAN even in the absence of **6**. Because it is probably impossible to form muconic acid from 1,4-benzoquinone, 1,4-benzoquinone and muconic acid should be formed through different pathways.

4-6 A proposed mechanism of the catalytic OBC reaction

On the basis of the product analysis and the kinetic studies mentioned above, a plausible mechanism for the OBC reaction catalyzed by **6** was proposed as shown in Figure 4-24. As the first step, the electrophilic addition of the Ru^{III}-O• complex, which is formed from catalyst **6**, to the benzene ring occurs to generate a radical-coordinated intermediate (step i in Figure 4-24). This step is reminiscent of the previously reported benzene oxidation with a Cu(II)-oxyl complex.^{16,17} The radical-bound intermediate releases a Ru(II) species that reproduces **6** in water and an arene oxide that can be in an equilibrium with oxepin (step ii).⁴⁷ Further oxidation of the arene oxide/oxepin mixture can afford *E/Z*-isomers of muconaldehyde as reported previously (step iii).⁴⁸ The aldehydes can be easily oxidized into the *E/Z* isomers of muconic acid (step iv), which are further oxidized into formic acid and carbon dioxide (steps v and vi). In addition, oxidation of arene oxide can also form 1,4-benzoquinone through a pathway different from that giving muconic acid (step vii). Such direct conversion of arene oxide into 1,4-benzoquinone has been proposed previously.⁴⁹ In the case of chloro- and bromobenzene, plausible products include chloro- and bromoformic acids (X = Cl or Br); however, the acids easily undergo nucleophilic attack of water molecules to decompose and afford CO₂ (step viii).

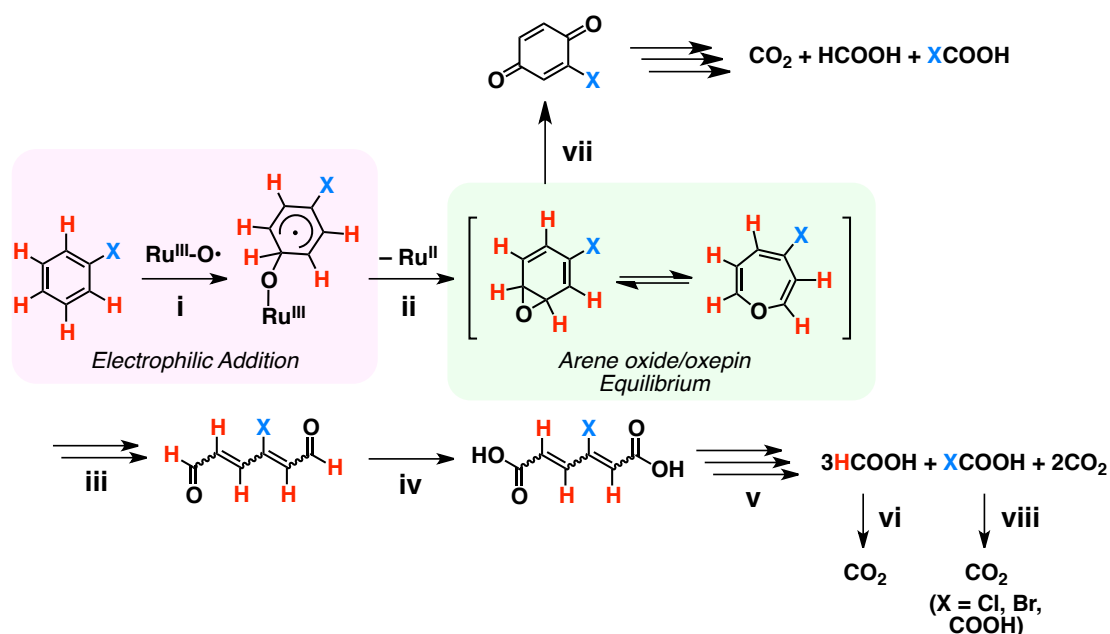


Figure 4-24. A proposed mechanism of the OBC reaction by the Ru^{III}-O• complex (X = CH₃, C₆H₅, Cl, Br, COOH, or CF₃).

4-7 Conclusions

An efficient OBC reaction of benzene and its derivatives has been established for the first time to obtain formic and carboxylic acids as products, the latter of which have substituents originally on the aromatic rings, by suppressing overoxidation of the products. The obtained formic acid can be used as a dihydrogen source in aqueous media at low temperatures; actually, the author succeeded in forming H₂ as a clean energy resource from the OBC reaction mixture using a Rh^{III} catalyst with simple pH adjustment of the reaction solution.²⁰ In addition, the author has revealed that substituent effects on the aromatic rings can switch the oxidation sites; *i.e.*, the benzylic C-H moiety attached to an electron-deficient aromatic ring was oxidized through the C-H abstraction (see Chapter 3),¹⁸ whereas the C-C double bonds of the electron-rich aromatic rings were oxidatively cleaved. The clear selectivity of the aromatic-ring oxidations in the OBC reaction derives from the electrophilic and strong radical character of the Ru^{III}-O• complex as the active species and the OBC reactions proceed through the electrophilic addition of the Ru^{III}-O• complex to the aromatic ring.

4-8 Experimental section

General.

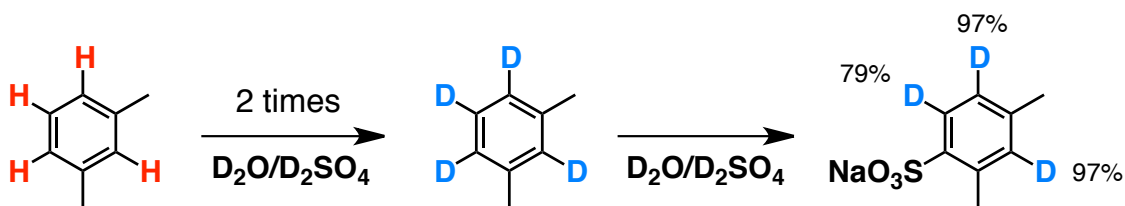
NMR measurements were performed on Bruker Avance 400 and Avance III HD 400 spectrometers and JEOL JNM-ECS400 spectrometers. DSS (= 3-(trimethylsilyl)- propane-sulfonate sodium salt) was used as an internal standard for ¹H NMR spectral measurements in D₂O. Gas chromatography was performed using a Shimadzu GC-2014 equipped with a thermal conductivity detector (TCD) and a packed column with molecular sieves 5A or a packed column with activated carbon. ESI-TOF-MS spectra were obtained on a JEOL JMS-T100CS mass spectrometer. UV-Vis absorption spectra were measured on a Shimadzu UV-2450 spectrophotometer. GC-MS measurements were performed using a Shimadzu GC-2010 Plus equipped with a Shimadzu GCMS-QP2020 and a Shimadzu SH-Rxi-5ms capillary column (30 meter, ID 0.25, DF 0.25). High-performance liquid column chromatography (HPLC) analyses were performed using an HPLC system, purchased from JASCO Co and composed of a column oven CO-4060 equipped with ODS column (Unifinepak C18, Model 04250-5M), a pump PU-4180, and a photo diode array detector MD-4010. Dynamic light scattering (DLS) measurements were conducted on an Otsuka Electronics Model FDLS-3000.

Ru^{IV}O₂ was purchased from Wako. Co. and Ru^{III}Cl₃·nH₂O was purchased from Furuya metal Co. [Ru^{II}(BPIIm)(bpy)(OH₂)](ClO₄)₂ (**1**; BPIIm = 1,3-bis(2-pyridylmethyl)-imidazol-2-ylidene, bpy = 2,2'-bipyridyl) was synthesized according to the literature (Chapter 3).¹⁸ [Rh^{III}(Cp*)(bpy)(OH₂)](PF₆)₂ (Cp* = 1,2,3,4,5-pentamethylcyclopentadienyl),⁵⁰ [Ru^{II}(PY5Me₂)(OH₂)](PF₆)₂ (PY5Me₂ = 2,6-bis[1,1-bis(2-pyridyl)ethyl]pyridine),²⁶ and [Ru^{II}(N4Py)(OH₂)](PF₆)₂ (N4Py = *N,N*-bis(2-pyridylmethyl)-*N*-bis(2-pyridyl)-methylamine)²⁷ were also synthesized according to the literature procedures.

Synthesis.

Sodium *m*-xylenesulfonate-*d*₃ (*mXS-d*₃).

Synthesis of this compound was conducted by a modified method of deuteration of mesityrene,⁵¹ followed by the sulfonation. *m*-Xylene (1.5 mL, 12 mmol) was dispersed in a mixture of D₂O (0.2 g) and D₂SO₄ (1.5 g) and stirred overnight at room temperature in a flame-shielded ampoule. Then, the reaction mixture was separated into three phases; the upper phase (1 mL) consisting of *m*-xylene derivative partially deuterated at the benzene ring but not sulfonated, the middle phase consisting of partially deuterated *m*-xylene-sulfonic acid, and the lower phase was the mixture of D₂O and D₂SO₄ not used in the reaction. The



upper phase was collected and further reacted in D_2O (0.2 g) and D_2SO_4 (1.5 g) overnight. After the reaction, similar separation into three phases was observed and the upper phase (0.5 mL) was obtained. The upper phase was reacted again in D_2O (0.2 g) and D_2SO_4 (1.5 g) overnight. The reaction mixture was separated into two phases; the upper phase consisting of partially deuterated *m*-xylene-sulfonic acid, and the lower phase was the mixture of D_2O and D_2SO_4 not used in the reaction. The upper phase was poured into distilled water (5 mL), and the solution was neutralized by addition of excess amount of NaOH aq and the solution pH was adjusted by adding H_2SO_4 aq to pH 7.6. The solvent was removed under reduced pressure and then dried under vacuum. White solid obtained was dispersed into EtOH (200 mL) and insoluble solids were filtered off. The volatiles in the filtrate were evaporated and the residue was dried under vacuum and white crystalline solid (486 mg, 2.3 mmol) was obtained in 19% yield. NMR spectra of *mXS* and *mXS-d₃* are shown in Figure 4-25. 2H NMR: δ 7.72 (br s), 7.13 – 7.19 (br s). 1H NMR: δ 7.73 (s, 79% deuterium-labeled), 7.22 (s, 97% deuterium-labeled), 7.15 (s, 97% deuterium-labeled), 2.55 (s, 3H), 2.34 (s, 3H).

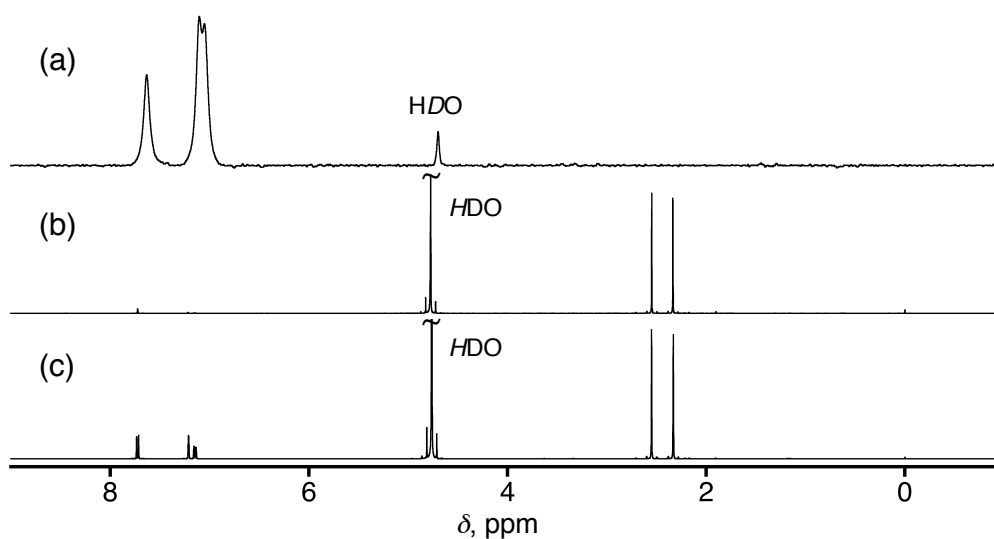


Figure 4-25. (a) 2H NMR spectrum of *mXS-d₃* in H_2O . (b) 1H NMR spectrum of *mXS-d₃* in D_2O . (c) 1H NMR spectrum of *mXS* in D_2O .

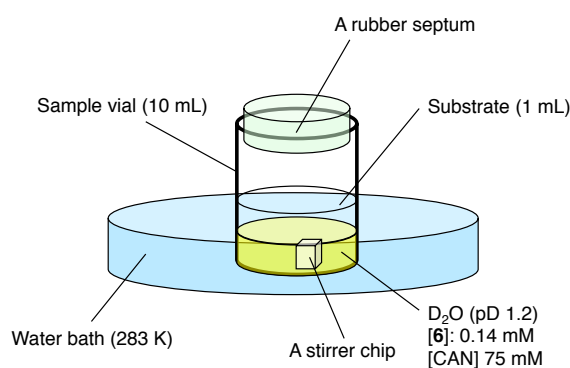


Figure 4-26. Simple representation of the experimental setup for the OBC reactions.

General procedure for oxidative cracking of benzene derivatives.

A sample vial (10 mL) shielded by a rubber septum was filled with a biphasic reaction mixture consisting of D₂O solution (1 mL) of **6** (0.14 mM) and (NH₄)₂[Ce^{IV}(NO₃)₆] (CAN, 75 mM) as an aqueous layer, whose pD was set to be 1.2 by addition of acidic CAN, and 1 mL of a substrate as an organic layer. In most cases, the reactions were performed at 283 K in a water bath equipped with a temperature controller (COOL STIRRER SAC-900). A schematic representation of the reaction setup is shown in Figure 4-26.

Kinetic analysis on the OBC reactions of sodium *m*-xylenesulfonate and its deuterated derivative (*m*XS and *m*XS-*d*₃, respectively).

The ¹H NMR signals of formic and acetic acids derived from oxidation of *m*XS were monitored to follow the reaction progress in D₂O (pD 1.2). The amounts of formic and acetic acids were determined using DSS as an internal standard. As for *m*XS-*d*₃, only the formation of acetic acid was monitored, because formic acid derived from *m*XS-*d*₃ was deuterated and insensitive ²H NMR spectroscopy did not allow us to quantify DCOOD in an appropriate period of reaction time for kinetic analysis. A linear least-squares fitting was conducted for the time profile of the product amounts observed in the range of 0 – 50 min and the slopes of the fitting lines obtained were used as the initial rates (*v*₀) of *m*XS and *m*XS-*d*₃ oxidation. The *v*₀ values for formic and acetic acid formation were determined at various catalyst concentrations and the catalytic rate constants, *k*_{catH} and *k*_{catD}, were determined with eq 1.

$$v_0 = k_{\text{cat}}[\mathbf{6}] \quad (1)$$

Determination of *K*_m and *V*_{max} values for the OBC reaction of *m*XS.

The initial rates, *v*₀, for the OBC reactions of *m*XS at various concentrations (1.1 – 18 mM) were obtained according to the procedure described above. The obtained *v*₀ values were plotted versus the substrate concentration. The *v*₀ values exhibited saturation behavior with respect to concentration (see Figure 4-19(d)). On the basis of the Michaelis-Menten equation as described in eq 2, the Michaelis constant, *K*_m, and the maximum rate in the system, *V*_{max}, were determined by fitting analysis.

$$v_0 = (V_{\text{max}}[m\text{XS}]) / (K_m + [m\text{XS}]) \quad (2)$$

References and notes.

- (1) S. M. Arnold, J. Angerer, P. J. Boogaard, M. F. Hughes, R. B. O'Lone, S. H. Robinson, A. R. Schnatter, *Crit. Rev. Toxicol.* **2013**, *43*, 119–153.
- (2) S. H. Lamm, W. Grünwald, *Science* **2006**, *312*, 998b–999b.
- (3) C. He, J. Li, J. Cheng, L. Li, P. Li, Z. Hao, Z. P. Xu, *Ind. Eng. Chem. Res.* **2009**, *48*, 6930–6936.
- (4) S. S. Tamhankar, K. Tsuchiya, J. B. Riggs, *Appl. Catal.* **1985**, *16*, 103–121.
- (5) J. M. Weiss C. R. Downs, *J. Chem. Educ.* **1925**, *2*, 1178–1180.
- (6) M. Farhadian, C. Vachelard, D. Duchez, C. Larroche, *Bioresour. Technol.* **2008**, *99*, 5296–5308.
- (7) H. Masumoto, F. Kurisu, I. Kasuga, D. M. Turlousse, H. Furumai, *Chemosphere* **2012**, *86*, 822–828.
- (8) D. A. Lashof, D. R. Ahuja, *Nature* **1990**, *344*, 529–531.
- (9) Y. Inagaki, M. Nakamoto, A. Sekiguchi, *Nat. Commun.* **2014**, *5*, 3018.
- (10) D. Ellis, D. McKay, S. A. Macgregor, G. M. Rosair, A. J. Welch, *Angew. Chem., Int. Ed.* **2010**, *49*, 4943–4945.
- (11) S. Hu, T. Shima, Z. Hou, *Nature* **2014**, *512*, 413–415.
- (12) A. Sattler, G. Parkin, *Nature* **2010**, *463*, 523–526.
- (13) M. T. Nuñez, V. S. Martín, *J. Org. Chem.* **1990**, *55*, 1928–1932.

- (14) J. A. Caputo, R. Fuchs, *Tetrahedron Lett.* **1967**, *8*, 4729–4731.
- (15) C. Djerassi, R. R. Engle, *J. Am. Chem. Soc.* **1953**, *75*, 3838–3840.
- (16) T. Tsuji, A. A. Zaoputra, Y. Hitomi, K. Mieda, T. Ogura, Y. Shiota, K. Yoshizawa, H. Sato, M. Kodera, *Angew. Chem., Int Ed.* **2017**, *56*, 7779–7782.
- (17) L. Vilella, A. Conde, D. Balcells, M. M. Diaz-Requejo, A. Lledós, P. J. A. Pérez, *Chem. Sci.* **2017**, *8*, 8373–8383.
- (18) Y. Shimoyama, T. Ishizuka, H. Kotani, Y. Shoita, K. Yoshizawa, K. Mieda, T. Ogura, T. Okajima, S. Nozawa, T. Kojima, *Angew. Chem., Int. Ed.* **2016**, *55*, 14041–14045. (See Chapter 3)
- (19) T. C. Johnson, D. J. Morris, M. Wills, *Chem. Soc. Rev.* **2010**, *39*, 81–88.
- (20) S. Fukuzumi, T. Kobayashi, T. Suenobu, *ChemSusChem* **2008**, *1*, 827–834.
- (21) The details of general reaction conditions are shown in Methods in the Experimental Section. **6**: 0.14 mM, CAN: 75 mM, $T = 283$ K, time: 24 h. Liquid substrate (1 mL) was added to the reaction vessel.
- (22) T. Nash, *Biochem. J.* **1953**, *55*, 416–421.
- (23) A. R. Parent, R. H. Crabtree, G. W. Brudvig, *Chem. Soc. Rev.* **2013**, *42*, 2247–2252.
- (24) S. A. Shafiee, J. Aarons, H. H. Hamzah, *J. Electrochem. Soc.* **2018**, *165*, H785–H798.
- (25) S. Fukuzumi, T. Suenobu, *Dalton Trans.* **2013**, *42*, 18–28.
- (26) S. Ohzu, T. Ishizuka, H. Kotani, T. Kojima, *Chem. Commun.* **2014**, *50*, 15018–15021.
- (27) T. Ishizuka, S. Ohzu, H. Kotani, Y. Shiota, K. Yoshizawa, T. Kojima, *Chem. Sci.* **2014**, *5*, 1429–1436.
- (28) T. Kojima, K. Nakayama, K. Ikemura, T. Ogura, S. Fukuzumi, *J. Am. Chem. Soc.* **2011**, *133*, 11692–11700.
- (29) M. S. Thompson, T. J. Meyer, *J. Am. Chem. Soc.* **1982**, *104*, 5070–5076.
- (30) P. B. Merkel, P. Luo, J. P. Dinnocenzo, S. Farid, *J. Org. Chem.* **2009**, *74*, 5163–5173.
- (31) M. Asaka, H. Fujii, *J. Am. Chem. Soc.* **2016**, *138*, 8048–8051.
- (32) C. Hansch, A. Leo, R. W. Taft, *Chem. Rev.* **1991**, *91*, 165–195.
- (33) Benzoic acid is probably oxidized to afford oxalic acid as one of the products (X = COOH in Figure 4-16). Oxalic acid formed should be oxidized under the reaction conditions to afford CO₂ as the product, which was confirmed by oxidation of oxalic acid as a substrate to afford CO₂ in 162% yield. Reaction conditions are as follows: [6] = 0.14 or 0 mM, [CAN] = 75 mM, [sodium oxalate] = 10 mM, $T = 283$ K Reaction time: 2 h. In addition, this reaction proceeded even in the absence of 6 as a catalyst in the comparable yield.
- (34) M.-J. Kang, W. J. Song, A.-R. Han, Y. S. Choi, H. G. Jang, W. Nam, *J. Org. Chem.* **2007**, *72*, 6301–6304.
- (35) S. P. de Visser, K. Oh, A.-H. Han, W. Nam, *Inorg. Chem.* **2007**, *46*, 4632–4641.
- (36) K. R. Korzekwa, D. C. Swinney, W. F. Trager, *Biochemistry* **1989**, *28*, 9019–9027.
- (37) Reaction conditions were as follows: [6] = 0.14 mM, [CAN] = 225 mM, [mXS] = 5 mM, time: 24 h, $T = 283$ K, solvent: D₂O (pD 1.2).
- (38) A. Karich, M. Kluge, R. Ullrich, M. Hofrichter, *AMB Express* **2013**, *3*, 5–13.
- (39) Since two acetic acid molecules are released from one mXS molecule based on stoichiometry on the catalytic oxidation of mXS, the value of $k_{\text{catA}}^{\text{H}}$ should be normalized as $2.1 \times 10^{-3} \text{ s}^{-1}$ by dividing by 2. Therefore, the substantial catalytic rate constant of the OBC reactions of mXS should be $2.1 \times 10^{-3} \text{ s}^{-1}$. The discrepancy of the rates is derived from further oxidation of formic acid to CO₂, which reduces the amount of formic acid formed to lower the k_{catF} value.
- (40) D. Wang, M. Wang, Z. Li, *ACS Catal.* **2015**, *5*, 6852–6857.
- (41) R. Augusti, A. O. Dias, L. L. Rocha, R. M. Lago, *J. Phys. Chem. A* **1998**, *102*, 10723–10727.

- (42) Y.-R. Luo, *Handbook of Bond Dissociation Energies in Organic Compounds*, 1st ed., CRC Press LLC: Boca Raton, FL, 2003; p 39.
- (43) Y. Morimoto, S. Bunno, N. Fujieda, H. Sugimoto, S. Itoh, *J. Am. Chem. Soc.* **2015**, *137*, 5867–5870.
- (44) J. Xu, Y. Chen, Y. Hong, H. Zheng, D. Ma, B. Xue, Y.-X. Li, *Appl. Catal. A* **2018**, *549*, 31–39.
- (45) K. Ohkubo, T. Kobayashi, S. Fukuzumi, *Angew. Chem., Int. Ed.* **2011**, *50*, 8652–8655.
- (46) The reason why the ¹H NMR signals observed were not completely matched with the signals of authentic *trans,trans*-muconic acid is probably that stereoisomers of muconic acid (e.g. *cis,cis*- or *cis,trans*-muconic acid) were also formed.
- (47) E. Vogel, H. Günther, *Angew. Chem., Int. Ed. Engl.* **1967**, *6*, 385–401.
- (48) B. T. Golding, M. L. Barnes, C. Bleasdale, A. P. Henderson, D. Jiang, X. Li, E. Mutlu, H. J. Petty, M. M. Sadeghi, *Chem. -Biol. Interact.* **2010**, *184*, 196–200.
- (49) R. Ramu, W. H. Wanna, D. Janmanchi, Y.-F. Tsai, C.-C. Liu, C.-Y. Mou, S. S.-F. Yu, *Mol. Catal.* **2017**, *441*, 114–121.
- (50) J. Huang, M. Antonietti, J. Liu, *J. Mater. Chem. A* **2014**, *2*, 7686–7693.
- (51) J. T. Groves, R. Quinn, T. J. McMurry, M. Nakamura, G. Lang, B. Boso, *J. Am. Chem. Soc.* **1985**, *107*, 354–360.

Chapter 5

Catalytic oxidative cracking of halogenated benzene derivatives by a palladium(II)-NHC complex in water

5-1 Introduction

Halogenated benzene derivatives (HBDs) have been widely utilized as solvents, insecticides, and synthetic intermediates in medicines and chemicals.¹ In particular, polychlorinated biphenyls (PCBs) had been frequently employed since 1929 through the mid 1970 as dielectric materials, heat-transfer fluids in electrical apparatus owing to its high thermodynamic, chemical and biological durability.² However, since 1967, PCBs had been gradually recognized to be toxic and persistent pollutants for long time.^{2,3} In spite of the fact that HBDs such as PCBs have serious toxicity, development of the degradation methods effective for HBDs including PCBs has been strongly required but extremely challenging,⁴ because combustion of highly stable HBDs should accompany formation of dioxins, showing much stronger toxicity than PCBs. Currently, chemical degradation processes of mono- or di-chlorobenzenes as model compounds of dioxins or PCBs have been developed using oxidation reactions.^{5,6} However, these degradation processes of HBDs have required high thermal energy at least 200 °C. To realize the degradation of HBDs under mild conditions, activation of Ar-Cl bonds by Pd⁰ or Pd^{II} complexes has been developed through an oxidative addition pathway.⁷ Additionally, there are reports on homogeneous activation reactions of Ar-Cl bonds conducted by using Pd complexes as catalysts in water as a non-toxic, non-flammable, and inexpensive solvent.⁸ However, since water is a strongly polar solvent, involvement of hydrophobic Pd⁰ species, which cannot keep the homogeneity due to low solubility in water, is not desirable for the homogeneous catalysis in water.⁹ In order to provide catalytic systems workable in water, involvement of cationic high-valent palladium species as reactive species derived from Pd^{II} catalysts should be of interest and valuable,¹⁰ since the cationic high-valent palladium species exhibit good solubility in polar solvents such as water.¹¹ There are several reports on functionalization of arenes using Pd^{II} catalysts as shown in Figure 5-1a-c to generate Pd^{IV} complexes as reactive species;¹²⁻¹⁴ however, these systems utilize harmful oxidants such as hyper-valent iodoarene^{12,13} or fluorinating reagent¹⁴ as shown in Figure 5-1d and e. Thus, toward the oxidative degradation of harmful HBDs, inorganic and non-toxic oxidants such as Oxone[®] or Na₂S₂O₈ should be better for formation of Pd(IV) complexes as reactive species. Oxone[®] (= KHSO₄·K₂SO₄·2KHSO₅, DuPont) has

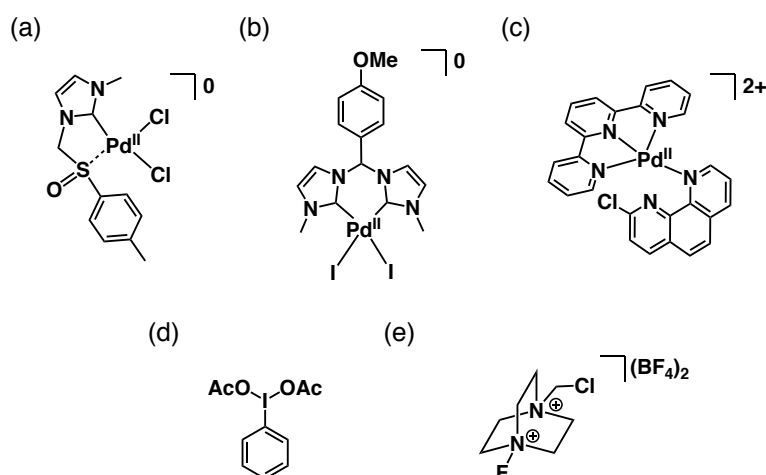


Figure 5-1. Schematic descriptions of structures of Pd^{II} catalysts for oxidative functionalization of arenes (a, b) with PhI(OAc)₂ (d),^{12,13} a Pd^{II} catalyst (c) for fluorination of arenes with a fluorinating reagent (e).¹⁴

been widely used as a cheaper and environmentally benign oxidant in aqueous media and is a stable triple salt under ambient conditions.¹⁵ Although HSO_5^- ion itself is not stable, the triple salt is remarkably stable at room temperature and commercially available in large scale; the K^+ and PPh_4^+ salts of the HSO_4^- ion are isolable as single crystals to determine the crystal structure.¹⁶ Sanford and co-workers used Oxone[®] as a sacrificial oxidant for catalytic conversion of aryl halide, having amide moieties as directing groups, to acetoxyated or methoxylated products by $\text{Pd}^{\text{II}}(\text{OAc})_2$ as a catalyst in acetic acid or methanol.¹⁷ In this case, the key intermediate of the functionalization has been suggested as an octahedral Pd^{IV} species (Figure 5-2). However, catalytic degradation of HBDs has yet to be reported using transition-metal catalysts and cheaper, environmentally benign oxidants in water.

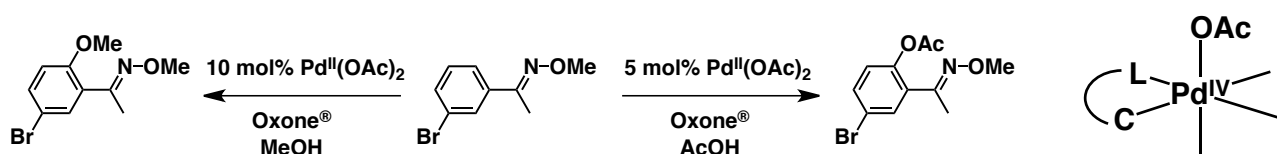


Figure 5-2. Catalytic functionalization of arenes by $\text{Pd}^{\text{II}}(\text{OAc})_2/\text{Oxone}^{\text{®}}$ system in acetic acid or methanol (left) and its key intermediate identified as Pd^{IV} species (right).¹⁷

In Chapter 4, the author has described that a Ru^{II} -aqua complex, having an *N*-heterocyclic carbene (NHC) ligand, catalyzes oxidative cracking of benzene derivatives (OBC) with Ce^{IV} complexes as sacrificial oxidants to afford carboxylic acids such as formic acid under mild conditions.¹⁸ Chlorinated benzenes, however, have not been oxidized effectively under the conditions due to the electron-withdrawing nature of the chloro groups, since the unique catalytic OBC reactions rely on the electrophilicity of the $\text{Ru}^{\text{III}}-\text{O}^{\bullet}$ species as the active species derived from proton-coupled electron-transfer oxidation of the Ru^{II} -aqua catalyst. In addition, the sacrificial oxidant, Ce^{IV} salts (e.g. $(\text{NH}_4)_2[\text{Ce}^{\text{IV}}(\text{NO}_3)_6]$ and $\text{Ce}^{\text{IV}}(\text{SO}_4)_2$) are not so practical in light of their high commercial prices. Therefore, it should be required to develop an appropriate catalytic system, which involves reactive intermediates showing high reactivity in oxidation of electron-deficient aromatic rings, with cheaper and more accessible oxidants than the Ce^{IV} complexes.

Palladium catalysts having NHC ligands have been widely investigated for various purposes so far (see Chapter 1 of this thesis).¹⁹ NHC ligands have been used not only to enhance the catalytic activity²⁰ but also to stabilize unique palladium-oxygen species.²¹ Pd-NHC complexes have been widely utilized as catalysts even in water.²² In this chapter, a palladium(II)-aqua complex, having a tridentate NHC ligand as a catalyst, has been employed toward catalytic OBC reactions of HBDs with Oxone[®] as a cheap sacrificial oxidant in water under mild conditions. In addition, mechanistic insights into the OBC reactions by the Pd – NHC complex are gained on the basis of the product analysis and kinetic investigation.

5-2 Synthesis and characterization of a palladium(II)-NHC complex

A palladium(II) catalyst, $[\text{Pd}^{\text{II}}(\text{BPBIm})(\text{OH}_2)](\text{PF}_6)_2$ (**9**) (BPBIm = 1,3-bis(2-pyridylmethyl)-benzimidazol-2-ylidene), was synthesized by mixing $[\text{Pd}^{\text{II}}\text{Cl}(\text{BPBIm})](\text{PF}_6)_2$ and 1.1 equiv. of silver(I) trifluoromethanesulfonate in distilled water at 50 °C in the dark (Figure 5-3). Characterization of complex **9** was conducted by ^1H NMR and UV-Vis spectroscopies, ESI-TOF-MS spectrometry, elemental analysis, and X-ray crystallography.

In a ^1H NMR spectrum of **9** in D_2O , seven ^1H NMR signals based on the C_{2v} symmetry of the complex

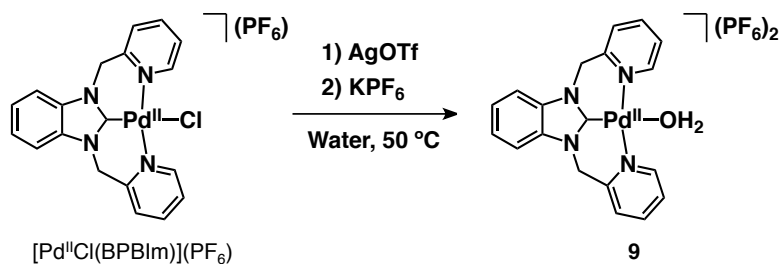


Figure 5-3. Synthesis of a Pd^{II}-aqua complex, **9**·(PF₆)₂.

were observed in the range of 4 ~ 9 ppm (Figure 5-4(a)). In an ESI-TOF-MS spectrum of **9** measured in acetone, a peak cluster derived from a divalent cation was clearly observed at $m/z = 232.02$ (sim. for [**9** - OH₂ + C₃H₆O]²⁺: $m/z = 232.04$) as a major peak cluster (Figure 5-4(b)). In the single-crystal X-ray crystallography of **9**, the palladium complex showed C₂ symmetry, which was not consistent with the ¹H NMR spectroscopic analysis (Figure 5-4(c)). This inconsistency between the crystal structure and ¹H NMR analysis can be explained by the seesaw-like fast flipping to exchange the positions of the left and right NHC nitrogen atoms (N2 and N3) above and below the equatorial plane of the square-planar Pd^{II} complex at room temperature in the NMR time scale. The bond lengths of Pd-C7 and Pd-O1 in **9** are 1.917(2) Å and 2.1155(19) Å, respectively. The value of Pd-C bond length is within the range of the corresponding bond lengths observed in other Pd^{II} complexes, having an NHC ligand (1.90 – 2.05 Å),²⁴ and the value of Pd-O1 bond length is also within the range of corresponding bond lengths in literature (2.04 – 2.14 Å).²⁵

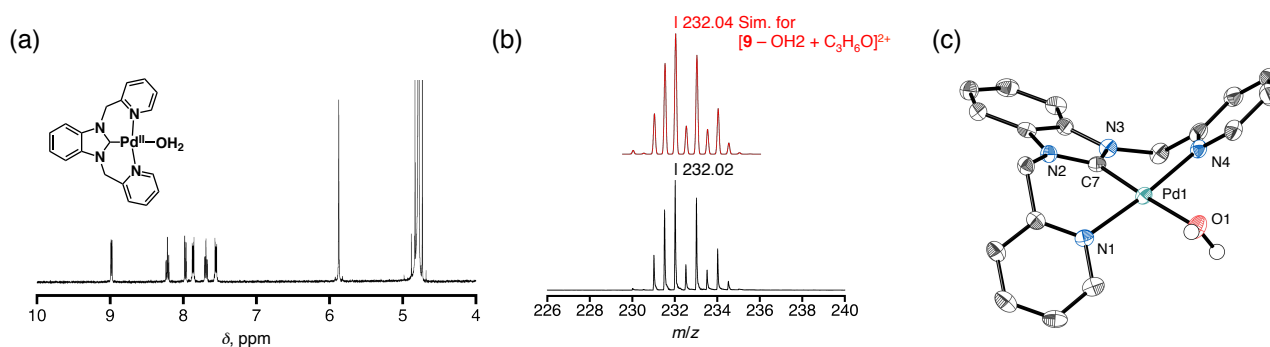


Figure 5-4. (a) ¹H NMR spectrum of **9** in D₂O. (b) ESI-TOF-MS spectrum of **9** measured in acetone. (c) ORTEP drawings of complex **9** with thermal ellipsoid of 50% probability.

5-3 Catalytic OBC reactions of HBDS

An OBC reaction was performed at room temperature under air using **9** as a catalyst as follows: 1 mL of *o*-dichlorobenzene was added to the D₂O solution (pD 2.0, 1 mL) of **9** (0.1 mM), followed by addition of Oxone[®] (100 mM) and the biphasic reaction mixture was stirred vigorously. After 24 h, the aqueous phase of the reaction mixture was analyzed spectroscopically to identify the products (Figure 5-5). In the ¹H NMR spectrum of the reaction mixture, a signal assignable to ¹HCOOH was observed at δ 8.29 ppm (Figure 5-5(a)) and a ¹³C NMR signal due to H¹³COOH was observed at δ 166 ppm in the ¹H-decoupled ¹³C NMR spectrum (Figure 5-5(b)). The two-dimensional heteronuclear single quantum coherence (HSQC) spectrum of the reaction mixture exhibited a correlation cross peak between the ¹H NMR signal at δ 8.29 ppm and the ¹³C NMR one at δ 166 ppm (Figure 5-5(c)). Thus, the product, observable in the NMR spectra, of the OBC reaction of *o*-dichlorobenzene was assigned to formic acid.

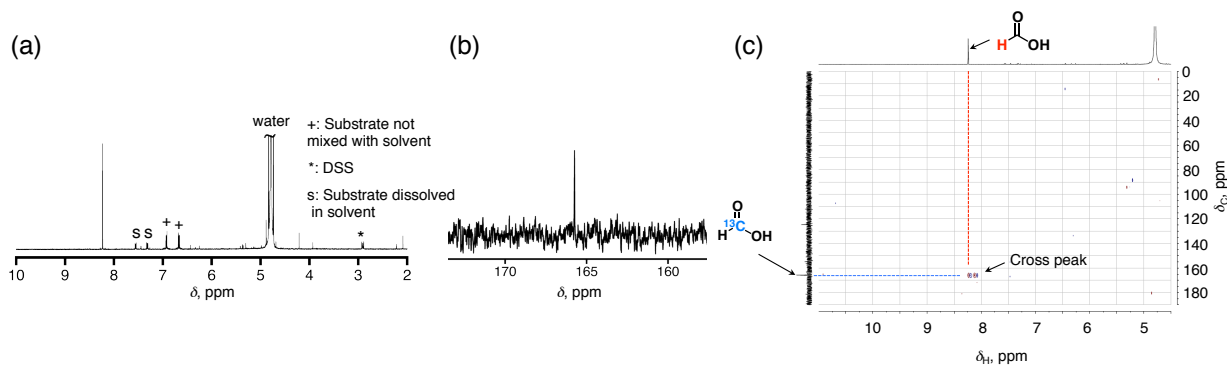


Figure 5-5. (a) ^1H NMR spectrum of the aqueous phase of the reaction mixture after stirring for 24 h in the presence of catalyst **9** (0.1 mM). The reactions were performed at 298 K in D_2O , the pH was set at pD 2.0, and the mixture included Oxone[®] (100 mM). (b) ^{13}C NMR spectrum of the aqueous phase of the reaction mixture, described above in the presence of **9** after stirring for 24 h. (c) HSQC spectrum of the aqueous phase of the reaction mixture in the presence of **9** after stirring for 24 h. ^1H NMR, ^{13}C NMR, and HSQC spectra were measured at 298 K.

The concentration of formic acid in the aqueous phase of the reaction mixture was determined by ^1H NMR spectroscopy with use of DSS (= sodium 4,4-dimethyl-4-silapentane-sulfonate) as an internal standard; the turnover number (TON) of the catalysis was determined to be 46. In the gas chromatogram (GC) of the gaseous phase of the sealed reaction vial, a peak derived from CO_2 was observed at the retention time of 7.2 min (Figure 5-6). The amount of CO_2 formed was determined by GC and the TON based on the amount of the catalyst was calculated to be 39. Carbon monoxide was not observed in the gaseous phases.²⁶

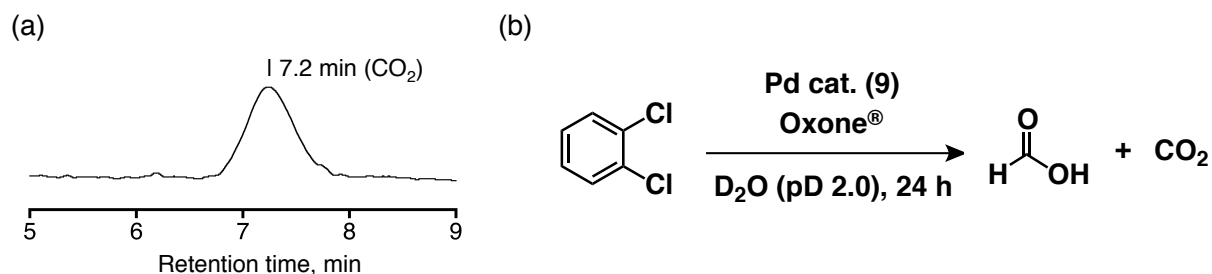


Figure 5-6. (a) A GC chart of the gaseous phase in the sealed reaction vial. (b) Schematic representation of the OBC reaction of *o*-dichlorobenzene as a substrate.

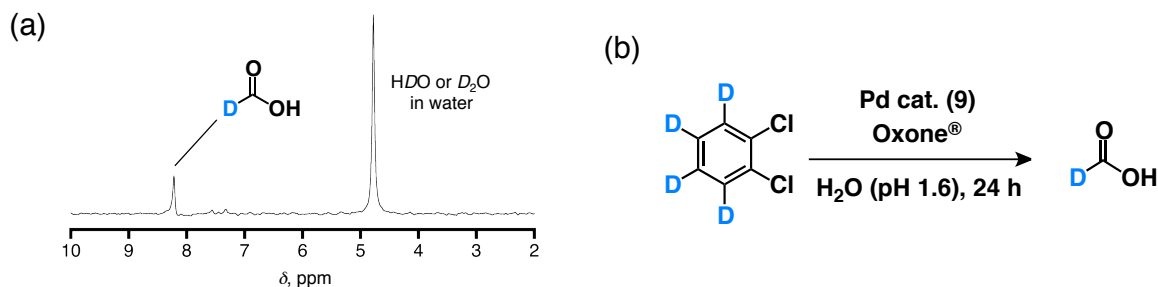


Figure 5-7. (a) ^2H NMR spectra of the reaction mixture for the OBC reaction of *o*-dichlorobenzene- d_4 in the presence of Oxone[®] (0.1 M) and **9** (0.1 mM) at pH 1.6. (b) Schematic representation of the catalytic OBC reactions of *o*-dichlorobenzene- d_4 in H_2O .

The efficiencies of the oxidation processes was calculated with the following equations: $100 \times \{([\text{HCOOH}] \times 3)/([\text{HSO}_5^-] \times 2)\}$ for formic acid, $100 \times \{([\text{CO}_2] \times 5)/([\text{HSO}_5^-] \times 2)\}$ for CO_2 . Thus, the efficiencies were determined to be 3.4% for formic acid and 4.8% for CO_2 . In addition, to improve the TON, the author performed the OBC reaction of benzene with lower concentration of **9** (10 μM) and higher concentration of Oxone[®] (0.3 M) at higher temperature (323 K) and the TONs for formic acid and CO_2 reached to 1560 and 5050, respectively at the reaction time of 24 h.

To confirm the origin of formic acid, deuterium-labeled *o*-dichlorobenzene- d_4 was used as a substrate for the catalytic OBC reaction in H_2O (pH 1.6). The ^2H NMR spectroscopic analysis on the reaction mixture showed a ^2H NMR signal assigned to DCOOH at δ 8.2 ppm (Figure 5-7(a)). Thus, we concluded that formic acid formed was definitely derived from benzene as the substrate in the OBC reaction. In addition, to confirm the origin of the oxygen atoms of formic acid obtained from the OBC reaction of *o*-dichlorobenzene under helium, ^{18}O -labeled water (H_2^{18}O) was used as a solvent, and peak clusters were observed at $m/z = 50$ for $\text{HC}^{18}\text{O}^{18}\text{OH}$ as well as at $m/z = 46$ for $\text{HC}^{16}\text{O}^{16}\text{OH}$ in the GC-MS spectra (Figure 5-8). Thus, the oxygen atoms of formic acid obtained are derived from both of water as a solvent and HSO_5^- as an oxidant. Since the oxygen atoms in HSO_5^- have been reported not to undergo exchange with a water molecule,²⁷ the observation of $\text{HC}^{16}\text{O}^{16}\text{OH}$ even in the reaction in H_2^{18}O indicates that the origin of the oxygen atoms are Oxone[®] as the oxidant. However, the author cannot determine the true origin of the oxygen atoms in $\text{HC}^{18}\text{O}^{18}\text{OH}$, because it should be possible that the reactive intermediates derived from **9** undergo rapid exchange of the oxygen atom with a water molecule during the reaction (see Figure 5-16(b)) or a water molecule is directly involved in the formation of oxidized intermediates derived from *o*-dichlorobenzene.

Other sacrificial oxidants were also examined for these catalytic OBC reactions. Comparing the TON

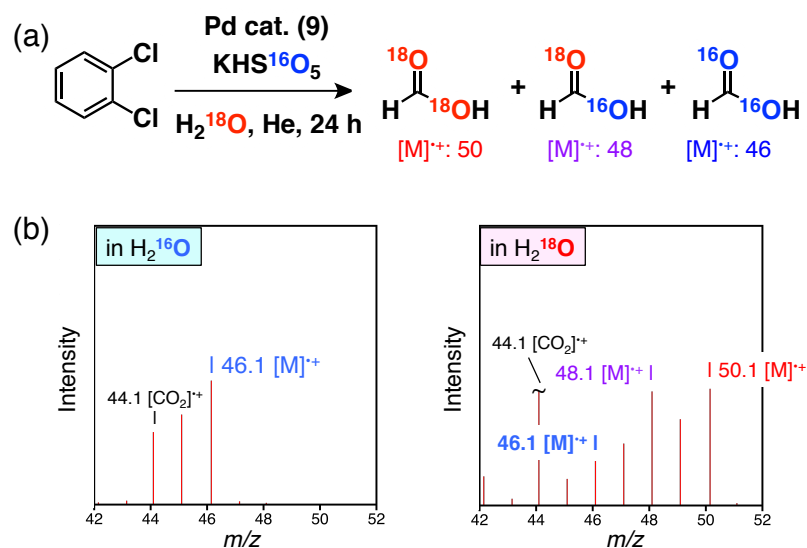


Figure 5-8. (a) Schematic representation for the catalytic OBC reaction of *o*-dichlorobenzene in H_2^{18}O . (b) EI-MS spectra of the fraction eluted at the retention time of 1.5 min obtained from the reactions in H_2^{16}O (left) and H_2^{18}O (right). $[\mathbf{9}] = 0.10 \text{ mM}$, $[\text{Oxone}^{\text{®}}] = 100 \text{ mM}$, $T = 298 \text{ K}$. The reactions were conducted under helium for 24 h. Parameters on GC-MS measurements are as follows: split mode (split ratio: 1/50), $T(\text{interface}) = 240 \text{ }^\circ\text{C}$, $T(\text{detector}) = 200 \text{ }^\circ\text{C}$. The temperature program was set as follows: $40 \text{ }^\circ\text{C}$ (2 min) – $20 \text{ }^\circ\text{C}/\text{min}$ – $200 \text{ }^\circ\text{C}$ (5 min). SH-Rxi-5ms capillary column (30 meter) was employed and helium was used as the carrier gas.

values and efficiencies, Oxone[®] was found to be most efficient for catalytic OBC reactions among other oxidants examined such as CAN mentioned in Chapter 3 (Entry 3 in Table 5-1). Despite the fact that the other oxidants, (NH₄)₂[Ce^{IV}(NO₃)₆] (CAN) and Ce^{IV}(SO₄)₂, also have high reduction potentials, formic acid was obtained in very low yields upon using these oxidants. This is because the reactive species is not formed from complex **9** with these electron-transfer oxidants due to its redox-innocent character of **9** (see below). Other palladium(II)-aqua complexes and metal salts were also employed as catalysts for the OBC reaction of *o*-dichlorobenzene in place of **9**; palladium catalysts also catalyzed the OBC reactions under the same conditions, comparable to **9** (Tables 5-2). Among these palladium complexes, [Pd^{II}(tpy)(OH₂)]²⁺ showed a relatively lower TON value. The results are probably derived from the ligand rigidity that inhibits structural changes of the Pd^{II} catalyst from square-planar Pd^{II} species to Pd^{III} or Pd^{IV} species in a different geometry.²⁸

Table 5-1. Effects of oxidants on the TON of the OBC reaction using *o*-dichlorobenzene as a substrate^a

Entry	Oxidant	TON(HCOOH)	Efficiency(HCOOH)	<i>E</i> _{red} (V vs SCE)
1	Oxone [®] (100 mM)	46	3.4	+1.58 ^c
2	Ce ^{IV} (SO ₄) ₂ ·4H ₂ O (100 mM) ^b	N. D.	N. D.	+1.20 ^c
3	CAN (400 mM)	5	0.4	+1.37 ^c
4	Na ₂ S ₂ O ₈ (200 mM)	2	0.2	+0.4 ^d

^a Reaction conditions are as follows: [**9**] = 0.1 mM, *T* = 298 K. Time: 24 h. *o*-Dichlorobenzene (1 mL) was used as the substrate. ^b H₂SO₄ in D₂O (pD 1.0) was used as a solvent for increasing solubility of the cerium salt. ^c ref. 29. ^d ref. 30.

Table 5-2. Comparison of the catalytic performance in the OBC reaction of *o*-dichlorobenzene among palladium complexes, or palladium or nickel salts as catalysts^a


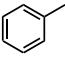
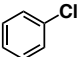
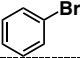
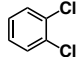
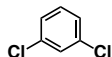
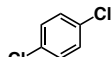
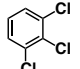
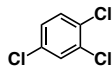
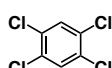
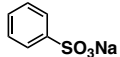
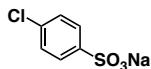
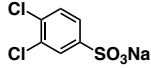
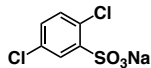
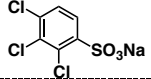
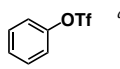
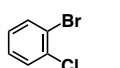
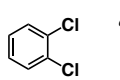
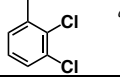
Catalyst	TON(HCOOH)	Efficiency(HCOOH) ^d
9 ·(PF ₆) ₂	46	3.4
Pd ^{II} (bpy)(OH ₂) ₂ ^b	37	2.8
Pd ^{II} (tpy)(OH ₂) ^c	16	1.2
Pd ^{II} SO ₄	42	3.2
Ni ^{II} SO ₄ ·4H ₂ O	7	0.5
none	–	–

^a [catalyst] = 0.1 mM, [Oxone[®]] = 100 mM, *T* = 298 K. Time: 24 h. ^b ref. 31. ^c ref. 32. ^d [efficiency] = 100([HCOOH] × 3 / [Oxone[®]] × 4). bpy = 2,2'-bipyridyl. tpy = 2,2';6',2''-terpyridyl.

5-4 Scope and limitation in the OBC reaction of benzene- and halogenated-benzene derivatives

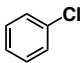
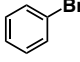
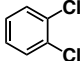
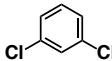
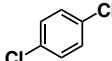
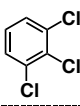
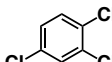
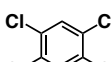
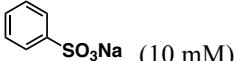
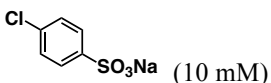
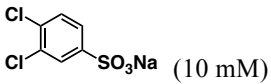
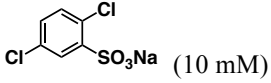
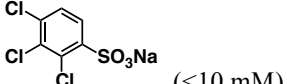
The OBC reaction catalyzed by **9** was also applied to other aromatic compounds as listed in Table 5-3. It is noteworthy that introduction of methyl groups as an electron-donating substituent decreased the TON values of formic acid as a product (entries 1 and 2 in Table 5-3), whereas that of chloro groups as an electron-withdrawing substituent increased the TONs (entries 3, 5, and 12 in Table 5-3). In comparison among chloro-substituted benzene derivatives, introduction of a sulfonate (SO₃⁻) group as an electron-withdrawing group decreased the TONs (entries 12 – 15 in Table 5-3), indicating electrophilic character of the reactive species (see below). However, benzene derivatives substituted by three or four chloro groups were not oxidized effectively, compared to the dichloro derivatives (entries 8, 9, 10, and 15 in Table 5-3), probably due to the poor solubility of the substrates in water.³³ The TONs of formic acid were

Table 5-3. Catalytic OBC reactions of various benzene and HBDs with **9** as the catalyst and Oxone[®] as the sacrificial oxidant in D₂O at 298 K.

Entry	Substrate	Product	TON ^b	Efficiency ^c
1		Formic acid	22	1.6
2		Formic acid Acetic acid	10 12	0.8 0.9
3		Formic acid	20	1.5
4		Formic acid	5	0.4
5		Formic acid	46	3.4
6		Formic acid	24	1.8
7		Formic acid	23	1.7
8		Formic acid	5	0.4
9		Formic acid	12	0.9
10		Formic acid	1	0.1
11	 (20 mM)	Formic acid	7	0.6
12	 (10 mM)	Formic acid	18	1.4
13	 (10 mM) ^d	Formic acid	9	0.7
14	 (10 mM) ^d	Formic acid	6	0.4
15	 (<10 mM) ^d	Formic acid	3	0.2
16	 ^d	Formic acid	5	0.4
17	 ^d	Formic acid	2	0.2
18	 ^d	Formic acid	15	1.1
19	 ^d	Formic acid Acetic acid	17 15	1.3 1.1

^a Solvent: D₂O (pD 2.0), [**9**] = 0.1 mM, [Oxone[®]] = 0.1 M, *T* = 298 K. Time: 24 h under air. ^b TON = [Product]/[Catalyst]. ^c Efficiency (%) = 100 × {([Product] × n)/([Oxone[®]] × 4)}. n = number of electrons required to produce one molecule of the product. ^d under Ar.

Table 5-4. Catalytic OBC reactions of various benzene and HBDs in the absence of **9** as the catalyst and Oxone[®] as the sacrificial oxidant in D₂O at 298 K.^a

Entry	Substrate	Product	Efficiency ^b
1		Formic acid	0.07
2		Formic acid	N. D.
3		Formic acid	0.06
4		Formic acid	0.06
5		Formic acid	0.11
6		Formic acid	0.06
7		Formic acid	0.07
8		Formic acid	0.03
9	 (10 mM)	Formic acid	N. D.
10	 (10 mM)	Formic acid	N. D.
11	 (10 mM)	Formic acid	N. D.
12	 (10 mM)	Formic acid	N. D.
13	 (<10 mM)	Formic acid	N. D.

^a Solvent: D₂O (pD 2.0), [**9**] = 0 mM, [Oxone[®]] = 0.1 M, *T* = 298 K. Time: 24 h under air. ^b Efficiency (%) = 100 × {([Product] × n) / ([Oxone[®]] × 4)}. n = number of electrons required to produce one molecule of the product.

not significantly affected by the position of the chloro groups on benzene rings (entries 13 and 14 in Table 5-3). No effect of the substituted positions of chloro groups on the reaction rates was also observed in kinetic analysis described in Section 5-6 in this chapter.

Substrates listed in Table 5-3 were oxidized with formation of negligible amounts of formic acid in the absence of **9** as a catalyst (Table 5-4). In addition, catalytic OBC reactions of substrates, having good leaving groups such as trifluoromethanesulfonate and bromo groups, were conducted (entries 4 and 16 in Table 5-3).

Comparing the TON values of formic acid as a product, both phenyl triflate and bromobenzene were oxidized with TON values of 5 and 11, respectively, lower than that of chlorobenzene as a substrate. These results indicate that this catalytic OBC reaction has proceeded not through oxidative addition of the substrates to the Pd^{II} center, which involves formal Pd^{II}/Pd^{IV} redox processes.

To scrutinize the electronic effects on the OBC reaction of chlorinated benzene derivatives, 1-bromo-2-chlorobenzene and 3-methyl-1,2-dichlorobenzene were used as substrates under Ar (entries 17 – 19 in Table 5-3). Despite the fact that all of these substrates have chlorobenzene moieties in the structures, substitution of a chloro group in *o*-dichlorobenzene with a bromo group significantly lowered the TON values of the products (entries 17 and 18 in Table 5-3). Since the Hammett parameter (σ) of the bromo group is very similar to that of the chloro group, the lower TON for the bromo derivative (entry 17 in Table 5-3) is not derived from the electronic effect of the bromo substituent. Thus, the bulkiness of the bromo group probably is assumed to have a negative impact for lowering the TON values of the products through steric hindrance.³⁴ In contrast, introduction of methyl group in *o*-dichlorobenzene increased the TON values (entries 18 and 19 in Table 5-3). This result indicates that electron-rich chlorobenzenes are easily oxidized by the reactive species. On the basis of these observations, it is suggested that the catalytic OBC reaction, described in this chapter, proceeds through an electrophilic reaction of the reactive species at the *ipso* position of the chloro groups.³⁵ It should be noted that the TON value of formic acid in entry 18 of Table 5-3 was lower than that of entry 5. The difference strongly suggests that molecular oxygen in the atmosphere enhances the formation of formic acid, probably due to the involvement of radical intermediates derived from the substrates in the course of the OBC reaction.³⁶ This is in sharp contrast to the OBC reaction by the Ru^{III}-O• complex as described in Chapter 4, in which no influence of O₂ has been observed on the TONs.¹⁸

5-5 Mechanistic insights on the OBC reaction of dihalogenated benzenesulfonates

On the basis of the observation that the OBC reactions are particularly enhanced by introduction of chloro groups, comparison of the degradation rates of HBDs, *o*-X₂PhS (X = F, Cl, or Br), in the OBC reactions was conducted (Figure 5-9(a)). As the result, initial degradation rates were determined to be 0.5 ×

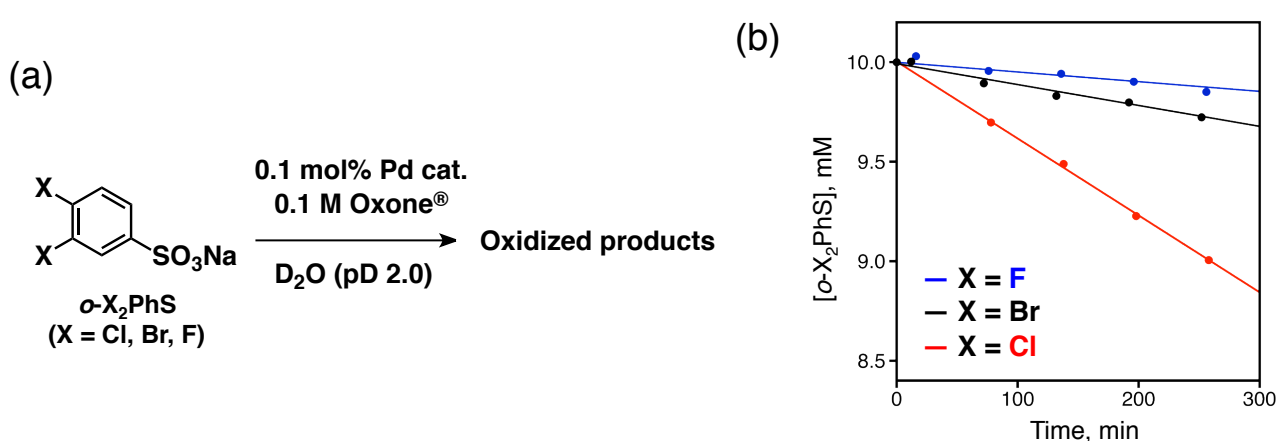


Figure 5-9. (a) Schematic representation of degradation of sodium *o*-dihalogenated benzenesulfonates, *o*-X₂PhS. (b) Comparison of the initial degradation rates of *o*-X₂PhS. Conditions: [9] = 0.1 mM, [*o*-X₂PhS] = 10 mM, [Oxone[®]] = 0.1 M, *T* = 298 K, under air. Sodium acetate was used as an internal standard to determine the concentrations of *o*-X₂PhS in the reaction mixtures.

10^{-3} , 3.9×10^{-3} , and 1.0×10^{-3} for $X = \text{F}$, Cl , and Br , respectively (Figure 5-9(b)). This tendency was not matched with their bond dissociation energies (BDE) of the C-X bonds (C-F: 125 kcal/mol, C-Cl: 95.5 kcal/mol, and C-Br: 80.4 kcal/mol in ref. 37). These results also reflect that this catalytic OBC reaction proceeds not through oxidative addition involving formal $\text{Pd}^{\text{II}}/\text{Pd}^{\text{IV}}$ redox couples as mentioned above.

In the ^{19}F NMR spectrum of the reaction mixture obtained from the OBC reaction of *o*-difluoro-

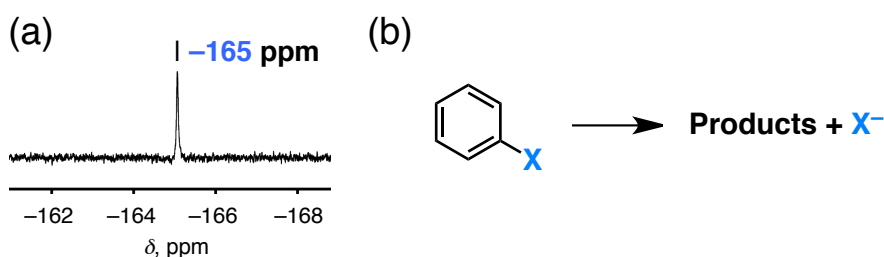


Figure 5-10. (a) A ^{19}F NMR signal derived from F^- obtained from the OBC reaction of *o*-difluorobenzenesulfonate as a substrate. $[\mathbf{9}] = 0.1 \text{ mM}$, $[\text{Oxone}^{\text{®}}] = 0.1 \text{ M}$, $T = 298 \text{ K}$, time: 48 h. (b) Schematic representation for dissociation of a halide group from substrate.

benzenesulfonate, a ^{19}F NMR signal derived from F^- ion was observed at -165 ppm (Figure 5-10(a)).³⁸ This indicates that this OBC reaction accompanies elimination of halide ions from benzene rings (Figure 5-10(b)).

Kinetic analysis has been also performed on the OBC reaction using sodium *o*-dichlorobenzenesulfonate (*o*- Cl_2PhS) as a substrate by ^1H NMR spectroscopy (Figure 5-11). The rate constants were investigated particularly with regards to the dependence on the concentrations of the substrate, oxidant, and catalyst. On the basis of time-courses of the substrate concentration in the initial stage of the reaction, the initial reaction rates (v_0) were determined (Figure 5-11). The dependence of the v_0 values on the substrate concentration exhibited saturation at higher concentrations (Figure 5-11(a)), which was analyzed on the basis of the Michaelis-Menten equation (eq 1):³⁹

$$v = V_{\text{max}}[\text{S}]/(K_{\text{m}} + [\text{S}]) \quad (1)$$

where, v is a rate of product formation and $[\text{S}]$ is a concentration of a substrate. The Michaelis constant, K_{m} , and the maximum rate, V_{max} , were determined to be $(5.6 \pm 2.5) \text{ mM}$ and $(7.0 \pm 0.9) \times 10^{-3} \text{ mM min}^{-1}$, respectively. This small K_{m} value indicates that there are relatively strong interactions between the substrate and the reactive species prior to the oxidation reaction. The dependence of the v_0 value on the oxidant and catalyst concentration was investigated to determine the catalytic rate constants (k_{cat}) under the conditions, where the substrate concentration was high enough to show the saturation of the v_0 value. As a result, v_0 showed first-order dependence on the oxidant concentration as well as the catalyst concentration in the OBC reaction of *o*- Cl_2PhS (Figure 5-11(b), (c)). Based on the linear relationships, k_{Oxone} and k_{cat} were determined to be $6.5 \times 10^{-5} \text{ min}^{-1}$ and $5.6 \times 10^{-2} \text{ min}^{-1}$, respectively. On the basis of these observation, there should be a pre-equilibrium process between the reactive species and substrate and the rate-determining step in the presence of a large excess amount of substrate should be a reaction of the palladium complex and Oxone[®] to afford a reactive species. In addition, to clarify effects of the substitution positions of chloro groups on the initial rates of the OBC reactions, sodium *p*-dichlorobenzenesulfonate (*p*- Cl_2PhS) was used as a substrate instead of *o*- Cl_2PhS . As a result, the dependence of the v_0 values on the substrate concentration also showed

saturation behavior at higher concentrations, which was also analyzed on the basis of the Michaelis-Menten equation (Figure 5-12).

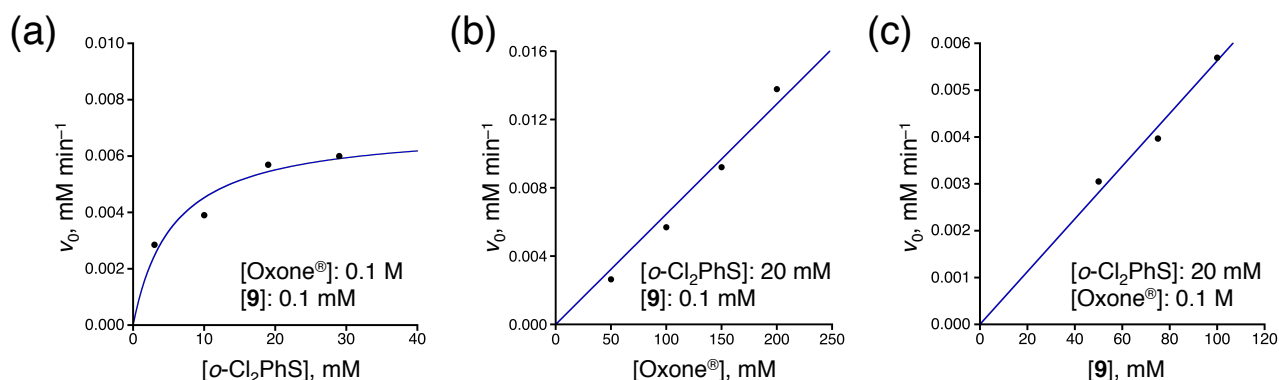


Figure 5-11. Dependence of the initial rates of degradation of $o\text{-Cl}_2\text{PhS}$ at 298 K in the OBC reaction, (a) on the concentration of $o\text{-Cl}_2\text{PhS}$ and the fitting curve based on the Michaelis-Menten equation (blue solid line), (b) on the concentration of Oxone[®], and (c) on the concentration of **9**. The concentrations of $o\text{-Cl}_2\text{PhS}$ were determined by ¹H NMR spectral measurements using sodium acetate as an internal standard.

The Michaelis constant, K_m , and the V_{\max} value were determined to be $(4.5 \pm 2.3) \text{ mM}$ and $(7.7 \pm 1.0) \times 10^{-3} \text{ mM min}^{-1}$, respectively. In comparison with the values of $o\text{-Cl}_2\text{PhS}$, no significant differences were recognized. This indicates that the positions of the chloro substituents are not influential to the reaction mechanism.

Furthermore, a dimethylated dichlorobenzene derivative, sodium *p*-dichloro-*p*-xylenesulfonate (*p*-Cl₂XyS) was used for comparison of the initial rates of the degradation. The initial rate of degradation

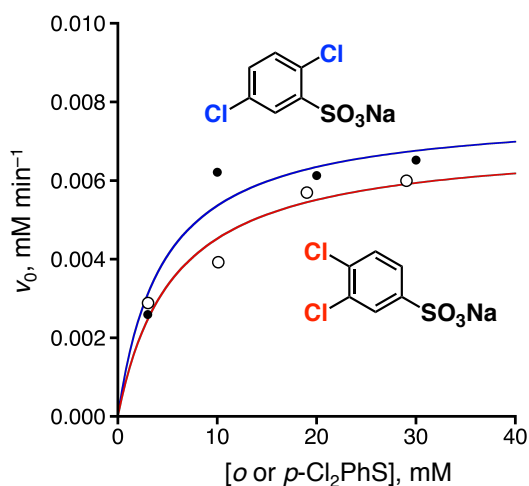


Figure 5-12. Overlaid plots for dependence of the initial rates of substrate degradation on the substrate concentrations: blue fitting curve and black-filled circles for *p*-Cl₂PhS and red fitting curve and white circles for *o*-Cl₂PhS. The fitting curves were provided based on the Michaelis-Menten equation (eq 1).

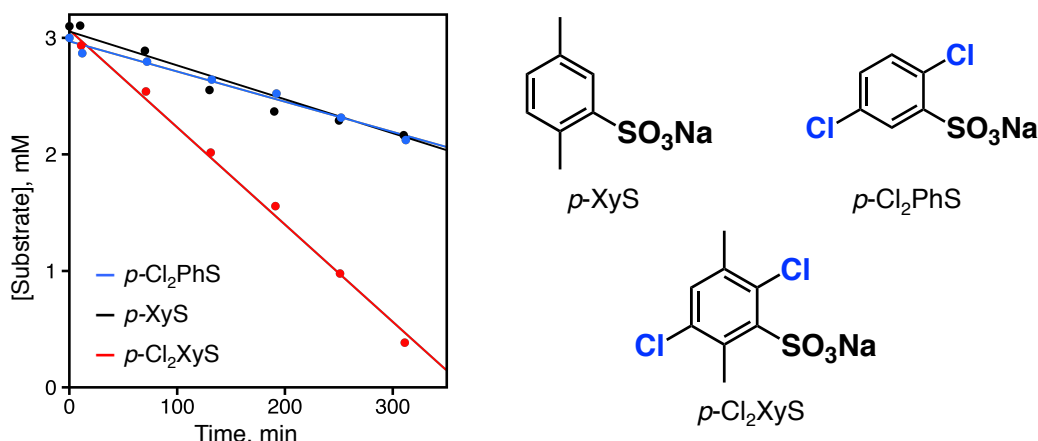


Figure 5-13. Comparison of the initial rates for degradation of *p*-Cl₂XyS, *p*-Cl₂PhS, and *p*-XyS. Solvent: D₂O (pD 2.0), [9] = 0.1 mM, [Oxone[®]] = 0.1 M, [Substrate] = 3 mM, *T* = 298 K. Concentration changes of the substrates were determined by ¹H NMR spectroscopy using sodium pivalate as an internal standard.

of *p*-Cl₂XyS was more than 3 times faster than that of *p*-Cl₂PhS (Figure 5-13). This acceleration of the degradation was not observed in the case of sodium *p*-xylenesulfonate (*p*-XyS) as a substrate. These comparisons indicate that the catalytic OBC reaction of HBDs should be accelerated by introduction of both electron-donating substituents and chloro groups on the benzene ring. It is consistent with the comparison of catalytic reactivity as mentioned in Table 5-3 (entries 18 and 19).

5-6 Formation and characterization of palladium-oxygen species

To reveal the reaction mechanism of the catalytic OBC reactions of HBDs by 9 in water, reactive intermediates generated from the reaction of 9 with Oxone[®] has been investigated. First of all, electrochemical measurements of 9 were conducted in acidic water. Within the potential window under the

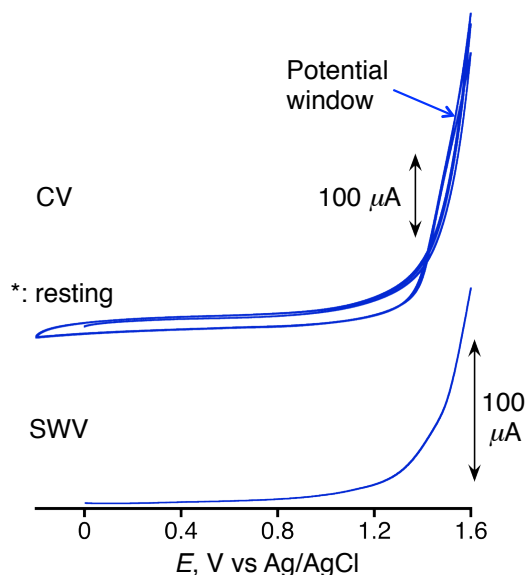


Figure 5-14. CV and SWV of 9 in H₂SO₄ aq (pH 1.6). [9] = 1.0 mM. Electrolyte: 0.1 M Li₂SO₄, working electrode: glassy carbon, counter electrode: Pt wire, reference electrode: Ag/AgCl. Temperature: RT.

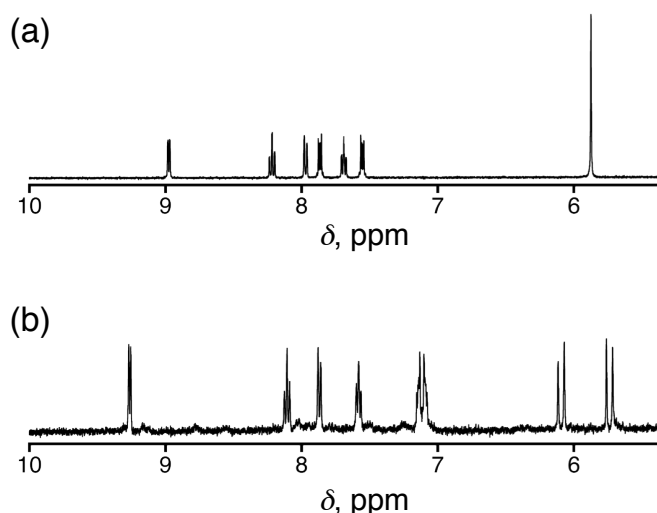


Figure 5-15. (a) ^1H NMR spectra of **9** in D_2O at 298 K. (b) ^1H NMR spectrum **9** in D_2O after 30 min of addition of 7 mol eq. of Oxone[®] at 278 K.

conditions, no redox wave derived from **9** was observed (Figure 5-14). On the other hand, the reduction potential of Oxone[®] has been reported to be +1.58 V vs SCE.²⁹ The electrochemical measurements indicate that Oxone[®] does not work as an electron-transfer oxidant, but probably as an oxo-transfer reagent in the OBC reactions.

In the ^1H NMR spectral analysis on the reaction of **9** with Oxone[®], a spectral change upon addition of 7 mol equiv of Oxone[®] ($[\text{HSO}_5^-]$: 14 mM) was observed in the diamagnetic region at 278 K (Figure 5-15). For example, the characteristic AB quartet derived from the methylene bridges was observed at 5.9 ppm (Figure 5-15(b)), indicating that the symmetry of complex **9** changed from C_{2v} to C_s symmetry. The ^1H NMR signals in the aromatic region shifted to upper and lower fields; however, the chemical shifts were in the range of those reported in Pd^{II} complexes (9.4 – 7.0 ppm).^{23–25} This desymmetrized palladium complex observed in the ^1H NMR spectral measurements is numbered as complex **10**.

In the ESI-TOF-MS measurement of the reaction mixture containing **9** and Oxone[®] after 2-min incubation, a peak cluster derived from a palladium complex was observed at $m/z = 518.96$ in acetonitrile/water = 4:1 (v/v) (Figure 5-16(a)). This peak cluster was assigned as $[\mathbf{9} - \text{OH}_2 + \text{HSO}_5^-]^+$, which was confirmed by comparison to the simulation ($m/z = 519.00$). Therefore, the ^1H NMR signals of **9** upon addition of 7 mol equiv Oxone[®] should be $[\text{Pd}^{\text{II}}(\text{BPBIm})(\text{HSO}_5)]^+$ (**10**).⁴⁰ In addition, a peak cluster for another palladium complex, formed by the reaction of **9** with Oxone[®] after 4-min incubation, was also observed at $m/z = 421.04$ (Figure 5-16(b)). This peak cluster was assigned as $[\text{Pd}(\text{BPBIm})(^{16}\text{O}) - \text{H}^+]^+$, which was confirmed by the simulation ($m/z = 421.03$). Furthermore, this peak cluster was shifted ($m/z = 423.01$) in acetonitrile/ H_2^{18}O instead of acetonitrile/ H_2^{16}O . Based on this observation, complex **10** releases an HSO_4^- ion to afford complex **11**, having an exchangeable terminal oxygen atom with water.⁴¹

To explain the desymmetrized ^1H NMR signals, DFT calculations of **10** were conducted at the RB3LYP/SDD level of theory. In the DFT-optimized structure of **10**, an HSO_5^- ligand was coordinated to the palladium center in a η^2 manner involving the oxygen atom of the peroxide moiety and the oxygen atom of the S-O moiety (Figure 5-17). Therefore, the molecular environments were different above and below the equatorial plane of **10**, which resulted in the desymmetrized ^1H NMR signals (see above). The stretching vibration frequencies of the O-O bond in HSO_5^- ligand were also calculated to be 1011 and 1035 cm^{-1} .⁴²

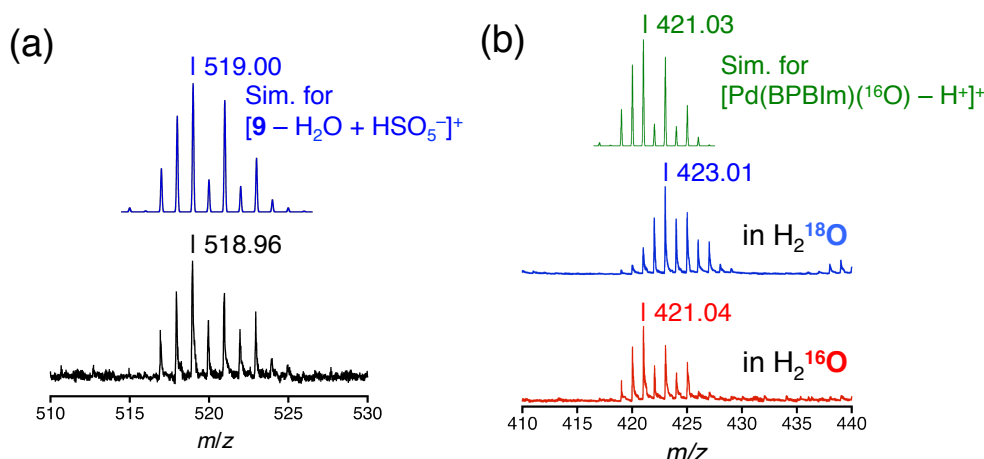


Figure 5-16. (a) ESI-TOF-MS spectrum of **9** upon addition of 7 equiv Oxone[®] in acetonitrile/water = 4 : 1 (v/v), after 2-min incubation to form **10** and the simulated spectrum for [**10**]⁺ (blue). (b) ESI-TOF-MS spectra of **9** upon addition of 7 equiv Oxone[®] in acetonitrile/H₂¹⁶O = 4:1(v/v) (red), and in acetonitrile/H₂¹⁸O (blue), after 4-min incubation. The simulated spectrum for [Pd(BPBIIm)(¹⁶O) – H⁺]⁺ is shown at the top (green). These samples were prepared as follows: 1 mM solution of **9** in 1 mL of H₂SO₄ aq (pH 1.6) or 200 μL of H₂¹⁸O was added to 4.2 mg or 0.8 mg of Oxone[®], respectively, at RT. Then, 200 μL of the reaction mixture was diluted with 800 μL of acetonitrile and colorless precipitates formed were removed by filtration before the measurements.

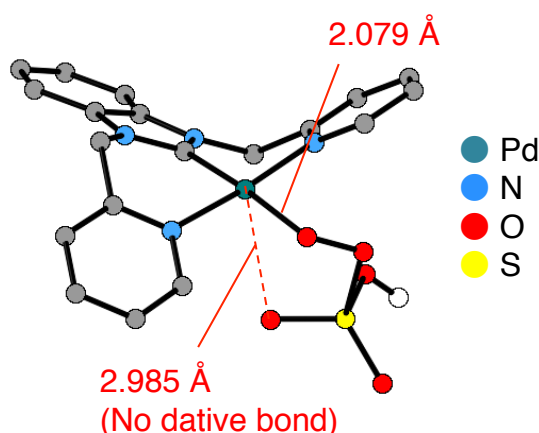


Figure 5-17. DFT-optimized structure of **10** at RB3LYP/SDD level of theory.

In the UV-vis spectral measurements, absorption bands of **9** decreased the absorbance around 280 nm and showed a new weak band at 360 nm upon addition of Oxone[®]. The newly observed absorption band at 360 nm was assigned to metal-to-ligand charge-transfer (MLCT) transitions of **10** from the palladium(II) center to the HSO₅⁻ ligand on the basis of the TD-DFT calculations of **10** (Figure 5-18). In addition, complex **10** was characterized by resonance Raman (rR) spectroscopy with laser excitation at 355 nm, which was consistent with the MLCT band (Figure 5-19). In the rR spectrum, a Raman band derived from the stretching vibration of the O-O bond was observed at 1017 and 1040 cm⁻¹. These values are consistent with those estimated by the DFT calculations.

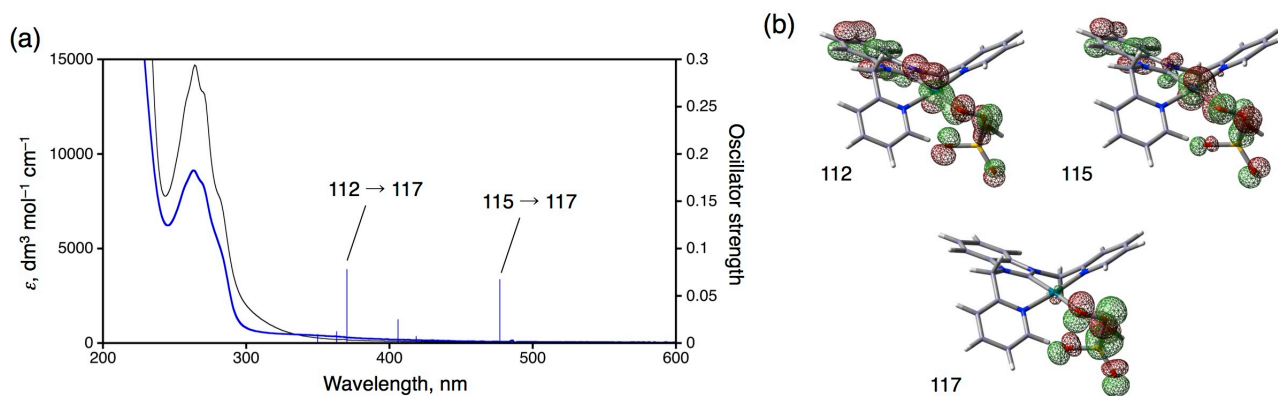


Figure 5-18. (a) Time-course measurements of UV-vis spectra of **9** (1 mM) in D₂O (pD 2.0) upon addition of 7 equiv of Oxone[®] measured at 0 s (black) and 200 s (blue) at 298 K. An isosbestic point was observed at $\lambda = 327$ nm. The optical path length of a cell used was 1 mm. Oscillator strengths are shown with blue lines, obtained by TD-DFT calculations of **10** at the RB3LYP/SDD level of theory. (b) Corresponding molecular orbitals (112, 115, and 117) related to the oscillators.

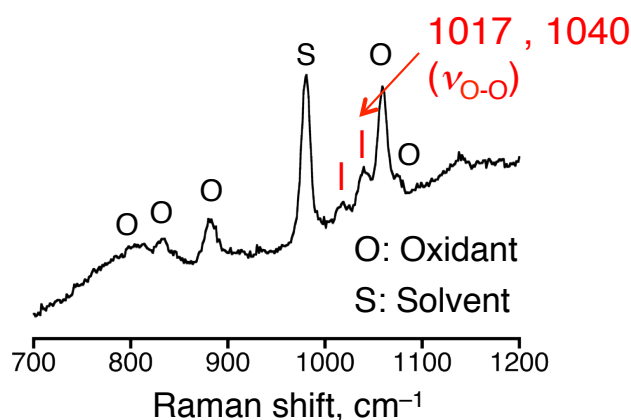


Figure 5-19. Resonance Raman spectrum of complex **10**, generated *in situ* from **9**. [**9**] = 10 mM, [Oxone[®]] = 70 mM, $T = 276$ K, solvent: H₂SO₄ aq (pH 1.6). Excitation wavelength: 355 nm.

Further conversion of complex **10** was investigated spectroscopically at 278 K. Complex **10** did not show any further spectral change at least for 1 h. In contrast, at 298 K, spectral changes of **10** were observed around 350 nm in the UV-vis spectra, and the color of the solution changed from pale-yellow to yellow (Figure 5-20(a)). In the ¹H NMR spectra, rapid decomposition of complex **10** was observed after 30 min to afford a complicated mixture at 298 K (Figure 5-20(b)). These observations imply that complex **11** formed from **10** underwent rapid decomposition at 298 K.

However, complex **10** did not show any spectral change upon addition of *p*-Cl₂XyS as a substrate at 278 K (Figure 5-21). This indicates that complexes **10** and **11**, derived from decomposition of **10**, are not reactive species in the catalytic OBC reaction catalyzed by **9**. Based on the fact that the catalytic OBC reactions of HBDs require a large excess amount of Oxone[®], the true reactive species should not be complex **11** itself, but a species obtained from further reaction of **11** with Oxone[®]. Unfortunately, such reactive species have yet to be detected by any spectroscopic measurements.

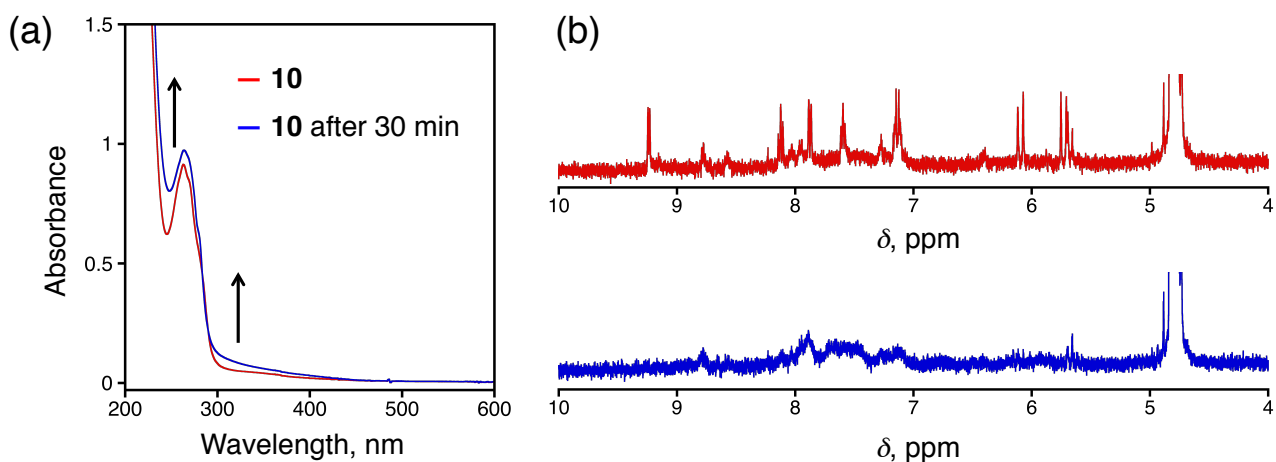


Figure 5-20. (a) UV-Vis spectral change of **10** in D₂O (pD 2.0) at 298 K. No isosbestic point was observed in the course of the measurements. (b) ¹H NMR spectra of complex **10** in D₂O (pD 2.0) measured right after starting the reaction (red) and 30 min later (blue) at 298 K. Complex **10** was generated *in situ* according to the following procedure: Complex **9** (1 mM) in D₂O (pD 2.0) was added to Oxone[®] (4.3 mg) at RT. The reaction mixture was transferred to an UV-cell (Optical path: 1 mm) for UV-vis spectroscopy or an NMR tube for ¹H NMR spectroscopy at 298 K.

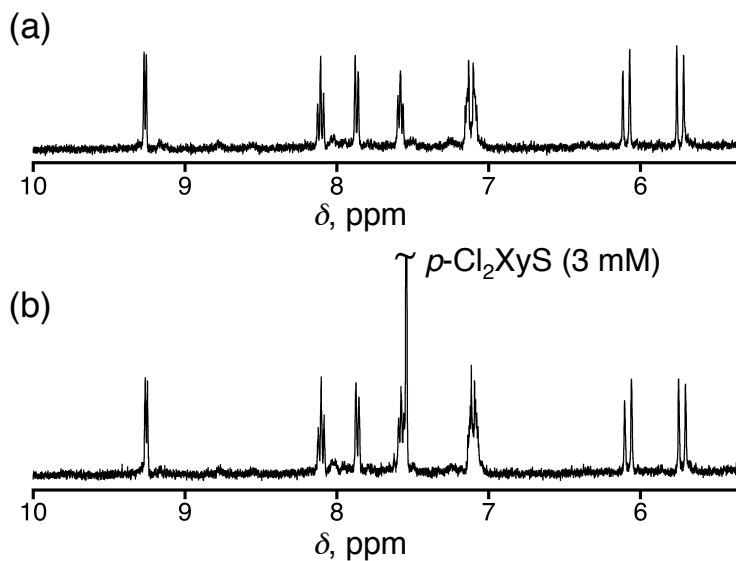


Figure 5-21. ¹H NMR spectrum of **10** (1 mM) in D₂O (pD 2.0) (a) and that after addition of *p*-Cl₂XyS (3 mM, saturated) as a substrate (b) at 278 K.

5-7 A proposed mechanism of the catalytic OBC reaction by **9** with Oxone[®]

On the basis of the product analysis and the kinetic studies mentioned above, a plausible mechanism for the OBC reaction of *o*-dichlorobenzene catalyzed by **9** has been proposed as shown in Figure 5-22. In the first step, complex **9** reacts with Oxone[®] to afford complex **10**. Then, complex **10** releases HSO₄⁻ to afford complex **11**. Further reaction of complex **11** and Oxone[®] affords the true reactive species named as “Pd-O” in Figure 5-22. The “Pd-O” exhibits a pre-equilibrium process to interact with *o*-dichlorobenzene, followed by electrophilic addition to substrates coupled with removal of a Cl⁻ ion. Chlorobenzoquinone is formed as one of the intermediates, which was observed in the GC-MS spectral measurements of the reaction mixture (Figure 5-23).

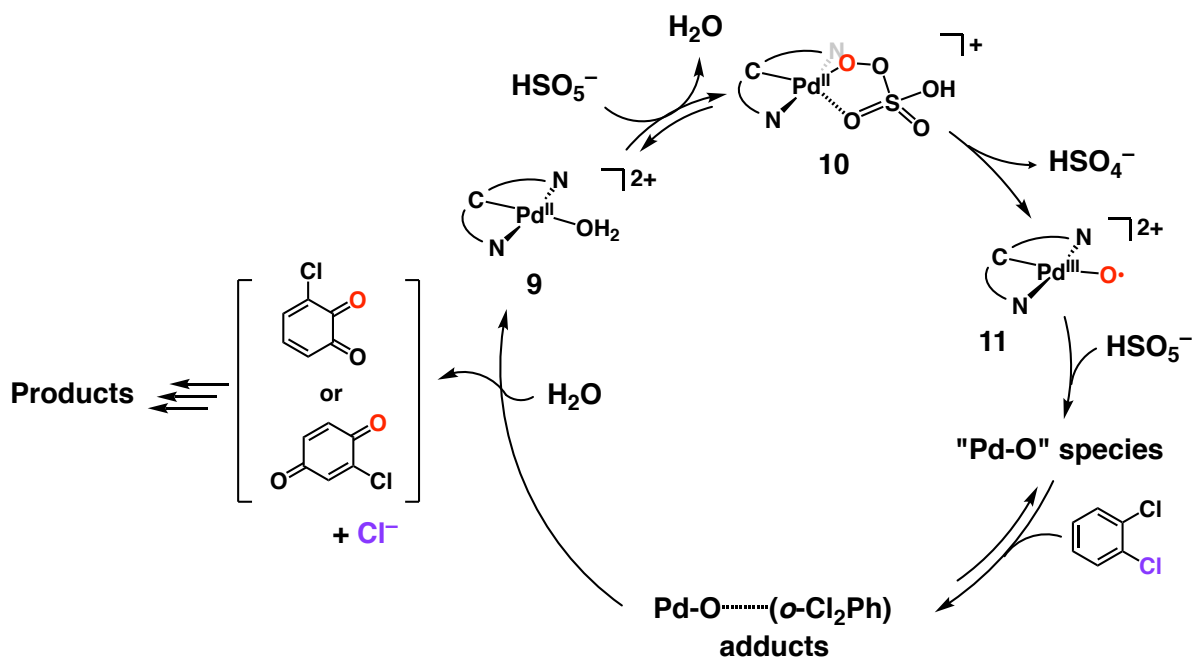


Figure 5-22. A proposed mechanism of the OBC reaction catalyzed by **9**.

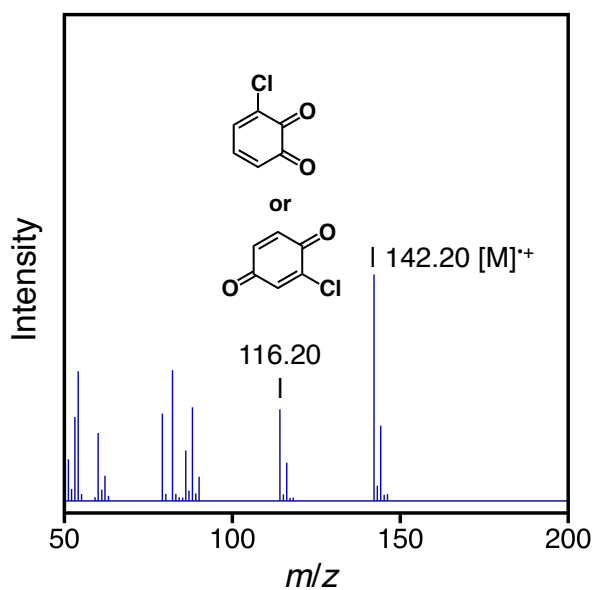


Figure 5-23. EI-MS spectrum of chlorobenzoquinone, observed at the retention time of 6.9 min in the GC chart for the reaction mixture of the catalytic OBC reaction of *o*-dichlorobenzene.

5-8 Conclusions

Catalytic OBC reactions of HBDs, which were not achieved even by $\text{Ru}^{\text{III}}\text{-O}\cdot$ species described in Chapter 4, were successfully established to obtain formic acid and carbon dioxide under mild conditions. In addition, the author has revealed that introduction of electron-donating substituents on the aromatic rings of chlorobenzene derivatives can increase the rates of degradation of the substrates. Also, a palladium- HSO_5^- complex (**10**) was characterized by several spectroscopic methods, although complex **10** and the $\text{Pd}^{\text{III}}\text{-O}\cdot$ species (**11**) derived from **10** did not work as reactive species. In the catalytic cycle, the true reactive species,

formed by the reaction between the Pd^{III}-O• species **11** and HSO₅⁻, should react with HBDs accompanying adduct formation between the reactive species and the substrate. The catalytic OBC reaction of HBDs, developed in this chapter, will provide a novel methodology for degradation of HBDs including PCBs to afford useful materials under mild conditions in water.

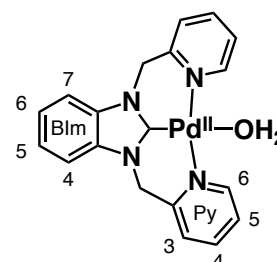
5-9 Experimental section

General.

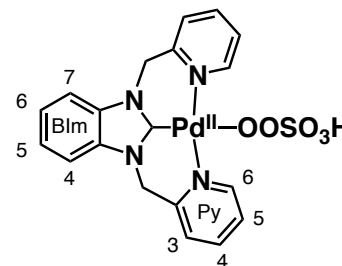
NMR measurements were performed on Bruker Avance 400 and Avance III HD 400 spectrometers and JEOL JNM-ECS400 spectrometers. DSS (= 3-(trimethylsilyl)-propane-sulfonate sodium salt) or sodium acetate was used as internal standards for ¹H NMR spectral measurements in D₂O. Gas chromatography was performed using a Shimadzu GC-2014 equipped with a thermal conductivity detector (TCD) and a packed column with molecular sieves 5A or a packed column with activated carbon. ESI-TOF-MS spectra were obtained on a JEOL JMS-T100CS mass spectrometer. UV-Vis absorption spectra were measured on an Agilent 8453 photodiode-array spectrophotometer. GC-MS measurements were performed using a Shimadzu GC-2010 Plus, equipped with a Shimadzu GCMS-QP2020 and a Shimadzu SH-Rxi-5ms capillary column (30 meter, ID 0.25, DF 0.25).

Synthesis.

[Pd^{II}(BPBIm)(OH₂)](PF₆)₂ (9**·(PF₆)₂).** A solution of Ag^I(OTf) (102 mg, 396 μmol) in distilled water (5 mL) was added to the suspension of [Pd^{II}Cl(BPBI)](PF₆) (200 mg, 341 μmol) in water (20 mL). Then, the reaction mixture was stirred and heated at 50 °C overnight in the dark. After colorless precipitate was observed, the reaction mixture was filtered by membrane filter to remove the precipitate. Addition of an excess amount of saturated KPF₆ aq (300 mg in 5 mL of water) to the filtrate resulted in formation of colorless or pale-yellow crystalline powder, and then the powder was filtered and washed by small amount of water. Finally, the powder was dried under vacuum. Pale-yellow powder (151 mg, 206 μmol) of the title compound was obtained in 60% yield. ¹H NMR (D₂O, 278 K): δ 8.98 (d, *J* = 8.0 Hz, Py-6, 2H), 8.22 (t, *J* = 8.0 Hz, Py-4, 2H), 7.97 (d, *J* = 7.1 Hz, Py-3, 2H), 7.87 (m, BIm-5 and -6, 2H), 7.69 (t, *J* = 8.0 Hz, Py-5, 2H), 7.55 (m, BIm-4 and -7, 2H), 5.87 (s, Py-CH₂-Im, 4H). ESI-TOF-MS (Acetone): *m/z* = 232.02 (sim for [**9** - OH₂ + C₃H₆O]²⁺: *m/z* = 232.04). Anal. Calcd. for C₁₉H₁₈N₄Opd·2PF₆·0.5H₂O: H 2.65, C 31.53, N 7.74; Found: H 2.44, C 31.42, N 7.59.



[Pd^{II}(HSO₅)(BPBIm)]⁺ (10**).** A solution of **9** (1 mM) in D₂O (1 mL, pD 2.0, controlled by conc. H₂SO₄) was added to the Oxone[®] (4.28 mg, 7.0 μmol) in an ice bath. Within 30 min, the color of solution gradually turned from colorless to pale-yellow. ¹H NMR (D₂O, 278 K): δ 9.26 (d, *J* = 5.6 Hz, Py-6, 2H), 8.10 (t, *J* = 7.7 Hz, Py-4, 2H), 7.86 (d, *J* = 7.8 Hz, Py-3, 2H), 7.57 (t, *J* = 6.4 Hz, Py-5, 2H), 7.1 (m, BIm-4, -5, -6, and -7, 4H), 6.09 (ABq, *J* = 18 Hz, Py-CH₂-Im, 2H), 5.7 (ABq, *J* = 18 Hz, Py-CH₂-Im, 2H). ESI-TOF-MS (MeCN/water): *m/z* = 518.96 (sim for [**9** - OH₂ + HSO₅]⁺: *m/z* = 519.00).



General procedure for oxidative cracking of HBDs.

A sample vial (10 mL) sealed by a rubber septum was filled with a biphasic reaction mixture consisting of a D₂O solution (1 mL) of **9** (0.1 mM) and Oxone[®] (= KHSO₄·K₂SO₄·2KHSO₅, 100 mM) as an

aqueous layer, whose pD was adjusted to be 2.0 by addition of acidic Oxone[®], and 1 mL of a substrate as an organic layer. In most cases, the reactions were performed at 298 K in a water bath equipped with a temperature controller (COOL STIRRER SAC-900). A schematic representation of the reaction setup is shown in Figure 5-24.

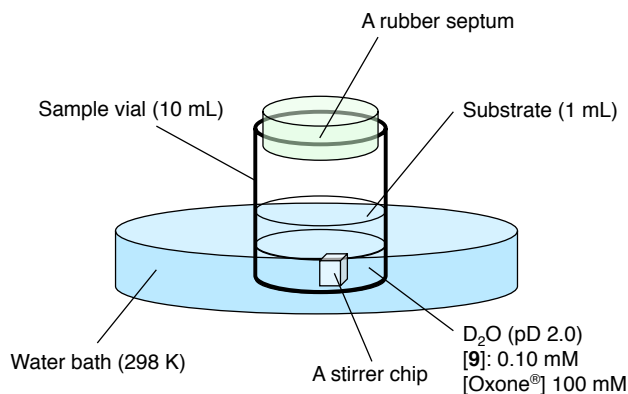


Figure 5-24. Simple cartoon of the experimental setup used in this work.

Kinetic analysis on the OBC reactions of sodium *o*-dichlorobenzenesulfonate (*o*-Cl₂PhS).

The ¹H NMR signals of *o*-Cl₂PhS were observed to monitor the reaction progress in D₂O (pD 2.0). The amounts of *o*-Cl₂PhS were determined using anhydrous sodium acetate as an internal standard. A linear least-squares fitting was conducted for the time profile of amounts of decaying substrates observed in the range of 0 – 360 min and the slopes of the fitting lines obtained were used as the initial rates (v_0) of *o*-Cl₂PhS oxidation. The v_0 values for *o*-Cl₂PhS degradation were determined at various catalyst and oxidant concentrations and the catalytic rate constants, k_{cat} and k_{Oxone} , were determined with eqs 2 and 3.

$$v_0 = k_{\text{cat}}[\mathbf{9}] \quad (2)$$

$$v_0 = k_{\text{Oxone}}[\text{Oxone}^{\text{®}}] \quad (3)$$

Determination of K_m and V_{max} values for the OBC reaction of *o*-Cl₂PhS.

The initial rates, v_0 , for the OBC reactions of *o*-Cl₂PhS at various concentrations (4 – 30 mM) were obtained according to the procedure described above. The obtained v_0 values were plotted versus the substrate concentrations. The v_0 values exhibited saturation behavior with respect to the substrate concentration (see Figure 5-11(a)). On the basis of the Michaelis-Menten equation³⁹ as described in eqs 1 and 4, the Michaelis constant, K_m , and the maximum rate in the system, V_{max} , were determined by fitting analysis.

$$v_0 = (V_{\text{max}}[o\text{-Cl}_2\text{PhS}]) / (K_m + [o\text{-Cl}_2\text{PhS}]) \quad (4)$$

X-ray crystallography.

Single crystals of $\mathbf{9} \cdot (\text{PF}_6)_2$, suitable for X-ray crystallography, were obtained by recrystallization with slow condensation of an aqueous solution of $\mathbf{9} \cdot (\text{PF}_6)_2$. One of the crystals was mounted using a mounting loop. All diffraction data were collected on a Bruker APEXII diffractometer at 120 K with a graphite-monochromated Mo K α radiation source ($\lambda = 0.71073 \text{ \AA}$) by the 2θ scan. All structure refinements were performed using the Yadokari-XG crystallographic software package.⁴³ The structures were solved by a direct method using SIR97 and SHELX97.⁴⁴ Crystallographic data for $\mathbf{9} \cdot (\text{PF}_6)_2 \cdot \text{H}_2\text{O}$ are summarized in Table 5-6.

Table 5-6. Crystallographic data for **9·(PF₆)₂·H₂O**

Compound	9·(PF₆)₂
MW	732.73
Formula	C ₁₉ H ₁₈ N ₄ OPd·2PF ₆ ·H ₂ O
Crystal system	Orthorhombic
Space group	<i>Pbca</i>
<i>a</i> , Å	15.8888(16)
<i>b</i> , Å	18.2937(18)
<i>c</i> , Å	17.2587(17)
α , °	90
β , °	90
γ , °	90
<i>V</i> , Å ³	5016.5(9)
<i>Z</i>	8
<i>R</i> 1	0.0291
<i>wR</i> 2	0.1021
GOF	0.966

Resonance Raman spectroscopy.

The sample solution of **10** was prepared by the following procedure; complex **9·(PF₆)₂** (7.41 mg, 10 μ mol) was suspended into water (pH 1.6, 1 mL), and Oxone[®] (42.9 mg, 70 μ mol) was added to the suspension in ice bath. Resonance Raman spectroscopic measurements were conducted using the solution. Resonance Raman scattering was made by excitation at 355 nm with a He-Cd laser (Kimmon Koha, IK5651R-G), dispersed by a single polychromator (Chromex, 500IS) and detected by a liquid-nitrogen-cooled CCD detector (Roper Scientific, Spec10:400B/LN). The resonance Raman measurements were carried out at 276 K using a spinning cell (outer diameter = 5 mm, wall thickness = 0.2 mm) at 135° scattering geometry.

DFT calculations.

The global minima on the potential energy surfaces were searched to optimize the structures by using the restricted or unrestricted B3LYP method.⁴⁵ To reproduce the absorption and emission spectra, TD-DFT calculations⁴⁶ were performed on the basis of the optimized structures. For all of the atoms, we used the SDD basis sets.⁴⁷ The Gaussian 09 program package⁴⁸ was used for all DFT calculations.

References and notes.

- (1) (a) R. Jayaraj, P. Megha, P. Sreedev, *Interdiscip. Toxicol.* **2016**, *9*, 90–100. (b) A. Biffis, P. Centomo, A. D. Zotto, M. Zecca, *Chem. Rev.* **2018**, *118*, 2249–2295. (c) J. F. Hartwig, *Angew. Chem., Int. Ed.* **1998**, *37*, 2046–2067. (d) K. Müller, C. Faeh, F. Diederich, *Science* **2007**, *317*, 1881–1886.
- (2) M. D. Erickson, R. G. Kaley II, *Environ. Sci. Pollut. Res.* **2011**, *18*, 135–151.
- (3) (a) K. Hornbuckle, L. Robertson, *Environ. Sci. Technol.* **2010**, *44*, 2749–2751. (b) C. Porte, J. Albaigés, *Arch. Environ. Contam. Toxicol.* **1993**, *26*, 273–281.
- (4) D. H. Evans, M. Pirbazari, S. W. Benson, T. T. Tsotsis, J. S. Devinny, *J. Hazard. Mater.* **1991**, *27*, 253–272.

- (5) (a) C. E. Hetrick, F. Patcas, M. D. Amiridis, *Appl. Catal. B: Environmental* **2011**, *101*, 622–628. (b) L. Becker, H. Förster, *J. Catal.* **1997**, *170*, 200–203. (c) Y. Liu, Z. Wei, Z. Feng, M. Luo, P. Ying, C. Li, *J. Catal.* **2001**, *202*, 200–204. (d) J. Wang, X. Wang, X. Liu, J. Zeng, Y. Guo, T. Zhu, *J. Mol. Catal. A: Chemical* **2015**, *402*, 1–9. (e) X. Ma, X. Suo, H. Cao, J. Guo, L. Lv, H. Sun, M. Zheng, *Phys. Chem. Chem. Phys.* **2014**, *16*, 12731–12740.
- (6) (a) K. Nomiyama, T. Tanizaki, H. Ishibashi, K. Arizono, R. Shinohara, *Environ. Sci. Technol.* **2005**, *39*, 8762–8769. (b) L. Huang, G. Su, A. Zhang, Y. Shi, C. Xia, H. Lu, L. Li, S. Liu, M. Zheng, *J. Hazard. Mater.* **2013**, *261*, 451–462.
- (7) (a) G. A. Grasa, M. S. Viciu, J. Huang, S. P. Nolan, *J. Org. Chem.* **2001**, *66*, 7729–7737. (b) M. R. Biscoe, B. P. Fors, S. L. Buchwald, *J. Am. Chem. Soc.* **2008**, *130*, 6686–6687.
- (8) (a) L. Botella, C. Nájera, *Angew. Chem., Int. Ed.* **2002**, *41*, 179–181. (b) P. Nehra, B. Khungar, K. Pericherla, S. C. Sivasubramanian, A. Kumar, *Green Chem.* **2014**, *16*, 4266–4271. (c) R. Garrido, P. S. Hernández-Montes, Á. Gordillo, P. Gómez-Sal, C. López-Mardomingo, E. de Jesús, *Organometallics* **2015**, *34*, 1855–1863.
- (9) G.-J. ten Brink, I. W. C. E. Arends, R. A. Sheldon, *Science* **2000**, *287*, 1636–1639.
- (10) (a) A. J. Hickman, M. S. Sanford, *Nature* **2012**, *484*, 177–185. (b) K. Muñoz, *Angew. Chem., Int. Ed.* **2009**, *48*, 9412–9423.
- (11) W. Oloo, P. Y. Zavalij, J. Zhang, E. Khaskin, A. N. Vedermikov, *J. Am. Chem. Soc.* **2010**, *132*, 14400–14402.
- (12) F. Tato, A. García-Domínguez, D. J. Cárdenas, *Organometallics* **2013**, *32*, 7487–7494.
- (13) S. P. Desai, M. Mondal, J. Choudhury, *Organometallics* **2015**, *34*, 2731–2736.
- (14) K. Yamamoto, J. Li, J. A. O. Garber, J. D. Rolfes, G. B. Boursalian, J. C. Borghs, C. Genicot, J. Jacq, M. van Gastel, F. Neese, T. Ritter, *Nature* **2018**, *554*, 511–514.
- (15) (a) A. V. Narsaiah, *Synlett* **2002**, 1178–1179. (b) J. Cornely, L. M. S. Ham, D. E. Meade, V. Dragojlovic, *Green Chem.* **2003**, *5*, 34–37. (c) R. Song, A. Sorokin, J. Bernadou, B. Meunier, *J. Org. Chem.* **1997**, *62*, 673–678.
- (16) (a) S. Campestrini, M. Crisma, *Molecules* **2000**, *5*, 886–894. (b) E. O. Schlemper, R. C. Thompson, C. K. Fair, F. K. Ross, E. H. Appelman, L. J. Basile, *Acta Cryst.* **1984**, *C40*, 1781–1785.
- (17) L. V. Desai, H. A. Malik, M. S. Sanford, *Org. Lett.* **2006**, *8*, 1141–1144.
- (18) Y. Shimoyama, T. Ishizuka, H. Kotani, T. Kojima, *ACS Catal.* **2019**, *9*, 671–678.
- (19) (a) G. C. Fortman, S. P. Nolan, *Chem. Soc. Rev.* **2011**, *40*, 5151–5169. (b) E. A. B. Kantchev, C. J. O'Brien, M. G. Organ, *Angew. Chem., Int. Ed.* **2007**, *46*, 2768–2813.
- (20) M. Muehlhofer, T. Strassner, W. A. Herrmann, *Angew. Chem., Int. Ed.* **2002**, *41*, 1745–1747.
- (21) X. Cai, S. Majumdar, G. C. Fortman, C. S. J. Cazin, A. M. Z. Slawin, C. Lhermitte, R. Prabhakar, M. E. Germain, T. Palluccio, S. P. Nolan, E. V. Rybak-Akimova, M. Temprado, B. Captain, C. D. Hoff, *J. Am. Chem. Soc.* **2011**, *133*, 1290–1293.
- (22) (a) H. D. Velazquez, F. Verpoort, *Chem. Soc. Rev.* **2012**, *41*, 7032–7060. (b) E. Levin, E. Ivry, C. E. Diesendruck, N. G. Lemcoff, *Chem. Rev.* **2015**, *115*, 4607–4692. (c) F. Godoy, C. Segarra, M. Poyatos, E. Peris, *Organometallics* **2011**, *30*, 684–688. (d) H. Türkmen, L. Pelit, B. Çetinkaya, *J. Mol. Catal. A: Chemical* **2011**, *348*, 88–93.
- (23) Q.-X. Liu, H.-L. Li, X.-J. Zhao, S.-S. Ge, M.-C. Shi, G. Shen, Y. Zang, X.-G. Wang, *Inorg. Chim. Acta* **2011**, *376*, 437–445.
- (24) (a) H. Shirasaki, M. Kawanishi, H. Yamada, R. Arakawa, S. Sakaguchi, *J. Organomet. Chem.* **2013**, *726*, 46–55. (b) D. T. Weiss, P. J. Altmann, S. Haslinger, C. Jandl, A. Pothig, M. Cokoja, F. E. Kuhn,

- Dalton Trans.* **2015**, *44*, 18329–18339.
- (25) (a) B. F. M. Kimmich, W. J. Marshall, P. J. Fagan, E. Hauptman, R. M. Bullock, *Inorg. Chim. Acta* **2002**, *330*, 52–58. (b) Ž. D. Bugarčić, S. T. Nandibewoor, M. S. A. Hamza, F. Heinemann, R. van Eldik, *Dalton Trans.* **2006**, 2984–2990.
- (26) Dioxygen was observed by GC-MS measurements in the gas phase of the reaction mixture. In spite of usage of H₂¹⁸O as a reaction solvent, only ¹⁶O₂ instead of ¹⁶O¹⁸O or ¹⁸O₂ was observed. This result suggests that the dioxygen was derived from decomposition of HSO₅⁻ ions. Such decomposition of Oxone[®] to evolve O₂ in the presence of transition-metal ions has been reported in literature. See: O. Gimeno, J. Rivas, M. Carbajo, T. Borralho, *World Acad. Sci., Eng. Tech.* **2009**, *57*, 223–226.
- (27) J. Limburg, J. S. Vrettos, H. Chen, J. C. de Paula, R. H. Crabtree, G. W. Brudvig, *J. Am. Chem. Soc.* **2001**, *123*, 423–430.
- (28) The importance of flexibility of ancillary ligands in accessing to the high-oxidation state of a palladium complex has been reported in literature. See: J. R. Khusnutdinova, N. P. Rath, L. M. Mirica, *Inorg. Chem.* **2014**, *53*, 13112–13129.
- (29) A. R. Parent, R. H. Crabtree, G. W. Brudvig, *Chem. Soc. Rev.* **2013**, *42*, 2247–2252.
- (30) S. A. Shafiee, J. Aarons, H. H. Hamzah, *J. Electrochem. Soc.* **2018**, *165*, H785–H798.
- (31) A. A. Shoukry, M. S. Mohamed, *Spectrochim. Acta A: Mol. Biomol. Spect.* **2012**, *96*, 586–593.
- (32) Ž. D. Bugarčić, G. Liehr, R. van Eldik, *J. Chem. Soc., Dalton Trans.*, **2002**, 951–956.
- (33) S. H. Yalkowsky, R. J. Orr, S. C. Valvani, *Ind. Eng. Chem. Fundam.* **1979**, *18*, 351–353.
- (34) Effects of steric hindrance in C-X bond cleavage of *o*-bromochlorobenzene have been reported in literature. See: C. Park, C. Menini, J. L. Valverde, M. A. Keane, *J. Catal.* **2002**, *211*, 451–463.
- (35) (a) C. L. Perrin, G. A. Skinner, *Org. Biol. Chem.* **1971**, *93*, 3389–3394. (b) T. Shoji, S. Ito, T. Okajima, J. Higashi, R. Yokoyama, K. Toyota, M. Yasufumi, N. Morita, *Eur. J. Org. Chem.* **2009**, 1554–1563.
- (36) The involvement of molecular oxygen in benzene oxygenation has been reported to suggest formation of radical intermediates in the course of the reaction. See ref.: (a) G. V. Buxton, J. R. Langan, J. R. L. Smith, *J. Phys. Chem.* **1986**, *90*, 6309–6313. (b) R. Volkamer, B. Klotz, I. Barnes, T. Imamura, K. Wirtz, N. Washida, K. H. Becker, U. Platt, *Phys. Chem. Chem. Phys.* **2002**, *4*, 1598–1610.
- (37) Y.-R. Luo, *Handbook of Bond Dissociation Energies in Organic Compounds*, 1st ed., CRC Press LLC: Boca Raton, FL, 2003; p 39.
- (38) The author has compared the ¹⁹F NMR signal of KF (10 mM) in D₂O in the presence of 0.1 M Oxone[®] as an authentic sample to unify the measurement conditions.
- (39) A. Karich, M. Kluge, R. Ullrich, M. Hofrichter, *AMB Express* **2013**, *3*, 5–13.
- (40) This is the first observation of a Pd^{II}-HSO₅ complex; however, a Pd^{II}-OO^tBu complex has been already reported by Akita and co-workers. See: T. Miyaji, M. Kujime, S. Hikichi, Y. Moro-oka, M. Akita, *Inorg. Chem.* **2002**, *41*, 5286–5295.
- (41) A palladium complex, having a terminal oxygen ligand, has been proposed based on theoretical studies. See: D. Munz, *Chem. Sci.* **2018**, *9*, 1155–1167.
- (42) The vibration frequency at 1011 cm⁻¹ was shifted from the parent frequency of the O-O bond stretching at 1035 cm⁻¹ due to coupling with stretchings of the pyridine and benzene rings in **10**.
- (43) C. Kabuto, S. Akine, T. Nemoto, E. Kwon, *J. Cryst. Soc. Jpn.* **2009**, *51*, 218–224.
- (44) G. M. Sheldrick, SIR97 and SHELX97, Programs for Crystal Structure Refinement, University of Göttingen, Göttingen (Germany), 1997.
- (45) (a) A. D. Becke, *Phys. Rev. A* **1988**, *38*, 3098–3100. (b) C. Lee, W. Yang, R. G. Part, *Phys. Rev. B* **1988**, *37*, 785–789.

- (46) M. E. Casida, C. Jamorski, K. C. Casida, D. R. Salahub, *J. Chem. Phys.* **1998**, *108*, 4439–4449.
- (47) M. Dolg, H. Stoll, H. Preuss, *Theor. Chim. Acta* **1993**, *85*, 441–450.
- (48) Gaussian 09, Revision D.01, M. J. Frisch, G. W. Trucks, H. B. Schlegel, G. E. Scuseria, M. A. Robb, J. R. Cheeseman, G. Scalmani, V. Barone, B. Mennucci, G. A. Petersson, H. Nakatsuji, M. Caricato, X. Li, H. P. Hratchian, A. F. Izmaylov, J. Bloino, G. Zheng, J. L. Sonnenberg, M. Hada, M. Ehara, K. Toyota, R. Fukuda, J. Hasegawa, M. Ishida, T. Nakajima, Y. Honda, O. Kitao, H. Nakai, T. Vreven, J. A. Montgomery, Jr., J. E. Peralta, F. Ogliaro, M. Bearpark, J. J. Heyd, E. Brothers, K. N. Kudin, V. N. Staroverov, R. Kobayashi, J. Normand, K. Raghavachari, A. Rendell, J. C. Burant, S. S. Iyengar, J. Tomasi, M. Cossi, N. Rega, J. M. Millam, M. Klene, J. E. Knox, J. B. Cross, V. Bakken, C. Adamo, J. Jaramillo, R. Gomperts, R. E. Stratmann, O. Yazyev, A. J. Austin, R. Cammi, C. Pomelli, J. W. Ochterski, R. L. Martin, K. Morokuma, V. G. Zakrzewski, G. A. Voth, P. Salvador, J. J. Dannenberg, S. Dapprich, A. D. Daniels, Ö. Farkas, J. B. Foresman, J. V. Ortiz, J. Cioslowski, D. J. Fox, Gaussian, Inc., Wallingford CT, 2009.

Concluding remarks

In this research, the author has prepared and characterized 4d-transition-metal complexes having *N*-heterocyclic carbene (NHC) ligands to develop unique catalytic systems for providing useful reactions as effective methods to tackle environmental and energy issues, which should be solved by world-wide efforts in the future. Especially, the author has focused on the preparation and characterization of metal-oxyl complexes and the development of unique catalytic reactions in water based on the oxyl complexes as reactive species.

In Chapter 2, the author has described synthesis and characterization of novel two Ru^{II} complexes with pincer-type tridentate ligands on the basis of crystallographic and spectroscopic analyses. The methylene-bridged NHC ligand coordinated in a meridional manner with large structural distortion, which is maintained even in solution in the temperature range of 298 – 348 K. In the complexes, intramolecular CH/ π interaction between *i*Pr groups of the NHC moieties and one of the pyridine rings in the bpy ligand assists the fixation of the distorted structure of the tridentate NHC ligand. The NHC ligands have been demonstrated to show a strong σ -donating ability to the Ru^{II} center, compared to pyridine or its π -conjugated analogs, lowering the oxidation potentials of the Ru^{II}/Ru^{III} redox couples. These two Ru^{II} complexes can be oxidized by a 1e⁻-oxidant in acetonitrile to afford the corresponding Ru^{III} complexes, which have been characterized by several spectroscopic analyses and theoretical studies.

In Chapter 3, on the basis of the properties of NHC ligands in ruthenium complexes, the author has described successful formation and characterization of the first Ru^{III}-oxyl (Ru^{III}-O•) complex, which is electronically equivalent to the corresponding Ru^{IV}=O species, with use of a tridentate NHC ligand in acidic water. The strategy to elongate the metal-oxo bond by the strong *trans* influence of the NHC ligands to reduce the π -bonding interaction between the metal center and the oxo ligand allows the author to provide the Ru^{III}-oxyl complex bearing strong radical character as a new category of reactive metal-oxygen species. The Ru^{III}-O• complex exhibits high reactivity in catalytic oxidation of organic substrates, including benzaldehyde derivatives in the presence of a Ce^{IV} complex as a sacrificial oxidant in acidic water. In addition, the oxidation reaction includes hydrogen-atom abstraction from the substrate in a pure radical manner as the rate-determining step due to the strong radical character.

In the research described in Chapter 4, the strong radical character of Ru^{III}-O• species, as elucidated in Chapter 3 of this thesis, has been applied to an efficient catalytic oxidative cracking of benzene rings (OBC) of benzene and its derivatives for the first time. The OBC reaction has been demonstrated to afford formic acid and carboxylic acids as products, the latter of which inherit substituents originally attached to the aromatic rings. Formic acid is used as a dihydrogen source in water at low temperatures; actually, successful H₂ evolution has been achieved from the OBC reaction mixture using a Rh^{III} catalyst with simple pH adjustment of the reaction solution. In addition, substituent effects on the aromatic rings switched the oxidation sites; *i.e.*, the benzylic C-H moiety attached to an electron-deficient aromatic ring is oxidized through C-H abstraction, whereas the C=C bonds of the electron-rich aromatic rings are oxidatively cleaved in the OBC reaction. The clear selectivity of the aromatic-ring oxidations in the OBC reaction derives from the electrophilic and strong radical character of the Ru^{III}-O• complex as the active species, and the OBC reactions proceed through the electrophilic addition of the Ru^{III}-O• complex to the aromatic ring.

In the work described in Chapter 5, halogenated benzene derivatives, which have not been oxidized effectively by Ru^{III}-O• species developed in Chapters 3 and 4, have been catalytically oxidized by a palladium complex having a tridentate NHC ligand with the use of Oxone[®] as a cheaper sacrificial oxidant

than Ce^{IV} salts used for the reactions mentioned in Chapters 3 and 4. In particular, chlorinated benzene derivatives can be effectively oxidized compared to brominated or fluorinated one. Introduction of electron-donating substituents to the chlorinated benzenes promotes the reaction, whereas bulky bromo substituents decelerate the reaction, indicating that the reaction proceeds through electrophilic addition of reactive species to the *ipso* position of the chloro groups on the aromatic rings. The kinetic analysis on the reactions has revealed a pre-equilibrium process between the reactive species and substrates. Although the reactive species in the system have yet to be clarified, precursors formed from the reaction of the Pd^{II} catalyst with Oxone[®] have been characterized as $\text{Pd}^{\text{II}}\text{-HSO}_5$ and $\text{Pd}^{\text{III}}\text{-O}\cdot$ species.

Throughout this research, the author has provided a break-through in metal-oxo chemistry using strongly σ -donating NHC ligands, as represented by a rule-breaking $\text{Ru}^{\text{III}}\text{-O}\cdot$ complex, and also has developed unique catalytic oxidations in water, which are in sharp contrast to those performed by conventional $\text{Ru}^{\text{IV}}\text{=O}$ complexes. Consequently, this work has provided useful conversion of harmful and inert pollutants to useful materials such as formic acid as a hydrogen reservoir using metal-oxyl complexes as reactive intermediates and deeper mechanistic insights into the reaction. Therefore, the $\text{Ru}^{\text{III}}\text{-O}\cdot$ complex and a probable $\text{Pd}^{\text{III}}\text{-O}\cdot$ species presented in this thesis should be recognized as important species in oxidation chemistry from viewpoints of not only academic interests in basic research but also world-wide efforts to solve energy and environmental problems in the future. Hopefully, my research will pave a reliable way to the establishment of a sustainable society and improvement of our lives through the selective and oxidative conversion of persistent pollutants in environments into useful energy sources under mild conditions.

List of publications and supplementary publications

List of publications

- [1] Ruthenium(II) complexes having a pincer-type ligand with two *N*-heterocyclic carbene moieties
Yoshihiro Shimoyama, Tomoya Ishizuka, Hiroaki Kotani, Takahiko Kojima
Z. Anorg. Allg. Chem. **2018**, *644*, 611–615.
- [2] A ruthenium(III)-oxyl complex bearing strong radical character
Yoshihiro Shimoyama, Tomoya Ishizuka, Hiroaki Kotani, Yoshihito Shiota, Kazunari Yoshizawa, Kaoru Mieda, Takashi Ogura, Toshihiro Okajima, Shunsuke Nozawa, Takahiko Kojima
Angew. Chem., Int. Ed. **2016**, *55*, 14041–14045.
- [3] Catalytic oxidative cracking of benzene rings in water
Yoshihiro Shimoyama, Tomoya Ishizuka, Hiroaki Kotani, Takahiko Kojima
ACS Catal. **2019**, *9*, 671–678.

Supplementary publications

- [4] Catalytic substrate oxidation by ruthenium(II)-aqua complexes bearing *N*-heterocyclic carbene ligands
Yoshihiro Shimoyama
Bull. Jpn. Soc. Coord. Chem. **2017**, *69*, 72–74 (Award paper).

List of patents

- [5] 有害芳香族化合物の分解方法
Takahiko Kojima, Yoshihiro Shimoyama, Tomoya Ishizuka, Hiroaki Kotani
特開 2018-138082
- [6] 酸化触媒、ハロゲン化芳香族化合物の酸化分解方法
Takahiko Kojima, Yoshihiro Shimoyama, Tomoya Ishizuka, Hiroaki Kotani
特願 2018-035192

Acknowledgements

The author gives his maximum appreciation to Professor Takahiko Kojima for his tremendous direction of the author's research. Prof. Kojima frequently encouraged him and gave him fruitful on-target comments for not only his research but also ideal attitudes in his future life. The author also sincerely thanks Prof. Kojima for his efforts to complete not only all of the author's thesis but also published papers.

The author also appreciates Dr. Tomoya Ishizuka for his guidance in the author's research with a plenty of academic, scientific advices and patience. The author sincerely thanks Dr. Ishizuka for his thoughtful efforts to improve not only this thesis but also the author's master, bachelor thesis, and published papers.

The author's thanks are also given to Dr. Hiroaki Kotani for his kind suggestions and advices in the author's research and life.

The author also would like to express his gratitude to Ms. Miyuki Nakahara for her kind supports and thoughtful preparation of manuscripts for his business trip to measurements and conferences.

The author would like to appreciate all of collaborators in his research. Prof. Kazunari Yoshizawa and Prof. Yoshihito Shiota in Institute for Materials Chemistry and Engineering and International Research Center for Molecular Systems, Kyushu University, should be appreciated due to their efforts to perform DFT calculations and valuable comments required to accomplish the author's research. The author would like to thank the late Prof. Takashi Ogura, Prof. Minoru Kubo, Dr. Sachiko Yanagisawa, Ms. Kaoru Mieda, Ms. Shoko Watanabe in University of Hyogo for their kind help in resonance Raman spectroscopic measurements and helpful discussion. The author appreciates Dr. Toshihiro Okajima in Kyushu Synchrotron Light Research Center for his efforts to measure X-ray absorption spectroscopy. Prof. Shunsuke Nozawa in High Energy Accelerator Research Organization should be also appreciated for his kind effort to measure X-ray absorption spectroscopy and to teach how to analyze EXAFS data.

The author also would like to thank Prof. Hirotaka Nagao, Dr. Tomoyo Suzuki-Misawa and the other students in Sophia University and Dr. Yumiko Nakajima and the other students in silicon chemistry team in National Institute of Advanced Industrial Science and Technology (AIST) for fruitful comments to the author's research in attendance of joint seminars.

The author would like to thank all of members he has shared a period of time so far in the Kojima laboratory (listed up below): Dr. Dachao Hong, Dr. Yuji Inui, Kazuhisa Ohtake, Dr. Shingo Ohzu, Dr. Takuya Sawaki, Dr. Hiroumi Mitome, Hidemi Ochiai, Dr. Yuta Saegusa, Kouhei Matsuzaki, Ryouyuke Kobayashi, Suzue Kaida, Misaki Makino, Atsuko Watanabe, Ryo Itagaki, Fumiya Ogishima, Hiroki Kajii, Takumi Sugiyama, Tomomi Yagi, Bianca Pokrandt, Wataru Suzuki, Keiyu Komamura, Chiaki Takayama, Miki Fujino, Shumpei Ohkawa, Kenta Satonaka, Hiroaki Shiiba, Bruno Ogawa, Masaki Itogawa, Aya Oshiro, Takahisa Nishibu, Yuto Tsukakoshi, Takako Tsunematsu, Taichi Kogawa, Muneaki Hashimoto, Momoka Horimoto, Mitsuyo Takeuchi, Takuya Kawanishi, Shogo Tanaka, Hinatsu Shimomura, Hiroto Fujisaki, Wang Dan, Emi Aoki, Keiichi Sasaki, Takafumi Suzuki, Yui Shinagawa, Nanase Namura.

Finally, the author sincerely appreciates his father, mother and little sister for their emotional and financial supports in his 9-years academic life.

February 2019
Yoshihiro Shimoyama

Kojima laboratory
Department of Chemistry
University of Tsukuba